Growth and Spectroscopy of the Two-dimensional Topological Insulator Bismuthene on SiC(0001)

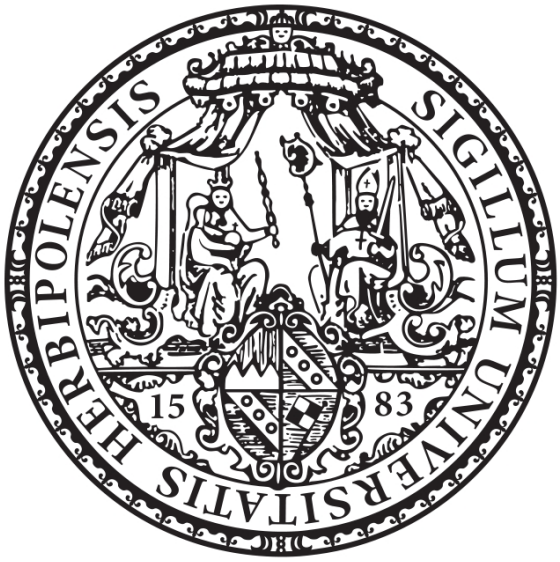

Dissertation zur Erlangung des
naturwissenschaftlichen Doktorgrades der
Julius-Maximilians-Universität Würzburg

vorgelegt
von

Rudolf Raul Albert Stühler
aus Würzburg

Würzburg, im September 2022

Eingereicht bei der Fakultät für Physik und Astronomie am

26.09.2022

Gutachter der Dissertation

1. Gutachter: Prof. Dr. Ralph Claessen
2. Gutachter: Prof. Dr. Friedrich Reinert
3. Gutachter: Prof. Dr. Peter Wahl

Prüfer des öffentlichen Promotionskolloquiums

1. Prüfer: Prof. Dr. Ralph Claessen
2. Prüfer: Prof. Dr. Friedrich Reinert
3. Prüfer: Prof. Dr. Peter Wahl
4. Prüfer: Prof. Dr. Giorgio Sangiovanni

Tag des öffentlichen Promotionskolloquiums:

02.06.2023

Doktorurkunde ausgehändigt am:

Abstract

A plethora of novel material concepts are currently being investigated in the condensed matter research community. Some of them hold promise to shape our everyday world in a way that silicon-based semiconductor materials and the related development of semiconductor devices have done in the past. In this regard, the last decades have witnessed an explosion of studies concerned with so called "quantum materials" with emerging novel functionalies. These could eventually lead to new generations of electronic and/or spintronic devices. One particular material class, the so called topological materials, play a central role. As far as their technological applicability is concerned, however, they are still facing outstanding challenges to date.

Predicted for the first time in 2005 [1–3] and experimentally verified in 2007 [4], two-dimensional topological insulators (2D TIs) (a.k.a. quantum spin Hall insulators) exhibit the outstanding property of hosting spin-polarized metallic states along the boundaries of the insulating 2D bulk material, which are protected from elastic single-particle backscattering and give rise to the quantum spin Hall effect (QSHE). Owing to these peculiar properties the QSHE holds promise for dissipationless charge and/or spin transport. However, also in todays best 2D TIs the observation of the QSHE is still limited to cryogenic temperatures of maximum 100 K [5]. Here, the discovery of bismuthene on SiC(0001) [6, 7] has marked a milestone towards a possible realization of the QSHE at or beyond room-temperature owing to the massively increased electronic bulk energy gap on the order of 1 eV. This thesis is devoted to and motivated by the goal of advancing its synthesis and to build a deeper understanding of its one-particle and two-particle electronic properties that goes beyond prior work in Refs. [6–8].

Regarding the aspect of material synthesis, an improved growth procedure for bismuthene is elaborated that increases the domain size of the material considerably (by a factor of $\approx 3.2 - 6.5$ compared to prior work in Ref. [7]). The improved film quality is an important step towards any future device application of bismuthene, but also facilitates all further basic studies of this material.

Moreover, the deposition of magnetic transition metals (Mn and Co) on bismuthene is investigated. Thereby, the formation of ordered magnetic Bi-Mn/Co alloys is realized, their structure is resolved with scanning tunneling microscopy (STM), and their pristine electronic properties are resolved with scanning tunneling spectroscopy (STS) and photoemission spectroscopy (PES). It is proposed that these ordered magnetic Bi-Mn/Co-alloys offer the potential to study the interplay between magnetism and topology in bismuthene in the future.

In this thesis, a wide variety of spectroscopic techniques are employed that aim to build an understanding of the single-particle, as well as two-particle level of description of bismuthene's electronic structure. The techniques involve STS and angle-resolved PES (ARPES) on the one hand, but also optical spectroscopy and time-resolved ARPES (trARPES), on the other hand. Moreover, these experiments are accompanied by advanced numerical modelling in form of *GW* and Bethe-Salpeter equation calculations provided by our theoretical colleagues. Notably, by merging many experimental and theoretical techniques, this work sets a benchmark for electronic structure investigations of 2D materials in general.

Based on the STS studies, electronic quasi-particle interferences in quasi-1D line defects in bismuthene that are reminiscent of Fabry-Pérot states are discovered. It is shown that they point to a hybridization of two pairs of helical boundary modes across the line defect, which is accompanied by a (partial) lifting of their topological protection against elastic single-particle backscattering.

Optical spectroscopy is used to reveal bismuthene's two-particle elecronic structure. Despite its monolayer thickness, a strong optical (two-particle) response due to enhanced electron-hole Coulomb interactions is observed. The presented combined experimental and theoretical approach (including *GW* and Bethe-Salpeter equation calculations) allows to conclude that two prominent optical transitions can be associated with excitonic transitions derived from the Rashba-split valence bands of bismuthene. On a broader scope this discovery might promote further experiments to elucidate links of excitonic *and* topological physics.

Finally, the excited conduction band states of bismuthene are mapped in energy and momentum space employing trARPES on bismuthene for the first time. The direct and indirect band gaps are succesfully extracted and the effect of excited charge carrier induced gap-renormalization is observed. In addition, an exceptionally fast excited charge carrier relaxation is identified which is explained by the presence of a quasi-metallic density of states from coupled topological boundary states of domain boundaries.

Zusammenfassung

Zahlreiche neuartige Materialkonzepte werden derzeit in der Festkörperforschung untersucht. Einige von ihnen haben das Potenzial, unsere Alltagswelt in einer Weise zu beeinflussen, wie es Halbleitermaterialien auf Siliziumbasis und die damit verbundene Entwicklung von Halbleiterbauelemente in der Vergangenheit getan haben. In diesem Zusammenhang gab es in den letzten Jahrzehnten eine regelrechte Flut von Untersuchungen zu so genannten "Quantenmaterialien" mit völlig neuen Funktionalitäten. Diese könnten in Zukunft schließlich zu einer neuen Generation von elektronischen und/oder spintronischen Bauelementen führen. Eine spezielle Materialklasse, die so genannten topologischen Materialien, spielen dabei eine wichtige Rolle. Hinsichtlich ihrer technologischen Anwendbarkeit stehen sie jedoch bis heute vor großen Herausforderungen.

Zweidimensionale topologische Isolatoren (2D TIs) (auch bekannt als Quanten Spin Hall Isolatoren) wurden erstmals 2005 vorhergesagt [1–3] und schließlich 2007 experimentell bestätigt [4]. Diese Materialien haben die außergewöhnliche Eigenschaft, dass sie spinpolarisierte metallische Zustände entlang der Grenzen des isolierenden 2D-Volumenmaterials aufweisen, die vor elastischer Ein-Teilchen-Rückstreuung geschützt sind und damit den Quanten-Spin-Hall-Effekt (QSHE) begründen. Aufgrund dieser besonderen Eigenschaften verspricht der QSHE einen dissipationsfreien Ladungs- und/oder Spintransport. Allerdings ist die Beobachtung des QSHE auch in den gegenwärtig am besten entwickelten 2D-TIs immer noch auf kryogene Temperaturen von maximal 100 K [5] beschränkt. In diesem Zusammenhang war die Entdeckung von Bismuthen (engl. bismuthene) auf SiC(0001) [6, 7] ein Meilenstein in Bezug auf eine mögliche Realisierung des QSHE bei oder oberhalb von Raumtemperatur aufgrund der massiv vergrößerten elektronischen Volumenenergielücke in der Größenordnung von 1 eV. Dieser Arbeit liegt das Ziel und die Motivation zugrunde, die Synthese von Bismuthen zu verbessern und darüber hinaus das derzeitige Verständnis der elektronischen Ein- und Zweiteilchen-Eigenschaften dieses Materials (vgl. die Arbeiten von Refs. [6–9]) zu erweitern.

Was den Aspekt der Materialsynthese betrifft, so wird ein verbessertes Wachstumsverfahren für Bismuthen erarbeitet, das die Domänengröße des Materials beträchtlich erhöht (um einen Faktor von $\approx 3.2 - 6.5$ im Vergleich zu früheren Arbeiten in Ref. [7]). Die verbesserte Filmqualität stellt einen wichtigen Schritt in Hinblick auf zukünftige Anwendungen von Bismuthen dar, erleichtert darüber hinaus aber auch alle grundlegenden Untersuchungen mit diesem Material.

Darüber hinaus wird die Deposition von magnetischen Übergangsmetallen (Mn und Co) auf Bismuthen erforscht. So konnten geordnete magnetische Bi-Mn/Co-Legierungen hergestellt werden, deren Struktur mit Rastertunnelmikroskopie (STM) und deren elektronische Eigenschaften mit Rastertunnelspektroskopie (STS) und Photoemissionsspektroskopie (PES) aufgelöst wurden. Es wird nahe gelegt, dass diese geordneten magnetischen Bi-Mn/Co-Legierungen das Potenzial bieten, die Wechselwirkung zwischen Magnetismus und Topologie in Bismuthen in Zukunft zu untersuchen.

In dieser Dissertation werden eine Vielzahl von spektroskopischen Techniken eingesetzt, die darauf abzielen, die elektronische Struktur von Bismuthen auf der Ein-Teilchen- und Zwei-Teilchen-Ebene zu verstehen. Die Techniken umfassen einerseits STS und winkelaufge-

löste PES (ARPES), andererseits aber auch optische Spektroskopie und zeitaufgelöste ARPES (trARPES). Darüber hinaus werden diese Experimente durch umfangreiche numerische Modellierungen in Form von *GW*-Rechungen und Lösungen der Bethe-Salpeter-Gleichung unterstützt, die von unseren theoretischen Kollegen durchgeführt wurden. Durch die Verknüpfung zahlreicher experimenteller und theoretischer Methoden setzt diese Arbeit auch einen Maßstab für die Untersuchung der elektronischen Struktur von 2D-Materialien im Allgemeinen.

Basierend auf den Untersuchungen mit STS werden elektronische Quasiteilchen Interferenzen in quasi-1D Liniendefekten in Bismuthen entdeckt, die an Fabry-Pérot Zustände erinnern. Dabei wird gezeigt, dass diese Interferenzen auf eine Hybridisierung zweier Paare helikaler Grenzmoden über den Liniendefekt hinweg hinweisen, was mit einer (teilweisen) Aufhebung ihres topologischen Schutzes gegen elastische Ein-Teilchen-Rückstreuung einhergeht.

Mit Hilfe optischer Spektroskopie wird die elektronische Zwei-Teilchen-Struktur von Bismuthen untersucht. Dabei ist trotz der Einzelschichtdicke eine starke optische, d.h. Zwei-Teilchen-, Antwort aufgrund der starken Elektron-Loch Coulomb-Wechselwirkungen zu beobachten. Der kombinierte experimentelle und theoretische Zugang (einschließlich *GW* Rechnungen und Lösungen der Bethe-Salpeter-Gleichung) erlaubt den Nachweis, dass zwei markante optische Übergänge Exzitonenanregungen sind, die von Valenzbändern von Bismuthen stammen, welche durch die Rashba-Wechselwirkung getrennt sind. Im weiteren Kontext könnte diese Entdeckung Anlass zu künftigen Experimenten sein, um die Zusammenhänge zwischen exzitonischer *und* topologischer Physik zu untersuchen.

Schließlich werden erstmals die angeregten Leitungsbandzustände von Bismuthen mit Hilfe von trARPES energie- und impulsaufgelöst gemessen. Dabei ist es gelungen, die direkte und indirekte Bandlücke zu ermitteln und zudem den Effekt einer Ladungsträger induzierten Bandlücken-Renormalisierung zu beobachten. Darüber hinaus wird eine außergewöhnlich schnelle Relaxation angeregter Ladungsträger nachgewiesen, die durch das Vorhandensein einer quasi-metallischen Zustandsdichte aufgrund gekoppelter topologischer Randmoden an Domänengrenzen erklärt wird.

CONTENTS

1 Introduction **1**
1.1 The rise of topological insulators in condensed matter physics 1
1.2 Outline of this thesis 3

I Background and Experimental Methods **7**

2 Bismuthene on SiC(0001): Paradigmatic blueprint for a large-gap 2D TI **9**
2.1 The atomic structure model 9
2.1.1 Silicon carbide as epitaxial growth template 9
2.1.2 The bismuthene monolayer 10
2.2 The electronic structure of bismuthene on SiC(0001) from DFT 11
2.2.1 Origins of the large band gap opening 11
2.2.2 2D bulk electronic structure calculation 12
2.2.3 The emergence of helical boundary states 14
2.3 Low-energy effective model 15
2.4 Observation of a (helical) Tomonaga-Luttinger liquid in the edge states of bismuthene 18

3 Methods for surface characterization **21**
3.1 Low energy electron diffraction 21
3.2 Scanning tunneling spectroscopy & microscopy 22
3.2.1 The tunneling current 23
3.2.2 Lock-in spectroscopy 25
3.2.3 Real-space imaging 25
3.3 Photoemission spectroscopy 26
3.3.1 The (time-independent) photoemission process 26
3.3.2 Angle-resolved photoemission spectroscopy 31
3.3.3 Time- and angle-resolved photoemission spectroscopy 32
3.3.4 X-ray photoemission spectroscopy 35
3.3.5 Resonant photoemission spectroscopy 35
3.4 Photo-modulated reflectance 36
3.4.1 Experimental setup 37
3.4.2 Derivation of the PR lineshape 38

II Results and Discussion 41

4 Optimization of bismuthene film epitaxy 43
- 4.1 Preparation of the SiC(0001) (1 × 1) surface by H-etching . . . 43
  - 4.1.1 The dehydrogenated SiC(0001) (1 × 1) surface . . . 46
- 4.2 Molecular beam epitaxy of bismuthene films . . . 49
  - 4.2.1 Setup for molecular beam epitaxy and basic bismuthene growth recipe 50
  - 4.2.2 Strategy to achieve larger domains . . . 51
  - 4.2.3 Achieving a full bismuthene surface coverage . . . 55
  - 4.2.4 Optimized bismuthene growth . . . 58
  - 4.2.5 Discussion . . . 60

5 Growth and spectroscopy of manganese- and cobalt-induced alloys on bismuthene 61
- 5.1 Manganese-induced surface reconstruction on bismuthene samples . . . 62
  - 5.1.1 Growth and structural investigation . . . 62
  - 5.1.2 Electronic band structure of the Bi/Mn-alloy . . . 64
  - 5.1.3 Tunneling spectroscopy at the bismuthene – Bi/Mn-alloy interface . . 67
- 5.2 Cobalt-induced surface reconstruction on bismuthene samples . . . 70
  - 5.2.1 Growth and structural investigation . . . 70
  - 5.2.2 Photoemission spectroscopy on the Bi/Co-alloy . . . 73
  - 5.2.3 Tunneling spectroscopy at the bismuthene – Bi/Co-alloy interface . . 76
- 5.3 Discussion . . . 78

6 Coupling of topological edge states in 1D line defects of bismuthene 81
- 6.1 Structural properties of bismuthene domain boundaries . . . 82
  - 6.1.1 Formal classification and topographic characterization . . . 82
  - 6.1.2 Origin of internal asymmetry and candidate atomic structure models 83
- 6.2 Proximity induced lifting of topological protection in bismuthene domain boundaries . . . 86
  - 6.2.1 Concept of inter-edge coupling: the free bismuthene edge *vs.* the domain boundary . . . 86
  - 6.2.2 Lifting of topological protection by proximity induced coupling of helical edge states . . . 90
  - 6.2.3 Linear dispersion relation of electronic Fabry-Pérot states . . . 94
  - 6.2.4 Coupling between two Fabry-Pérot resonators . . . 96
- 6.3 Discussion . . . 99

7 Optical spectroscopy of bismuthene and the detection of excitons 101
- 7.1 Single-particle band gap: Experiment vs. theory . . . 101
- 7.2 Optical spectroscopy, optical gap and excitonic resonances . . . 105
  - 7.2.1 Protection of bismuthene against oxidation for optical experiments . . 106

7.2.2 Optical response of the bismuthene monolayer . . . 108
7.2.3 Interpretation of the A- and B-peak in photo-reflectance as excitons based on Bethe-Salpeter equation calculations . . . 111
7.3 Discussion . . . 113

8 Mapping the excited state gap and temporal dynamics of transiently occupied charge carriers in bismuthene 115
8.1 Excited state electronic structure mapping . . . 115
8.1.1 Excitation with $h\nu_{\mathrm{pump}} = 1.55\,\mathrm{eV}$ . . . 117
8.1.2 Excitation with $h\nu_{\mathrm{pump}} = 3.10\,\mathrm{eV}$ . . . 121
8.2 Determination of the excited state band-gap . . . 125
8.3 Energy and momentum resolved relaxation of excited charge carriers . . . 127
8.3.1 Decay time: planar vs. stepped sample . . . 130
8.3.2 Arrival time: planar vs. stepped sample . . . 131
8.4 Discussion . . . 131

9 Conclusion 133

III Appendix 137

A Theoretical concepts for describing condensed matter 139
A.1 The many-body Hamiltonian . . . 139
A.2 Concepts of density functional theory . . . 140
A.3 Concepts of many-body perturbation theory . . . 142
A.4 The Bethe-Salpeter equation . . . 145
A.5 Topological classification of condensed matter . . . 146
A.5.1 Berry phase, Berry connection, and Berry curvature . . . 147
A.5.2 $\mathcal{Z}_2$ topological invariant . . . 148

B Additional Information on the growth of bismuthene on miscut SiC substrates 149

C Additional Information on the growth and spectroscopy of manganese- and cobalt-induced alloys on bismuthene 151
C.1 STM line profile of the Bi/Mn-alloy . . . 151
C.2 ARPES from a mixed phase of bismuthene and Bi/Mn-alloy . . . 152
C.3 STM topography of Co-induced defects on bismuthene . . . 153
C.4 CLAHE applied to Bi/Co-alloy constant energy ARPES maps . . . 154

D XPS of bismuthene, Bi/Mn-alloy, and Bi/Co-alloy samples 155
D.1 XPS of pristine bismuthene . . . 155
D.2 XPS of bismuthene after storage in N_2 inert gas atmosphere . . . 156
D.3 XPS and STM of bismuthene after exposure to oxygen . . . 157

D.4 XPS of the Bi/Co-alloy . . . 158
D.5 XPS of the Bi/Mn-alloy . . . 159
D.6 XPS fit results . . . 160

E Additional Information on domain boundaries in bismuthene 161
E.1 STM of a long domain boundary . . . 161
E.2 Mirror operation on free zigzag edge . . . 162
E.3 Fabry-Pérot states in different domain boundaries . . . 163
E.4 Variation of the valence band onset measured at different domain boundaries 167

F Additional Information on optical spectroscopy of bismuthene 169
F.1 Spatial variation of the STS bulk spectrum . . . 169
F.2 Influence of bismuthene oxidation on the photo-reflectance spectrum . . . 171

G Additional Information on trARPES of bismuthene 173
G.1 EDC fit of excited states at the K-point . . . 173
G.2 Band mapping at $h\nu = 1.55\,\mathrm{eV}$ . . . 174
G.3 Simulation of photoemission matrix element effects in constant energy ARPES 175
G.4 EDC fits at $h\nu = 3.10\,\mathrm{eV}$ . . . 177
G.5 Thickness dependence of the DFT band structure of bismuthene . . . 179
G.6 Numerical fit of excited state valence and conduction band dispersions . . . 180

Bibliography 181

List of publications 197

Danksagung 199

List of Figures

1.1 Helical edge states at the boundary of a 2D TI 2

2.1 Atomic structure model and reciprocal lattice of Bi/SiC 10
2.2 2D DFT band structure of bismuthene on SiC(0001) 13
2.3 DFT and open-boundary tight-binding calculations of bismuthene on SiC(0001) ribbon slabs 15
2.4 Band structure of the minimal tight-binding model of bismuthene on SiC(0001) 17
2.5 Helical Tomonaga-Luttinger liquid in the edge channels of bismuthene 19

3.1 Schematic illustration of LEED 21
3.2 Schematic illustration of STM 23
3.3 The photoemission process 28
3.4 The angle-resolved photoemission process 32
3.5 The time-resolved ARPES setup 33
3.6 The photoreflectance setup 37

4.1 Target temperature curve for H-etching of SiC 44
4.2 Overview STM images of flat and stepped SiC substrates after H-etching . . 45
4.3 Controlling the step distribution on 4° miscut SiC(0001) substrates 46
4.4 Thermal desorption of hydrogen from the SiC surface 48
4.5 Molecular beam epitaxy setup and temperature curve for bismuthene growth 50
4.6 Schematics of atomistic processes during bismuthene growth 51
4.7 Initial stage of bismuthene growth 53
4.8 Evolution of bismuthene film coverage with time 55
4.9 Sensitivity of bismuthene growth to small variations of the sample temperature 57
4.10 Domain size distribution after completed film growth 59

5.1 Manganese induced surface reconstruction on a bismuthene sample 63
5.2 ARPES band structure of the Bi/Mn-alloy 65
5.3 Tunneling spectroscopy at the bismuthene – Bi/Mn-alloy interface 68
5.4 Cobalt induced surface reconstruction on a bismuthene sample 71
5.5 Photoemission spectroscopy on the Bi/Co-alloy 74
5.6 Atomically resolved spectroscopy at the bismuthene – Bi/Co-alloy interface . 77

6.1 Schematic of domain boundary formation 83
6.2 STM characterization of a domain boundary 84
6.3 57-edge and 558-domain boundary 86
6.4 Free vs. coupled helical edge states 87

6.5 Domain boundary and zigzag edge topography . . . 89
6.6 Electronic properties of free zigzag edge states . . . 91
6.7 Electronic properties of a domain boundary . . . 93
6.8 Linear dispersion of Fabry-Pérot states . . . 95
6.9 Spectroscopy of a coupled Fabry-Pérot resonator . . . 97
6.10 2D TI Fabry-Pérot devices . . . 99

7.1 Bismuthene sample characterization . . . 102
7.2 Protection of bismuthene by inert gas atmosphere . . . 108
7.3 PR measurements on a bismuthene monolayer . . . 109
7.4 Spatial modulation of the optical response of bismuthene . . . 111
7.5 Ab-initio *GW*+BSE results . . . 112

8.1 Fundamental, optical, and excited state gap . . . 116
8.2 Mapping of the excited charge carriers in bismuthene with $h\nu_{\mathrm{pump}} = 1.55\,\mathrm{eV}$ 118
8.3 Mapping of the excited charge carriers in bismuthene with $h\nu_{\mathrm{pump}} = 3.10\,\mathrm{eV}$ 122
8.4 Time-resolved band gap renormalization . . . 126
8.5 Excited charge carrier relaxation dynamics. . . . 129

B.1 Growth of bismuthene with high edge state density . . . 150

C.1 STM line profile of the Bi/Mn-alloy . . . 151
C.2 ARPES from a mixed phase of bismuthene and Bi/Mn-alloy . . . 152
C.3 Co induced atomic defects on bismuthene . . . 153
C.4 CLAHE applied to Bi/Co-alloy constant energy ARPES maps . . . 154

D.1 XPS of pristine bismuthene . . . 155
D.2 XPS of bismuthene after storage in N_2 inert gas atmosphere . . . 156
D.3 XPS and STM of bismuthene after exposure to oxygen . . . 157
D.4 XPS of the Bi/Co-alloy . . . 158
D.5 XPS of the Bi/Mn-alloy . . . 159

E.1 STM constant current image of long domain boundary . . . 161
E.2 Mirror operation on free zigzag edge . . . 162
E.3 Fabry-Pérot states in different domain boundaries with varying lengths . . . 164
E.4 Variation of the valence band onset measured at the vicinity of DBs . . . 167

F.1 Local variations of STS spectra . . . 170
F.2 Influence of oxidation on PR spectrum . . . 171

G.1 Numerical fit of excited state spectrum EDC at the *K*-point . . . 173
G.2 Transiently occupied in-gap states (complementary to Fig. 8.2**b**) . . . 174
G.3 ARPES simulation using the *chinook* program . . . 176
G.4 Excited state mapping with $h\nu_{\mathrm{pump}} = 3.10\,\mathrm{eV}$ (complementary to Fig. 8.3) . 177

G.5 Thickness dependence of DFT band structure 179
G.6 EDC fits for the determination of the band gap re-normalization 180

List of Tables

4.1 Growth parameters for Fig. 4.7 55
4.2 Growth parameters for Fig. 4.10 59

8.1 EDC fits vs. *GW* in Fig. 8.3 122
8.2 Best fit results of decay spectra in Fig. 8.5**e** 128

D.1 XPS peak fit results 160

E.1 Scan parameters for DB segments in Fig. E.3 163

G.1 Parameters for ARPES simulation in Fig. G.3**d** using the *chinook* program . 175
G.2 Best fit results for EDC fits in Fig. G.4 177

List of Acronyms

1D One-dimensional

2D Two-dimensional

3D Three-dimensional

ARPES Angle-resolved photoemission/photoelectron spectroscopy

ARIPES Angle-resolved inverse photoemission/photoelectron spectroscopy

a. u. / arb. units arbitrary units

Bi/SiC Bismuthene on 4H-SiC(0001)

BSE Bethe-Salpeter equation

BZ Brillouin zone

CLAHE Contrast limited adaptive histogram equalization

DFT Density functional theory

DOS Density of states

EDC Energy distribution curve

FFT Fast Fourier transform

FWHM Full width at half maximum

GGA Generalized gradient approximation

IQHE Integer quantum Hall effect

LDOS Local density of states

LEED Low-Energy electron diffraction

MBE Molecular beam epitaxy

MDC Momentum distribution curve

QHE Quantum Hall effect

QPI Quasi-particle interference

QSHE Quantum spin Hall effect

QSHI Quantum spin Hall insulator

PES Photoemission/Photoelectron spectroscopy

PR Photoreflectance/Photomodulated reflectance

ResPES Resonant photoemission/photoelectron spectroscopy

RSM Reciprocal space mapping

SEM Scanning electron microscopy

SiC Silicon carbide

SOC Spin-orbit coupling

STM Scanning tunneling microscopy/microscope

STS Scanning tunneling spectroscopy/spectrum

SX Soft X-ray

TEM Transmission electron microscopy

TEY Total electron yield

TLL Tomonaga-Luttinger liquid

TMD Transmission metal dichalcogenide

trARPES Time- and angle-resolved photoemission/photoelectron spectroscopy

UHV Ultrahigh vacuum

XAS X-ray absorption spectroscopy

XPS X-ray photoemission/photoelectron spectroscopy

i Imaginary unit

$\vec{\sigma}$ Vector of standard Pauli matrices σ_1, σ_2, and σ_3

ϵ_0 dielectric constant of the vacuum: $8.854\,187\,812\,8 \times 10^{-12}\,\mathrm{F\,m^{-1}}$

$m_\mathbf{e}$ electron rest mass: $9.109\,383\,701\,5 \times 10^{-31}\,\mathrm{kg}$

e elementary charge: $1.602\,176\,634 \times 10^{-19}\,\mathrm{C}$

h Planck constant: $6.626\,070\,15 \times 10^{-34}\,\mathrm{J\,s}$

$\hbar$ $h/2\pi$: $1.054\,571\,817 \times 10^{-34}\,\mathrm{J\,s}$

CHAPTER 1

Introduction

This thesis advances the current state of research on the material system bismuthene on SiC(0001), a two-dimensional topological insulator (2D TI) reported for the first time in 2017 by Reis *et al.* [6].

1.1 The rise of topological insulators in condensed matter physics

It was a breakthrough to realize that topological properties of the electronic wavefunctions in condensed matter systems are connected to real experimental observables. The excitement for applying topological methods in solid state physics was sparked immensely when Thouless, Kohmoto, Nightingale, and den Nijs [10] discovered that the Hall conductivity (σ_{xy}) for a 2D electron gas forming Landau levels is quantized according to [11]

$$\sigma_{xy} \;=\; C\frac{e^2}{h}\,, \tag{1.1}$$

where the integer number C is a topological invariant called the Chern number [12, 13] (cf. Appendix Eq. (A.25)). Importantly, their theoretical description allowed to explain the near to perfect quantization of the Hall conductivity found by von Klitzing in the integer quantum Hall effect (IQHE) [14]. Within the theoretical framework of topology, it was possible to explain the astonishingly robust conductivity in the quantum Hall device by the fact that perturbations to the bulk system leave the topology (and therefore also C in Eq. (1.1)) unchanged as long as they do not close the energy gap or break the bulk symmetries. In that sense, the conductance quantization of σ_{xy} is said to be "topologically protected". Its independence on the impurity concentration as well as on the extent of the system is in stark contrast to electron transport in a topologically trivial material where impurities cause single-particle scattering events that can ultimately lead to localization. Naturally, this discovery has inspired expectations for novel applications of topological materials [15].

In 1988, Haldane established a Chern insulator model based on a graphene-like lattice which is subject to a specific alternating magnetic field that vanishes on the average [16]. In the following years, his discovery lead to an increased application of honeycomb lattice toy models as a paradigm for realizing also other topological insulator phases. Most notably, in 2005 Kane and Mele [1] discovered the topological class of 2D TIs, a.k.a. quantum spin Hall insulators (QSHI). The outstanding achievement was to recognize for the first time that a topological phase transition could be driven by the atomic spin-orbit coupling (SOC) instead of the strong magnetic field typically used in experiments to realize the quantum Hall phase [14]. This newly-discovered topological phase was characterized by a different

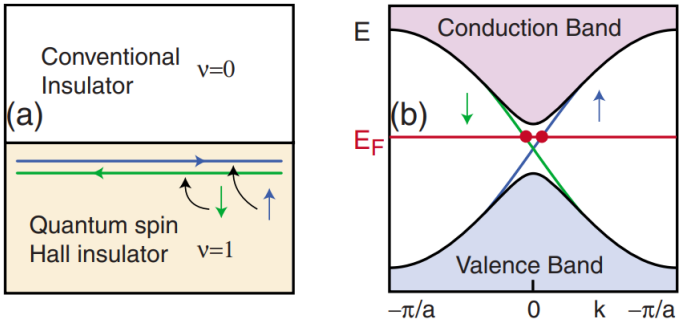

Figure 1.1: Helical edge states at the boundary of a 2D TI. – **(a),** A QSHI in direct proximity to an ordinary insulator. The bulk-boundary correspondence assures the presence of helical edge states strictly localized at the interface. **(b),** The band structure shows that the helical edge states, which are spin-polarized, disperse across the bulk energy gap of the 2D TI material. *Figure reprinted with permission from Ref. [11]. Copyright ©2010 by the American Physical Society.*

topological invariant, namely the $\mathcal{Z}_2$ index [17–19]. Different from the Chern number (C) which can take any integer value, the $\mathcal{Z}_2$ index (ν) only takes the values 0 or 1 (see Appendix Sec. A.5.2). Therefore, according to this $\mathcal{Z}_2$ topological classification any insulator is either a trivial insulator ($\nu = 1$) or a QSHI ($\nu = 1$).

The outstanding novel property of 2D TIs is that they give rise to the quantum spin Hall effect (QSHE), i.e., the emergence of helical electronic states located at the boundary of the material. In this context, "helical" means that the electron spin is tied to the direction of motion of the electrons. As in the case of the Chern insulators and the IQHE, the presence of crystalline defects that would typically act as (weak) potential scatters can not result in single-particle backscattering in the helical states of a 2D TI. But, why do these boundary states arise in the first place? Their existence is rooted in the inability to adiabatically transform a system with non-trivial topology into a system with trivial topology. Thus, at the interface of a topological and a trivial system (also at the boundary of a topological system and vacuum) the bulk energy gap must close which inevitably leads to the formation of metallic boundary states [11, 20], see Fig. 1.1. In general, this gives rise to the so-called *bulk-boundary correspondence*, which relates the bulk topology of the system to the presence of gapless boundary modes [11].

The 2D TI material studied and understood most profoundly to date is the HgTe/CdTe quantum well structure. In this material system, the proposed longitudinal conductance quantization of $G = 2e^2/h$ [1] could be measured for the first time [4]. Here, each helical edge state contributes as a single ballistic quantum channel with a conductance of $G = e^2/h$ [21]. Soon after, it was proven that the conductance was mediated indeed by edge channel transport [22] and, moreover, that these edge channels are spin polarized [23]. Since then, very sophisticated and extremely elaborate nanofabrication methods have been developed for this system. However, one of the major limiting factors still is the need to keep these samples at cryogenic temperatures ($\approx 15\,\mathrm{K}$) to make practical use of their helical edge states [24].

Considerable research effort in condensed matter physics to date is therefore devoted to

finding superior 2D TI materials. In this regard, the exfoliated van-der-Waals material 1T'-WTe_2 can be considered a milestone discovery. In this material the QSHE could be measured at a significantly higher temperature of up to 100 K [5]. But although van-der-Waals material based 2D TIs offer a plethora of new fundamental study cases, e.g., the interplay of topology and electron-electron correlations [25–27], these materials particularly suffer one adverse aspect, namely very poor production scalability. This is becasue either monolayers need to be exfoliated from a bulk crystal which is error prone and slow, or else if molecular beam epitaxy is employed for growth, so far only islands with sizes on the nanometer scale could be realized [28]. Thus, although a huge progress has been achieved in the study and development of 2D TIs since their first discovery, the gap between the state of fundamental research and real applications is still huge and most probably will require novel material systems to finally make practical use of the QSHE for a broader field of applications.

1.2 Outline of this thesis

The motivation of this work is to contribute filling this gap. Most importantly, in my work I was concerned with advancing the current state of knowledge and research about a very recently found 2D TI with superior material properties: bismuthene on SiC(0001) (a.k.a. Bi/SiC, or simply bismuthene) [6, 7]. It is a two-dimensional crystalline arrangement of bismuth atoms in a honeycomb lattice placed on the (0001) surface of the wide band gap semiconductor SiC. Due to its 2D bulk energy gap of ~ 1 eV, bismuthene is a prime candidate for achieving the QSHE at room-temperature and beyond. My work on bismuthene specifically included the following aspects:

- development of an optimized film growth, which is an important step towards a broader future application perspective of this material;
- broadening the basic knowledge of its (single-particle and multi-particle) electronic properties from tunneling, photoemission, and optical spectroscopy; and
- contrasting these experimental results with state of the art DFT, GW and Bethe-Salpeter equation calculations that were specifically provided to us in a reasearch collaboration.

On a broader perspective, this experimental work sets a benchmark for electronic structure investigations of 2D materials in general, as it combines a wide variety of spectroscopic techniques in combination with a very strong theoretical support. In the following, an overview of the content of the individual chapters of this thesis is provided.

Part I: Background and Experimental Methods

Chapter 2: Bismuthene on SiC(0001): Paradigmatic blueprint for a large-gap 2D TI

This chapter reviews the basic properties of bismuthene. Thereby, the basic structural and theoretical properties of bismuthene corresponding to the state of research prior to this

thesis are described in a nutshell.

Chapter 3: Methods for surface characterization

This chapter provides an overview of key concepts and methods used in this work to characterize and study bismuthene and surface systems in general with regard to their structural, electronic, and chemical properties.

Part II: Results and Discussion

Chapter 4: Optimization of bismuthene film epitaxy

First, the preparation of the SiC substrate by a dry hydrogen gas etching procedure for epitaxial growth of bismuthene is introduced. It is important to bear in mind, that the SiC substrate not only serves to stabilize the bismuthene monolayer, but is also a crucial component for shaping its desired electronic properties. Moreover, the hitherto poorly understood process of dehydrogenation of the SiC surface that is involved in the growth of bismuthene is analyzed.

It follows the eleboration of an advanced epitaxial growth scheme of bismuthene on the SiC substrate compared to the one presented in Refs. [6, 7]. One of the main deficiencies of prior work has been that the bismuthene film was suffering the formation of very small domains. In an attempt to enlarge the domain sizes, a substantial part of the phase space of growth parameters is explored and a deeper understanding of the microscopic processes during film growth is developed. To this end, a substantial increase of the domain size by a factor of $\approx 3.2-6.5$ compared to prior work in Ref. [7] is achieved, which is an important step to better resolve its intrinsic material properties and towards the applicability of bismuthene in future devices.

Chapter 5: Growth and spectroscopy of manganese- and cobalt-induced alloys on bismuthene

This chapter studies magnetic transition metal atoms (manganese and cobalt) deposited onto the bismuthene film in an attempt to intentionally modify time-reversal symmetry, which is fundamental to the realization of a quantum spin Hall state. This idea is motivated by the possibility to gain insights into the fundamentals of the celebrated topological protection of the helical edge states against single-particle backscattering. Instead of studying the effect of single magnetic atoms, which was impeded by a very high mobility of the atoms on the surface, the growth of ordered sub-monolayer thick surface reconstructions containing Mn- or Co-atoms in coexistence with pristine bismuthene was achieved. Intriguingly, the Mn- or Co-induced surface reconstructions grow as islands forming atomically precise interfaces to the bismuthene film. After having presented the preparation of these systems, their fundamental structural and electronic properties are studied by scanning tunneling microscopy (STM)

and photoemission spectroscopy (PES). Interestingly, indications are found in the angle-resolved PES (ARPES) band structure that point towards the prominent role of SOC in these new material systems.

Chapter 6: Coupling of topological edge states in 1D line defects of bismuthene

The growth of bismuthene on SiC(0001) is inevitably connected with the formation of domains that are separated by quasi-1D line defects, so called domain boundaries (DBs). Being (most probably) detrimental for the detection of a clean conductance quantization in future transport experiments, DBs can also be viewed as a functional element owing to their peculiar electronic characteristics. Their structural properties are inspected by STM, followed by scrutinizing their electronic properties on the atomic scale by scanning tunneling spectroscopy (STS). The emergence of quasi-particle scattering within the DBs is discovered, which is reminiscent of Fabry-Pérot resonances. This observation is coherently explained by an inter-edge coupling of two pairs of helical edge states mediated by their close proximity across the DB. The mutual edge coupling gives rise to enabled single-particle backscattering of right(left)-moving electrons on one side of the DB with left(right)-moving electrons of like spin character on the other side. The main result of the presented study is that spin-momentum locking and with it the topological protection is (partially) lifted without the need to break time-reversal symmetry. This observation is in line with theoretical proposals that motivate the use of such a helical edge state coupling scenario for the implementation of a spin-charge valve in a 2D TI device controlled by additionally applied gate voltage [29].

Chapter 7: Optical spectroscopy of bismuthene and the detection of excitons

This chapter addresses the electronic two-particle spectral properties of bismuthene on SiC(0001). As bismuthene can be regarded a representative of the class of two-dimensional materials, which are known to stand out in the field of excitons, a strong interest of studying excitons also in this 2D TI arises naturally. Bismuthene proves to be a prime study candidate due to its easily accessible optical band gap. Here, the electronic as well as the optical band-gap of bismuthene are compared by employing photo-modulated reflectivity (PR) and STS, combined with ab-initio *GW* and Bethe-Salpeter equation calculations. Moreover, signatures of exciton formation in bismuthene are reported for the first time.

These results present the first observations of excitons in a large-gap 2D TI. In contrast to optical studies conducted with topologically trivial transition metal dichalcogenides (TMDs), for which it is known that the combination of the hexagonal lattice geometry, a broken inversion symmetry, and strong spin-orbit interaction lead to optical selection rules altered by the *local* topology of the involved bands at the valleys [30], with the presented optical measurements on bismuthene the foundations may be laid to start the experimental scrutiny of finding a direct link between excitonic physics and *global* topology.

Chapter 8: Mapping the excited state gap and temporal dynamics of transiently occupied charge carriers in bismuthene

In this chapter, the full excited state electronic structure and decay dynamics of excited electronic states of bismuthene on SiC(0001) are mapped by ultra-fast time- and angle-resolved photoemission spectroscopy (trARPES). The involved temporal pump-probe cross-correlation in the femtosecond range allows us to dynamically observe the impact of photo-ionization, i.e., the generation of excitations between Fermi and vacuum level that are unoccupied in the ground state, and the subsequent relaxation of the electronic system. Specifically, the direct and indirect excited state electronic band gaps are extracted, the effect of a time-dependent band-gap renormalization due to a modified charge carrier screening is studied, and the ultra-fast relaxation pathway of excited charge carriers in momentum space is scrutinized for the first time. It is shown that the ultra-fast relaxation of excited charge carriers in bismuthene is likely to be mediated by the quasi-metallic density of states of the DBs, which arises from coupled helical edge states.

Part I

Background and Experimental Methods

CHAPTER 2

Bismuthene on SiC(0001): Paradigmatic blueprint for a large-gap 2D TI

Bismuthene is a 2D material with a honeycomb lattice structure. Owing to its orbital character and the essential influence of the substrate, the effective description according to the original Kane-Mele paradigm [1] of realizing the 2D TI phase is no longer suitable (in stark contrast to graphene and graphene related group-IV analogues [31]). Instead the synergy of the lattice-, orbital-, substrate-, and large SOC-induced effects in bismuthene establish a new paradigm for realizing a large-gap 2D TI [9]. This concept, which leads to a large energy gap in bismuthene, can serve as a blueprint for the realization of other large-gap 2D TIs.

In this chapter, the atomic structure model of the monolayer/substrate system bismuthene on SiC(0001) is introduced in Sec. 2.1. Then, Sec 2.2 presents the ab-initio electronic structure modelling based on DFT calculations from Ref. [6] followed by the description in terms of the effective tight-binding modeling from Ref. [6] in Sec. 2.3. Lastly, Sec. 2.4 is devoted to recent experimental finding that the metallic edge states of bismuthene host a (helical) Luttinger liquid.

2.1 The atomic structure model

2.1.1 Silicon carbide as epitaxial growth template

Silicon carbide mainly suits three demands. First, it forms a support with proper atomic structure to provide a matching epitaxial template. Second, it tailors the electronic properties of the bismuthene monolayer by covalent bonding of the topmost Si-atoms of the substrate to the Bi-atoms in the monolayer. Third, being a wide band gap semiconductor it is able to accommodate the low-energy electronic states of bismuthene, specifically the helical edge states, within a sizable electronic band gap (3.27 eV in the case of 4H-SiC [32]). The latter is an essential prerequisite to facilitate helical edge transport in future bismuthene transport devices. Intriguingly, only in recent years has SiC emerged as an important epitaxial substrate for novel topological insulators such as bismuthene [6–8] and indenene [33], which can be attributed to its complicated surface preparation which will be explained in Sec. 4.1.

In general, the stacking sequence of Si-C bilayers leads to different possible polytypes which can be categorized in cubic polytypes, in which the stacking sequence is along the [111] direction, and hexagonal polytypes, in which the stacking sequence is along the [0001] direction. It is a general property of all polytypes, however, that Si and C atoms are

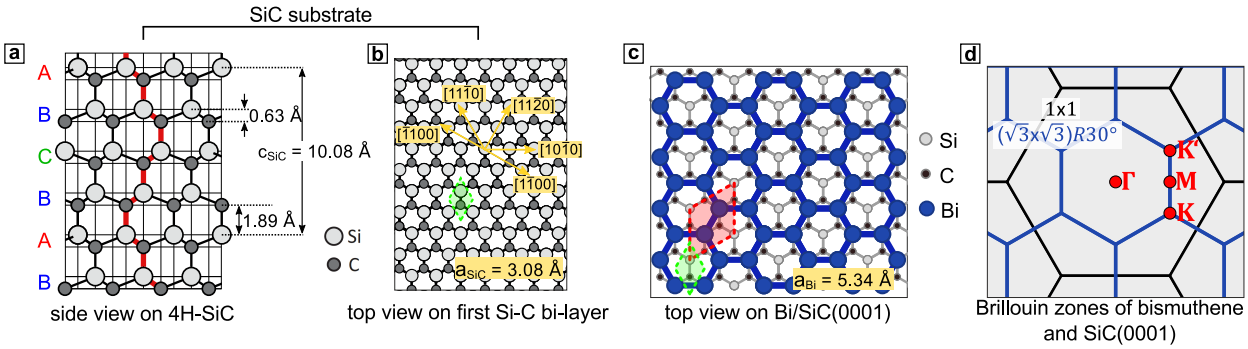

Figure 2.1: Atomic structure model and reciprocal lattice of Bi/SiC. – **(a),** Side view of the 4H-SiC atomic structure without bismuthene. The crystal is built up of stacks of Si-C bi-layers (shown in **b**) in an *A, B, C, B, ...* stacking sequence. **(b),** Top view on the atomic structure of the first Si-C bi-layer of SiC(0001) without bismuthene. The high-symmetry directions (yellow arrows), the unit cell (green rhomb), and the lattice constant (a_{SiC}) are indicated. **(c),** Top view on the atomic lattice structure of bismuthene on SiC(0001). For simplicity, only the first SiC bi-layer is shown. The unit cells of bismuthene (red rhomb) and SiC (green rhomb) are indicated. The lattice constants are $a_{\mathrm{Bi}} = 5.34\,\text{Å}$ and $a_{\mathrm{SiC}} = 3.08\,\text{Å}$ respectively. The Bi-atoms sit 2.75 Å above the Si-atom center position and form covalent bonds with the Si dangling bonds. **(d),** Surface Brillouin zones of the bismuthene monolayer and SiC(0001). Black lines indicate the (1×1) BZ of SiC(0001), and blue hexagons indicate the $(\sqrt{3} \times \sqrt{3})R30°$ BZ of the bismuthene layer. High symmetry points of bismuthene's BZ are indicated.

covalently bonded in tetragonal sp^3 hybridized coordination [34]. In Figs. 2.1**a, b** the atomic structure model of the 4H polytype of SiC is shown which is used throughout this work[1]. Here, the Si-C bilayers are stacked according to an *A*, *B*, *A*, *C*, ... sequence in [0001] direction as seen in Fig. 2.1**a**. It can be seen that the tetragonal sp^3 orientation is rotated by 60° around [0001] direction every two Si-C bilayers. The lattice parameters of 4H-SiC are $a_{\mathrm{SiC}} = 3.08\,\text{Å}$ and $c_{\mathrm{SiC}} = 10.08\,\text{Å}$ [35].

2.1.2 The bismuthene monolayer

The atomic structure of the planar bismuthene monolayer on the SiC(0001) surface is shown in Fig. 2.1**c**. The substrate defines the (1×1) surface unit cell indicated by a green rhomb with a lattice constant of $a_{\mathrm{SiC}} = 3.08\,\text{Å}$. The bismuthene monolayer is chemisorbed 2.75 Å above the topmost Si-atoms of the substrate[2] and forms a $(\sqrt{3} \times \sqrt{3})R30°$ surface reconstruction with respect to the SiC(0001) surface. Its unit cell therefore has a lattice constant of $a_{\mathrm{Bi}} = 5.34\,\text{Å}$ and is indicated by a red rhomb which is very close to the lattice constant of 5.27 Å reported to lead to a minimum of the total energy in DFT calculations of free-standing planar bismuth monolayers in Ref. [37]. The reciprocal lattice of bismuthene on SiC(0001) is presented in Fig. 2.1**d**. It will be important in the discussion of bismuthene's

[1] SiC wafers were delivered by either the company *Prime Wafers* or *TankeBlue Semiconductor Co. Ltd.* in an epi-ready polished grade.

[2] This calculated value is in very good agreement with X-ray standing wave measurements on bismuthene which give 2.64 Å [36].

electronic band structure. Here, the high symmetry points Γ, K, K', and M of bismuthene's $(\sqrt{3}\times\sqrt{3})R30^\circ$ Brillouin zone are highlighted.

2.2 The electronic structure of bismuthene on SiC(0001) from DFT

The density functional theory (DFT) calculations presented in the following have been the latest state of electronic structure modeling of bismuthene on SiC(0001), before the work for this thesis started. Specifically, these are the DFT calculations performed in Ref. [6]. They are suited to explain the essential characteristics of the electronic band structure, such as the orbital character, and to reveal its topological character. However, it is emphasized that these calculations are insufficient to serve as a proper theoretical basis for comparison with some of the experimental results that will be presented in this thesis. This concerns especially the comparison with optical measurements performed in Ch. 7 and the pump-probe ARPES measurements performed in Ch. 8. In anticipation to the discussion presented in these chapters, it is noted that in this context a significantly advanced modeling of bismuthene's electronic structure by the *GW* method and Bethe-Salpeter equation calculations will be presented.

2.2.1 Origins of the large band gap opening

The physics underlying the electronic band structure of Bi/SiC(0001) can be regarded a paradigm for the realization of the QSHE above room-temperature [9] which exploits the following synergistic effects to realize a topological band gap on the order of $\sim 1\,\mathrm{eV}$.

Honeycomb lattice geometry: As realized in the Kane-Mele model [1] the honeycomb lattice provides the foundation for having band inversions and gap openings at two distinct high-symmetry points of the BZ, i.e., at the $K(K')$-points. This provides the possibility to achieve a topological phase driven by band inversion.

Extended low-energy orbital space: Extending the low-energy orbital basis to p_x, p_y, and p_z orbitals which originates from the valence electrons of Bi-atoms opposed to a one-electron orbital basis proposed by the Kane-Mele model [1] (e.g., a p_z orbital as in graphene) plays a pivotal role in driving the SOC induced topological gap opening on the order of $\sim 1\,\mathrm{eV}$ [38,39]. This can readily be seen with the expression of the SOC Hamiltonian ($\mathcal{H}_{\mathrm{SOC}}$) in a condensed matter system given by Eq. (A.4) in the Appendix and with the help of the quantum mechanical algebraic relations for angular momentum. It is found that only p_x and p_y orbitals exhibit non-zero off-diagonal on-site matrix elements of the SOC lattice Hamiltonian according to:

$$\mathcal{H}_{\mathrm{SOC}} \propto \lambda_{\mathrm{SOC}}\,\mathbf{l}\cdot\mathbf{s} \quad = \quad \lambda_{\mathrm{SOC}}\left(\frac{l_+ s_- + l_- s_+}{2} + l_z s_z\right) \tag{2.1}$$

$$\langle i|\,\mathcal{H}_{\mathrm{SOC}}\,|j\rangle \quad \propto \quad \lambda_{\mathrm{SOC}} \begin{array}{c} \\ z_{\uparrow/\downarrow} \\ y_{\uparrow/\downarrow} \\ x_{\uparrow/\downarrow} \end{array} \begin{array}{c} \begin{array}{ccc} z_{\uparrow/\downarrow} & y_{\uparrow/\downarrow} & x_{\uparrow/\downarrow} \end{array} \\ \begin{pmatrix} 0_{2\times2} & i\sigma_1 & -i\sigma_2 \\ -i\sigma_1 & 0_{2\times2} & i\sigma_3 \\ i\sigma_2 & -i\sigma_3 & 0_{2\times2} \end{pmatrix}_{ij} \end{array}, \tag{2.2}$$

where $l_\pm$ and $s_\pm$ are orbital momentum and spin ladder operators, respectively, λ_{SOC} is the atomic SOC parameter, and the spin-full basis of p orbitals $\{z_\uparrow, y_\uparrow, x_\uparrow, z_\downarrow, y_\downarrow, x_\downarrow\}$ is used. In the original proposal of Kane and Mele, however, the SOC was mediated by p_z orbitals via a next-nearest neighbor term [1]. It is therefore also essential for bismuthene to ensure that the SOC induced gap-opening is not governed by the p_z orbitals, but only by the p_x and p_y orbitals.

Substrate-induced orbital filtering: The selective substrate-induced orbital filtering effect relates to the idea of removing p_z orbital related bands from the Fermi level by intentional covalent bonding between the p_z orbitals and the substrate surface Si orbitals. Therefore, the effective low-energy Hilbert subspace of flat bismuthene covalently bonded to the SiC(0001) surface is governed by p_x and p_y orbitals, only. Notably, the idea of orbital filtering has also been described in Refs. [39–43] and a related mechanism of adsorption of atoms or molecules, i.e., chemical functionalization, can lead to similar effects and has been reported in Refs. [39, 44, 45].

Heavy-atom enhanced SOC: It can be shown that under the given approximations presented in Appendix Sec. A.1 the SOC in a condensed matter system scales as $\sim Z^4$, where Z is the atomic number. As a result of using Bi-atoms ($Z = 83$), the topological band gap is tremendously increased compared to other QSHIs that incorporate only lighter atoms.

2.2.2 2D bulk electronic structure calculation

In this section, the ab-initio electronic structure modeling by DFT (as performed in Ref. [6]) is presented. First, bismuthene's electronic band structure is discussed without the inclusion of SOC, but together with the projection of the band character to the atomic Bi 6s and 6p orbitals in Fig. 2.2**a**[3]. The circle size corresponds to the relative weight of the orbital character in each subpanel of Fig. 2.2**a**. All band structures are plotted along a path in bismuthene's Brillouin zone (BZ) which connects the high symmetry points M-Γ-K-M (cf. Fig. 2.1**d**). Importantly, the bands in the vicinity of the $K(K')$-point have mainly p_x and p_y orbital character. It is also apparent that the p_z orbitals are removed from the low-energy sector, as a result of the mentioned covalent bonding to the surface Si dangling bonds of the substrate. Instead of being located close to Fermi energy, as would be expected for a freestanding monolayer (cf Ref. [39]), they are shifted to significantly higher binding energies of ($E - E_{\mathrm{F}} \approx -2\,\mathrm{eV}$).

In the next step, SOC is included in the ab-initio modeling. The corresponding band structure is shown in Fig. 2.2**b**. In order to better estimate the size of the expected gap opening, the calculation was performed using a Heyd-Scuseria-Ernzerhof (HSE) hybrid functional [49]. This approach takes into account non-local Coulomb screening effects by intermixing the

[3] These were performed by Gang Li using the Vienna Ab-Initio Simulation Package *VASP* [46] that uses the projector augmented-wave method [47], and implements the approximations to the exchange correlation functional in the generalized gradient approximation (GGA) in Perdew, Burke and Enzerhof (PBE) parametrization [48].

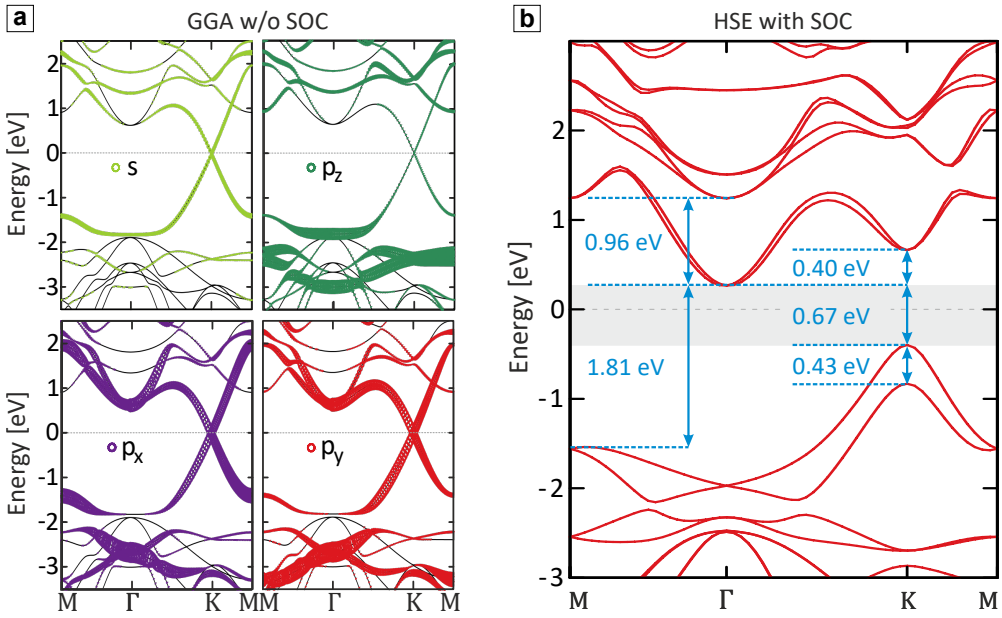

Figure 2.2: 2D DFT band structure of bismuthene on SiC(0001). – **(a)**, The band structures are calculated using the GGA exchange functional and do not include SOC. Each subpanel presents the projection of the orbital character to atomic Bi s and p orbitals, where the size of the colored circles corresponds to the orbital weight. The band strucuture is characterized by linearly dispersing Dirac-like bands with crossings at the $K(K')$-points. The Dirac-like bands near the $K(K')$-points predominantly originate from sp^2 hybridized Bi s, p_x and p_y orbitals forming σ-type bonds that lie in the plane of the bismuthene layer. The Bi p_z orbitals do (almost) not mix with the other Bi orbitals due to the planar bismuthene structure and are pushed to higher binding energies due to the covalent bonding with the Si substrate. **(b)**, DFT band structure (HSE06 hybrid exchange functional) with SOC included in the calculation. The band structure shows a gap opening at the $K(K')$-points of $E^{K-K}_{\text{gap, HSE}} = 1.07\,\text{eV}$. Moreover, substrate induced Rashba-type SOC splits the VBs at the $K(K')$-points by $E^{K}_{\text{R, HSE}} = 0.43\,\text{eV}$. The global band gap lies between the $K(K')$-points and the Γ points and amounts to $E^{K-\Gamma}_{\text{gap, HSE}} = 0.67\,\text{eV}$. *Reprinted figure with permission from Ref. [6] conveyed through Copyright Clearance Center,Inc.. Copyright ©2017 by the American Association for the Advancement of Science.*

PBE exchange energy with a certain fraction of the exact non-local Fock exchange energy. Specifically, the HSE06 [50] hybrid functional was chosen, which is frequently used for obtaining more realistic electronic band gaps for semiconductors. It can be seen in Fig. 2.2**b** that the inclusion of SOC has led to the expected gap opening at the $K(K')$-points. Importantly, the gap sizes are large and amount to $E^{K-K}_{\text{gap, HSE}} = 1.07\,\text{eV}$ for the direkt gap, and $E^{K-\Gamma}_{\text{gap, HSE}} = 0.67\,\text{eV}$ for the indirect between the K- and Γ-point, which therefore also represents the fundamental gap. Moreover, the substrate induced Rashba-type SOC leads to a splitting of the VBs at the $K(K')$-points of $E^{K}_{\text{R, HSE}} = 0.43\,\text{eV}$.

It is important to emphasize that the estimation of the energy gaps given above is still to some extent erroneous and they do not correspond to the physically correct electronic gaps. This is because the DFT band structure does not represent the energy eigenvalues obtained from solving the many-body Hamiltonian, but are instead Lagrangian multipliers according

to the Khon-Sham scheme of DFT [51, 52]. Here, effective single-particle Schrödinger-like eigenvalue problems are solved which contain a functional derivative of an approximation to the exchange-correlation functional [53]. It is a well known problem of any implementation of DFT that energy gaps show a systematic error which results from a discontinuity of the functional derivative of the exchange correlation functional with respect to the electronic density [54] (cf. Appendix Sec. A.2 and Eq. (A.9)). This deficiency can be overcome by many-body perturbation theory, specifically the *GW* method developed by Hedin [55] (cf. Appendix Sec. A.3 and Ref. [53]). The electronic band structure of bismuthene calculated with the *GW* method will be presented in Ch. 7.

2.2.3 The emergence of helical boundary states

The bulk-boundary correspondence in 2D TIs [11] implies the existence of metallic edge channels at the interface to a material with different (e.g., trivial) topology. These states connect the bulk valence and conduction bands of the 2D TI. The emergence of metallic edge channels is therefore oftentimes seen as a strong indication of the non-trivial topology of a material and can be simulated within DFT. To do so, one simulates a larger unit cell of the system and introduces boundaries that run along one direction in the 2D plane of the material. It is important to take care that the unit cell is sufficiently large to prevent detrimental coupling effects between the created open boundaries, e.g., inter-edge hybridization of edge states across the film. Due to the symmetries of the honeycomb lattice, it is convenient and interesting to consider two different types of 1D boundaries: the armchair type and the zigzag type, see Figs. 2.1**a, b**, respectively. The calculations presented in Ref. [6] implemented unit cells for these two types. Here, the width of the single bi-layer of SiC has been chosen significantly larger than the bismuthene film width in order to avoid coupling of bismuthene edge states upon periodic continuation of the unit cell (red rectangle), i.e., forming a torus.

The DFT calculations yielded the iso-charge surfaces of the charge density at energies within bismuthene's bulk energy gap and are plotted as orange clouds in Figs. 2.3**a, b**. These edge states derive solely from the bismuthene layer (i.e., no significant substrate contribution), which is best seen in the side view images. Their lateral confinement to the respective edge is characterized by a decay length of $\sim 5\,\text{Å}$ towards the bulk. Therefore, they are essentially one-dimensional, which leads to enhanced e-e correlation and must be taken into account in the framework of Tomonaga-Luttinger liquids as shown in Ref. [8] and presented in Sec. 2.4.

In order to calculate the ribbon band structure and to infer the edge state's dispersion, a tight-binding Hamiltonian was constructed from the ab-initio DFT calculation by projection onto maximally localized Wannier functions. Figures 2.3**c, d** show the resulting band structure projected onto the periodic dimension of the armchair edge terminated ribbon and the zigzag edge terminated ribbon, respectively. In these figures, bismuthene's 2D bulk valence and conduction bands are shaded in green, whereas states localized at the boundaries of the ribbons are colored in red and blue. It can be seen that these states connect the

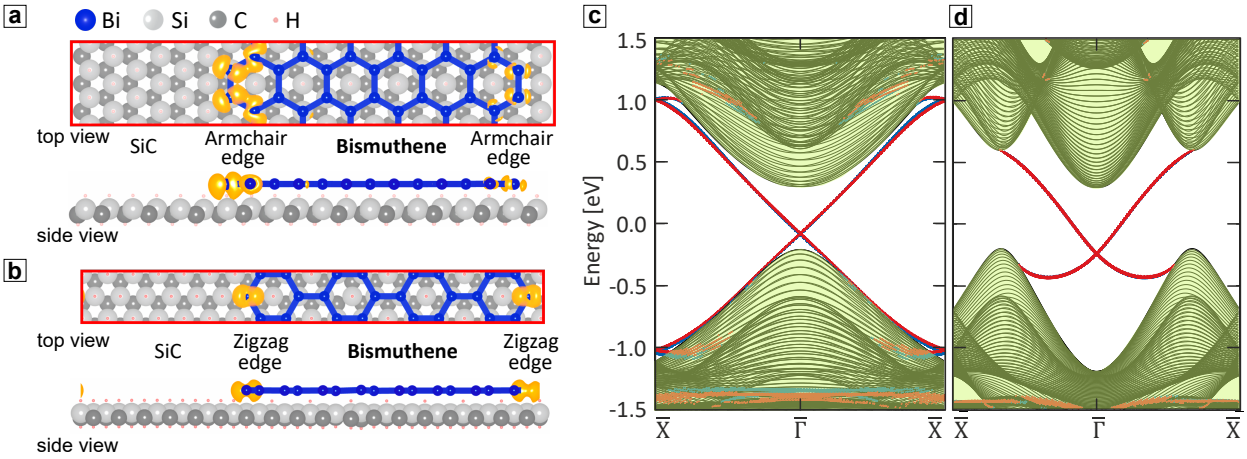

Figure 2.3: DFT and open-boundary tight-binding calculations of bismuthene ribbon slabs. – **(a), (b),** Top and side views of the ribbon slab unit cells for the construction of armchair and zigzag terminated bismuthene films on SiC(0001), respectively. The orange clouds indicate the iso-charge surfaces derived from the helical in-gap state DOS, see also **c, d**. The lateral confinement of these states is characterized by a decay length of ~ 5 Å towards the bulk which renders them quasi-1D. The spatially limited extent of the iso-charge clouds indicates that these states derive solely from the bismuthene layer without substantial substrate contribution. **(c), (d),** Electronic band structure of the ribbons in **a, b**, respectively, but derived from a open-boundary tight-binding model of the slab (see Ref. [6] for details of the calculation). Apart from the 2D bulk states (green), linearly dispersing and crossing in-gap states (red and blue) have formed. They correspond to the helical 1D edge channels in **a, b** and are a hallmark of a QSH system. *Reprinted figure with permission from Ref. [6] conveyed through Copyright Clearance Center,Inc.. Copyright ©2017 by the American Association for the Advancement of Science.*

valence and conduction band states and span the entire energy gap, which is a necessary constraint found in all topological insulators. Moreover, the dispersion of the states at the two boundary types are different. Whereas in the armchair edge terminated ribbons the in-gap states show a near to perfect linear dispersion over the entire gap (see Fig. 2.3**c**), the dispersion of the in-gap states is linear only in the vicinity of the crossing point in the case of the zigzag edge terminated ribbons (see Fig. 2.3**d**). Overall, the existence of edge states in the DFT modeling of terminated bismuthene films is a strong indication that it is a 2D TI. Additionally to this indirect evidence, the $\mathcal{Z}_2$ index (ν, cf. Appendix Eq. (A.26)) of bismuthene on SiC(0001) was numerically calculated in Ref. [6] and indeed yielded the non-trivial topological case, i.e., $\nu = 1$.

2.3 Low-energy effective model

The seminal Kane-Mele model [1] is not suited to model the low-energy electronic structure of bismuthene on SiC(0001). This section discusses the more sophisticated tight-binding model developed in Ref. [6] (see also Ref. [9]) which is suited to reproduce the electronic structure of bismuthene on SiC(0001) from DFT calculations as presented in Sec. 2.2.

The total effective tight-binding Hamiltonian can be written as $\mathcal{H} = \mathcal{H}_{\text{kin}} + \mathcal{H}_{\text{SOC}} + \mathcal{H}_{\text{R}}$

and consists of three parts: the kinetic energy, the atomic (onsite) SOC and the Rashba-type SOC induced by the substrate. In this description, any onsite orbital energies have been set to zero. The explicit representation of the Hamiltonian can be given in the following basis which spans the Hilbert space from the spin ($\uparrow$ / $\downarrow$), sublattice (A/B), and orbital (x/y) degrees of freedom:

$$\left\{|p^A_{x\uparrow}\rangle\,,\ |p^A_{y\uparrow}\rangle\,,\ |p^B_{x\uparrow}\rangle\,,\ |p^B_{y\uparrow}\rangle\,,\ |p^A_{x\downarrow}\rangle\,,\ |p^A_{y\downarrow}\rangle\,,\ |p^B_{x\downarrow}\rangle\,,\ |p^B_{y\downarrow}\rangle\right\}\,. \tag{2.3}$$

Note that the p_z orbitals have been projected out from the low-energy sector to lowest order in perturbation theory. This is why only the p_x and p_y orbitals are left in the basis. Moreover, the real and reciprocal space unit cell vectors can be chosen as $\mathbf{a_1} = (1,0)^T$, $\mathbf{a_2} = (-\frac{1}{2}, \frac{\sqrt{3}}{2})^T$ and $\mathbf{b_1} = (2\pi, \frac{2\sqrt{3}}{3}\pi)^T$, $\mathbf{b_2} = (0, \frac{4\sqrt{3}}{3}\pi)^T$, respectively.

The kinetic energy part ($\mathcal{H}_{\text{kin}}$) is obtained within the Slater-Koster approach for the linear combination of atomic orbitals [56]. It is diagonal in the spin ($\uparrow$ / $\downarrow$) subspace and reads:

$$(\mathcal{H}_{\text{kin}})_{\uparrow\uparrow} = (\mathcal{H}_{\text{kin}})_{\downarrow\downarrow} = \begin{pmatrix} 0 & 0 & h^{AB}_{xx} & h^{AB}_{xy} \\ 0 & 0 & h^{AB}_{yx} & h^{AB}_{yy} \\ \dagger & \dagger & 0 & 0 \\ \dagger & \dagger & 0 & 0 \end{pmatrix}\,, \tag{2.4}$$

where $h^{AB}_{xx} = V^1_{pp\pi} + \frac{1}{2}(3V^1_{pp\sigma} + V^1_{pp\pi})e^{i\frac{\sqrt{3}}{2}k_y}\cos\frac{k_x}{2}$, $h^{AB}_{xy} = h^{AB}_{yx} = i\frac{\sqrt{3}}{2}(V^1_{pp\sigma} - V^1_{pp\pi})e^{i\frac{\sqrt{3}}{2}k_y}\sin\frac{k_x}{2}$, and $h^{AB}_{yy} = V^1_{pp\sigma} + \frac{1}{2}(V^1_{pp\sigma} + 3V^1_{pp\pi})e^{i\frac{\sqrt{3}}{2}k_y}\cos\frac{k_x}{2}$. Here, $V^1_{pp\sigma}$ and $V^1_{pp\pi}$ denote nearest-neighbor two-center Slater-Koster integrals.

The atomic SOC ($\mathcal{H}_{\text{SOC}}$) contribution can be obtained from Eq. (2.2). It is diagonal in the sublattice (A/B) space and in the spin ($\uparrow$ / $\downarrow$) subspace. Therefore, in the $\mathrm{p}_x/\mathrm{p}_y$ subspace it reads:

$$(\mathcal{H}_{\text{SOC}})^{AA}_{\uparrow\uparrow} = (\mathcal{H}_{\text{SOC}})^{BB}_{\uparrow\uparrow} = -\,(\mathcal{H}_{\text{SOC}})^{AA}_{\downarrow\downarrow} = -\,(\mathcal{H}_{\text{SOC}})^{BB}_{\downarrow\downarrow} = \lambda_{\text{SOC}}\,\sigma_2\,, \tag{2.5}$$

where λ_{SOC} parametrizes the strength of the SOC interaction and σ_2 is the second Pauli matrix.

Lastly, the Rashba-type SOC contribution ($\mathcal{H}_{\text{R}}$), which originates from the symmetry breaking of the substrate, reads:

$$(\mathcal{H}_{\text{R}})_{\uparrow\downarrow} = (\mathcal{H}_{\text{R}})^\dagger_{\downarrow\uparrow} = \lambda_{\text{R}} \begin{pmatrix} 0 & 0 & a & b \\ 0 & 0 & b & c \\ d & e & 0 & 0 \\ e & f & 0 & 0 \end{pmatrix}\,, \tag{2.6}$$

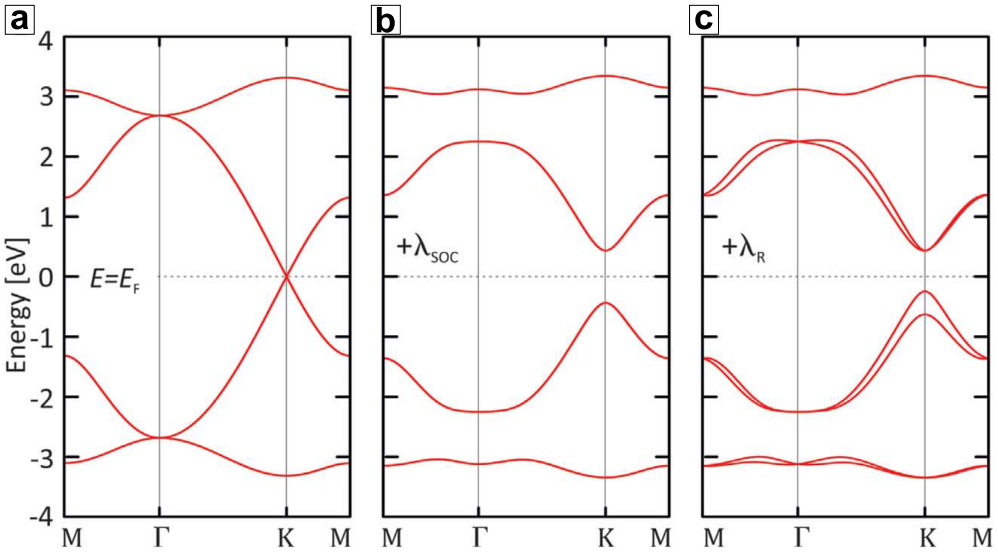

Figure 2.4: Band structure of the minimal tight-binding model of bismuthene on SiC(0001). – The electronic band structure of bismuthene on SiC(0001) from the minimal tight-binding model described in the main text is plotted for three characteristic model parameters. **(a)**, The atomic and the Rashba SOC are set to zero, i.e., $\lambda_{\mathrm{SOC}} = \lambda_{\mathrm{R}} = 0\,\mathrm{eV}$. The sp^2 hybridized low-energy states cross at the $K(K')$ point and therefore the system is semi-metallic. **(b)**, Here, only the Rashba SOC is set to zero, i.e., $\lambda_{\mathrm{SOC}} = 0.435\,\mathrm{eV}$, $\lambda_{\mathrm{R}} = 0\,\mathrm{eV}$. The states at the $K(K')$ point gap out. The gapped system is in a QSHI state. **(c)**, Both the atomic and the Rashba SOC take finite values, i.e., $\lambda_{\mathrm{SOC}} = 0.435\,\mathrm{eV}$, $\lambda_{\mathrm{R}} = 0.032\,\mathrm{eV}$. The degeneracy of the valence band states at the $K(K')$ point is lifted. *Reprinted figure with permission from Ref. [6] conveyed through Copyright Clearance Center,Inc.. Copyright ©2017 by the American Association for the Advancement of Science.*

with the definitions [6, 9]

$$\begin{aligned} a &= -2\sqrt{3}ie^{i\frac{\sqrt{3}}{2}k_y}\sin\frac{k_x}{2} \quad , \quad b = [1 - e^{i\frac{\sqrt{3}}{2}k_y}(\cos\frac{k_x}{2} + \sqrt{3}\sin\frac{k_x}{2})] \\ c &= -2i[1 - e^{i\frac{\sqrt{3}}{2}k_y}\cos\frac{k_x}{2}] \quad , \quad d = -2\sqrt{3}ie^{-i\frac{\sqrt{3}}{2}k_y}\sin\frac{k_x}{2} \\ e &= -[1 - e^{-i\frac{\sqrt{3}}{2}k_y}(\cos\frac{k_x}{2} - \sqrt{3}\sin\frac{k_x}{2})] \quad , \quad f = 2i[1 - e^{-i\frac{\sqrt{3}}{2}k_y}\cos\frac{k_x}{2}] \,. \end{aligned} \tag{2.7}$$

The band structure calculations in Fig. 2.4 illustrate the effects of each of the terms of the Hamiltonian. The model paramters that are listed in the follwoing were obtained in Ref. [6, 9] by fitting the tight-binding band structure to the DFT band structure presented in Sec. 2.2 in the vicinity of the $K(K')$-points. First setting $\mathcal{H}_{\mathrm{SOC}} = 0$ and $\mathcal{H}_{\mathrm{R}} = 0$, the band structure shows crossing states at the $K(K')$-points and is therefore gapless, see Fig. 2.4**a**. Here, the two-center Slater-Koster integrals were chosen as $V^1_{pp\sigma} = 2.0\,\mathrm{eV}$, $V^1_{pp\pi} = -0.21\,\mathrm{eV}$. Once the SOC is turned on, i.e., $\mathcal{H}_{\mathrm{SOC}} \neq 0$ and $\lambda_{\mathrm{SOC}} = 0.435\,\mathrm{eV}$, an energy gap opens at the $K(K')$-points, see Fig. 2.4**b**. This already drives the system into the topological insulator

regime as proved in Ref. [6]. Lastly, the effect of including the Rashba SOC term, i.e., $\mathcal{H}_{\mathrm{R}} \neq 0$ and $\lambda_{\mathrm{R}} = 0.032\,\mathrm{eV}$, is mainly that the degeneracy of bands becomes lifted. This effect is most prominently seen by a splitting of the valence bands at the $K(K')$-points, see Fig. 2.4**c**. Another effect is that the global energy gap is slightly reduced compared to the case with only atomic SOC, because the topmost valence band shifts towards the Fermi energy induced by the Rashba interaction.

2.4 Observation of a (helical) Tomonaga-Luttinger liquid in the edge states of bismuthene

So far, only the single-particle electronic structure of bismuthene on SiC(0001) has been discussed. However, interelectronic interactions can lead to effects that can not be captured adequately in this way and need a description on the two-particle level. The celebrated property of prohibited elastic *single*-particle backscattering in the helical edge states of a 2D TI in the presence of time-reversal symmetry has already been stressed. However, *two*-particle scattering is not impeded by the topological protection and can arise if interelectronic interactions like Coulomb scattering play a significant role. It is well-established that the dimensionality of an electronic system can be decisive in this regard [57, 58]. There have been plenty of examples of quasi-1D electronic systems in which the Fermi liquid description, i.e., the interelectronic interactions are well captured in the picture of "dressed" quasiparticles that behave similar to fermionic particles, breaks down and the (low-energy) description is dominated by collective bosonic excitations in the framework of the Tomonaga-Luttinger liquid theory instead [59, 60]. Examples for which this applies are semiconducting GaAs quantum wires [61], metallic single wall carbon nanotubes [62], polymer nanofibers [63], atomic gold chains on vicinal Ge surfaces [64], domain boundaries in a TMD [65], and chiral edge states of a fractional quantum Hall system [66]. The helical boundary states of bismuthene on SiC(0001) are stronlgy localized to the boundary within only a few Angstrom. This has been proved experimentally by local STM measurements in Refs. [6, 8]. Therefore, also the helical edge states of bismuthene on SiC(0001) fall into the category of a quasi-1D electronic system. Indeed, theoretically the helical Tomonaga-Luttinger liquid model [57, 58] has proved to adequately describe the highly-localized edge electrons in 2D TIs as long as the electronic interaction is weaker than the band gap of the 2D bulk material [67]. It was already reported in Ref. [68] that the measured deviations from a sharply quantized conductance of $G = 2e^2/h$ in transport experiments at very low temperatures in the 2D TI quantum well system InAs/GaSb could be due to electronic interactions.

In the recent study in Refs. [8] and [7] it was shown that STS spectra of metallic edge states at bismuthene film boundaries terminated at SiC substrate steps show hallmark signatures of a (helical) Tomonaga-Luttinger liquid. Specifically, a strongly suppressed edge conductance $\approx \pm 100\,\mathrm{meV}$ around the Fermi energy was observed. This suppression of the differential conductivity which is related to the edge LDOS exhibited a *universal scaling* behavior in

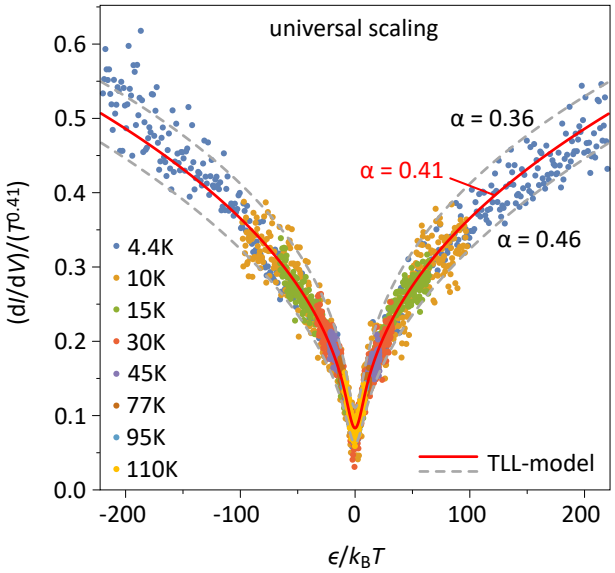

Figure 2.5: Helical Tomonaga-Luttinger liquid in the edge channels of bismuthene. – The temperature dependent differential tunneling conductivity spectra plotted with rescaled axes collapse onto a single universal curve with a power law shape. This behavior is predicted for the tunnelling into a Tomonaga-Luttinger liquid. The power-law exponent α is related to the Luttinger parameter K and yields $K = 0.42 \pm 0.05$. *Reprinted figure from Ref. [8].*

both energy and temperature captured by the expression [62]:

$$\rho_{\mathrm{TLL}}(\epsilon, T) \propto T^{\alpha} \cosh\left(\frac{\epsilon}{2k_B T}\right) \left|\Gamma\left(\frac{1+\alpha}{2} + i\frac{\epsilon}{2\pi k_B T}\right)\right|^2 . \tag{2.8}$$

From the power law exponent $\alpha \equiv \frac{1}{2}(K + 1/K - 2)$, the helical TLL parameter $K \approx [1 + W/\pi\hbar v_{\mathrm{F}}]^{-1/2}$, where W denotes the Coulomb interaction, could be extracted (see Fig. 2.5) and yielded $K = 0.42 \pm 0.05$. While for non-interacting electrons it holds that $K = 1$, the extracted value for edge ststes in bismuthene corresponds to an intermediate to strong Coulomb repulsion.

CHAPTER 3

Methods for surface characterization

The samples studied in this work are surface systems. More specifically, bismuthene is a monolayer placed on top of SiC as a substrate. This chapter provides an overview of key concepts and methods used to characterize and study these material systems with regard to their structural, electronic, and chemical properties.

3.1 Low energy electron diffraction

In low energy electron diffraction (LEED) experiments (see Fig. 3.1) electrons are accelerated to energies typically between 20 eV and 100 eV. The accelerated electrons emitted from the electron gun that hit the sample surface perpendicularly with such low kinetic energy interact strongly with matter via the Coulomb interaction [69]. This leads to an inelastic mean free path on the order of only a few monolayers [70]. Therefore, the signal from backscattered electrons monitored with a fluorescent screen (purple shaded in Fig. 3.1) is strongly dominated by the atomic structure of the first $\sim 1-2$ monolayers (atoms indicated as red spheres in Fig. 3.1). This signal is thus perfectly suited for a structural analysis of the surface.

The LEED measurements conducted in this work are evaluated on the basis of geometrical theory of diffraction. To explain the position of diffraction maxima (Bragg peaks) it is necessary to account for the quantum mechanical wave character of electrons, according to which electrons with mass m_e and kinetic energy E_{kin} can be assigned a wavelength: $\lambda = 2\pi/|\mathbf{k}| = h/\sqrt{2m_e E_{\text{kin}}}$, where $\mathbf{k}$ is the electron wave vector. The constructive interference condition for electron diffraction at the periodic arrangement of atoms in a crystal lattice is then obtained with the Laue condition:

$$\Delta\mathbf{k} = \mathbf{k}_f - \mathbf{k}_i = \mathbf{G}\,. \tag{3.1}$$

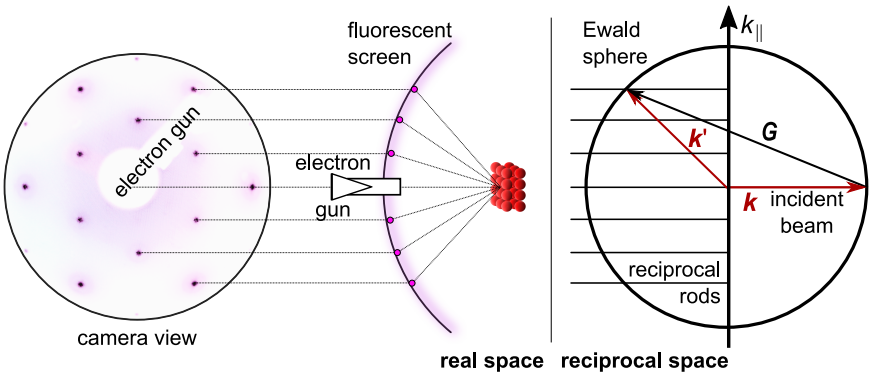

Figure 3.1: Schematic illustration of LEED. Left: The LEED process is scetched in real space. Details are given in the main text. **Right:** The Laue condition is visualized by the Ewald sphere construction in reciprocal space.

Here, $\mathbf{G}$ is a reciprocal space lattice vector of the crystal and $\mathbf{k}_f$ and $\mathbf{k}_i$ denote the final and initial electron wave vectors. The mean free path length of low-energy electrons is only a few angstroms. Consequently, there is no diffraction condition in the direction perpendicular to the sample surface. Therefore, the Laue condition of Eq. (3.1) reduces to a 2D form in the case of diffraction at a surface.

The Ewald construction depicted in the right half of Fig. 3.1 is a geometrical visualization of the Laue condition that also translates into the identification of the diffraction spots on the fluorescent screen of the LEED instrument, see left half of Fig. 3.1. According to the Ewald sphere construction, the Laue condition Eq. (3.1) is fulfilled for all diffracted electrons with wave vectors $\mathbf{k}_f$ pointing at intersections of a sphere with radius $|\mathbf{k}_i|$ with the reciprocal lattice rods $k_\perp$ of the 2D surface, as seen in the right half of Fig. 3.1.

3.2 Scanning tunneling spectroscopy & microscopy

The invention of the scanning tunneling microscope (STM) by Binnig and Rohrer in 1982 [71] marked a revolution in surface science. For the first time, individual surface atoms could be studied at an unprecedented spatial resolution [72]. Since then STM has been employed as an incredibly powerful real-space imaging method and used to infer the atomic arrangement on surfaces. Another immensely valuable application of STM lies in the ability to obtain information about the electronic structure of the sample based on the effect of quantum mechanical tunneling of electrons from the STM tip to the sample or vice versa. This technique is termed scanning tunneling spectroscopy (STS), as it refers to the detection of tunneling current as a function of a continuously varied parameter. The varied parameter is either the tip-sample separation (z) at a constant set-point bias voltage (V_{set}). In this case the recorded spectrum is called the $I(z)|_{V_{\text{set}}}$-curve. Or, it is the bias voltage (V) at a constant tip-sample separation (z). In this case the recorded spectrum is called the $I(V)|_{z_{\text{set}}}$-curve. All STS measurements conducted in this work are $I(V)|_{z_{\text{set}}}$-curves.

This work uses a commercial STM instrument from *Scienta Omicron*©. The STM itself is kept inside a UHV chamber at a base pressure of $p = 3 \times 10^{-11}\,\text{mbar}$. The receiving sample stage of the STM is thermally coupled to a cryostat and can operate at $T = 4.35\,\text{K}$ by filling the cryostat with liquid helium. A lock-in amplifier from *SRS (Stanford Research Systems)* is connected to the electronic control system to perform lock-in spectroscopy, see Sec. 3.2.2. The following briefly outlines the physical concepts of STM and STS with focus on the applications used in this work.[4] The working principle of STM and STS is based on the quantum mechanical tunneling effect. Therefore, an expression for the tunneling current is derived and explained along the lines of Ref. [75], first.

[4]For a more complete review, the reader is referred to the books of Wiesendanger [73] and Chen [74], and the review article by Fischer *et al.* [75].

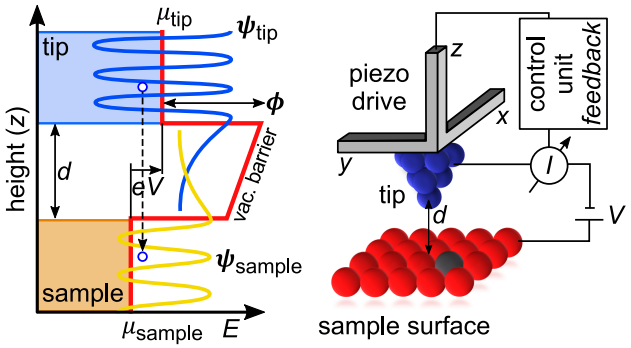

Figure 3.2: Schematic illustration of STM. Left: Schematic of quantum mechanical tunneling of electrons from filled states in the STM tip to empty states in the sample through the vacuum potential barrier (see main text for details). **Right:** Schematic of main parts of an STM. A voltage bias V is applied between tip and sample, and the recorded tunneling current I is used as feedback signal for controlling the tip-to-sample distance d. The tip is moved in $x-y-z$ direction by piezoelectric drives. *Figure reprinted with permission from Ref. [75]. Copyright ©2007 by the American Physical Society.*

3.2.1 The tunneling current

For STM measurements a metallic tip is approached to the sample surface at a distance d of a few angstrom, see Fig. 3.2. The vacuum barrier between tip and sample establishes a tunneling barrier for the electrons in both materials. By applying a bias voltage (V) between tip and sample these electrons can tunnel through the vacuum potential barrier (ϕ) and give rise to a tunneling current (I). It is generally a good approximation to model electron tunneling experiments within an equilibrium theory, as the time between two tunneling events is much longer than the typical quasi-particle relaxation time [75]. Based on Bardeen's approach [76], the single-particle tunneling between STM tip and the sample is then described by the Hamiltonian:

$$H = H_{\text{tip}} + H_{\text{sample}} + H_{\text{T}}. \tag{3.2}$$

Here, H_{tip} and H_{sample} are Hamiltonians of the tip and sample, respectively. They fully characterize the individual respective system and are supposed to be fully independent from each other (i.e., all operators commute). The last term (H_{T}) in Eq. (3.2) describes electron tunneling between the tip and the sample.

The tunneling current (I) is evaluated as the average rate of particle number (N) change in the sample (or in the tip) as [77]

$$I = |e|\langle \dot{N}_{\text{s}} \rangle, \tag{3.3}$$

where the convention is met that current has a positive sign when electrons flow from tip to sample. Within linear response theory one then arrives at the single-particle tunneling

current (details are given in Ref. [75])

$$I(V) = \frac{2\pi|e|}{\hbar} \int d\omega \, [f(\omega - |e|V) - f(\omega)] \times \sum_{t,s} |T_{\mathrm{ts}}|^2 A_t(\omega - |e|V) A_s(\omega), \tag{3.4}$$

where T_{ts} is the tunnel matrix element between tip and sample states, $A_{\mathrm{t}}(\omega)$ and $A_{\mathrm{s}}(\omega)$ are the single-particle spectral functions of the independent tip and sample states, respectively, and $f(\omega)$ is the Fermi-Dirac function. A further simplification to Eq. (3.4) can be reached by applying the Tersoff and Hamann model [78,79] for modeling the tip-sample STM junction. Within this model the tip apex is considered to be terminated by a spherical potential well centered at the center of the tip apex ($\mathbf{x}$). It effectively assumes an "atomically sharp" STM tip geometry. It is then found that Bardeen's tunnel matrix element is proportional to the sample wave function at $\mathbf{x}$ [75]: $|T_{ts}|^2 \propto |\phi_s(\mathbf{x})|^2$. By leveraging the relations of real-space spectral functions to the local density of states (LDOS) N, Eq. (3.4) can be simplified to:

$$I(\mathbf{x}, V) \;\; \propto \;\; \int d\omega \, [f(\omega - |e|V) - f(\omega)] \times N_{\mathrm{t}}(\omega - |e|V) N_{\mathrm{s}}(\mathbf{x}, \omega). \tag{3.5}$$

A mathematical derivation can be found in Ref. [75]. Equations (3.4) and (3.5) indicate that a finite tunneling current is only measured, if the tunnel matrix element $|T_{ts}|^2$ does not vanish, and given that empty states in the tip DOS align with occupied states in the sample DOS, or vice versa. The relative alignment of occupation in tip and sample is controlled via the applied bias voltage V.

The unique strength of the STM lies in its ability to obtain information about the local electronic density of states (LDOS) of the sample (N_{s}) at the atomic scale. In order to obtain a direct measure of N_{s} one considers the derivative of the tunneling current (I) in Eq. (3.5) with respect to the bias voltage (V) which is the differential conductivity (dI/dV). Assuming that the tip DOS is essentially featureless, i.e., $N_{\mathrm{t}}(E - E_{\mathrm{F}}) = \text{const.}$ in the energy range of interest, which is often times a valid approximation for metallic STM tips in the range of $-1\,\mathrm{eV} \lessapprox E - E_{\mathrm{F}} \lessapprox 1\,\mathrm{eV}$, the derivative simplifies to

$$\left.\frac{dI(\mathbf{x}, V)}{dV}\right|_{V=U} \;\; \propto \;\; \int d\omega \left[-\left.\frac{df(\omega - |e|V)}{dV}\right|_{V=U} \right] \times N_{\mathrm{s}}(\mathbf{x}, \omega). \tag{3.6}$$

The above given and commonly applied interpretation of the (differential) tunneling current is adopted throughout this work. It is indeed the foundation of its widespread use and allows spatially resolved electron spectroscopy at the atomic scale.

In order to record the electronic DOS, the tunneling current ($I(V)$) is continuously recorded over a finite bias voltage (V) range at a fixed lateral position of the tip with respect to the sample. The numerical calculation of the differential conductance by differentiation of $I(V)$, however, is prone to result in a computational amplification of noise, by which the $dI/dV(V)$-curve suffers from a poor signal-to-noise ratio. To reduce such detrimental effects the lock-in amplifier technique as explained in the next section is commonly

applied in practice.

3.2.2 Lock-in spectroscopy

As the name suggests, this technique is based on the idea of homodyne detection with a lock-in amplifier. Therefore, the tunneling voltage (V) is superimposed with a known ac carrier voltage ($V_{\mathrm{ac}} = V_{\mathrm{m}} \cos(\omega_{\mathrm{m}} t)$)[5]. For the modulated tunneling current one gets (to first order in V_m) [75]

$$I(x, V) \propto I(x, V) + \left.\frac{dI(\mathbf{x}, U)}{dU}\right|_{U=V} V_{\mathrm{m}} \cos(\omega_{\mathrm{m}} t) + \mathbb{O}(V_{\mathrm{m}}^2), \tag{3.7}$$

which limits the resolution of the read out tunneling current I_{out} to [80, 81]

$$I_{\mathrm{out}}(x, V) \propto \int_{-V_m}^{V_m} dV' \left.\frac{dI(\mathbf{x}, U)}{dU}\right|_{U=V+V'} \sqrt{V_m^2 - V'^2}. \tag{3.8}$$

However, due to the demodulation of the ac signal by the lock-in any contribution to the signal by noise is limited to a narrowed frequency bandwidth. Specifically, contributions of noise to the signal will be filtered out by the demodulation of the ac signal via the lock-in amplifier which enhances the signal-to-noise ratio (SNR) according to [82]:

$$\mathrm{SNR} = \frac{I_{ac}}{\sqrt{P_{\mathrm{noise}}}} = I_{ac} \times \left(\int_{-\infty}^{\infty} d\omega \, S(\omega) \big| H(\omega) \big|^2 \right)^{-1/2}, \tag{3.9}$$

where $S(\omega)$ is the power spectral density which also contains the noise signal with a wide range of frequencies. Moreover, $H(\omega)$ is the transfer function of the lock-in amplifier low-pass filter. For example, for an analog RC filter the transfer function is $H(\omega) = (1+i\omega\tau)^{-1}$, where $\tau = RC$ is the filter time constant, and R and C are the resistance and capacitance of the RC filter, respectively. Thus, by choosing lock-in amplifier filters with narrower bandwidths one can in principle always enhance the signal-to-noise ratio. This comes, however, with the tradeoff of an increased settling time, which in turn demands slower data acquisition rates. For more details and best practices related to the lock-in spectroscopy technique in STS, the reader is referred to Ref. [82].

3.2.3 Real-space imaging

Apart from its spectroscopic capabilities the STM can also be used to acquire real-space information of a sample surface on the atomic scale. To achieve the required sensitivity one exploits that the tunneling current through the vacuum barrier decreases exponentially with

[5] In order not to disturb the feedback loop of the STM regulator the modulation frequency ω_{m} has to be much faster than the regulation frequency cutoff of the feedback loop.

the tip-sample distance d as [75]:

$$I \sim e^{-2\kappa d}, \qquad \kappa = \sqrt{2m\phi/\hbar^2} \approx 0.5\sqrt{\phi(eV)}\text{Å}^{-1}. \tag{3.10}$$

The tunneling current (I) can be used in two different scanning modes for real-space imaging. These are the *constant current mode* and the *constant-height mode*. This work uses exclusively the constant current mode for the structural characterization of samples. In this mode (see Fig. 3.2), the tunneling current is amplified, recorded and used as a feedback signal for a control unit to adjust the tip-to-sample separation (d) while the tip is scanned over the sample in order to regulate the tunneling current (I) to a predefined set-point tunneling current (I_{set}). Piezoelectric elements are used as driving elements to move the tip with sub-Å precision. In fact, a simple estimate with Eq. (3.10) and a work function of $\phi = 5\,\text{eV}$ readily gives that the tunneling current changes by about one order of magnitude for one angstrom change in the tip-to-sample distance. To reconstruct a "topographic" image of the surface the feedback signal of the controller, i.e., the relative changes (Δz) in tip-to-sample separation, is used. For completeness it is noted that in the alternative constant-height mode, the tip-to-sample separation (d) is kept constant at a predefined value and the spatially resolved tunneling current is used for the reconstruction of a "topographic" image.

3.3 Photoemission spectroscopy

This section introduces concepts of photoemission spectroscopy (a.k.a. photoelectron spectroscopy) (PES) along the lines of Ref. [83] with focus on the relevant applications for this work. For a more complete review, the reader is referred to the book of Hüfner [84] and the reviews of Refs. [83, 85].

3.3.1 The (time-independent) photoemission process

Dating back to 1887, it was experimentally found by Hertz [86, 87] and later explained by Einstein in 1905 [88] that photons incident on a sample can liberate its electrons. The free electron itself acquires a maximum kinetic energy of $h\nu - \phi$, where ν is the photon frequency and ϕ is the work function of the material. This seemingly simple quantum mechanical process has since led to a plethora of experimental techniques and is the foundation of all PES experiments used in solid-state physics. These aim to exploit the information that the electron carries about the solid-state system from which it escaped [83, 85, 89, 90]. The power of PES lies in the fact that the momentum and energy distribution of the escaped photoelectrons in principle comprises all the many-body physics that electrons encounter in the material, e.g., electron-phonon interactions, electron-electron interactions, but also spin-orbit coupling [85]. The applications of PES that are relevant for this work can be roughly devided on the basis of two photon energy ranges. The reason for this distinction is illustrated in Fig. 3.3 and is based on the corresponding energetics of a photoelectron emission process. The photon energy range of ultraviolet radiation, i.e., $h\nu \approx 20\,\text{eV} - 200\,\text{eV}$, is particularly relevant for studying the electronic properties of delocalized valence band

states in crystalline samples. In this case one can also speak of ultraviolet photoelectron spectroscopy (UPS). The second energy range involves the use of X-rays to probe the element specific binding energies of core levels. It is thus called X-ray photoelectron spectroscopy (XPS) and provides a tool to resolve the chemical composition of the samples.

The emission of a photoelectron from a material is formally described by a transition probability (w_{fi}) of an N-electron initial state $|\psi_i^N\rangle$ to an excited final state $|\psi_f^N\rangle$ with the photoelectron in a time-inverted scattering state. For weak perturbations (this excludes the treatment of multiphoton absorption) such a transition is well described by Fermi's golden rule [85]

$$w_{fi} = \frac{2\pi}{\hbar} \left| \langle \psi_i^N | \, H_{\text{int}} \, | \psi_f^N \rangle \right|^2 \cdot \delta \left(E_f^N - E_i^N - h\nu \right), \tag{3.11}$$

where E_f^N and E_i^N are the initial- and final-state energies of the N-electron system respectively. The perturbation that drives the transition is encoded in H_{int} and describes the interaction of the electronic system with the photon. In a semi-classical approach of using Peierls substitution for the electron momentum operator $\mathbf{p} \to \mathbf{p} - q\mathbf{A}$, where q denotes the charge, one approximates H_{int} in Eq. 3.11 with [85]

$$H_{\text{int}} = \frac{1}{2m_{\text{e}}} \left(\mathbf{p} + \frac{e}{c}\mathbf{A} \right)^2 - e\Phi - \frac{\mathbf{p}^2}{2m_{\text{e}}} \tag{3.12}$$

$$\approx \frac{e}{2m_{\text{e}}c} \left(\mathbf{A} \cdot \mathbf{p} + \mathbf{p} \cdot \mathbf{A} \right) \tag{3.13}$$

$$\approx \frac{e}{m_{\text{e}}c} \mathbf{A} \cdot \mathbf{p} \tag{3.14}$$

where $\mathbf{p}$ is the electron momentum operator, and $\mathbf{A}$ and Φ are the vector potential and scalar potential of the electromagnetic field, respectively. In the second line, the Weyl gauge was chosen, such that $\Phi = 0$. Moreover, two-photon processes $\mathbf{A}^2$ were neglected. In the last line the dipole approximation $[\mathbf{A}, \mathbf{p}] = 0$ was used, which holds when $\mathbf{A}$ is constant over atomic distances. While this condition is explicitly violated at the surface due to the involved change of the dielectric function within a distance on the order of an interatomic distance, it impacts the perpendicular momentum component $\mathbf{k}_\perp$ of the photoelectron. This has no impact on the evaluation of the presented experiments, as only the in plane momentum component $\mathbf{k}_\parallel$ of the photoelectrons will be of interest.

The three-step model of photoemission

In order to simplify the scattering problem connected to Eq. (3.11), the photoemission process has been widely discussed in the so called *three-step model* [91]. This model is phenomenological and does not describe the physically correct picture of a coherent photoemission process according to which photon absorption, electron excitation, and electron detection are treated as a single coherent process in the *one-step model* [92,93]. The following description still adheres to the three-step model, as it has proven to be useful in simplifying

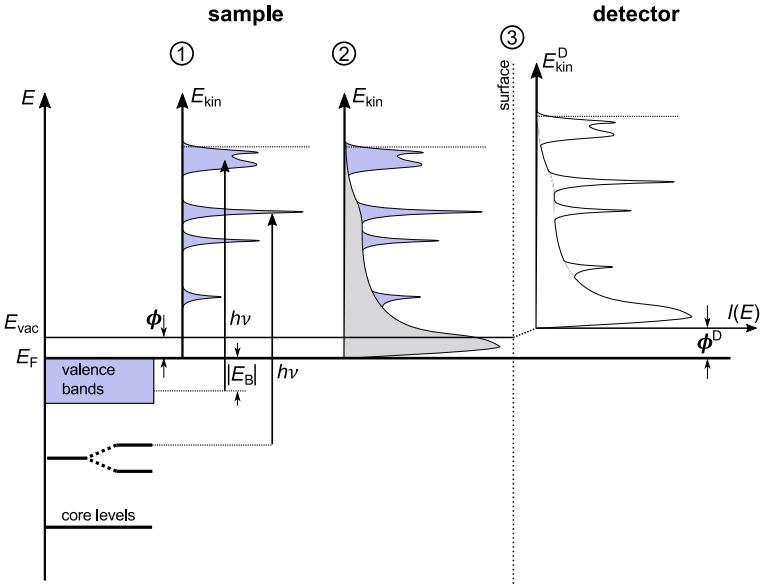

Figure 3.3: The photoemission process. Schematic of the three-step-model of PES described in the main text. In step (1), photons with energy $h\nu$ excite electrons in the solid by the photoelectric effect. After traveling to the surface in step (2) and transmission through the surface in step (3), the detector measures the photoelectron current I as a function of the kinetic energy $E^{\mathrm{D}}_{\mathrm{kin}}$ of the photoelectrons measured with the detector (and possibly also emission angle). Typically the binding energy $E_{\mathrm{B}} := h\nu - E^{\mathrm{D}}_{\mathrm{kin}} - \phi^{\mathrm{D}}$, where ϕ^{D} is the work function of the detector, is used as energy scale (assuming that the Fermi energy of detector and sample is perfectly aligned).

the interpretation of experimental data. According to the three-step model the photoemission process is subdivided into the following independent and sequential steps, each connected to probabilities that directly influence the probed photoemission intensity [85]:

① **Excitation of the electron in the material by a photon.**
→ The excited electron carries all the information on the intrinsic electronic structure of the material, i.e, its spectral function.

② **Propagation of the photoelectron to the surface.**
→ Inelastic scattering processes can affect the energy and momentum of the photoelectron. This process is described in terms of an effective mean free path λ_{MFP}. In general, these processes are the source for an inelastic background signal.

③ **Emission of the electron into the vacuum.**
→ By transmitting through the surface barrier, the photoelectron occupies a free-electron plane wave state in the vacuum that extends to the detector.

The transmission of the photoelectron through the surface potential barrier leads to a reduction of the emitted electron's kinetic energy by the work function of the material: $E_{\mathrm{kin}} = h\nu - E_B - \Phi$. The absence of translational symmetry perpendicular to the surface has a crucial impact on the possibility to retrieve the electron's momentum. Although all components of the electrons wavevector $\mathbf{k}$ were conserved during step ①, after transmission through the surface only the surface-parallel components $\mathbf{k}_{\parallel}$ are conserved, i.e., $k_{\parallel} = \frac{1}{\hbar}\sqrt{2m_{\mathrm{e}}E_{\mathrm{kin}}}\sin\theta$ (θ is the emission angle of the electron from the surface normal). The perpendicular component has to be recovered for example by assuming that the final-state dispersion of the photoelectron in step ① could be parametrized by a parabolic free-electron dispersion with a phenomenological offset parameter V_0. By matching the final state energy

with the energy of the free-electron states in vacuum one arrives at an approximate formula for the out-of-plane momentum component: $k_\perp = \frac{1}{\hbar}\sqrt{2m_\mathrm{e}\,(E_\mathrm{kin}\cos^2\theta + V_0)}$. This circumstance is of no relevance to the experiments in this work, as only the in-plane momentum components of the probed 2D electronic systems are considered.

Photoemission and the many-body spectral function

The following concentrates on the first step of the three-step model. In the case of non-interacting electrons the explicit calculation of the transition rate (w_{fi}) in Eq. (3.11) is simple and instructive. In this case both the initial and final states can be factorized as

$$|\psi_f^N\rangle = \underbrace{\mathcal{A}}_{\substack{\text{anti-sym.}\\ \text{operator}}} \underbrace{|\phi_f^\mathbf{k}\rangle}_{\substack{\text{electron after}\\ \text{photoexcitation}}} \otimes \underbrace{|\psi_f^{N-1}\rangle}_{\substack{\text{final state of}\\ \text{remaining (N-1)}\\ \text{electrons}}} \tag{3.15}$$

$$|\psi_i^N\rangle = \mathcal{A} \underbrace{|\phi_i^\mathbf{k}\rangle}_{\substack{\text{electron before}\\ \text{photoexcitation}}} \otimes \underbrace{|\psi_i^{N-1}\rangle}_{\substack{\text{initial state of}\\ \text{remaining (N-1)}\\ \text{electrons}}} \tag{3.16}$$

In the above description ϵ_f and $\epsilon_\mathbf{k}$ denote the energies of the states $|\phi_f^\mathbf{k}\rangle$ and $|\phi_i^\mathbf{k}\rangle$, respectively, which both describe an electron with momentum $\mathbf{k}$. The momentum of the photon has been neglected. The anti-symmetrization operator ($\mathcal{A}$) enforces the Pauli principle. Importantly, the removal of an electron state does not affect the rest of the states in the non-interacting scenario. This leads to a tremendous simplification by identifying $|\psi_i^{N-1}\rangle = |\psi_f^{N-1}\rangle$. The transition probability from Eq. (3.11) then becomes

$$w_{fi}(\mathbf{k},\epsilon_f) = \frac{2\pi}{\hbar}|\underbrace{\langle\phi_f^\mathbf{k}|\,H_\mathrm{int}\,|\phi_i^\mathbf{k}\rangle}_{M_{fi}^\mathbf{k}}|^2 \cdot \delta\left(\epsilon_f - \epsilon_\mathbf{k} - h\nu\right), \tag{3.17}$$

where $M_{fi}^\mathbf{k}$ is the one-electron dipole matrix element. It contains microscopic information about the initial state wave function $|\phi_i^\mathbf{k}\rangle$ which in principle can be used to experimentally access information such as the orbital character (at least symmetries) of the associated bands throughout the Brillouin zone (see, e.g., Refs. [94–96]). While bearing in mind that the total photocurrent (I) measured at the detector will be related to the total of all possible transitions, i.e., $I \sim \sum_{fi} w_{fi}$, Eq. (3.17) illustrates that in the hypothetical non-interacting limit the photocurrent traces the electronic band dispersion $\epsilon_\mathbf{k}$ encoded in the Dirac function.

In the interacting case it is obvious that the excitation of an electron in the photoemission process will in general not leave the left over $(N-1)$-electron system unaffected. The factorization of the N-particle wave functions $|\psi_f^N\rangle$ and $|\psi_i^N\rangle$ used before is thus not applicable. Therefore, for the critical assessment of the established method of interpreting PES data in terms of the one-electron spectral function $A(\mathbf{k},\omega)$ (cf. Eq. (A.17)), the physically relevant question to ask is whether (or to what extent) the photoelectron interacts with the

left over final state $(N-1)$-electron system. Assuming that the photoelectron is liberated from the N-electron initial state, i.e., $c_{\mathbf{k}} |\psi_i^N\rangle$ ($c_{\mathbf{k}}$ is the annihilation operator of an electron with momentum $\mathbf{k}$) in such a way as to leave the final state in any superposition of excited $(N-1)$-electron states $|\psi_m^{N-1}\rangle$ not correlated with the photoelectron, the transition probability from Eq. (3.11) becomes [85]

$$w_{fi}(\mathbf{k}, \epsilon_f) = |\langle \phi_f^{\mathbf{k}}| H_{\text{int}} |\phi_i^{\mathbf{k}}\rangle|^2 \sum_m \left|\langle \psi_m^{N-1}| c_{\mathbf{k}} |\psi_i^N\rangle\right|^2 \cdot \delta\left(\epsilon_f + E_m^{N-1} - E_i^N - h\nu\right) \tag{3.18}$$

$$= |M_{fi}^{\mathbf{k}}|^2 A^-(\mathbf{k}, \omega = h\nu - \epsilon_f) \ , \tag{3.19}$$

where the last step introduced the one-electron removal spectral function

$$A^-(\mathbf{k}, \omega) = \sum_m \left|\langle \psi_m^{N-1}| c_{\mathbf{k}} |\psi_i^N\rangle\right|^2 \cdot \delta\left(\omega - E_m^{N-1} + E_i^N\right) \ , \tag{3.20}$$

which relates to the full spectral function (cf. Eq. (A.17)) by $A^-(\mathbf{k}, \omega) = f(\omega) A(\mathbf{k}, \omega)$ with $f(\omega)$ being the Fermi-Dirac function. While it is often times stated that this interpretation is valid only if the experiment is in the *sudden limit*, i.e., the "instantaneous" liberation of the photoelectron which does not interact with the left over final state (valid in the limit of high photoelectron energies), in reality the above description might also be valid to a very high degree of accuracy, if the experiment is only in a *sudden regime* compared to specific electronic excitations (e.g., plasmons). Experiments have provided evidence that in certain materials this is the case even for photoelectrons excited with a photon energy as low as $h\nu = 6\,\text{eV}$ [97].

To arrive at the central result for interpretation of photoemission spectra, it must be recalled that the total photocurrent $I(\mathbf{k}, E_{\text{kin}}^{\text{D}})$ measured at the detector will be related to the total of all possible transitions, i.e., $I \sim \sum_{fi} w_{fi}$, and therefore

$$I(\mathbf{k}, E_{\text{kin}}^{\text{D}}) \sim \sum_{fi} \left|M_{fi}^{\mathbf{k}}\right|^2 f(h\nu - E_{\text{kin}}^{\text{D}} - \phi^{\text{D}}) A(\mathbf{k}, h\nu - E_{\text{kin}}^{\text{D}} - \phi^{\text{D}}) \ , \tag{3.21}$$

where $E_{\text{kin}}^{\text{D}}$ is the kinetic energy of the photoelectrons measured with the detector and ϕ^{D} is the work function of the detector, assuming that the Fermi energy of detector and sample is perfectly aligned, see Fig. 3.3.

The spectral function for the non-interacting and interacting case is given by the Eqs. (A.15) and (A.17) in the Appendix A.3. In connection with Eq. (3.21), they provide the theoretical basis for the interpretation of the photoelectron current in PES experiments. It is important to remember that self-energy corrections can give rise to substantial re-normalization of the non-interacting quasi-particle energies. By applying the inverse argument, one can see that in principle it is possible to retrieve the self-energy of the many-particle system from a full direct and inverse photoemission experiment.

Inelastically transmitted photoelectrons

While Eqs. (3.21) and (A.17) are the basis to reveal the intrinsic spectral properties of the system, they do not account for the effects of inelastic scattering events related to step ② in the three-step-model. These are frequently termed "extrinsic losses". Inelastically scattered photoelectrons appear as an additional background in the detected signal. While these processes can be modeled by a convolution of the intrinsic spectrum with the electron energy loss spectrum [98], a widely used method is to subtract a Shirley background from the photoemission signal [99]. This work applies the subtraction of a Shirley background for the line-shape analysis of XPS core-level spectra, which refers to the iterative method of calculating a background-corrected signal according to

$$I^{n+1}(E) = I_{\mathrm{exp}}(E) - I_{\mathrm{exp}}(E_1)\left(\frac{\int_E^{E_2} I^n(E')dE'}{\int_{E_1}^{E_2} I^n(E')dE'}\right) , \tag{3.22}$$

where $I_{\mathrm{exp}}(E)$ is the measured spectrum, E_1 and E_2 are the start and end values of the kinetic energies for which the background is calculated, and n is the iterative index.

3.3.2 Angle-resolved photoemission spectroscopy

After having provided the theoretical description of PES, the following concentrates on a description of the main components of the experimental setup for angle-resolved PES (ARPES) experiments used in this work. The description is limited to the onsite laboratory setup, which is used predominantly in this work. When experiments were performed at a beamline instead, it is explicitly mentioned. If not otherwise stated, the central components of the experimental setup (from the laboratory on site) are the following:

① **The light source:** A *UVS 300* He duoplasmatron non-monochromatized gas discharge lamp from *SPECS Surface Nano Analysis GmbH* is used. UPS was always performed with the He Iα line, i.e., $h\nu = 21.22\,\mathrm{eV}$.

② **The goniometer:** A six-axis *Carving* manipulator from *SPECS Surface Nano Analysis GmbH* was used as goniometer. It provides three rotational (ϑ, φ, τ) and three translational (x, y, z) degrees of freedom, see Fig. 3.4. Moreover, it provides a sample receptacle that can be cooled by a LHe flow to cool the sample to $\approx 10\,\mathrm{K}$.

③ **The spectrometer:** A *Phoibos 100* hemispherical electron energy analyzer (HEA) from *SPECS Surface Nano Analysis GmbH* was used, which is characterized by a 24 meV energy resolution.

The kinematics involved in the ARPES experiment is explained alongside the schematic image in Fig. 3.4. After the creation of photoelectrons by photons with energy $h\nu$ the HEA collects these photoelectrons, images them onto a slit entrance of the hemispherical deflectors, and uses a radial electric field generated in between the two concentric hemispherical deflector electrodes to force the photoelectrons onto elliptical orbits. The two-dimensional coordinates $(E^D_{\mathrm{kin}}, \alpha)$ at which the photoelectrons impinge onto the detector are determined

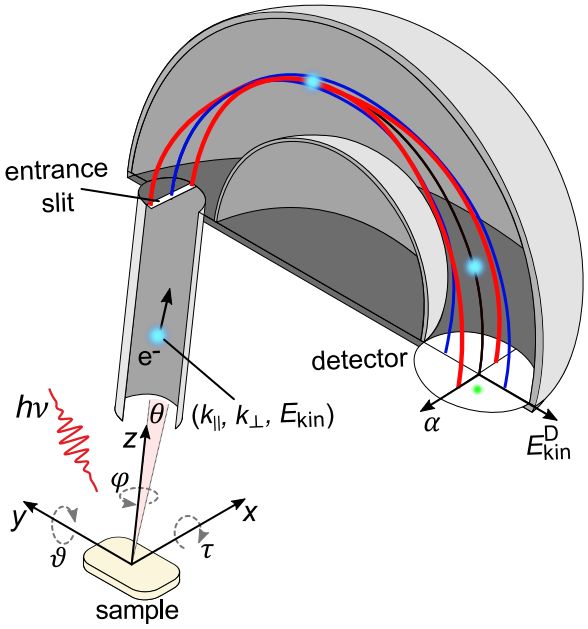

Figure 3.4: The angle-resolved photoemission process. The sample is illuminated by photons with energy $h\nu$. Photoelectrons are emitted into the full upper half space of the sample by the photoelectric effect. A fraction of the photoelectrons that pass the entrance slit are collected by the hemispherical electron energy analyzer. The photoelectrons are deflected by an electrostatic field and their emission angle (θ) and kinetic energy (E_{kin}) are retrieved. The photoelectron's in plane crystal momentum in the sample's reference frame can be calculated from the angle orientation of the sample relative to the detector given by the angle coordinates (ϑ, φ, τ), see Eq. (3.24).

by the radial displacement, which is a function of their kinetic energy (E_{kin}), and by the position orthogonal to this direction, which is determined by the photoelectron's emission angle (θ) within the entrance window accepted by the slit. Therefore, the detector records the 2D distribution of the photocurrent $I(E^{\mathrm{D}}_{\mathrm{kin}}, \alpha)$. The k-space mapping with the HEA is performed by subsequently scanning the angular degrees of freedom with the goniometer. For the geometrical setup depicted in Fig. 3.4 the in-plane momentum components k_{x}, k_{y} of the photoelectron in the rest frame of the sample can be retrieved according to

$$k_x = \hbar^{-1}\sqrt{2m_{\mathrm{e}}E_{\mathrm{kin}}}\,[\sin(\alpha-\vartheta)\,\cos\varphi + \cos(\alpha-\vartheta)\,\sin\tau\,\sin\varphi] \tag{3.23}$$

$$k_y = \hbar^{-1}\sqrt{2m_{\mathrm{e}}E_{\mathrm{kin}}}\,[\cos(\alpha-\vartheta)\,\sin\tau\,\cos\varphi - \sin(\alpha-\vartheta)\,\sin\varphi]\ , \tag{3.24}$$

where positive angles define rotations of the coordinate system in the mathematically positive sense.

3.3.3 Time- and angle-resolved photoemission spectroscopy

A substantial part of the presented work has also been conducted in cooperation with the "Dynamics of Correlated Materials" group led by Laurenz Rettig at the Fritz Haber Institute of Physical Chemistry in Berlin, where time- and angle-resolved PES experiments (trARPES) have been performed. Figure 3.5 is a schematic of the trARPES setup used. The following limits the description of this setup to the essential components, only. The reader is referred to Refs. [100, 101] for a more detailed description.

① **The light source:** The ultra-fast light source for femtosecond pulse generation in the extreme ultraviolet (XUV) spectral range is the central component and essential for a time-resolved mapping. Importantly it provides a photon energy that is large enough to access bismuthene's low-energy electronic structure over the entire first BZ. Laser light

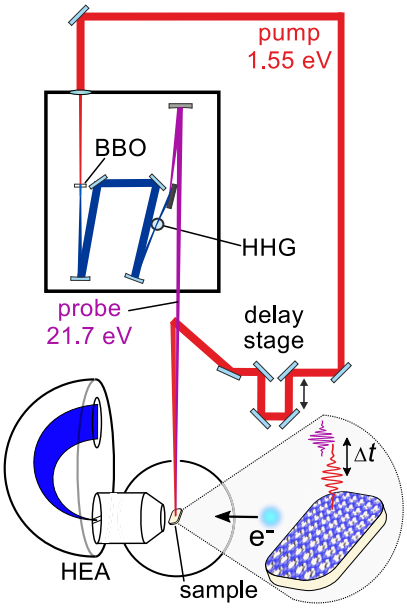

Figure 3.5: The time-resolved ARPES setup [100, 101]. The optical setup provides an s-polarized pump-pulse ($h\nu$ = 1.55 eV) at a repetition rate of 500 kHz and with a FWHM temporal broadening of 40 fs. The p-polarized probe-pulses ($h\nu$ = 21.7 eV, 110 meV bandwidth) are generated via a frequency doubling using a β-barium borate crystal followed by selecting the 7$^{\text{th}}$ harmonic in an ultraviolet-driven higher harmonic generation. The pump- and probe-pulse are focused onto the sample which sits on a six-axis manipulator inside the UHV analysis chamber. The FWHM spot sizes on the sample are 260 × 200 µm^2 and 80 × 80 µm^2, respectively. The delay stage of the optical setup controls the delay time Δt between incident pump- and probe- pulse. The achieved pump-probe cross-correlation is 40 fs. Photoelectrons are detected either by a HEA (*SPECS Phoibos 150*), or a time-of-flight momentum microscope (*SPECS METIS 1000*, not shown) to record the photoelectron current $I(E_{\text{kin}}, k_{\parallel})$, or $I(E_{\text{kin}}, k_x, k_y)$, respectively.

generation in the XUV range is technologically challenging. Here, it relies on a combination of crystal based frequency doubling of an s-polarized pump-pulse with photon energy $h\nu_{\text{pump}}$ = 1.55 eV (FWHM bandwidth 80 meV [101]) with a β-barium borate (BBO) crystal (1.55 eV → 3.10 eV) and high-order harmonic generation (HHG) using atomic ionization processes of a noble gas [102] (in this case Argon) in the very strong laser light field ($\sim 1 \times 10^{14}$ W cm^2). The HHG produces odd multiples of the driving laser frequency. The presented experiments use the 7$^{\text{th}}$ harmonic, which results in a p-polarized probe pulse with photon energy $h\nu_{\text{probe}}$ = 7 × 3.1 eV = 21.7 eV (FWHM bandwidth 110 meV [101]). The probe-pulse is synchronized with an s-polarized pump-pulse of energy 1.55 eV (or 3.10 eV) and both operate at a repetition rate of 500 kHz (FWHM bandwidth 80 meV [101]). Both pump- and probe-pulse are characterized by a FWHM temporal broadening of ∼ 40 fs. For the pump-probe scheme, the relative time delay between pump- and probe-pulse is set by a high precision mechanical delay stage with a resolution of a few hundreds of nanometers. The achieved temporal resolution (determined by the pump-probe cross-correlation) is ∼ 40 fs and the energy resolution is ∼ 150 meV. To build the full trARPES spectra, the temporal delay Δt of pump- and probe-pulse is successively varied with the delay stage and at every delay time step the photoelectron current is measured.

② **The goniometer:** The sample sits on a six-axis *Carving* manipulator from *SPECS Surface Nano Analysis GmbH* as goniometer, which allows for angular scanning along all degrees of freedom. The pump- and probe-pulses are directed onto the sample surface inside the UHV analysis chamber and are characterized by spot sizes (FWHM) of 260 × 200 µm^2 and 80 × 80 µm^2 on the sample surface, respectively.

③ **The spectrometer:** The emitted photoelectrons are detected by an hemispherical energy analyzer (*SPECS Phoibos 150*) which enables the acquisition of a 2D photoelectron

signal $I(E_{\mathrm{kin}}, k_{\parallel})$ as a function of the photoelectron's kinetic energy E_{kin} and parallel momentum $k_{\parallel}$. Also the alternative method of momentum microscopy (see Ref. [103]) which employs an extractor lens to acquire a 3D photoelectron signal $I(E_{\mathrm{kin}}, k_{\mathrm{x}}, k_{\mathrm{y}})$ in full 2D momentum space (k_{x}, k_{y}) is used in this work. The momentum microscope is not shown in Fig. 3.5, but the technical details and a side-by-side comparison of these two acquisition techniques (hemispherical energy analyzer vs. momentum microscope) employed with the very same setup is given in Ref. [104].

Interpretation of the photoelectron current in trARPES

Conventional ARPES involves only a small perturbation to the system under investigation. It is therefore considered to measure its equilibrium state properties that are translationally invariant in time. This circumstance is lifted in trARPES, which first involves an optical excitation of charge carriers to energies below the vacuum-level by a pump pulse. These occupy quasi-particle states between Fermi- and vacuum-level that were unoccupied in the ground state. Then the so modified system is probed by a time-delayed probe pulse that leads to the emission of photoelectrons for ARPES [105].

A simplistic convention for the interpretation of trAPRES experiments assumes that at each delay time the photo-excited electrons are in quasi-equilibrium at an elevated temperature (T_{el}) compared to the lattice temperature (T_{ph}) [106]. This implies that the probed photoelectron current is proportional to $A(\mathbf{k}, \omega) f(\omega; T_{\mathrm{el}})$ similar to Eq. (3.21), but at the elevated temperature T_{el}. Moreover, at progressing delay times the effective temperature of the photo-excited electrons gradually cools by electron-phonon scattering events. The drawback of this simplified interpretation is that it does not take into account dynamical aspects that arise from an out-of-equilibrium state of the system, nor does it take into account the finite temporal width of the probe pulse [107]. While the latter can lead to a spectral broadening, which is qualitatively different from effective thermal broadening, the former can induce drastic changes to the electronic structure due to many-body effects (e.g., band-gap renormalization, excitons, ect.).

To account for the loss of time-translation symmetry in trARPES the experiment must in principle be described by a time dependent many-body Hamiltonian. The rigorous theoretical treatment provided in Ref. [107] proves that in the case of a probe pulse $s(t) = N(t - \Delta t, \sigma)$, i.e., a Gaussian temporal profile centered at time Δt and with FWHM σ, the trARPES photoelectron current is given by

$$I(\Delta t, \mathbf{k}, \omega) \propto \int_{-\infty}^{\infty} dt_2 \int_{-\infty}^{\infty} dt_1 \, N(t_1 - \Delta t, \sigma) N(t_2 - \Delta t, \sigma) \, e^{i\omega(t_2 - t_1)/\hbar} \, G^{<}_{\nu_1 \mathbf{k},\, \nu_2 \mathbf{k}}(t_1,\, t_2) \,. \quad (3.25)$$

Here, $G^{<}_{\nu_1 \mathbf{k},\, \nu_2 \mathbf{k}}(t_1,\, t_2)$ is the two-time lesser Green's function, which involves quantum states ν_1 and ν_2 near the Fermi level that can be excited by the pump pulse. From Eq. (3.25) a general trend is deduced: the width of the trARPES signal decreases as the probe pulse temporally broadens (increasing σ). Moreover, it can be shown that the steady state ARPES

experiment is recovered in the limits $\Delta t \to \infty$ and $\sigma \to \infty$. In this case $I(\Delta t, \mathbf{k}, \omega) \propto A^{-}(\mathbf{k}, \omega) f(\omega; T)$ [107, 108], which corresponds to the intuitive expectation that in the limit of vanishing and steady-state excitation the photoelectron current in trARPES becomes identical to the one from conventional ARPES. To date, most experimental works employing trARPES do however not use Eq. 3.25 as theoretical basis for the interpretation of the experiments, due to its large degree of complexity.

3.3.4 X-ray photoemission spectroscopy

Employing X-rays for PES (XPS) is useful for the chemical analysis of a sample, because X-rays provide enough energy to liberate core electrons from the sample. From the comparison of the energetic peak positions in the photoelectron current with atom-specific core level energies, the atomic constituents of the sample as well as its oxidation state can be determined. For the data analysis of XPS curves it is particularly important to take into account the contribution of the inelastic electron background that contributes to the photoelectron current. As explained in Sec. 3.3.1 in the context of the of the three-step model, this contribution can be taken into account by the Shirley background correction to the measured photocurrent given by Eq. (3.22).

If not otherwise stated, this work used the following central components of the onsite laboratory setup to perform XPS:

① **The light source:** X-ray tubes using the Al K_α spectral line with $h\nu = 1486.7\,\mathrm{eV}$, or the Mg K_α spectral line with $h\nu = 1253.7\,\mathrm{eV}$.

② **The spectrometer:** a *Phoibos 100* hemispherical electron energy analyzer (HEA) from *SPECS Surface Nano Analysis GmbH* with 24 meV energy resolution.

3.3.5 Resonant photoemission spectroscopy

Tuning the photon energy (E_{Ph}) in a photoemission experiment can lead to interference effects in the photoelectron intensity. Specifically, an enhancement of the photoemission intensity can be observed when the photon energy is tuned to an X-ray absorption edge of an atomic species of the specimen. In this case, the photon energy can not just be regarded as an offset for the photoelectron's kinetic energy anymore. The enhancement of the photoemission intensity is then connected to an interference of different photoemission channels that give rise to the same photoemission final state. The experimental technique that exploits this circumstance is called resonant photoemission spectroscopy (ResPES). The ResPES measurements for this thesis were performed at a synchrotron radiation facility, since a continuously tunable photon energy source is needed. More details are given in later sections together with the respective experiment.

The description of the involved microscopic processes here is limited to the valence band photoemission processes observed in the transition metal cobalt (relevant for the experiments presented later). In this case, the $3d$ states at photon energies near the $2p \to 3d$ X-ray absorption, which defines the L-edge, is relevant. Two transitions are involved in an L-

edge resonant photoemission process with Co atoms. These are the direct photoemission transition, i.e., $2p^6 3d^7 \xrightarrow{+h\nu} 2p^6 3d^6 + e^-$, and the autoionization channel triggered by the creation of a core hole (coherent Auger decay), i.e., $2p^6 3d^7 \xrightarrow{+h\nu} 2p^5 3d^8 \rightarrow 2p^6 3d^6 + e^-$. A quantum mechanical interference, and thus the possibility of a resonant enhancement of the photoemission current, is only realized, if the coherence of the final state is not lost in the intermediate state ($2p^5 3d^8$). Otherwise, the final states of the above two photoemission channels differ, which only leads to an additional additive contribution from the so called incoherent Auger decay process.

If coherence is preserved, the theoretical description of the interference process in ResPES can be considered a Fano resonance [109], i.e., the coupling of the continuum of free electron final states to the discrete intermediate state ($2p^5 3d^8$) in the coherent Auger decay. The line shape of a constant initial state spectrum, which is the photoemission current at constant binding energies as a function of photon energy, i.e., $I(E_{h\nu})$, is modulated by a Fano profile (F) [110]:

$$I(E_{h\nu}) \backsimeq F(E_{h\nu}; q, E_{\mathrm{res}}) = \frac{[q + (E_{h\nu} - E_{\mathrm{res}})/(2\pi V_{\mathrm{A}}^2)]^2}{(E_{h\nu} - E_{\mathrm{res}})^2/(4\pi^2 V_{\mathrm{A}}^4) + 1} \tag{3.26}$$

$$q = \frac{\langle \Psi_{3\mathrm{d}} | \, \mathbf{r} \, | \Psi_{2\mathrm{p}} \rangle}{\pi V_{\mathrm{A}} \langle \phi_f^{\mathbf{k}} | \, \mathbf{r} \, | \Psi_{3\mathrm{d}} \rangle}, \tag{3.27}$$

with the resonance energy E_{res} and the matrix element of the coherent Auger process V_{A}. Moreover, $|\Psi_{2\mathrm{p}}\rangle$ ($|\Psi_{3\mathrm{d}}\rangle$) represents the 2p (3d) Co states and $|\phi_f^{\mathbf{k}}\rangle$ the free electron final state with momentum $\mathbf{k}$. The resulting line shape can be described as follows. At photon energies far away from the resonance energy, the Fano profile approaches 1, because the discrete intermediate state has no influence. On the other hand close to the resonance energy, $I(E_{h\nu})$ is modulated significantly by the Fano profile with a maximum enhancement of $q^2 + 1$.

Since ResPES is performed at the X-ray absorption edge of an atomic species, it is important to also measure the X-ray absorption spectrum (XAS) of the specimen itself. It reflects the absorption cross section of the material as a function of photon energy. For a XAS measurement, the photon energy is varied. At energies at or above the excitation threshold for a transition of core electrons to the unoccupied states, the absorption process can be detected by recording the drain current that results from the excited electrons. This method is then referred to as a measurement of the *total electron yield* (TEY).

3.4 Photo-modulated reflectance

This section describes the experimental setup and analysis methods for a special kind of optical reflectivity measurement: photo-modulated reflectance (PR). This technique uses an external stimulus applied to the sample to disturb its electronic system periodically in time. In PR experiments a modulated light field is used for this purpose. The goal of modulated reflectivity measurements is to achieve a significantly enhanced signal-to-noise ratio by using

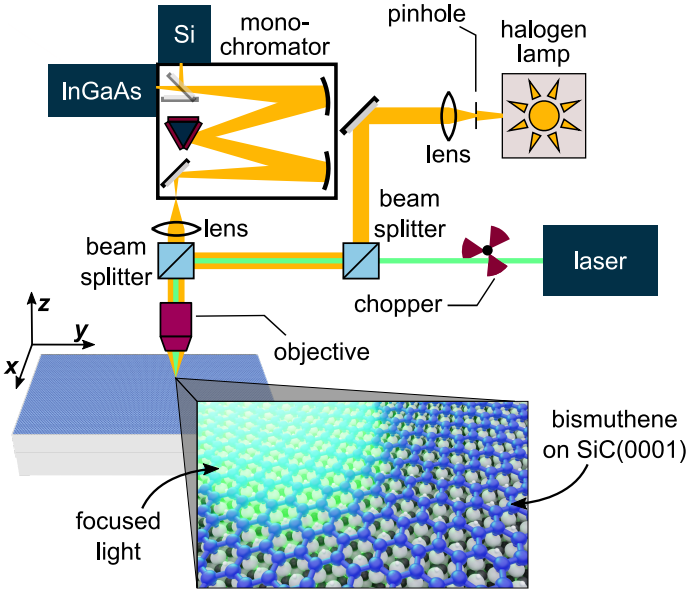

Figure 3.6: The photoreflectance setup. PR uses a modulated pump light source in combination with a lock-in filtering technique in order to achieve a significantly enhanced signal-to-noise ratio of the absorption spectra. The components of the depicted setup are described in the main text.

a lock-in filtering technique that extracts the signal from the noisy background.

3.4.1 Experimental setup

A schematic image of the experimental setup is depicted in Fig. 3.6. The source of modulation is a laser beam generated by a continuous-wave neodymium-doped yttrium aluminum garnet laser with photon wavelength of 532 nm, which is periodically interrupted at a frequency f_m with a mechanical chopper. The white light source for the reflectivity measurement is provided by a Halogen lamp. Both the modulated laser light and the white light are directed and focused onto the sample by use of a microscope objective ($\times 20$ magnification, 0.4 µm to 1.8 µm spectral range, 0.42 numerical aperture and 20 mm working distance). Its use has the effect that the spatial resolution of the PR experiment is determined by the spot size of the focused laser beam on the sample, which is ≈ 1 µm in diameter[6].

The bismuthene sample is mounted on a mechanical stage that provides three translational degrees of freedom (x-, y-, and z-movement in 0.1 µm steps). It allows to record spatially resolved PR spectra that can be compared with spatially dependent STM and/or LEED measurements performed on the same sample. The spectral analysis is performed with a spectrometer having a 0.3 m-focal-length grating monochromator in combination with either a Si diode (spectral range: 0.3 µm – 1.0 µm), or an InGaAs photo-receiver (spectral range: 0.9 µm – 1.5 µm). The detector readout is received by a lock-in amplifier (not shown in Fig. 3.6), which extracts the modulated signal at the carrier frequency (f_m) and enhances the signal-to-noise ratio significantly. An energy resolution of ≈ 4 meV is achieved with this PR setup.

[6]The spot from the white light source on the sample may be larger. However, since only the spatial region illuminated by the modulation laser can contribute to the PR signal after being filtered by the lock-in amplifier, the spatial resolution is set by the size of the modulating laser spot, only.

3.4.2 Derivation of the PR lineshape

Owing to the use of the lock-in filtering, the line shapes in PR experiments have a derivative character. The analysis of the PR line shape is based on an adapted model originally suggested by Shanabrook *et al.* [111]. Within this approach, the PR line shape is phenomenologically described as

$$\frac{\Delta R}{R} = \frac{1}{R}\frac{\mathrm{d}R}{\mathrm{d}\epsilon_\mathrm{r}}\Delta\epsilon_\mathrm{r} + \frac{1}{R}\frac{\mathrm{d}R}{\mathrm{d}\epsilon_\mathrm{i}}\Delta\epsilon_\mathrm{i} = \alpha\cdot\Delta\epsilon_\mathrm{r} + \beta\cdot\Delta\epsilon_\mathrm{i}\,, \tag{3.28}$$

where ϵ_r and ϵ_i are the real and imaginary part of the complex dielectric function ($\epsilon = \epsilon_\mathrm{r} + i\epsilon_\mathrm{i}$) of the material. Moreover, $\Delta\epsilon_\mathrm{r}$ and $\Delta\epsilon_\mathrm{i}$ are differentials of ϵ_r and ϵ_i, respectively, and α and β are Seraphin coefficients, which are generally wavelength dependent quantities [112]. An excitonic resonance involved in the optical transition is assumed to be of Lorentzian-type

$$\epsilon_\mathrm{r} + i\epsilon_\mathrm{i} \sim 1 + \frac{I}{E - E_\mathrm{gap} + i\Gamma} \tag{3.29}$$

where E_gap is the optical band-gap, Γ is the transition broadening, and I the intensity of the optical transition.

The change of the dielectric function ($\Delta\epsilon = \Delta\epsilon_\mathrm{r} + i\Delta\epsilon_\mathrm{i}$) is related to the modulating laser power P and takes a first derivative functional form [111, 113]:

$$\Delta\epsilon = \frac{\partial\epsilon}{\partial P} = \left[\frac{\partial\epsilon}{\partial E_\mathrm{gap}}\frac{\partial E_\mathrm{gap}}{\partial P} + \frac{\partial\epsilon}{\partial\Gamma}\frac{\partial\Gamma}{\partial P} + \frac{\partial\epsilon}{\partial I}\frac{\partial I}{\partial P}\right]\Delta P\,. \tag{3.30}$$

Defining $A_\mathrm{gap} \coloneqq \frac{\partial E_\mathrm{gap}}{\partial P}$, $A_\Gamma \coloneqq \frac{\partial\Gamma}{\partial P}$, $A_\mathrm{I} \coloneqq \frac{\partial I}{\partial P}$ and performing the partial differentiation of Eq. 3.29 yields the following expression for the dielectric function:

$$\Delta\epsilon = \left[A_\mathrm{gap}\left(\frac{I}{[(E - E_\mathrm{gap} + i\Gamma]^2}\right) - A_\Gamma\left(\frac{iI}{[(E - E_\mathrm{g}) + i\Gamma]^2}\right) + A_\mathrm{I}\left(\frac{1}{(E - E_\mathrm{g}) + i\Gamma}\right)\right]\Delta P\,. \tag{3.31}$$

Along the lines of Ref. [114] and Ref. [115] we assume that in Eq. 3.31 mainly the first two terms are important and thus arrive at the approximate expression:

$$\Delta\epsilon \approx \left[A_\mathrm{gap}\left(\frac{I}{[(E - E_\mathrm{gap} + i\Gamma]^2}\right) - A_\Gamma\left(\frac{iI}{[(E - E_\mathrm{gap}) + i\Gamma]^2}\right)\right]\Delta P\,. \tag{3.32}$$

Moreover, Eq. 3.32 can be further simplified by introducing the complex number $Ce^{i\theta} = I\Delta P\,(A_\mathrm{gap} - iA_\Gamma)$. Then,

$$\Delta\epsilon \approx \frac{Ce^{i\theta}}{[(E - E_\mathrm{gap}) + i\Gamma]^2}\,. \tag{3.33}$$

The value of the Seraphin coefficient β is negligible with respect to α in Eq. 3.28 at energies near the fundamental band-gap (E_gap) and can be omitted, see Refs. [111, 112]. This leads

to the final PR line shape formula for a single excitonic optical transition being:

$$\frac{\Delta R}{R} = \mathrm{Re}\left(Ce^{i\theta}(E - E_{\mathrm{gap}} + i\Gamma)^{-2}\right) . \tag{3.34}$$

Part II

Results and Discussion

CHAPTER 4

Optimization of bismuthene film epitaxy

Overview

A good crystalline quality of bismuthene is decisive to explore any of its inherent bulk properties, but ultimately also for potential use in future 2D TI devices. Therefore, experimental efforts have been directed towards improving the epitaxial growth ever since the first realization of the material [6, 7]. The originally established growth recipe, however, suffers from a lack of reproducibility, the emergence of a high defect density in the bismuthene film, and a bismuthene film that is divided into very small domains. This thesis carries on the work conducted in Ref. [7] and finds a largely improved growth scheme for bismuthene building on a newly gathered understanding of the involved growth dynamics, in particular about the evolution of film growth during epitaxy. These efforts lead to bismuthene monolayers with nearly 100% surface coverage, and to a substantial increase of domain sizes.

Because the preparation of bismuthene is divided into two steps, i.e., first the preparation of the (1×1) surface of the SiC substrate, and second the actual epitaxy of bismuthene on the prepared substrate surface, we first introduce the hydrogen etching method for SiC surface preparation in Sec. 4.1, followed by the stepwise optimization of the molecular beam epitaxy process of bismuthene on SiC presented in Sec. 4.2.

4.1 Preparation of the SiC(0001) (1×1) surface by H-etching

In recent years, SiC has proved to be a first-class epitaxial template for graphene in the context of monolayer epitaxy [116]. However, still it is a rarely used substrate for other monolayer materials. A major reason is the challenging preparation of its surface. In this regard, a sophisticated surface etching process using ultra-pure hydrogen gas is crucial to obtain atomically ordered surfaces [117]. Other widely used semiconductor surface cleaning procedures (e.g., flashing at high temperatures or Ar^+-ion sputtering) are not successful. Only in recent years has SiC emerged as an important epitaxial substrate for novel topological insulators such as bismuthene [6–8] and indenene [33].

In the present work, SiC substrates were prepared following the procedure used in Refs. [7, 117]. It consists of sequentially rinsing the substrates in ultra-pure acetone, iso-propanol and methanol for 2 min each to remove organic contaminants, followed by the process of *hydrogen etching*. The idea behind this process is to produce reactive H^+-ions by thermal cracking of H_2 molecules directly at the heated SiC sample that remove the Si and C atoms at the SiC surface in a layer-by-layer fashion [117]. In this work, a resistive DC heating method was used for heating the substrate. To facilitate the DC heating and also

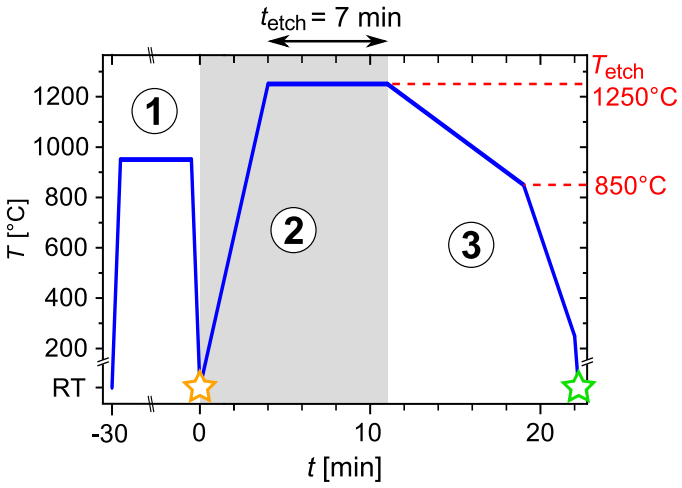

Figure 4.1: Target temperature curve for H-etching of SiC. The process is divided into three parts. In the first step the sample is heated to about 950 °C for 30 min to remove adsorbates from the sample surface. The second and third step relate to the actual hydrogen etching process, as decribed in the main text. Orange and green stars indicate the moment in time when ultrapure H_2 and He_2 gas is led into and pumped out of the UHV chamber, respectively. The temperature is measured with an optical pyrometer at emissivity $\epsilon = 85\%$ in all cases.

later characterization with STM, ARPES and LEED all SiC substrates used are doped with nitrogen to a resistivity in the range of 0.01 Ω cm to 0.03 Ω cm at room temperature. This amounts to a doping concentration between $5 \times 10^{18}\,\mathrm{cm}^{-3}$ and $1 \times 10^{19}\,\mathrm{cm}^{-3}$. After a successful hydrogen etching process the surface shows atomically flat terraces with a width of hundreds of nanometers [7,117]. Importantly, the dangling bonds of the SiC surface remain passivated by hydrogen atoms after etching which renders it a very inert surface [117].

Figure 4.1 shows the temperature (T) over time (t) curve, which is used in the hydrogen etching process. In step ① the substrate is annealed by DC current heating in UHV (at pressures of low 10^{-9} mbar) at 950 °C for at least 30 min to remove adsorbents and residual molecules from the SiC substrate. In a second step ② a constant flow[7] of 2 slm ultrapure (purity 7.0 and further purification with a palladium diffusion filter) H_2 and He gas is led into the UHV chamber at a pressure of 950 mbar. At this stage the actual H-etching is performed by heating the substrate to 1250 °C (1200 °C for a miscut SiC substrate, cf. Fig. 4.3) for 7 min to thermally crack the H_2 molecules, which then remove the Si-/C-atoms subsequently from the substrate surface by forming silanes and hydrocarbons [117]. In a third step ③ the substrate is cooled down to room-temperature in a controlled manner, i.e., → 850 °C within 8 min → 250 °C within 3 min → RT. In the last cooling step the power supply is simply turned off upon which the sample cools down to RT in ≈ 10 s. The gas flow is then stopped and the chamber is pumped again to UHV conditions.

The atomic flatness of a successful H-etching process is checked with STM constant current measurements as shown in Figs. 4.2**a**, **b** for a nominally flat and a miscut substrate, respectively. These two types of substrates were used to achieve a level of control over the density of the SiC step edges which will directly influence the density of bismuthene film edges later. Whereas the nominally flat substrates have a miscut angle in a range of $(0.0 \pm 0.5)°$, the miscut substrates (in the following referred to as *miscut* or *stepped* sub-

[7] It has been observed in Refs. [7,118] that the use of a constant hydrogen/helium-flow instead of a static gas atmosphere counteracts a re-deposition of silanes and hydrocarbons onto the etched surface.

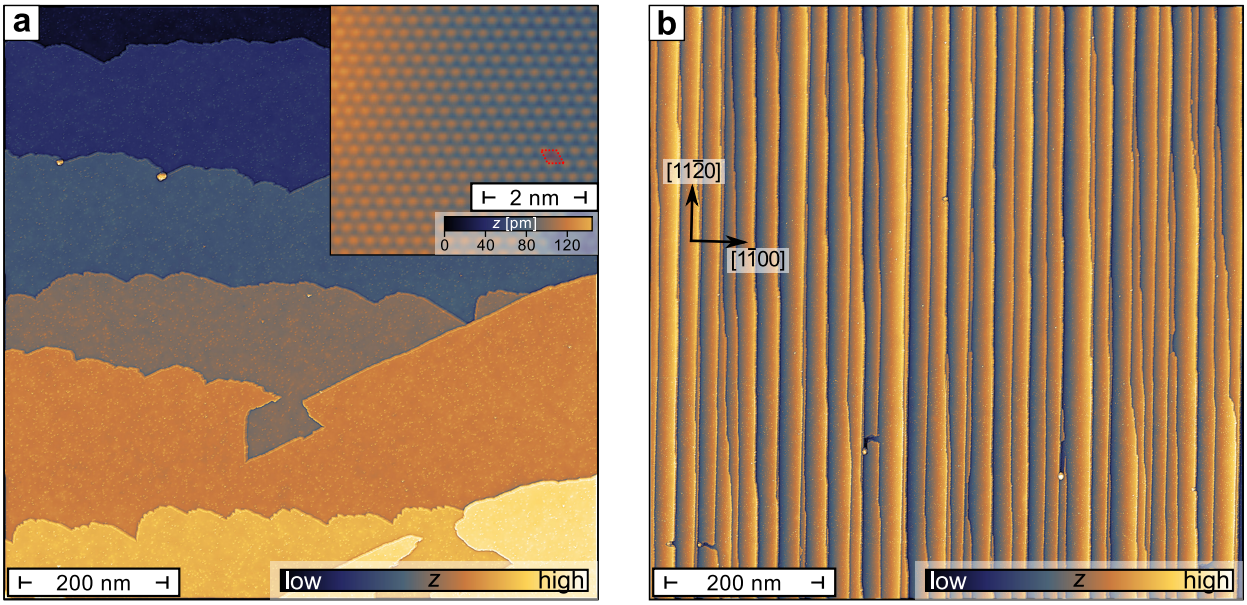

Figure 4.2: Overview STM images of flat and stepped SiC substrates after H-etching. **(a),** STM constant current image ($V_{\text{set}} = 3\,\text{V}$, $I_{\text{set}} = 50\,\text{pA}$, $T = 4.35\,\text{K}$) of a nominally flat SiC(0001) substrate after H-etching at $T_{\text{etch}} = 1250\,^{\circ}\text{C}$ for 7 min. The inset shows an atomically resolved STM constant current measurement of the H-etched SiC(0001) surface. The substrate unit cell is indicated by a red rhomb. **(b),** STM constant current image ($V_{\text{set}} = 3\,\text{V}$, $I_{\text{set}} = 50\,\text{pA}$, $T = 4.35\,\text{K}$) of a miscut SiC(0001) substrate after H-etching at $T_{\text{etch}} = 1200\,^{\circ}\text{C}$ for 7 min. The miscut of the SiC wafer is 4° towards the [1$\bar{1}$00] direction. A low-pass filter with an cut-off at 4 nm was applied to the measurements in **a** (not to the inset figure) and **b** in order to better visualize the steps in the false color plot.

strate) have an intentional miscut angle of $(4.0 \pm 0.5)^{\circ}$ towards the [1$\bar{1}$00] direction. In the case of the nominally flat SiC substrate the terrace step termination is neither isotropic, nor is the terrace width uniform. The terrace width varies approximately in the range of $\sim 200\,\text{nm} - 300\,\text{nm}$. Most importantly, however, the atomic flatness of the surface and its defect free atomic lattice within each terrace can be clearly confirmed, as is shown in the STM image in the inset of Fig. 4.2**a**.

The STM images on the H-etched miscut SiC substrates in Fig. 4.2**b** reveal the drastic increase of the density of the SiC step edges. Specifically, the cutting angle of the substrate, in this case 4° towards the [1$\bar{1}$00] direction, ultimately determines the density of step edges and therefore also bismuthene film edges after epitaxial growth. Indeed, as the regular terrace width is $\approx 15\,\text{nm}$, the density of SiC step edges has roughly increased by a factor of $\approx 13 - 20$ compared to the nominally flat substrates. Moreover, all the terrace steps run along the [11$\bar{2}$0] direction, which leads to longer straight edge segments. Nearly all substrate steps show a 4H-SiC unit cell height of 10.08 Å The distribution of the step height can to some extent be controlled by the etching temperature, which will be explained in the following.

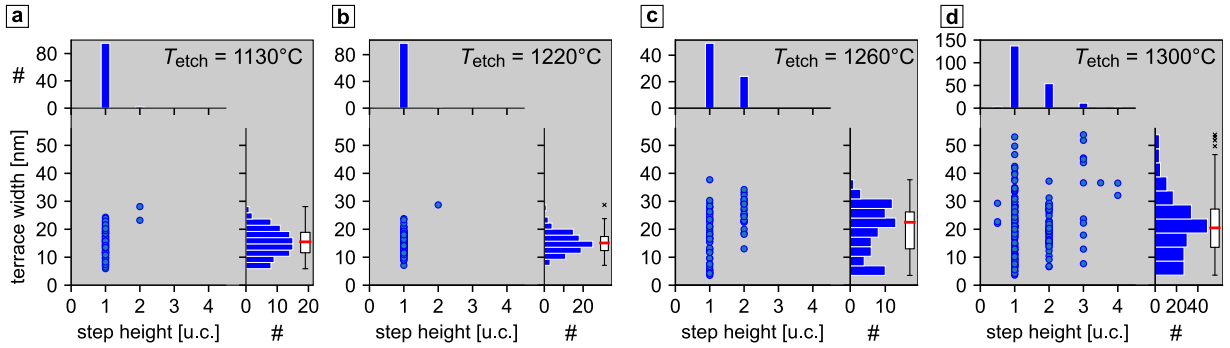

Figure 4.3: Controlling the step distribution on 4° miscut SiC(0001) substrates. (a) – (d), SiC step height and terrace width distributions of 4° miscut samples as a function of etching temperature T_{etch}. A box-and-whisker plot for the terrace width distribution is shown (box indicates range between the lower quartile Q_1 and the upper quartile Q_3; red line indicates median Q_2; whiskers indicate the most extreme data (lower and upper) point that is no more than $1.5 \times (Q_3 - Q_1)$ from the edge of the box; crosses indicate data points lying outside the whiskers). The sample is etched according to the H-etching procedure described in connection with Fig. 4.1 holding the etching temperature at the value indicated in the respective image for 4 min. The estimated error of T_{etch} is $\Delta T_{\mathrm{etch}} \approx \pm 25\,^{\circ}\mathrm{C}$ and is a consequence of a temperature gradient across the sample of $\approx 50\,^{\circ}\mathrm{C\,mm^{-1}}$. The data underlying the distributions was gathered by analyzing STM constant current measurements of a H-etched sample as in Fig. 4.2**b**. The step height is given in multiples of the 4H-SiC unit cell height ($a_{\mathrm{SiC}} = 10.08$ Å).

Influence of the etching temperature on the SiC step and terrace morphology

The effect of the etching temperature on the step height and terrace width distribution of the miscut SiC substrates is analyzed based on STM constant current measurements of etched substrates. The resulting distributions in Figs. 4.3**a**–**d** are illustrated as bivariate plots (main panel) with the univariate histogram plots of the terrace width and the step height given in the right and top marginal panel, respectively. It is readily seen that for $T_{\mathrm{etch}} = 1130\,^{\circ}\mathrm{C}$ in Fig. 4.3**b** and $T_{\mathrm{etch}} = 1220\,^{\circ}\mathrm{C}$ in Fig. 4.3**c**, respectively, the step height distributions consist almost exclusively of single 4H-SiC unit cell heights. An increase in temperature to $T_{\mathrm{etch}} = 1260\,^{\circ}\mathrm{C}$ (cf. Fig. 4.3**d**) is accompanied by the formation of steps with a height of two unit cells. As a result, the mean terrace width also increases and is accompanied by a wider spread. Increasing T_{etch} further to 1300 °C continues this trend and leads to step heights of three and even four unit cells, as well as only half unit cell steps. In conclusion, the step edge distribution is particularly sensitive to T_{etch} for the miscut SiC substrates. A temperature range of $T_{\mathrm{etch}} = 1130\,^{\circ}\mathrm{C} - 1220\,^{\circ}\mathrm{C}$ is optimal for achieving regular step height and terrace width distributions.

4.1.1 The dehydrogenated SiC(0001) (1×1) surface

After the H-etching process the SiC surface is left H-passivated, i.e., every surface Si-dangling bond is binding to an H-atom. This surface is chemically very inert, which facilitates removing any adsorbates from its surface after having transferred the substrate from

the hydrogen etching chamber into the UHV chamber for epitaxial growth of bismuthene with the help of a UHV suitcase (the load-lock pressure during transfer is in the range of 5×10^{-8} mbar $- 1 \times 10^{-7}$ mbar). However, it is a crucial requirement that the H-atoms that passivate the surface are removed before the growth of bismuthene. Only then, the Bi atoms can covalently bond to the surface Si atoms. For the development of the epitaxial growth of bismuthene it would be the most natural choice to adopt a thermal treatment that leads to a full desorption of hydrogen from the surface. However, the authors of Ref. [119] find that a thermal treatment that desorbs the H-atoms is not feasible without an accompanying transformation from the (1×1) to a $(\sqrt{3} \times \sqrt{3})R30°$ surface reconstruction. This reconstruction, however, would impede the growth of bismuthene and must be avoided. Here, combined STM and LEED measurements provide evidence that an unreconstructed and dehydrogenated 4H-SiC(0001) (1×1) surface *can* be prepared by thermal annealing.

Thermal desorption of hydrogen from the SiC surface

Independent of the hexagonal SiC polytype, the basic reconstructions of the Si-rich surfaces are the $(\sqrt{3} \times \sqrt{3})R30°$ and the (3×3) surface reconstructions [120]. Both types can be induced by thermal annealing of the (1×1) surface. In Figs. 4.4**a**–**g**, starting from the lowest temperature, the same sample is successively heated to the temperature T specified in the image and hold constant at this temperature for 10 min. LEED measurements continuously track the process of the $(1 \times 1) \rightarrow (\sqrt{3} \times \sqrt{3})R30°$ reconstruction induced by the thermal annealing steps. It is readily seen from Figs. 4.4**a**–**f** (note the logarithmic intensity scale that is suited to highlight also small intensities) that the pristine (1×1) SiC(0001) surface order persists up to $T = 596\,°\text{C}$. Only after the last annealing at $T = 602\,°\text{C}$ very faint additional $(\sqrt{3} \times \sqrt{3})R30°$ Bragg peaks are observed and marked by red lines in Fig. 4.4**g**. The presented measurements set an upper temperature limit for the thermally induced transition from $(1 \times 1) \rightarrow (\sqrt{3} \times \sqrt{3})R30°$ reconstruction, i.e., heating the substrate to $(599 \pm 3)\,°\text{C}$ for 10 min. However, from the LEED experiments it can not be judged at which stage of the thermal treatment the H-atoms actually desorbed from the SiC surface. This deficiency is overcome by conducting STM measurements at successive annealing steps of an initially H-passivated SiC sample.

The STM measurements in Figs. 4.4**h**–**k** reveal surface changes on the nanometer scale. To detect any surface reconstruction on a larger scale, again LEED was performed prior to every STM scan. Directly after the hydrogen etching process and the first annealing step at only $T = 500\,°\text{C}$ for 10 min the corresponding LEED image (cf. inset of Fig. 4.4**h**) confirms the presence of the (1×1) Bragg peaks only and, therefore, an unreconstructed surface. This surface is laced with very few point defects (yellow and dark spots), but the largest part of the surface area is defect free and is related to the H-passivated SiC surface. Upon a further annealing step at $T = 520\,°\text{C}$ for 10 min the surface morphology as seen from the STM constant current image has already changed, see Fig. 4.4**i**. The surface now exhibits more bright point defects (yellow dots) that are located on top of Si-sites (see inset of Fig. 4.4**i**).

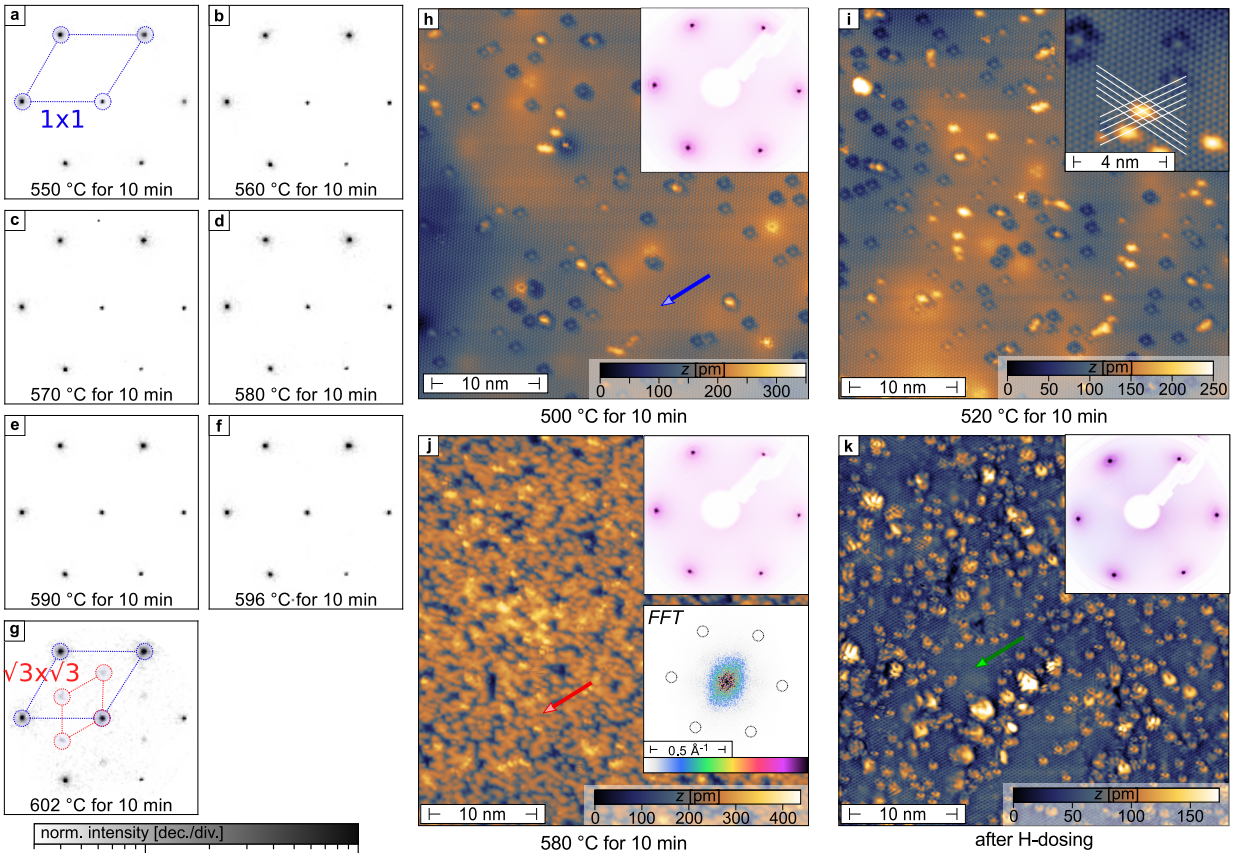

Figure 4.4: Thermal desorption of hydrogen from the SiC surface. (a) – (g), LEED (spot profile anlalysis LEED) images of the very same initially H-passivated SiC sample after successive temperature annealing steps as indicated in the respective image ($U_{\mathrm{Ch}} = 2050\,\mathrm{V}$, $E = 160\,\mathrm{eV}$). The intensity is normalized to the respective maximum intensity in each image and plotted on a logarithmic intensity scale. The temperature was measured by an optical single color pyrometer (emissivity $\epsilon = 0.85$). The SiC (1×1) and $(\sqrt{3} \times \sqrt{3})R30°$ Bragg peaks are marked with blue and red lines, respectively. **(h),** STM constant current measurement of the H-etched SiC surface after annealing at $T = 500\,°\mathrm{C}$ for 10 min. The blue arrow indicates an atomically flat and H-saturated area on the surface. Inset: The LEED image recorded at $E = 65\,\mathrm{eV}$ only shows (1×1) Bragg peaks of unreconstructed SiC. **(i),** STM constant current measurement of the H-etched SiC surface after a successive annealing at $T = 520\,°\mathrm{C}$ for 10 min. The density of point defects with larger apparent height (see inset figure for a detailed STM scan) has increased. **(j),** STM constant current measurement of the H-etched SiC surface after another successive annealing at $T = 580\,°\mathrm{C}$ for 10 min. This surface does not show any of the atomically flat areas (indicated by the blue arrow in **h**) anymore. This surface morphology (as indicated by the red arrow) can be associated with the desorption of hydrogen from the surface at the applied elevated temperature. Upper inset: The LEED image recorded at $E = 65\,\mathrm{eV}$ only shows (1×1) Bragg peaks of unreconstructed SiC. Lower inset: The FFT of the STM constant current image shows no signs of any ordering. Dashed circles indicate the positions at which SiC(0001) (1×1) spots would be monitored. **(k),** STM constant current measurement of an annealed surface as in **j** after additional hydrogen dosing. The surface again displays atomically flat areas as indicated by the green arrow. These are similar to the ones indicated by the blue arrow in **h**. Their appearance is a sign for the resaturation of the surface Si dangling bonds by hydrogen. STM scan parameters for **h**–**j**: $V_{\mathrm{set}} = 3.0\,\mathrm{V}$, $I_{\mathrm{set}} = 50\,\mathrm{pA}$, $T = 4.35\,\mathrm{K}$. STM scan parameters for **k**: $V_{\mathrm{set}} = 3.0\,\mathrm{V}$, $I_{\mathrm{set}} = 30\,\mathrm{pA}$, $T = 4.35\,\mathrm{K}$.

The most natural origin of these point defects are dangling bond states of the topmost Si atoms created by thermal desorption of hydrogen. Finally, after a further annealing step at $T = 580\,°\mathrm{C}$ for 10 min basically no H-passivated SiC surface areas are left and the point defect density (associated with dangling bonds) has drastically increased. However, it is hard to distinguish individual dangling bond states, since they do already spatially overlap. Moreover, these states do not seem to adapt to any periodicity. This is underpinned by considering the Fourier transformed image of the STM constant current image (cf. inset of Fig. 4.4**j**), which does not show interference peaks, especially not at the anticipated SiC (1×1) spots marked by dashed circles. The LEED image still only monitors the presence of the (1×1) SiC(0001) Bragg peaks very clearly (cf. inset Fig. 4.4**j**), which proves that the surface has not undergone any $(1 \times 1) \rightarrow (\sqrt{3} \times \sqrt{3})R30°$ reconstruction.

The steady increase of the point defect density with higher annealing temperatures is indicative of the de-hydrogenation of the surface Si bonds. Further indications for a dangling bond surface in Fig. 4.4**j** are that by redepositing atomic hydrogen to such a surface, a partial recovery of the H-passivated SiC surface is achieved. Therefore, hydrogen (purity 5.0 and further purification with a palladium diffusion filter) was dosed into the UHV chamber through a sputter gun ($p = 3.2 \times 10^{-5}\,\mathrm{mbar}$, $t = 10\,\mathrm{min}$, $I_{\mathrm{flux}} = 2\,\mu\mathrm{A}$, $U_{\mathrm{HV}} = 100\,\mathrm{V}$). The H_2-molecules pass the hot filament of the sputter gun and are cracked into hydrogen atoms directed onto the presumable dangling bond surface as in Fig. 4.4**j**. The STM image of the SiC surface after this hydrogen re-deposition process is shown in Fig. 4.4**k**. The surface partially recovers the typical defect free H-passivated areas as indicated by the green arrow in Fig. 4.4**h**, and, still the corresponding LEED image monitors a (1×1) surface reconstruction, only (see inset of Fig. 4.4**k**). With further hydrogen dosing, however, it was not possible to further improve the quality of the surface and restore the initial condition after hydrogen etching. A reason could be that the used hydrogen gas still suffered from a too low purity which leads to an accumulation of larger adsorbate clusters on the surface, as seen in Fig. 4.4**k**. However, the combined LEED and STM measurements show that thermal desorption of hydrogen from the SiC(0001) surface is possible, and is not necessarily accompanied by a $(1 \times 1) \rightarrow (\sqrt{3} \times \sqrt{3})R30°$ surface reconstruction. This insight is crucial for the feasibility of epitaxial bismuthene growth on this growth template.

4.2 Molecular beam epitaxy of bismuthene films

This section covers the process of molecular beam epitaxy for the controlled growth of bismuthene films on the H-etched SiC(0001) surface. Section 4.2.1 describes the experimental setup used for this process and explains the basic growth recipe. Section 4.2.2 sketches the employed strategy for achieving larger bismuthene domains. It consists of the basic idea to reduce the number of nucleation centers in the early stage of growth and to continuously monitor the formation of the bismuthene islands with STM. Section 4.2.3 focuses on achieving samples with full bismuthene surface coverage. Lastly, Sec. 4.2.4 compares bismuthene films grown according to the improved growth recipe with films grown according to the growth recipe of prior works.

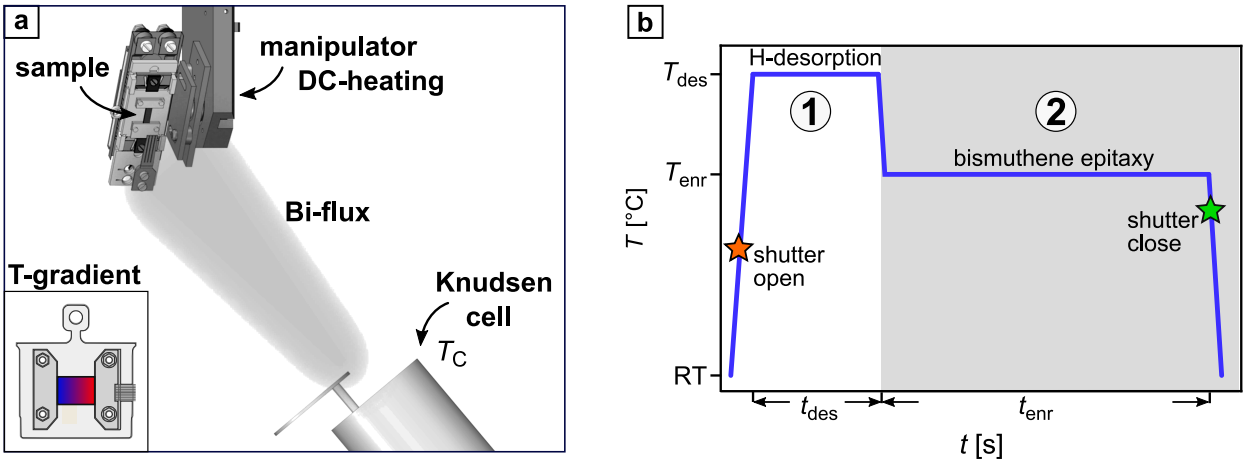

Figure 4.5: Molecular beam epitaxy setup and temperature curve for bismuthene growth. **(a)**, Schematic of the experimental setup for molecular beam epitaxy of bismuthene. The H-etched SiC substrate has been transferred into a UHV chamber that has a base pressure of $\sim 1 \times 10^{-10}$ mbar and is placed onto the stage of the manipulator head. The stage allows to heat the substrate resistively via applying a DC current. Bismuth is evaporated from a Knudsen cell equipped with a pyrolytic boron nitride crucible holding the high-purity (99.9999%) bismuth pellets. It can be heated to a temperature of T_C to produce and regulate the Bi-flux F_{Bi} directed towards the SiC substrate during the epitaxial growth. **(b)**, Target temperature curve over time used for the epitaxial growth of bismuthene. The growth is divided into two parts which are the *desorption of hydrogen* and the actual *epitaxy of bismuthene*. Details of the growth are described in the main text.

4.2.1 Setup for molecular beam epitaxy and basic bismuthene growth recipe

The basic experimental setup for the epitaxial growth of bismuthene is shown in Fig. 4.5**a**. The H-etched SiC substrate, which is mounted on the *ScientaOmicron* type sample holder, is placed on the stage of the manipulator and can be heated by applying a direct current (DC) to the substrate. This resistive heating method produces a temperature gradient along the SiC substrate, as depicted in the inset of Fig. 4.5**a**. The temperature gradient always extends over the SiC wafer strip from one sample holder clamp to the other and has a typical magnitude of $2\,°\mathrm{C\,mm^{-1}} - 4\,°\mathrm{C\,mm^{-1}}$, which will be important for the later analysis of the growth in Sec. 4.2.3. The sample surface is facing directly towards a Knudsen cell during growth. The pyrolytic boron nitride crucible of the cell is filled with bismuth pellets of 99.9999% purity and the temperature of the crucible T_C controls the generated Bi flux F_{Bi}.

The targeted sample temperature over time which is used for growing bismuthene is shown in Fig. 4.5**b**. The curve is divided into two steps, where step ① corresponds to the process of hydrogen desorption from the SiC surface in which the substrate temperature is raised to the hydrogen desorption temperature T_{des} within 45 s and held constant for the time of desorption ($t_{des} = 160$ s). In step ② the actual epitaxy of bismuthene takes place. For this step, the substrate temperature is lowered within ≈ 10 s to the Bi enrichment temperature

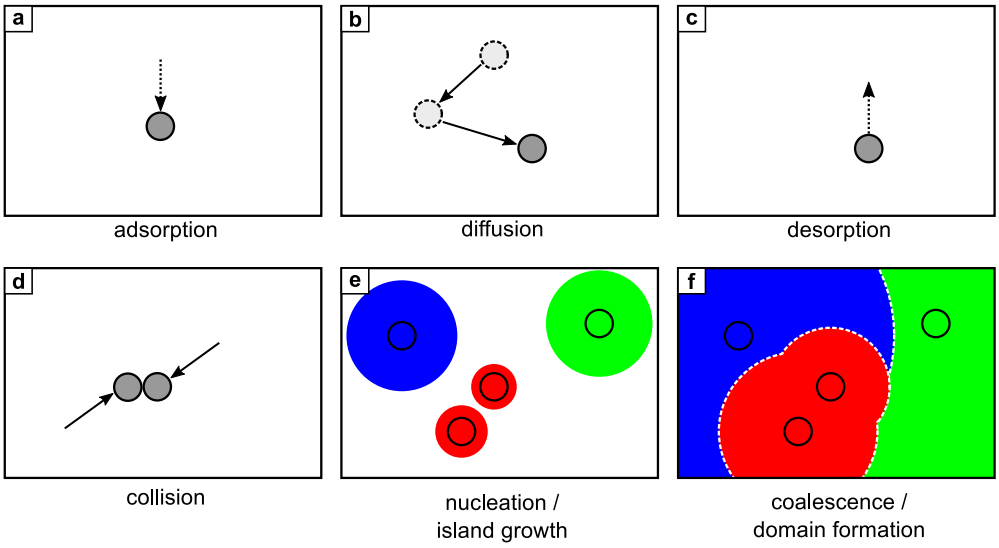

Figure 4.6: Schematics of atomistic processes during bismuthene growth. **(a)** – **(f)**, Pictorial illustration of microscopic processes during epitaxial film growth. The individual processes are explained in more detail in the main text.

T_{enr}, and held constant for the time of enrichment t_{enr}. This step ends by rapidly cooling down the sample to below 400 °C within 5 s, followed by a successive cooling down to room temperature.

As a key to advance and to understand the bismuthene growth we focused on studying the influence of the main three growth parameters that impact the morphology of the bismuthene film during the epitaxy. These are the sample temperature during the Bi enrichment T_{enr}, the time of Bi enrichment t_{enr}, and the temperature of the Bi cell T_C which controls the Bi flux.

4.2.2 Strategy to achieve larger domains

The last section identified three main growth parameters, namely T_{enr}, t_{enr}, and T_C. In principle these parameters span a parameter space which is far too large to be fully screened in regular steps. Therefore, the work of this section tries to apply a simple atomistic picture of the growth dynamics to help provide a strategy for how to tune these parameters systematically in order to achieve larger domains.

Atomistic processes involved in the epitaxial growth

In order to provide a starting point for systematic improvement of the growth, it is worth to first consider the atomistic processes on the surface of the sample during growth. The very basic processes are schematically depicted in Figs. 4.6**a**–**d**. These processes describe the adsorption of single atoms on the surface, their subsequent diffusion over the surface until they either desorb from the surface or collide with another single atom or a cluster of other atoms. All of these processes are governed by characteristic time scales τ that

are dependent on activation energies E as $\tau \sim \exp(E/k_\mathrm{B}T)$, where T is the substrate temperature. In principle, the growth dynamics are governed by a very complex system of coupled differential equations [121]. It is readily clear, however, that in a state of detailed balance, i.e., in a state where all these processes occur in both directions at equal time scales, while microscopically the system is still continually changing, no net film growth takes place. To achieve a net film growth the epitaxial process has to be in a non-equilibrium state, in which islands start to grow at a certain critical cluster size [121]. This picture will help us in the following.

One important aspect for the growth of bismuthene is that it forms a $(\sqrt{3} \times \sqrt{3})R30°$ superstructure on the (1×1) SiC(0001) surface. In this case the bismuthene islands can form with three distinct registries relative to the SiC(0001) surface (indicated by different colors in Fig. 4.6**e**). It means that bismuthene islands form as crystallites which are always strictly related to each other by translational shifts of multiples of the SiC(0001) lattice constant, but which in 2/3 cases can not merge to form a single coherent film. This leads to the unavoidable consequence that they are separated by domain boundaries, see Fig. 4.6**f**. Therefore it is clear, that a low number density of *stable* islands (N) is imperative for achieving large domains.

What role do the growth parameters T_enr, t_enr, and T_C play in this regard? A simple argument presented by Mo *et al.* [122] circumvents the need to explicitly solve the aforementioned large system of coupled differential equations. Following their reasoning, a low number density of stable islands is achieved, if the probability for an arriving adatom to nucleate at an existing island is higher than the probability to collide with another single adatom which would in turn result in a new seed for a stable island. It is readily apparent that these two scenarios are competing processes for the growth of large domains. According to the model by Mo *et al.* [122] the outcome of the two competing processes is dictated by mainly two parameters. The first is the diffusion coefficient D of the adatoms. The second parameter is the deposition rate R of adatoms onto the surface. The authors' result for the number density of stable islands N on the surface during growth is then [122, 123]:

$$N \propto \left(\frac{R}{D}\right)^{\frac{1}{3}} \tag{4.1}$$

Notably, this estimate is only approximately valid in an early stage of growth, when the domains are still small, and it does not take into account the desorption of adatoms. However, Eq. (4.1) provides us with an elementary starting point for adjusting the growth parameters in a targeted manner to reach larger domains. Either decreasing the deposition rate R by lowering the effusion cell temperature T_C, and/or increasing the diffusion coefficient D by increasing the sample temperature during bismuthene epitaxy T_enr is suited to reduce the number density of stable islands N.

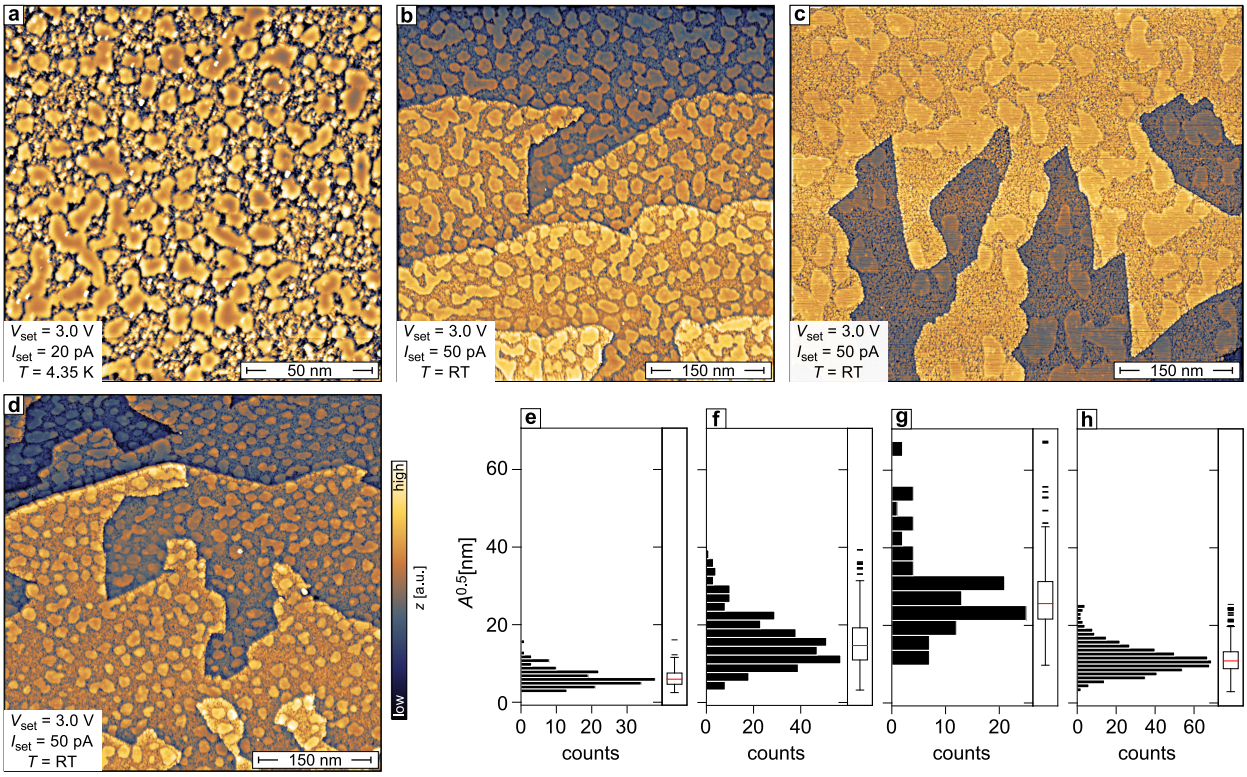

Figure 4.7: Initial stage of bismuthene growth. **(a) – (d),** STM constant current images of bismuthene with incomplete surface coverage. In this early stage of growth bismuthene is forming as islands (patches with smooth morphology) that are mostly unconnected. The rougher areas inbetween the islands are attributed to disordered bismuth atoms or clusters. The growth parameters for each growth are listed in Tab. 4.1. **(e) – (h),** Island size distributions showing $A^{0.5}$, i.e., the square root of surface area A of individual islands in **a**–**d**, respectively. The distributions are summarized by the corresponding box-and-whisker plot (box indicates range between the lower quartile Q_1 and the upper quartile Q_3; red line indicates median Q_2; whiskers indicate the most extreme data (lower and upper) point that is no more than 1.5 × $(Q_3 - Q_1)$ from the edge of the box; lines outside whiskers indicate data points lying outside the whiskers). The numerical values connected to the box-and-whisker plots are listed in Tab. 4.1.

Reducing the number density of stable islands in experiment

Focusing on the identification of trends associated with the variation of the relevant growth parameters T_C and T_{enr} in the initial stage of growth, the aforementioned strategy will be persued in the following. The bismuthene epitaxy process will be intentionally stopped at a very early stage, i.e., when nucleation centers have already formed and bismuthene islands begin to form around the nucleation centers, but the overall bismuthene coverage is still much lower than a complete monolayer. This is achieved by choosing the time of epitaxy t_{enr} intentionally much too short for a complete bismuthene film growth.

Figure 4.7 compares the initial island formation for four different sets of growth parameters listed in Tab. 4.1. In all cases the bismuthene growth was stopped when the total fraction of surface area covered with bismuthene was ≈ 30% – 40%. The visual inspection of the STM

constant current images in Figs. 4.7**a**–**d** reveals that at this point bismuthene forms small islands that have not grown to a closed film. It is also observed that the distributions of the bismuthene island sizes strongly differ between the different growths. The morphology in the surrounding of the islands appears amorphous, which can be related to unordered clusters of Bi-atoms.

Figures 4.7**e**–**f** show a quantitative analysis of the size distributions of bismuthene islands and consider the parameter $A^{0.5}$ as the relevant measure of size, where A is the surface area of an island. It is readily seen that the island size distributions of the different growth recipies summarized in Tab. 4.1 vary strongly. The island size distribution in Fig. 4.7**e** connected to the growth in Fig. 4.7**a** shows the smallest median island size of $A^{0.5}_{Q_2} = 5.9\,\mathrm{nm}$. This is the growth which followed the proposed recipe of the first realization of bismuthene given in Refs. [6, 7]. The small island size is a consequence of a very large number density of stable islands N according to Eq. (4.1) which impedes the formation of large domains later.

In a next step, a significant reduction of the cell temperature from $T_C = 580\,^\circ\mathrm{C}$ to $T_C = 530\,^\circ\mathrm{C}$ is applied for the growth shown in Fig. 4.7**b**. Its island size distribution is shown in Fig. 4.7**f** and has an improved median island size of $A^{0.5}_{Q_2} = 14.7\,\mathrm{nm}$. This observation is thus in accordance with the aforementioned considerations (cf. Mo *et al.* [122]) according to which a reduction of the deposition rate R mediated by the reduced cell temperature T_C leads to a reduction of the number density of stable islands N.

This trend can be continued by lowering the cell temperature further to $T_C = 500\,^\circ\mathrm{C}$. It results in a median island size of $A^{0.5}_{Q_2} = 25.6\,\mathrm{nm}$, see Figs. 4.7**c, g**. However, trying to lower the cell temperature further to $T_\mathrm{C} = 470\,^\circ\mathrm{C}$ while holding the sample temperature at $T_\mathrm{enr} = 530\,^\circ\mathrm{C}$ (not shown in Fig. 4.7) did not lead to a successful bismuthene growth, i.e., $(\sqrt{3} \times \sqrt{3})R30^\circ$ Bragg peaks of bismuthene were not observed in the LEED measurements. The probable reason is that with these conditions the desorption rate of Bi-atoms was larger than the characteristic time needed to form stable nucleation seeds and then bismuthene islands. To counteract this process, the sample temperature was lowered from 530 °C to 500 °C, while keeping the cell temperature at $T_\mathrm{C} = 470\,^\circ\mathrm{C}$. Figure 4.7**d** shows the resulting growth, which, however, exhibits no further improvement, i.e., the median size of the bismuthene island distribution yields $A^{0.5}_{Q_2} = 10.8\,\mathrm{nm}$ (see Fig. 4.7**h**), which is smaller than before.

In summary, while the whole parameter space of T_enr and T_C has not exhaustively been screened, improved values for these parameters were found that increased the median island size by a factor of ≈ 4.3 compared to what has been achieved with the "original" growth recipe given in Refs. [6, 7]. As Sec. 4.2.4 will show, the achieved reduction of the number density of stable islands N in the early stage of growth will indeed result in significantly larger bismuthene domains also in the case of a completed bismuthene monolayer growth.

Fig.	T_C	T_{enr}	t_{enr}	**coverage**	Q_1	Q_2	Q_3
4.7**a**	580 °C	(530 ± 3) °C	200 s	34%	4.6 nm	5.9 nm	7.5 nm
4.7**b**	530 °C	(540 ± 3) °C	300 s	40%	11.0 nm	14.7 nm	19.2 nm
4.7**c**	500 °C	(530 ± 3) °C	2445 s	29%	21.6 nm	25.6 nm	31.3 nm
4.7**d**	470 °C	(500 ± 3) °C	5865 s	30%	8.8 nm	10.8 nm	13.2 nm

Table 4.1: Temperature of the sample during epitaxy (T_{enr}), evaporator cell temperature (T_C), and time (t_{enr}) of epitaxy for the growths shown in Fig. 4.7. The estimated error $\Delta T_{enr} = 3\,°C$ is a result of the temperature gradient on the SiC samples while heating and the uncertainty connected in correlating positions on the sample with measured STM positions after the growth process. The coverage is given as the fraction of surface area that is covered by the bismuthene islands. The values Q_1, Q_2, Q_3 are the quartiles of the respective box-and-whisker plots in Fig. 4.7**e**–**h**. Prior to each bismuthene growth, hydrogen was desorbed by holding the substrate at $T_{des} = 595\,°C$ for $t_{des} = 160\,s$.

4.2.3 Achieving a full bismuthene surface coverage

The last section covered epitaxial processes that were stopped at an early stage in order to intentionally produce disconnected bismuthene islands. To achieve a full coverage of bismuthene, the time of epitaxy t_{enr} has to be adapted. Therefore, the growth parameters from the last section that resulted in the smallest number density of stable islands N are now chosen, i.e., $T_{enr} = 530\,°C$ and $T_C = 500\,°C$.

The overview STM constant current scans in Figure 4.8 continuously monitor the film growth on the very same sample after repeated growth steps. The axis depicted above the images indicates the aggregated time for epitaxy t_{enr} and the fraction of total surface area

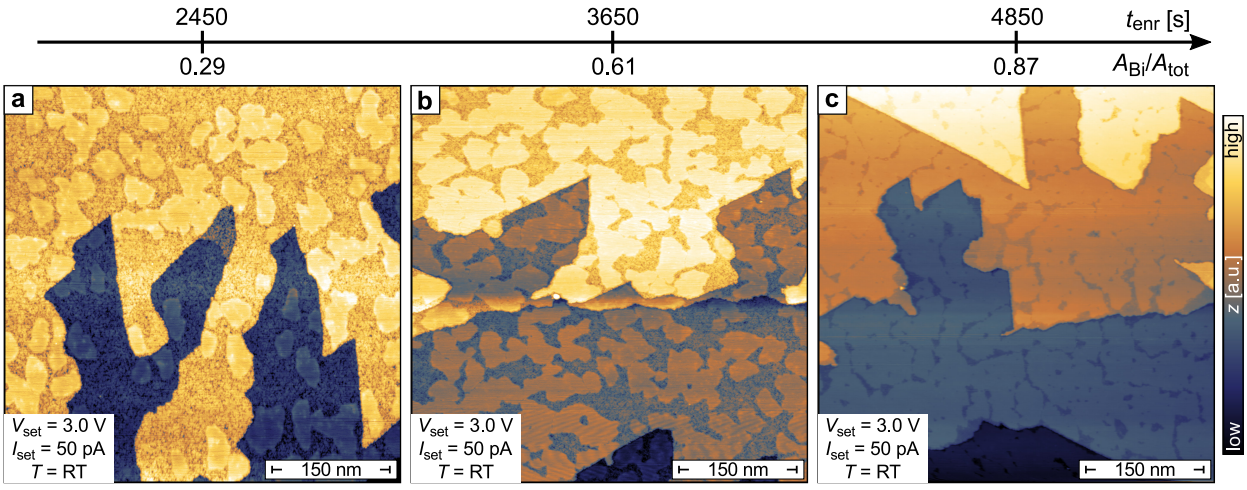

Figure 4.8: Evolution of bismuthene film coverage with time. **(a) – (c),** STM constant current images were recorded during three interuption steps of one bismuthene growth. The aggregated time of epitaxy and the aggregated bismuthene surface coverage are given at the top of the images. After each STM measurement the growth was resumed with the same growth parameters, i.e., $T_{enr} = (530 \pm 3)\,°C$, $T_C = 500\,°C$ in all cases. Hydrogen was desorbed only prior to the first growth in **a** by holding the substrate at $T_{des} = 600\,°C$ for $t_{des} = 160\,s$.

covered by bismuthene at each step, i.e., $(A_{\mathrm{Bi}}/A_{\mathrm{tot}})$ where A_{Bi} is the sum of the surface area covered by bismuthene and A_{tot} is the total surface area. After the first growth step shown in Fig. 4.8**a**, only small bismuthene islands have formed. A larger fraction of the surface is still covered by amorphous clusters that most probably relate to unordered Bi-atoms and/or Bi-clusters. Figure 4.8**b** indicates that larger bismuthene island have formed after the second growth step on this very same sample, and that these islands started to interconnect. Still, $\approx 39\%$ of the surface is not covered by bismuthene. Finally, after the third growth step on this very same sample depicted in Fig. 4.8**c**, the bismuthene layer has nearly grown to a completely closed monolayer. This evolution series reveals that the film coverage grows roughly linearly with time, although deviations from this roughly linear behavior is expected at the very beginning and end of the full epitaxial growth.

The implemented strategy of interrupted growth and subsequent STM characterization strengthens a pictorial understanding of the growth: The process starts with the formation of small bismuthene islands within a "soup" of mobile Bi-atoms that steadily adsorb onto, diffuse across, and desorb from the surface. These processes are, however, in a non-equilibrium state which results in a net film growth after reaching a certain critical cluster/island size [121]. It follows a continuous growth of the small islands to larger interconnected film sections that can ultimately result in a full bismuthene monolayer. Notably, the required time for a completed monolayer with the improved growth parameters is approximately 90 min. This is in stark contrast to the $\approx$ 3 min needed with the "original" growth recipe proposed in Refs. [6, 7]. This points to the fact that the improved growth parameters have led to a process that is much closer to a state of detailed balance of the growth kinetics [121] and is likely the reason for the creation of larger bismuthene domains.

Sensitivity to small variations of sample temperature

For optimal film growth all the parameters T_{C}, T_{enr}, and t_{des} must be adjusted simultanously and be matched together. The following focuses on how the film morphology is affected by small variations of T_{enr}. This is of particular importance, since the DC-heating technique of the SiC substrate always leads to a temperature gradient on the order of $2\,^{\circ}\mathrm{C\,mm^{-1}}$ – $4\,^{\circ}\mathrm{C\,mm^{-1}}$ across the sample and therefore the sample quality will always be position dependent on the substrate. Figure 4.9 shows STM constant current and LEED measurements that illustrate the effect of lower-than-optimal (Figs. 4.9**a, b**), optimal (Fig. 4.9**c**), and higher-than-optimal (see Figs. 4.9**d, e**) sample temperature T_{enr} during growth. The cell temperature T_{C} and time of epitaxy t_{enr} was the same in all cases.

First, the error of T_{enr} is estimated. This error results mainly from the inaccuracy of the performed optical pyrometric temperature measurement and the later cross-correlation with the STM measurement position on the sample. Since the optical pyrometer averages over ≈ 0.5 mm of the sample and the magnitude of the temperature gradient across the mounted SiC sample is $\approx 2\,^{\circ}\mathrm{C\,mm^{-1}} - 4\,^{\circ}\mathrm{C\,mm^{-1}}$, this relates to an error of $\approx 1\,^{\circ}\mathrm{C} - 2\,^{\circ}\mathrm{C}$. Moreover, the STM measurement positions on the sample can be cross-correlated with the position

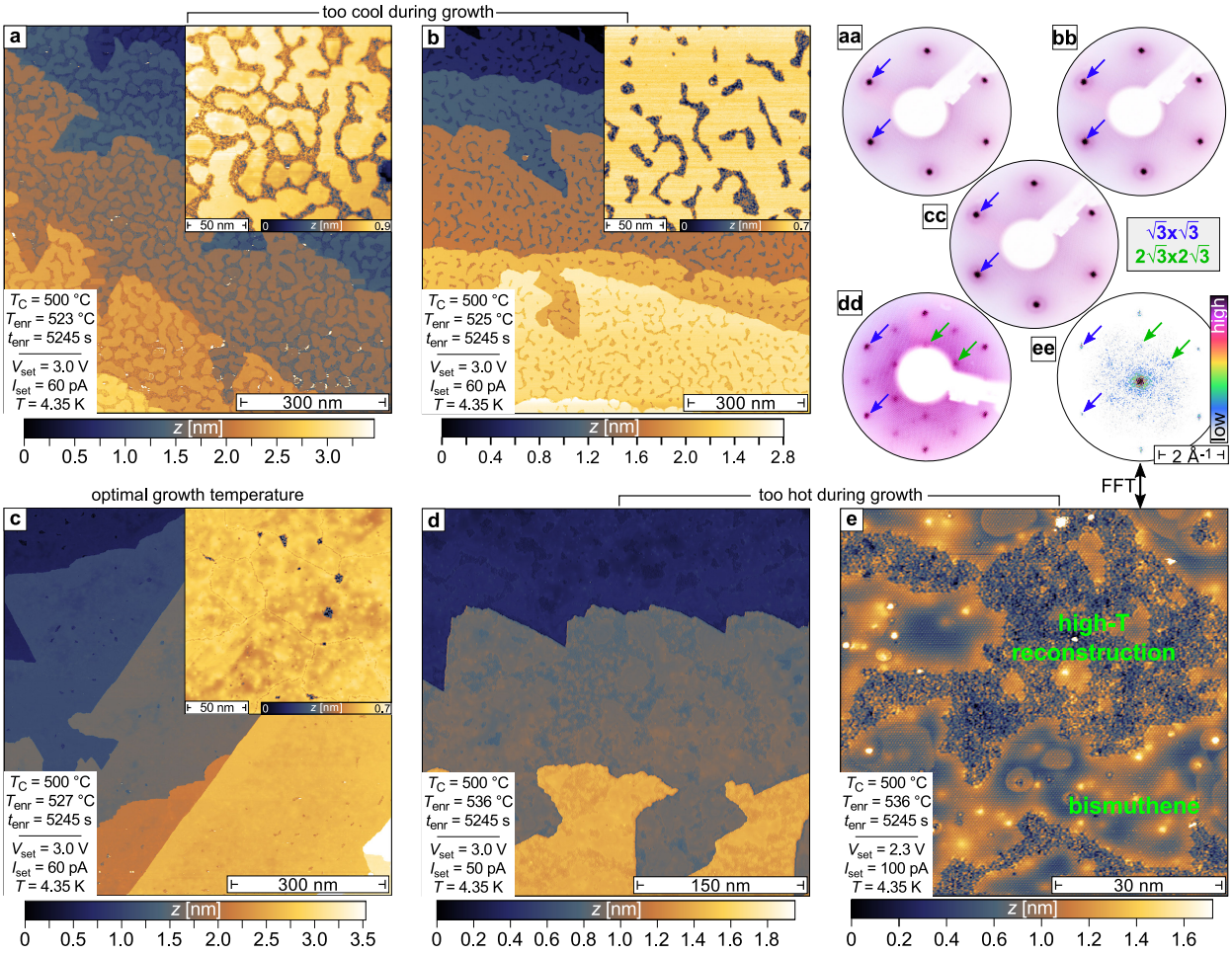

Figure 4.9: Sensitivity of bismuthene growth to small variations of the sample temperature. **(a) – (d),** STM constant current measurements of bismuthene grown under different growth conditions. The growth parameters are indicated inside each image. Hydrogen was desorbed at $T_{\mathrm{des}} = 595\,^{\circ}\mathrm{C}$ for $t_{\mathrm{des}} = 160\,\mathrm{s}$ prior to each growth. The corresponding LEED images are shown in **(aa) – (dd)**, respectively. The blue arrows indicate the $(\sqrt{3} \times \sqrt{3})R30^{\circ}$ Bragg peaks from the bismuthene layer and green arrows indicate $(2\sqrt{3} \times 2\sqrt{3})R30^{\circ}$ Bragg peaks from an additional high-T surface reconstruction (see **e, ee**). **(e),** Detailed STM constant current images of the same bismuthene film as in **d**. Here, bismuthene coexists with an additional high-T surface reconstruction. **(ee),** Fourier transform (FFT) of the STM constant current measurement in **e**. The marked peaks in the FFT correspond to the $(\sqrt{3} \times \sqrt{3})R30^{\circ}$ and $(2\sqrt{3} \times 2\sqrt{3})R30^{\circ}$ Bragg peaks observed in LEED. *Figure (e) reprinted and adapted from Ref. [124] under a Creative Commons Attribution 4.0 International (CC BY 4.0) License.*

at which the temperature was measured during the growth with an accuracy of $\approx 0.5\,\mathrm{mm}$. This adds an additional error of $\approx 1\,^{\circ}\mathrm{C}$ – $2\,^{\circ}\mathrm{C}$. Therefore, the total error is $\Delta T_{\mathrm{enr}} \approx 3\,^{\circ}\mathrm{C}$.

Figures 4.9**a, b** address the case of a lower-than-optimal temperature T_{enr}. While, the bismuthene film that grew with the lowest temperature exhibits a bismuthene surface coverage of 63%, see Fig. 4.9**a**, the bismuthene surface coverage improved to 82% by raising the substrate temperature during growth by only $(2 \pm 3)\,^{\circ}\mathrm{C}$, see Fig. 4.9**b**. Eventually, raising the substrate temperature by another $(2 \pm 3)\,^{\circ}\mathrm{C}$ results in the optimum bismuthene quality shown Fig. 4.9**c** with a bismuthene surface coverage of 97%. Although the three surfaces differ significantly in the STM measurements, in all three cases the LEED images are nearly equal and only show bismuthene $(\sqrt{3} \times \sqrt{3})R30^{\circ}$ Bragg peaks (cf. Figs. 4.9**aa**–**cc**). Notably, in the case of the growth shown in Fig. 4.9**a** the film morphology appears very similar to what was observed for the growth with higher T_{enr}, but shorter epitaxial time t_{enr} in Fig. 4.8**b**. So the bismuthene film in Fig. 4.9**a** might have improved further with a longer epitaxial time.

Turning to the case of a higher-than-optimal temperature T_{enr} in Figs. 4.9**d, e** it is seen that the bismuthene film also has large areas of incomplete growth. These areas, however, are of a different kind as in the case of the growth with lower-than-optimal temperature. In particular, Fig. 4.9**e** reveals that the bismuthene domains coexist with another (partially) ordered surface reconstruction, which is named "high-T reconstruction". Indeed, a fast-Fourier transform (FFT) of the real space STM image gives rise to additional $(2\sqrt{3} \times 2\sqrt{3})R30^{\circ}$ peaks as marked with green arrows in Fig. 4.9**ee**. These peaks are also found in the LEED image measured on this sample (see Fig. 4.9**dd**). This new phase might be a low coverage sub-monolayer phase, since the higher-than-optimal sample temperature during growth might have led to a slightly too large desorption rate of Bi-atoms from the surface.

In summary, the presented study revealed that the temperature window of T_{enr} for which the growth of bismuthene can be regarded optimal (at fixed growth parameters T_{C} and t_{des}) is as narrow as $\approx 5\,^{\circ}\mathrm{C} - 10\,^{\circ}\mathrm{C}$. Therefore, the sample temperature T_{enr} needs to be controlled with at least $5\,^{\circ}\mathrm{C}$ of accuracy to establish a reproducible growth with high coverage. The temperature gradient over the sample might be detrimental for future larger scale applications. At this point, however, it also provides the possibility to gain information on the influence of small T_{enr} variations via cross-correlation with position dependent STM, ARPES, and LEED experiments on one single sample.

4.2.4 Optimized bismuthene growth

For the technological applicability of helical edge transport in bismuthene, it is desirable to have domains large enough for lithographic processing. The so called *maximally inscribed disc radius* R_{i} (see inset of Fig. 4.10**c**) is a useful parameter to quantify the domain size. This quantity relates to the radius of the largest circle that fits into a single domain and, given the irregular shape of domains, is much better suited as a meaningful measure for the size of domains than the mere area. For example, R_{i} can be of particular interest with respect

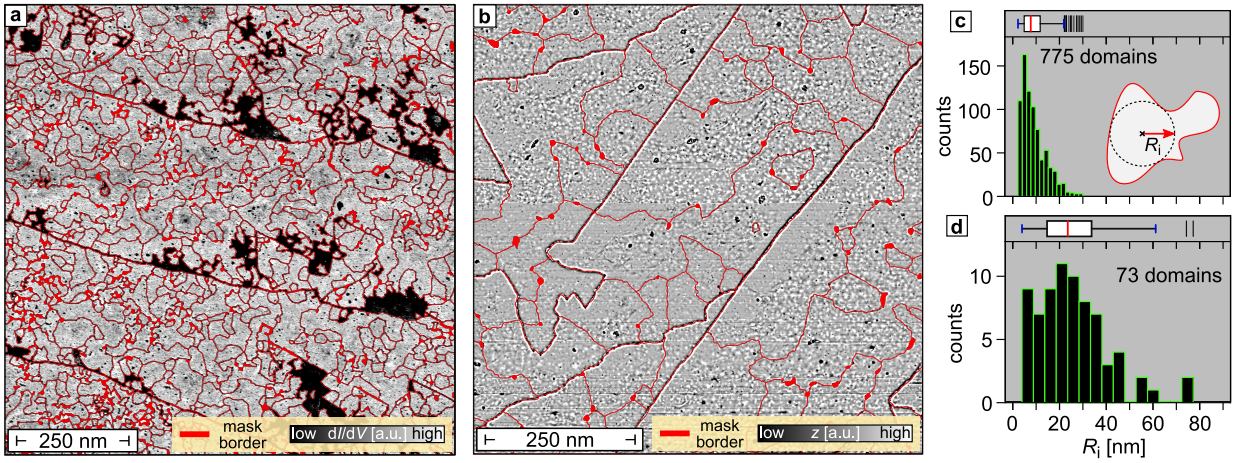

Figure 4.10: Domain size distribution after completed film growth. **(a),** Differential conductivity ($V_{\text{set}} = 3.0\,\text{V}$, $V_{\text{mod}} = 50\,\text{mV}$, $I_{\text{set}} = 10\,\text{pA}$, $T = 4.35\,\text{K}$) and **(b),** constant current ($V_{\text{set}} = 3.0\,\text{V}$, $I_{\text{set}} = 60\,\text{pA}$, $T = 4.35\,\text{K}$) overview maps after completed film growth according to the non-optimized (in **a**) and optimized (in **b**) growth recipe (cf. Tab. 4.2), respectively. The red lines indicate the mask that circumscribes each domain. It is used to quantitatively measure the domain size distribution. **(c), (d),** Domain size distribution of the measurements in **a** and **b**, respectively. The maximal inscribed disc radius R_i is used (schematically shown in the inset of **c**) as a measure for the domain size. The distributions are summarized by the corresponding box-and-whisker plot (box indicates range between the lower quartile Q_1 and the upper quartile Q_3; red line indicates median Q_2; blue whiskers indicate the most extreme data (lower and upper) point that is no more than $1.5 \times (Q_3 - Q_1)$ from the edge of the box; lines outside whiskers indicate data points lying outside the whiskers). The numerical values are listed in Tab. 4.2.

to lithographic processes, since it is a direct measure of the size of a structure that would fit into the domain without intersecting a domain boundary. The following concentrates on the domain size distribution which is achieved with the improved growth parameters after a completed monolayer growth and compares it with the domain size distribution from the "original" growth as given in Refs. [6, 7].

The STM measurement in Fig. 4.10**a** shows a spatially resolved differential conductivity map on a bismuthene sample grown according to the "original" growth recipe. The exact

Fig.	$T_{\mathbf{C}}$	$T_{\mathbf{enr}}$	$t_{\mathbf{enr}}$	Q_1	Q_2	Q_3
4.10 **a, c**	580 °C	(535 ± 3) °C	200 s	4.9 nm	7.7 nm	11.7 nm
4.10 **b, d**	500 °C	(527 ± 3) °C	5250 s	14.7 nm	23.5 nm	33.7 nm
6.6 in Ref. [7]	–	–	–	–	3.6 nm – 7.4 nm	–

Table 4.2: Temperature of the sample during epitaxy (T_{enr}), evaporator cell temperature (T_C), and time (t_{enr}) of epitaxy for the growths shown in Fig. 4.10. The estimated error $\Delta T_{\text{enr}} = 3\,°\text{C}$ is a result of the temperature gradient on the SiC samples while heating and the uncertainty connected in correlating positions on the sample with measured STM positions after the growth process. The values Q_1, Q_2, Q_3 are the quartiles of the respective box-and-whisker plots in Fig. 4.10**c**–**d**.

growth parameters are listed in Tab. 4.2 . This measurement is capable to clearly resolve all the bismuthene domain boundaries. A statistical grain analysis with regard to the maximally inscribed disc radius R_i is performed with the software tool *Gwyddion* using a mask that traces the domain boundaries (red lines in Fig. 4.10**a**). Careful visual inspection of the mask ensured that the individual grains were correctly separated and to result in a valid grain analysis. The same procedure was performed on a STM constant current image of a bismuthene sample grown with the optimized growth parameters (exact growth parameters are listed in Tab. 4.2), see Fig. 4.10**b**. Already by visual comparison of both images it is apparent that the domains resulting from the new optimized epitaxial process are significantly larger.

The quantitative analysis of the distributions of maximally inscribed disc radii R_i corresponding to domains in Figs. 4.10**a, b** are shown in Figs. 4.10**c, d**, respectively. The huge difference is readily apparent from the corresponding box-and-whisker plots on top of each figure for which the numerical values are summarized in Tab. 4.2. Notably, the grain analysis did not exclude domains that touch the border of the scan frame to achieve a decent grain statistics also in the case of very large domains. This is more relevant for the analysis of the growth connected to Fig. 4.10**b**. Here, the real distribution of the inscribed disc radius should be in average shifted to even larger values Fig. 4.10**d**. Overall the optimized growth parameters connected to the growth in Fig. 4.10**b** has led to an increase of the median inscribed disc radius by a factor of ≈ 3.1 compared to the growth shown in Fig. 4.10**a**, and by a factor of $\approx 3.2 - 6.5$ compared to the growth reported in Ref. [7].

4.2.5 Discussion

In summary, the adapted growth recipe improved the bismuthene film quality by reproducibly achieving bismuthene samples with near to complete surface coverage and substantially increased domain sizes. Finding these growth conditions has only been possible by shedding light on the formation process of the monolayer at different stages of the growth in order to understand how the main growth parameters influence its morphology. As a last remark, the long-sought goal of lithographic processing of devices, such as for example a Hall bar that contains only one single bismuthene domain, is discussed. The state of the art in lithography with van der Waals heterostructures is to built Hall bars of $\approx 3\,\mu\mathrm{m}$ – $10\,\mu\mathrm{m}$ size, and having $\approx 0.5\,\mu\mathrm{m}$– $2\,\mu\mathrm{m}$ sized electrodes. These are produced via electron beam evaporation and reactive ion etching, see for example Refs. [125–127]. Therefore, it has to be acknowledged that the median domain size (as measured by the inscribed disc radius) still needs to be enlarged roughly by a factor of ≈ 100 to reach comparable dimensions. An important complication for achieving this is the limitation set by the SiC terrace width of $\approx 200\,\mathrm{nm}$ – $300\,\mathrm{nm}$, see the STM overview image from a flat SiC wafer in Fig. 4.2 **a**. It is still not clear how this substrate related limitation can be circumvent.

CHAPTER 5

Growth and spectroscopy of manganese- and cobalt-induced alloys on bismuthene

Overview

Time-reversal symmetry is essential for the realization of a quantum spin Hall state [1–3,11]. Thus breaking this fundamental symmetry by magnetic fields is of great interest from both a theoretical and experimental perspective. The most direct consequence manifests in a possible gapping out of the protected crossing points in the helical edge spectrum of the 2D TI [1, 2, 17]. In a theoretical case study for bismuthene it was proposed to apply an external in-plane or out-of-plane magnetic field to study this effect [128]. It was found that the opening of an energy gap varies with the field strength, its direction and the bismuthene edge type (armchair or zigzag). This scenario was referred to as a fingerprint signature for the topological nature of the edge states.

An alternative concept for breaking time-reversal symmetry is to deposit individual magnetic impurity atoms directly onto the bulk or the boundary of the 2D TI. The first case may give rise to a long-range magnetic order and was identified as possible realization platforms for a quantum anomalous Hall effect [129,130]. As a consequence of time-reversal symmetry breaking, the boundaries of the quantum anomalous Hall material exhibit no longer helical, but chiral edge states that can still give rise to a dissipationless spin-polarized transport channel. Several related experiments on 3D TIs have used doping of the pristine material with magnetic transition metal atoms, such as Mn [131–133], Cr [134], and V [135]. Importantly, also for bismuthene it was theoretically calculated that an array of magnetically ordered adatoms can drive the system into a quantum anomalous Hall state [136]. The second case, i.e., to place magnetic impurity atoms at the boundaries of the 2D TI, can be accompanied by an energy gap formation in the spectrum of the helical edge states and the enabling of single-particle spin-flip scattering [137,138]. For the corresponding measurements the STM/STS technique is suited to investigate these effects on the atomic scale.

Unfortunately, an observed high mobility down to liquid helium temperatures ($T = 4.35\,\mathrm{K}$) of the Mn- and Co-atoms placed on top of the bismuthene surface impeded the study of single magnetic impurities, e.g., a magnetic impurity placed at a bismuthene edge. Deposited impurity atoms were still mobile enough at these low temperatures, to be unwillingly moved on, or be removed from the bismuthene surface by the STM tip while scanning or while recording tunneling spectra. Most importantly, however, repeated evaporation of Mn- or Co-atoms and subsequent annealing of the sample leads ordered (3×3) surface reconstructions. They combine the 2D TI bismuthene with magnetic impurity atoms and

are referred to as SiC(0001)–(3 × 3)–(Bi, Mn) and SiC(0001)–(3 × 3)–(Bi, Co), or short as Bi/Mn-alloy and Bi/Co-alloy, respectively. The following sections cover the preparation of these two novel materials and scrutinize their structural and electronic properties by tunneling and photoemission spectroscopy.

5.1 Manganese-induced surface reconstruction on bismuthene samples

5.1.1 Growth and structural investigation

The sample preparation was always conducted by depositing Mn-atoms from a heated rod (purity 99.9%) with an e-beam evaporator, while keeping the sample at room-temperature. After each deposition of Mn atoms, the sample was heated to 400 °C for 10 min. Importantly, annealing a pristine bismuthene film at 400 °C without deposition of Mn atoms does not induce any changes to the bismuthene film.

Upon sub-monolayer doping with Mn-atoms on a pristine bismuthene sample and subsequent annealing at $T = 400\,°\mathrm{C}$ for 10 min the surface exhibits a coexistence of two phases in STM constant current images: the bismuthene $(\sqrt{3} \times \sqrt{3})R30°$ surface reconstruction, and a Mn-induced (3 × 3) reconstruction, see Fig. 5.1**a**. The Mn induced (3 × 3) surface reconstruction appears in the form of isolated islands, which exhibit a (3 × 3) honeycomb structure (orange color) formed within the bismuthene film (blue color). As can be seen in the inset image of Fig. 5.1**a** (and also in the overview image), the Bi/Mn-alloy islands preferably form straight edge terminations. These give rise to an atomically precise interface to the regular bismuthene film preferably along the armchair direction of the bismuthene lattice.

The growth in Fig. 5.1**a** clearly indicates a below monolayer coverage of the Bi/Mn-alloy (3 × 3) surface reconstruction. The growth depicted in Fig. 5.1**b** proves that also a complete coverage can be achieved in the same manner. Here, the Bi/Mn-alloy covers the whole surface evenly with only a small amount of defective areas (darker appearance), but with substantial existence of large clusters (white color). Moreover, the straight line structures meandering across the film surface indicate the formation of domain boundaries. The LEED image of the sample shows very intense (3 × 3) Bragg peaks (marked by a green rhomb) from the Bi/Mn-alloy. Unfortunately, comparing the amount of deposited Mn-atoms in Fig. 5.1**a** and in Fig. 5.1**b** is not possible, since their growths were performed with differently mounted evaporation cells in the UHV chamber. However, the same characteristic ARPES band structure is measured on both the sample with sub-monolayer Bi/Mn-alloy growth, i.e., a mixed phase of bismuthene and Bi/Mn-alloy (Fig. 5.1**a**), and on the sample with full surface coverage of the Bi/Mn-alloy (Fig. 5.1**b**). See Appendix Fig. C.2 and Fig. 5.2 for the respective ARPES bandstructure. The close resemblance of both ARPES band structures is an indication that likewise the Bi/Mn-alloy of Fig. 5.1**b** relates to a monolayer. A rigorous Mn-flux dependent growth study needs to be conducted in forthcoming investigations.

The topography of the Bi/Mn-alloy is resolved with atomic resolution in Figs. 5.1**c, d** at two different tunneling voltages. A characteristic of the film is that it shows a strong

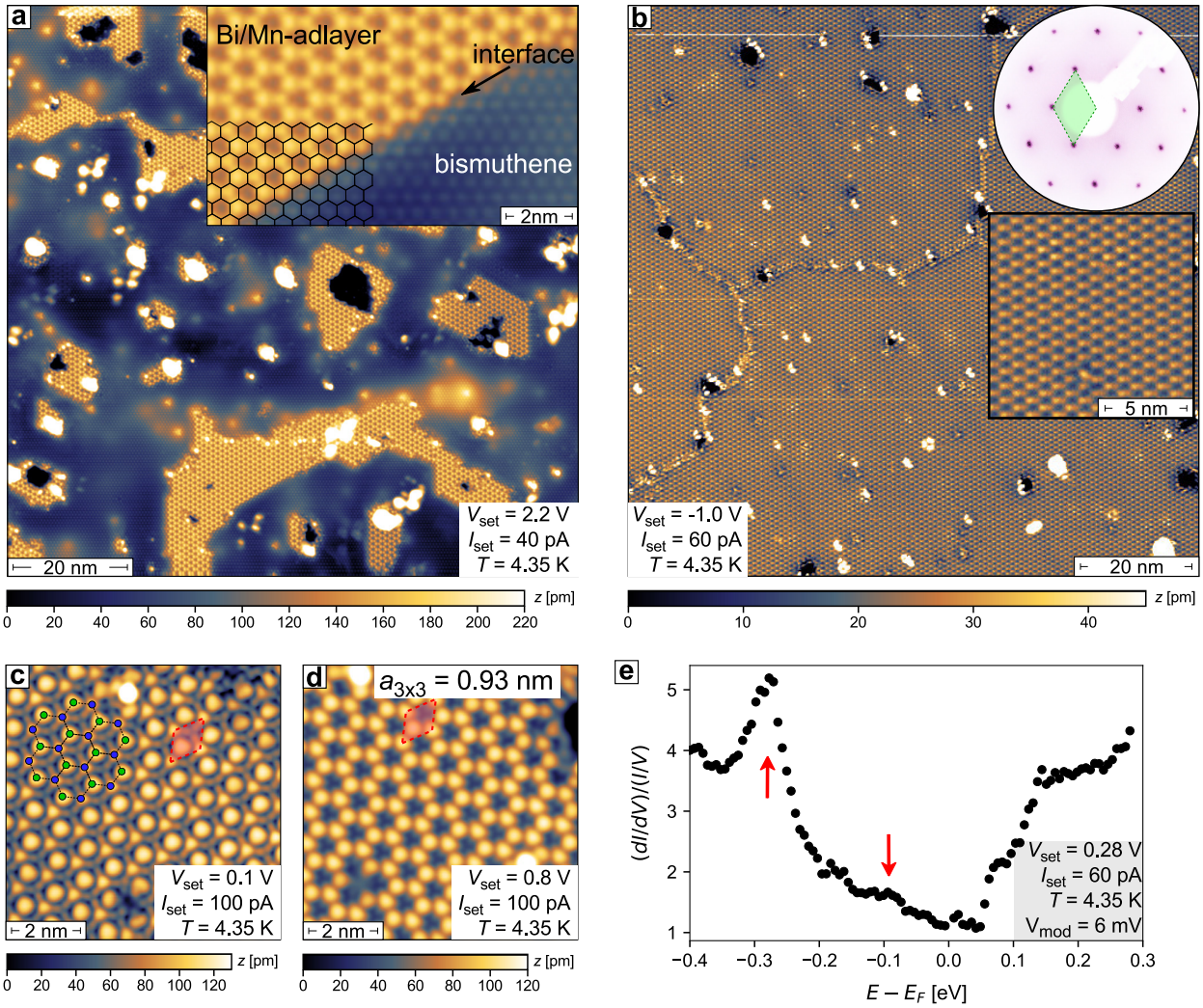

Figure 5.1: Manganese induced surface reconstruction on a bismuthene sample. (a), Constant current STM image of a bismuthene sample after Mn deposition at RT and subsequent annealing at 400 °C for 10 min. A Mn-induced (3×3) surface reconstruction (yellow appearance) coexists with the pristine bismuthene film (blue appearance) and forms isolated islands. Inset: Detailed view of a bismuthene – Bi/Mn-alloy interface. **(b),** Constant current STM image after deposition of a larger amount of Mn atoms and subsequent annealing (400 °C, 10 min). The precise amount of deposited Mn in comparison to **a** cannot be evaluated due to a different evaporator position. Yet, the complete coverage of the surface with the Mn-induced (3×3) surface reconstruction and additionally observed large clusters (white color) that may originate from excess Mn-atoms are indicative of a large amount of deposited Mn. The insets show a LEED image of the film with the (3×3) surface reconstruction indicated by a green rhomb, and a detail constant current STM image of the same surface. The ARPES spectrum of the film in **a** and in **b** share the same characteristic band features, see Appendix Fig. C.2 and Fig. 5.2. This points to a monolayer thickness of the Bi/Mn-alloy in **b**. **(c), (d),** Constant current images of the Bi/Mn-alloy at two different characteristic bias voltages. The new structure forms a (3×3) surface reconstruction and forms a honeycomb lattice (indicated by black lines in **c**). At 0.1 V bias voltage in **c** the A- and B-sublattice are strongly asymmetric (indicated by green and blue dots). The red rhomb indicates the unit cell of the Bi/Mn-alloy with a lattice constant of $a_{3\times3} = 0.93$ nm. **(e),** STS $\frac{dI}{dV}/\frac{I}{V}$ spectrum. Red arrows highlight spectroscopic features that can be assigned to band onsets in ARPES in Fig. 5.2**c**.

A-/B-sublattice asymmetry of the honeycomb lattice at a tunneling bias voltage of 100 mV above the Fermi energy (cf. blue and green lattice sites in Fig. 5.1**c**), whereas this sublattice asymmetry vanishes at higher tunneling bias voltages as in Fig. 5.1**d**. Although the STM constant current images suggest the formation of a buckled honeycomb lattice, the exact atomic structure model for this Bi/Mn-alloy may be more complicated and is not identified strictly at this stage. Non-contact atomic force microscopy measurements could help to resolve it. Having a much reduced sensitivity on the electronic LDOS, this technique has proven to be capable of resolving atomic scale topographic details beyond the capabilities of STM [139].

Notably, the electronic structure of the Bi/Mn-alloy is metallic, as seen from the tunneling spectrum in Fig. 5.1**e** measured on a completely covered film. The red arrows in the inset figure point at spectroscopic features which are in very good agreement with VB onsets observed in ARPES discussed in the next section (cf. red arrows in Fig. 5.2**b**). The observed metallicity in STS is also consistent with an asymmetric XPS line shape of Bi4f states that is observed on a Bi/Mn-alloy prepared in the aforementioned way and transferred with the UHV suitcase ($p \sim 5 \times 10^{-10}$ mbar) to the I09 beamline at the Diamond Light Source, see Appendix Fig. D.5 [140]. Here, a tail on the higher binding energy side of the main peak is observed, which is connected to the excitation of conduction electrons at the Fermi level by scattering events [141]. For comparison, an asymmetric shape is not observed for pristine bismuthene (cf. XPS spectrum in Appendix Fig. D.1).

5.1.2 Electronic band structure of the Bi/Mn-alloy

The following covers ARPES measurements performed on Bi/Mn-alloy samples with a complete surface coverage (as in Fig. 5.1**b**) to map the material's low-energy electronic band structure. Figures 5.2**a**–**c** show band maps along paths in k-space connecting high symmetry points Γ, K/K', and M of the hexagonal Brillouin zone of the Bi/Mn-alloy. The 3D visualization of the ARPES band structure in Fig. 5.2**f**, and the constant energy maps in Fig. 5.2**g, h** provide further orientation within the ARPES band structure. Importantly, the measurements prove the absence of bismuthene derived bands. Otherwise, the bismuthene related characteristic Rashba split VBs would be present at the Γ points of the (3×3) Brillouin zone, as is explicitly seen in ARPES experiments in Fig. C.2 performed on a sample where bismuthene and the Bi/Mn-alloy film coexist (as in Fig. 5.1**a**).

The Bi/Mn-alloy ARPES band structure in Figs. 5.2**a**–**c** shows a multitude of other prominent dispersive features, which are discussed in the following. Note that the measurements were performed with a non-monochromatized He lamp. Photoemission intensity from a satellite peak that originates from the SiC bulk band structure can therefore be observed in the energy range $E_\mathrm{B} = 0.2\,\mathrm{eV} - 0.6\,\mathrm{eV}$. Dashed black lines in all panels of Fig. 5.2 mark this spectral intensity. Moreover, at these energies, the ARPES band structure reveals four very distinct dispersing states $S1^-$, $S1^+$, $S2^-$, $S2^+$ marked by red or blue lines in Figs. 5.2**a, b**.

States S2$^-$, S2$^+$. – First, the states $S2^-$, $S2^+$ that disperse around the Γ points are

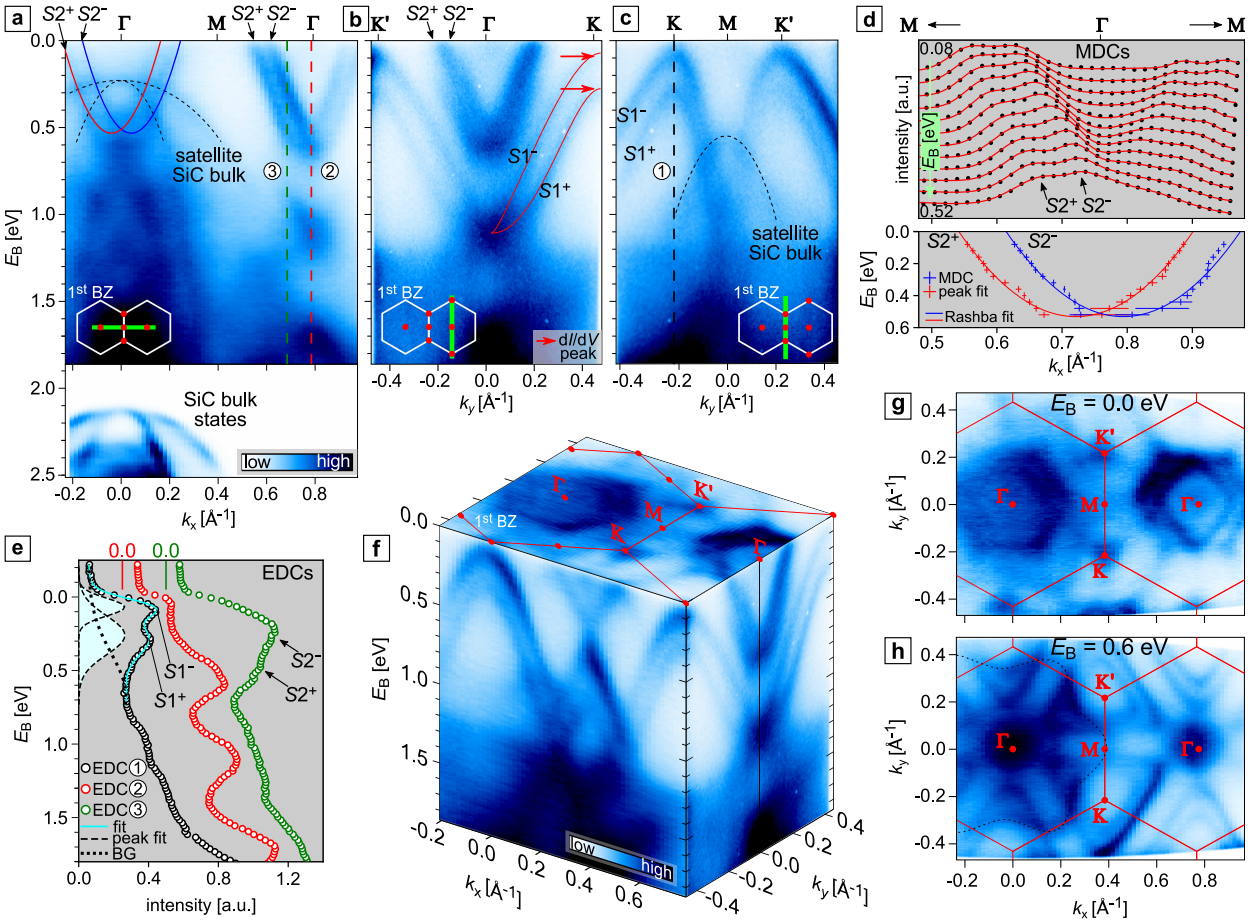

Figure 5.2: ARPES band structure of the Bi/Mn-alloy. All spectra were recorded at photon energy $h\nu = 21.22\,\mathrm{eV}$ (He I α, not monochromatized) at $T = 70\,\mathrm{K}$. Black dashed lines mark satellite intensities from SiC bulk states that appear replicated at a lower binding energy. **(a) – (c),** Band maps along paths in k-space connecting high symmetry points (Γ, K/K', and M) of the (3×3) surface BZ, see insets. Red and blue solid lines are guides to the eye for the observed dispersing states $S1^+$, $S1^-$, $S2^+$, and $S2^-$. Vertical dashed lines ①–③ mark positions for the EDCs in **e**. Note, that the false color scale in **a** at energies $E_\mathrm{B} > 1.86\,\mathrm{eV}$ is adapted to resolve the high intensities of the SiC bulk states in this energy range. **(d),** Upper panel: waterfall plot of MDCs extracted from a k_x cut through the Γ-point of the 2$^{\mathrm{nd}}$ (3×3) surface BZ (see **a**). Each MDCs is averaged over $\Delta k_\mathrm{y} = \pm 0.04\,\mathrm{Å}^{-1}$ and $\Delta E_\mathrm{B} = \pm 0.02\,\mathrm{eV}$. A splitting of the states $S2^+$ and $S2^-$ is clearly resolved. Red lines: least-square fits to the data using four Gaussian peaks and a linear background. Lower panel: data points with error bars are the fitted Gaussian peak positions to the MDCs in the upper panel. The error bars in k_y represent the estimated standard deviation from the square root of the covariance of the fit, and the error bars in E_B correspond to the energy averaging window. The data points are fitted according to the eigenenergies of the Rashba model given by Eq. (5.2). **(e),** EDCs at the positions indicated in **a** and **c**. An averaging window of $\Delta k_\mathrm{x} = \Delta k_\mathrm{y} = \pm 0.02\,\mathrm{Å}^{-1}$ was used. Turquoise line: least-square fit to the EDC ① using the sum of two Gaussian peaks and a Gaussian tail, and multiplied with a Fermi function. **(f),** 3D visualization of the ARPES band structure. **(g), (h),** Constant energy maps at two different binding energies. The splitting of the bands located around the Γ-points is nicely observed at $E_\mathrm{B} = 0\,\mathrm{eV}$. The splitting of the bands located around the K/K'-points is apparent at $E_\mathrm{B} = 0.6\,\mathrm{eV}$.

considered. They appear clearly separated from each other in the false color plot in Fig. 5.2**a** (note that the Γ-points in both the 1st and 2nd BZ are shown). The separation in energy is apparent in the EDC ③ depicted in Fig. 5.2**e**, which corresponds to the line cut indicated by a dashed green line in Fig. 5.2**a**. The waterfall plot of MDCs in the upper panel of Fig. 5.2**d** continuously tracks the splitting of these states. Here, the photoemission signal in the 2nd BZ was chosen, since satellite peak intensities from SiC bulk bands are not present in this energy and momentum region (this is not the case in the 1st BZ as indicated by black dashed lines in Fig. 5.2**a**). In the plotted MDCs, especially close to zero binding energy, it is unambiguously observed that they consist of four peaks. Consequently, a least-square fitting procedure with four gaussian peaks and a linear background is used to fit all MDCs (red lines in upper panel of Fig. 5.2**d**). The resulting fitted peak positions that trace the $S2^-$ and $S2^+$ states are plotted in the lower panel of Fig. 5.2**d**. The coloring of the data points represents one possible interpretation of these states according to the *linear Rashba model* [142, 143] explained in the following.

Rashba model. – This model has been extensively used to describe surface states of materials containing atoms with large SOC. These can be surface alloys of atoms with high atomic number [144], heavy atom adlayers on semiconductor surfaces [145–147], or even materials consisting of light elements in which the SOC was enhanced by the proximity to heavy elements [148]. The motivation behind studying material systems that resemble the Rashba model is that often times the surface inversion symmetry breaking leads to strong spin splitting. A simple qualitative relativistic argument for this observation can be given as follows [149]: The surface termination of a bulk crystal gives rise to a potential gradient perpendicular to the surface. The moving valence electron sees a magnetic field as a result of a Lorentz transformation of the surface electric field into the rest frame of the electron. This magnetic field induces a Zeeman splitting in the valence band states, which gives rise to an energy splitting of spin-up and spin-down states. Theoretically, for an ideal 2D quasi-free electron system this effect can be described in terms of the linear Rashba model Hamiltonian which takes the form [149]:

$$\mathcal{H}_{\mathrm{R}} = \frac{\hbar^2 \mathbf{k}^2}{2m^*} - \alpha_{\mathrm{R}} \left(i\sigma_{\mathrm{y}} k_{\mathrm{x}} - i\sigma_{\mathrm{x}} k_{\mathrm{y}} \right) , \tag{5.1}$$

where m^* is an effective electronic mass, $\mathbf{k}$ the wavevector of the electron, α_{R} is the Rashba coupling parameter, which depends on the atomic number Z and the strength of the surface potential gradient, and $\sigma_{\mathrm{x,y}}$ are standard Pauli matrices in the coordinate basis of the out-of-plane spin projection states. The eigenenergy spectrum of the Rashba model Hamiltonian is then [149]:

$$E_{\pm}(\mathbf{k}) = \frac{\hbar^2 \mathbf{k}^2}{2m^*} \pm \alpha_{\mathrm{R}} |\mathbf{k}| , \tag{5.2}$$

which gives rise to a characteristic form in which the free electron parabolae are shifted against each other in energy by $2\alpha_{\mathrm{R}}|\mathbf{k}|$. Consequently, the minima of the shifted parabolae are separated by momentum $2k_0 \equiv 2\alpha_{\mathrm{R}} m^*/\hbar^2$, which besides α_{R} is also an often cited

parameter. Moreover, the two energy bands cross at time-reversal invariant momenta, since the Rashba Hamiltonian $\mathcal{H}_\mathrm{R}$ respects time reversal symmetry. In the following, the Rashba model is used to interpret the ARPES data measured on the Bi/Mn-alloy system.

Best fit of MDCs within the Rashba model. – Equation (5.2) was used to fit the peak positions of the states $S2^-$ and $S2^+$ in the lower panel of Fig. 5.2**d**. It was assumed that red colored peaks belong to the first parabola $E_-(k)$ in Eq. (5.2) and that the blue colored peaks belong to the second parabola $E_+(k)$ in Eq. (5.2). The least-square fit (red and blue lines) describes the data very well (note that both parabolae are fitted in a combined fit), and yields the model parameters $m^* = 0.23 m_\mathrm{e}$ and $\alpha_\mathrm{R} = 1.19\,\mathrm{eV\,\AA}$. A comparison with surface Rashba systems places the Bi/Mn-alloy system close to what was found in the Bi $(\sqrt{3}\times\sqrt{3})R30°$ surface adlayer on Si(111) with a Rashba parameter of $\alpha_\mathrm{R}^{Bi/Si} = 1.37\,\mathrm{eV\,\AA}$ [145]. It is worth noting that the largest Rashba-type splitting so far has been found in the surface alloy Bi/Ag(111) with $\alpha_\mathrm{R}^{Bi/Ag} = 3.05\,\mathrm{eV\,\AA}$ [144] and the Rashba-parameter in Bi(111) surface states amounts to $\alpha_\mathrm{R}^{Bi(111)} = 0.56\,\mathrm{eV\,\AA}$ [150].

Spin-polarization. – Apart from this energy band alignment, one characteristic property of bands being described by the ideal Rashba model according to Eq. (5.1) is a peculiar spin texture. To see this, the spin expectation value of the eigenspinor wavefunctions $|\mathbf{k},\pm\rangle = \frac{1}{\sqrt{2}}\left(e^{-i(\phi\pm\pi/2)},\quad 1\right)$ is considered, and gives $\mathbf{S}_\pm = \frac{\hbar}{2}\left(\mp\sin\phi,\quad \pm\cos\phi,\quad 0\right)$, where $\phi = \arctan\left(k_\mathrm{y}/k_\mathrm{x}\right)$ [149]. It describes one clock-wise and one counter-clockwise rotating in-plane spin structure, each following the energy dispersion of one of the separated parabolae $E_\pm(\mathbf{k})$. The direction of the spin is always pointing perpendicular to the direction of $\mathbf{k}$ in the $k_\mathrm{x}-k_\mathrm{y}$ plane. Spin-resolved ARPES measurements are needed to clarify the spin-polarization of the states $S2^-$ and $S2^+$ of the Bi/Mn-alloy.

States S1$^-$, S1$^+$. – The other prominent dispersive features $S1^-$, $S1^+$ are located around the K/K'-points in the band maps in Figs. 5.2**b, c**. These states are also highly reminiscent of bands that are split due to a Rashba-type SOC, i.e., SOC in the presence of surface induced inversion symmetry breaking. These states show no crossing point at the high symmetry points K/K', which from symmetry considerations is also not necessary, since the K/K'-points are no time-reversal invariant momenta in contrast to the Γ- and the M-point. The energy splitting of the states at the K/K'-points is evaluated by a least-square fit to the EDC ① in Fig. 5.2**e**, which is extracted from the ARPES spectrum at the position marked by the dashed black line in Fig. 5.2**c**. The best fit positions of the Gaussian peaks reveals an energy splitting of the states $S1^-$, $S1^+$ at the K/K'-points of 0.19 eV. This is $\approx 40\%$ the energy splitting observed in the VB states of pristine bismuthene.

5.1.3 Tunneling spectroscopy at the bismuthene – Bi/Mn-alloy interface

Figure 5.1**a** has revealed atomically sharp and straight interfaces between the Bi/Mn-alloy islands and the pristine bismuthene at a sub-monolayer coverage of the Bi/Mn-alloy. In particular, this interface is typically oriented along the bismuthene armchair edge lattice

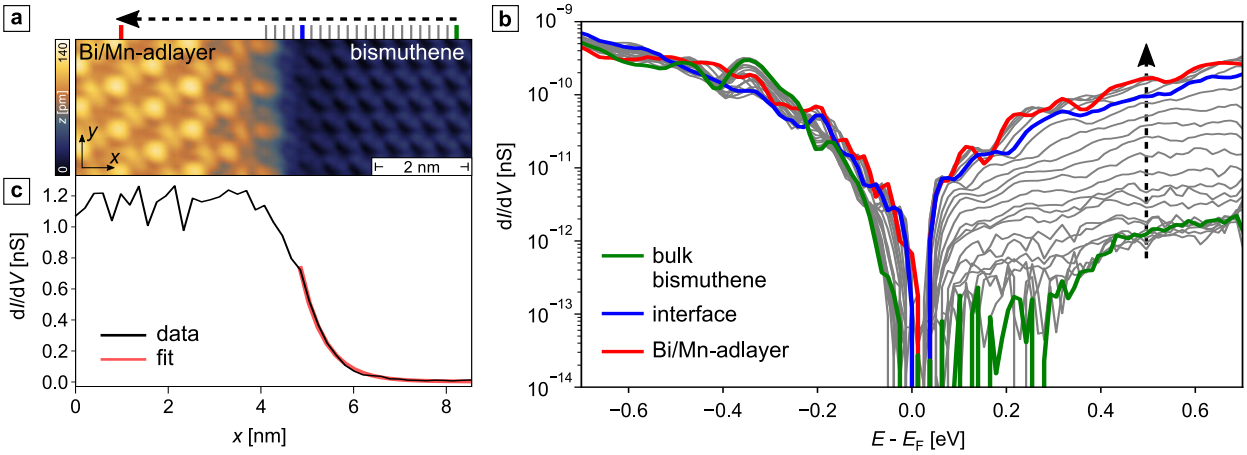

Figure 5.3: Tunneling spectroscopy at the bismuthene – Bi/Mn-alloy interface. (a), Constant current image of an interface between bismuthene (right) and the Bi/Mn-alloy (left). The colored marks on top of the image indicate the x-positions to which the differential conductivity spectra in **b** correspond. ($I_{\mathrm{set}} = 100\,\mathrm{pA}$, $V_{\mathrm{set}} = -0.9\,\mathrm{V}$, and $T = 4.35\,^{\circ}\mathrm{C}$) **(b),** Differential conductivity spectra across the bismuthene – Bi/Mn-alloy interface at x-positions indicated by colored marks on top of **a** and in the direction of the arrow. Each spectrum is an average of 15 single-point spectra along the y-direction in **a**. The gray spectra are measured at equally spaced x-coordinates starting in the bismuthene bulk area up until the interface is reached. The direction of the arrow corresponds with the direction of the arrow in **a**. Scan parameters: $I_{\mathrm{set}} = 120\,\mathrm{pA}$, $V_{\mathrm{set}} = -0.7\,\mathrm{pA}$, $V_{\mathrm{mod}} = 15\,\mathrm{mV}$, and $T = 4.35\,^{\circ}\mathrm{C}$. **(c),** Spatially dependent differential conductivity across the bismuthene – Bi/Mn-alloy interface at $E - E_{\mathrm{F}} = 0.4\,\mathrm{eV}$. An exponential fit (red line) to the differential conductivity from the interface towards the bismuthene bulk yields a $1/e$-decay constant of $(5.4 \pm 0.2)\,\text{Å}$.

termination. It has been shown by local STS measurements conducted in Refs. [6, 8] that bismuthene film terminations at SiC substrate steps host quasi-1D metallic edge states that are identified with the helical edge states. It is therefore reasonable to ask about the possibility of finding helical edge states at an interface of the Bi/Mn-alloy and bismuthene and the consequence of this proximity.

Figure 5.3 shows a tunneling spectroscopy experiment performed to inspect the local electronic structure at a bismuthene – Bi/Mn-alloy interface, as seen in Fig. 5.3**a**. Each of the $\mathrm{d}I/\mathrm{d}V$ spectra in Fig. 5.3**b** (log-plot) reflect an average of 15 single-point spectra along the y-extension of the area in Fig. 5.3**a**. The x-position of these spectra is indicated with colored marks at the top of Fig. 5.3**a**, while the arrows in Fig. 5.3**a** and Fig. 5.3**b** indicate the stacking order of the spectra. The spectral gap in the bismuthene region (cf. green spectrum in Fig. 5.3**b**) is already known from pristine bismuthene samples [6, 8] and results from a vanishing LDOS within this energy region. The spectral gap in Fig. 5.3**b** is substantially smaller than the expected bismuthene bulk band gap, because it is already affected by the exponentially decaying metallic interface states. Approaching the interface region (cf. gray spectra up until the blue spectrum in Fig. 5.3**b**) is connected with a continuous increase of the tunneling conductivity, which also points to an increasing LDOS. Within the Bi/Mn-

alloy (cf. red spectrum in Fig. 5.3**b**) the differential conductivity is metallic and roughly of the same magnitude as directly at the interface. This evolution is also resolved by plotting the x-dependent (y-averaged) $\mathrm{d}I/\mathrm{d}V$ amplitude across the interface at $E - E_\mathrm{F} = 0.4\,\mathrm{eV}$ in Fig. 5.3**c**. It shows that the LDOS within the Bi/Mn-alloy is varying around a constant value by only $\approx 10\%$ and that the LDOS directly at the interface ($x \approx 5\,\mathrm{nm}$) is exponentially decaying into the bismuthene film with a $1/e$-decay constant of $(5.4 \pm 0.2)\,\text{Å}$ (cf. red line in Fig. 5.3**c** is a least-square fit to the data with an exponential function).

Summarizing, the STS measurements prove the existence of a metallic LDOS directly at the bismuthene – Bi/Mn-alloy interface, which can be compared to metallic edge states of pristine bismuthene films terminated at SiC(0001) substrate steps. In both situations the metallic $\mathrm{d}I/\mathrm{d}V$-signal is exponentially decaying from the edge or the interface into the bismuthene film with similar $1/e$-decay constants (for the metallic edge state of bismuthene films terminated at SiC substrate steps a $1/e$-decay constant of $(4.1 \pm 0.3)\,\text{Å}$ was found [6]). What renders the comparison of these two situations complicated is the fact that in the case of the bismuthene – Bi/Mn-alloy interface the Bi/Mn-alloy, which is directly adjacent to the bismuthene edge, exhibits a metallic $\mathrm{d}I/\mathrm{d}V$-signal itself. Indeed, the ARPES measurements in Fig. 5.2 also revealed the existence of metallic states at the Γ-points of the (3×3) surface BZ, that were well captured by the Rashba model. Although a distinct interface signal, which would allow to infer the existence of any bismuthene related topological edge states, cannot be resolved, if present, the helical edge states and the Rashba states were expected to be hybridized at the mutual interface. Such a situation has not been studied experimentally before and deserves further investigations.

The following discusses the origin of differential conductivity suppression at small bias voltages observed in the spectra near the interface, as well as inside the Bi/Mn-alloy. Again, not being able to clearly discern a bismuthene related edge state impedes a robust explanation solely from the presented data. If bismuthene edge states were present, the situation would be reminiscent of the case of isolated bismuthene edge states at SiC substrate steps, where a power-law dip in the spectrum at zero bias was observed. These spectra showed the universal scaling behavior connected to the formation of a (helical) Tomonaga-Luttinger-liquid, i.e., a characteristic signature for its 1D nature in which the Coulomb interactions play an essential role for low-energy excitations [8]. The continuous evolution of the $\mathrm{d}I/\mathrm{d}V$ signal across the bismuthene – Bi/Mn-alloy interface, renders definite conclusions about a Tomonaga-Luttinger-liquid origin of the spectroscopic dip directly at the interface region difficult to draw.

Another scenario, which would open a gap in the spectrum of the topological edge states could be a magnetic interaction of the Bi/Mn-alloy with bismuthene. The magnetic properties of the Bi/Mn-alloy have not been investigated so far, but may be revealed for example via spin-resolved STM or X-ray magnetic circular dichroism measurements performed on a closed film. If the Bi/Mn-alloy showed a significant magnetic ordering, a gapping out of the helical edge states of bismuthene around the Dirac point would be expected. In this case the observation of a gap opening at zero bias voltage would be a coincidence, and indicate

that the Dirac crossing of the helical edge states is located at the Fermi energy.

The spectral gap measured inside the Bi/Mn-alloy (red spectrum in Fig. 5.3**b**) can have a different origin. Since at sub-monolayer coverage the Bi/Mn-alloy forms as islands with widths on the order of $\approx 5\,\text{nm} - 50\,\text{nm}$, they constitute metallic nano-islands on a semiconducting material. In such cases, the supression of tunneling conductivity at zero bias voltage can arise due to a (dynamical) Coulomb blockade [151].

5.2 Cobalt-induced surface reconstruction on bismuthene samples

Following up on the previous section, this section extends the study of magnetic atoms on bismuthene to cobalt as magnetic adatom species instead of manganese. Also Co adatoms deposited on the bismuthene surface exhibited high mobilities down to liquid helium temperature, which impeded the study of single Co-atoms adsorbed on bismuthene. Therefore, this section covers the Bi/Co-alloy that forms in a similar way as the Bi/Mn-alloy described in the previous section.

5.2.1 Growth and structural investigation

Co-atoms were deposited on a bismuthene sample at RT with an e-beam effusion cell (*FOCUS EFM 3*) by evaporation from a Co-rod (purity 99.95%). After each deposition, the sample was heated to 400 °C for 10 min. With STM constant current measurements it is possible to trace the formation of the Bi/Co-alloy at an early stage.

Initial stage of Bi/Co-alloy growth

The still untreated bismuthene film, i.e., before the first Co evaporation, shown in Fig. 5.4**a** initially exhibits a very homogeneous surface topography and covers the substrate evenly (golden color) with only some smaller areas of incomplete growth (darker appearance). After the evaporation of small amounts of Co-atoms and subsequent annealing, this surface topography changes significantly, see Fig. 5.4**b**. Numerous small and uniformly distributed clusters with an apparent lower height in the STM measurement at the selected bias voltage have formed throughout the priorly pristine bulk bismuthene film. Notably, the magnified inset images in Figs. 5.4**a, b** reveal that these new structures have also formed at former domain boundaries of bismuthene. Domain boundaries which appeared as "sharp" line structures before Co deposition, have changed to a "fuzzy" appearance.

The detailed topography of these novel structures is better resolved with STM constant current measurements at a smaller bias voltage as in Fig. 5.4**c**. It resolves the atomic structure of the Bi/Co-alloy, which, on the one hand, is observed as small clusters that consist of small trimer-like arrow-shaped constituents, and, on the other hand, as a larger structure that extends as longitudinal line-defect across the bismuthene film. Although the latter has formed at a bismuthene domain boundary, it does not resemble the original topography of it any longer (see Ch. 6 for a detailed study of domain boundaries). A closer inspection (cf. inset of Fig. 5.4**c** and line profiles of Fig. 5.4**c**) reveals that the Bi/Co-

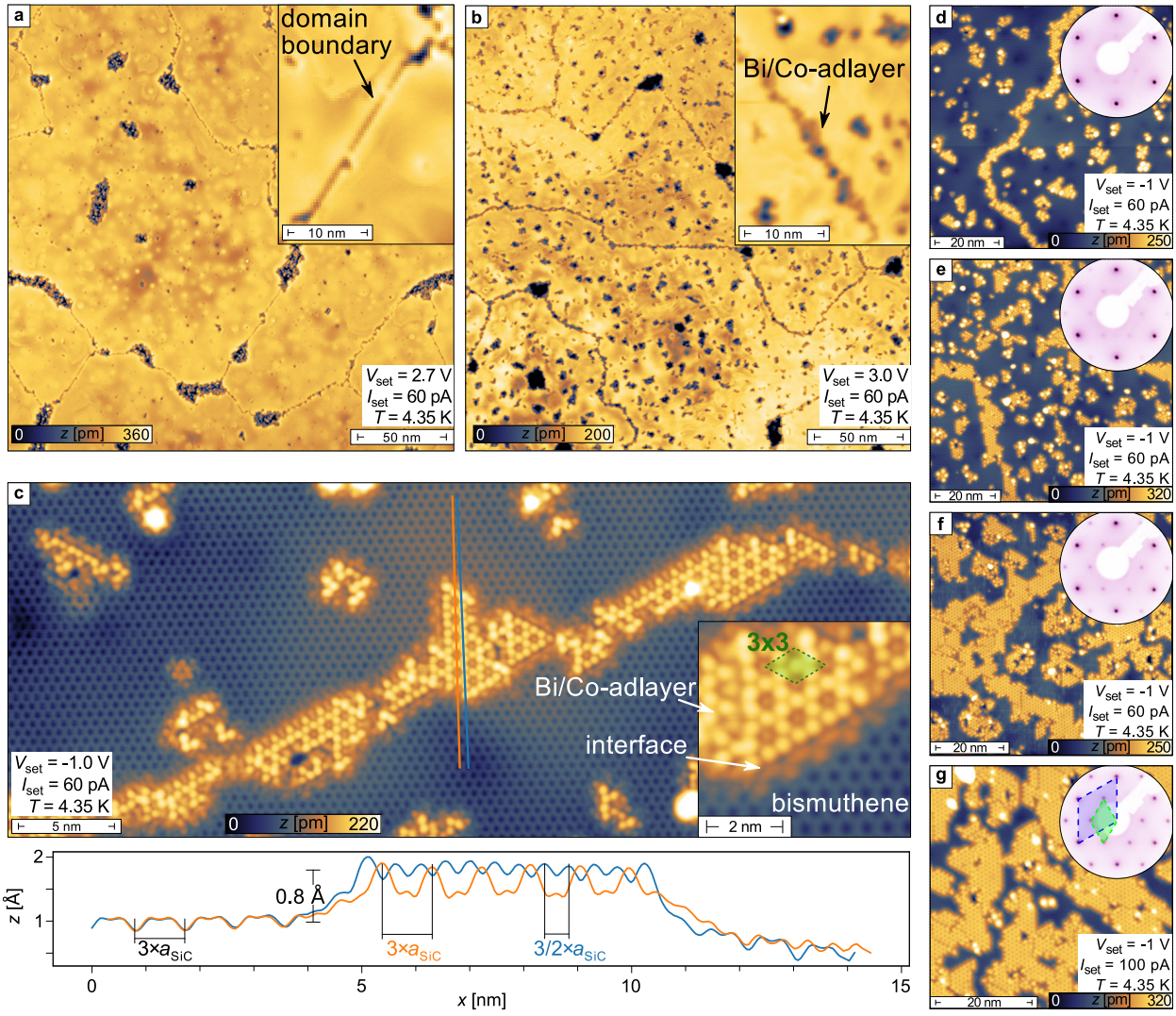

Figure 5.4: Cobalt induced surface reconstruction on a bismuthene sample. (a), (b), Constant current STM images before and after Bi/Co-alloy growth, respectively. The bismuthene film (yellow appearance) shows a homogenous topography with only small areas of incomplete growth (darker appearance) in **a**. After the Bi/Co-alloy growth the surface is speckled by many small areas of smaller apparent height in **b**. Insets: Domain boundaries appear as sharp line features in **a** and change to a "fuzzy" appearance in **b**. **(c),** Atomically resolved constant current image after the Bi/Co-alloy growth. The kagome lattice structure forms a (3×3) surface reconstruction. Inset: Line profiles along the blue and orange lines marked in **c**. **(d) – (g),** Constant current STM images tracking the continuous growth of the Bi/Co-alloy (yellow areas) after successive Co deposition and annealing steps. The respective total time integrated fluxes in **d**–**g** are: 4.8 µA s, 10.8 µA s, 15.6 µA s, and 21.6 µA s. The LEED images (E_{kin} = 40 eV) in the insets show a relative increase of (3×3) Bragg peak intensity (green rhomb) compared to the $(\sqrt{3} \times \sqrt{3})R30°$ Bragg peak intensity (blue rhomb).

alloy forms a kagome lattice with a lattice constant of 0.93 nm $\approx 3 \times a_{\mathrm{SiC}}$ and an apparent height of the kagome corner sites from the bismuthene film of $\approx$ 0.8 Å. The trimer-like structures are the basic constituents of the extended Bi/Co-alloy lattice, since when two or more of this trimer-like structures connect, they start to form the kagome lattice to form the extended (3×3) surface reconstruction. As an example, STM constant current images of two connecting trimer-like structures are shown in Appendix Fig. C.3**c**.

Evolution of Bi/Co-alloy growth

The coverage of the Bi/Co-alloy can be precisely controlled by repeated Co-atom deposition and heating steps as described above. The STM constant current measurements in Figs. 5.4**d**–**g** track the surface topography and the steady Bi/Co-alloy formation after successive growth steps. In each step a Co-deposition was performed with an approximately constant flux of Co-atoms (see caption of Fig. 5.4). The flux monitor of the e-beam evaporator, which for a given emission current I_{em} (here 10 nA) and high voltage U (here 800 V) is directly proportional to the flux of evaporated atoms, provides a relative measure of the amount of evaporated Co-atoms.

The STM constant current images in Figs. 5.4**d**–**g** show surface areas with higher apparent height (golden color) which are again related to the Bi/Co-alloy and surface areas with lower apparent height (blue color) which are related to pristine bismuthene. It is readily seen that the fraction of the total surface area that is covered by the Bi/Co-alloy increases from Fig. 5.4**d** to Fig. 5.4**g** as a result of the repeated growth steps. After the last growth step in Fig. 5.4**g** the Bi/Co-alloy has almost reached a complete monolayer coverage. The LEED images measured after each growth step complement this observation. The (3×3) Bragg peak intensity (green rhomb in Fig. 5.4**g**) associated with the Bi/Co-alloy steadily increases compared to the $(\sqrt{3} \times \sqrt{3})R30°$ Bragg peak intensity (blue rhomb).

For completeness, XPS measurements of a high coverage Bi/Co-alloy sample were performed at the I09 beamline at Diamond Light Source. The sample transfer was conducted with a UHV suitcase with a base pressure of $p \sim 5 \times 10^{-10}$ mbar. The XPS spectrum is depicted in Appendix D in Fig. D.4. Sharp photoemission peaks reveal the spin-orbit split Co2p and Co3p states. Moreover, the Bi4f states develop an asymmetric shape which is not observed for pristine bismuthene (cf. XPS spectrum in Appendix D Fig. D.1). The asymmetry in the Bi4f state signal is assigned to the developed metallicity of the Bi/Co-alloy and to the excitation of conduction electrons at the Fermi level by scattering events [140, 141]. The metallicity will also be observed in the ARPES measurements in the next section.

5.2.2 Photoemission spectroscopy on the Bi/Co-alloy

ARPES band structure

Having established a close to monolayer coverage of the Bi/Co-alloy, ARPES was employed to resolve the low-energy electronic valence band structure[8]. The ARPES band-map in Fig. 5.5**a** shows the electronic valence band structure composed from two paths between high symmetry points of the (3×3) surface BZ as indicated in the schematic image. It features a multitude of dispersive states that can be even better resolved by applying a 2^{nd} derivative filter with respect to the energy to the spectrum, see Fig. 5.5**b**. Importantly, all features found in the 2^{nd} derivative can also be identified in the original spectrum. Blue and purple dashed lines highlight these dispersing states named $S0$, $S1^-$, $S1^+$, $S2$, $S3$, and $S4$. The meaning of the different colors will be addressed later.

It can be seen that the characteristic Rashba split bands of bismuthene are absent. These bismuthene derived bands which are localized at K/K'-points of the $(\sqrt{3}\times\sqrt{3})R30°$ Brillouin zone of bismuthene would otherwise be detected at the Γ points of the (3×3) Brillouin zone due to backfolding (cf. ARPES spectra of a mixed phase of bismuthene and Bi/Mn-alloy sample in Appendix Fig. C.2 for comparison). This indicates a successful Bi/Co-alloy growth and the absence of pristine bismuthene covering a significant amount of surface area.

It is observed that the states $S1^+$ and $S1^-$ disperse along the $K - M - K'$ direction in the APRES band structure. The way these states split is reminiscent of Rashba split states with a crossing point at the time-reversal invariant momentum M of the hexagonal surfacec BZ. Section 5.1.2 provides a related discussion about Rashba systems induced by heavy metal atom adlayers on semiconductors or alloys. For completeness, a reference to the surface monolayer system $\beta - (\sqrt{3} \times \sqrt{3})R30°$ Bi/Si(111), i.e., a one-monolayer trimer structure, in which the Rashba SOC gives rise to similarly split bands at the M-points of the $(\sqrt{3} \times \sqrt{3})R30°$ surface BZ is noted here [152–154]. Again, the heavy Bi-atoms drive the observed large Rashba splitting in this case [155]. The origin of the other states $S2$, $S3$, and $S4$, remains unclear at this point and needs futher experimental clarification (note the peculiarity that $S2$ is not observed in the part of the ARPES spectrum from the higher surface BZs, i.e., the path along $M - K' - \Gamma$).

Lastly, the following discussion provides evidence that the underlying bands of the dispersive feature $S0$ (highlighted with blue dashed lines in Fig. 5.2**b**), which form three distinct parabolae, all originate from the same state, i.e., a large electron pocket centered around the Γ-points of the (3×3) surface BZs. Figure 5.5**c** is a schematic image of a Fermi surface map and elucidates the proposed situation. The green lines indicate the (3×3) reciprocal lattice and the circles colored in blue represent constant energy contours of repeating electron pockets, each centered around the Γ points. The resulting band dispersion of these states along a path marked by the red line results in the situation which is schematically drawn in

[8] The characterization and growth of the samples was performed as presented in Sec. 5.2.1. The ARPES experiments were performed on spots on the sample that showed the brightest (3×3) Bragg peak LEED intensity.

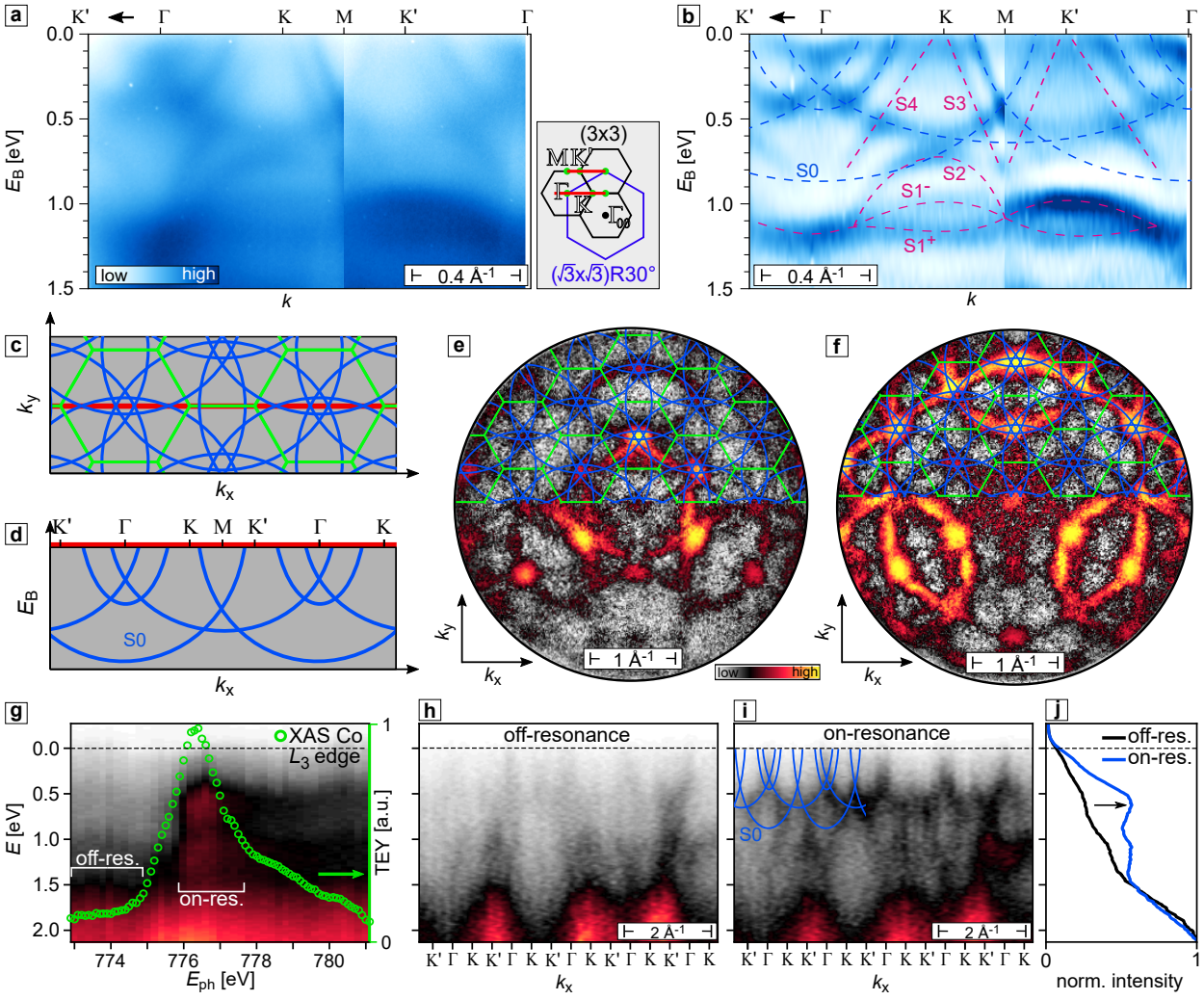

Figure 5.5: Photoemission spectroscopy on the Bi/Co-alloy. Direct **(a)** and 2nd derivative **(b)** ARPES band map along a path between high symmetry points of the Bi/Co-alloy (3×3) surface reconstruction, see schematic drawing. Dashed lines in **b** indicate guides to the eye of states named $S0$, $S1^-$, $S1^+$, $S2$, $S3$, and $S4$. Scan parameters: $h\nu = 21.22\,\mathrm{eV}$ (He I α, not monochromatized), $T = 90\,\mathrm{K}$. **(c),** Schematic of a proposed 2D Fermi surface. Blue lines indicate electron pockets centered at the Γ-points of the (3×3) surface BZs (green lines) with a radius $R = 1.07 \times k_{\Gamma-\Gamma}$. **(d),** Schematic dispersion of the electron pockets in **c** along the red path between high symmetry points in **c**. The electron pockets appear as three distinct parabolae. **(e), (f),** Constant energy maps recorded with a k-space microscope at the NanoESCA beamline at Trieste synchrotron (extraction voltage of 8 keV; p-polarized light; photon beam incident at 65° from the surface normal). The photon energies are $E_{\mathrm{Ph}} = 40\,\mathrm{eV}$ and $E_{\mathrm{Ph}} = 55\,\mathrm{eV}$ in **e** and **f**, respectively. Each map is an average of the photoemission intensity in the binding energy range $0\,\mathrm{eV} \leq E_{\mathrm{B}} \leq 0.3\,\mathrm{eV}$. A contrast limited adaptive histogram equalization routine was applied to enhance the contrast [156]. (Unprocessed data are plotted in the Appendix Fig. C.4.) The (3×3) reciprocal lattice and the proposed electron pockets from **c, d,** are indicated by green and blue lines, respectively. **(g) – (j),** ResPES at the Co L_3 edge. False color plot in **g**: Photon energy dependent ResPES spectrum averaged over the k_x range in **h, i**. A resonance around $E_{\mathrm{Ph}} = 776.5\,\mathrm{eV}$ is observed. Green spectrum in **g**: Total electron yield (TEY) as function of photon energy as a measure for the X-ray absorption at the Co L_3 edge. **(h), (i),** Off-/On-resonance photoemission spectra averaged over the respective off-/on-resonance photon energy ranges indicated in **g**. **(j),** Normalized Off-/On-resonance photoemission spectra averaged over the k_x range shown in **h, i**.

Fig. 5.5**d**. Since the radius of the electron pockets in Fig. 5.5**c** are slightly larger than the reciprocal lattice constant, the electron pockets appear as three distinct parabolae in the schematic of the $E_\mathrm{B} - k_\mathrm{x}$ map in Fig. 5.5**d**. This observation is in qualitative agreement with the dispersive state $S0$ marked in Fig. 5.5**b**. Further evidence for this agreement is based on constant energy maps in Fig. 5.5**e, f** recorded by k-space microscope measurements at the NanoESCA beamline at Trieste synchrotron, measured at photon energies $E_\mathrm{Ph} = 40\,\mathrm{eV}$ and $E_\mathrm{Ph} = 55\,\mathrm{eV}$, respectively, and extending to the 3^{rd} order (3×3) surface BZs. Both ARPES maps are averaged in energy in the range $0\,\mathrm{eV} \leq E_\mathrm{B} \leq 0.3\,\mathrm{eV}$, where E_B denotes the binding energy. The suggested electron pockets are drawn by blue circles having radii of $R = 1.07 \times k_{\Gamma-\Gamma}$ (chosen by eye to qualitatively match the experimental data, i.e., no numerical fit involved) and centered around each Γ point according to the suggestion in Fig. 5.5**c**. A qualitative agreement with main features of the ARPES band maps is reached in this way, which underlines that the state $S0$ indeed originates from one single electron pocket.

Resonant enhancement of photoemission at the Co L_3 edge

Scanning the photon energy E_Ph across the Co L_3 edge further clarifies, if the electronic valence band state $S0$ is derived from the Co atoms. The ResPES measurements in Figs. 5.5**g**–**j** were performed at the beamline I09 at the Diamond Light Source. The samples were grown in the home laboratory as described in Sec. 5.2.1 and transported to the beamline in a UHV suitcase ($p \sim 5 \times 10^{-10}\,\mathrm{mbar}$). Since it is known from XPS measurements that pristine bismuthene samples degrade in the presence of residual oxygen (cf. Appendix D Fig. D.3), also XPS measurements have been performed on the Bi/Co-alloy sample that was transferred with the UHV suitcase to the beamline. The XPS spectrum of the sample is depicted in Appendix D Fig. D.4. A small O1s peak is detected , however, the absence of oxygen induced Bi4f side peaks is a clear indication that the Bi/Co-alloy itself was not oxidized.

Regarding the ResPES measurements, Fig. 5.5**g** shows the low-energy valence band states in a false color plot. Here, the photon energy E_Ph is scanned across the Co L_3 absorption edge (2p-3d photon absorption) in 200 meV steps. The photoemission signal is averaged over a momentum range that spans over almost six (3×3) surface BZs, i.e., specifically the momentum range k_x of Figs. 5.5**h, i**. A strong enhancement of photoemission intensity of the states in the energy range $0 \leq E \lesssim 1.5\,\mathrm{eV}$ is observed at a photon energy between $E_\mathrm{Ph} = 776\,\mathrm{eV}$ and $777\,\mathrm{eV}$ (cf. false color plot of Fig. 5.5**g**). The photon energy position for this resonant enhancement indeed coincides with a peak in the X-ray absorption spectrum (XAS) of the Co L_3 edge that is overlaid in the same image by green dots. Here, the total electron yield (TEY) was acquired as function of photon energy as a measure for the X-ray absorption. The enhancement in the ResPES spectrum can be explained by a constructive interference of the direct photoemission transition, i.e., $2p^6 3d^7 \xrightarrow{+h\nu} 2p^6 3d^6 + e^-$, and the autoionization channel triggered by the creation of a core hole (coherent Auger decay), i.e., $2p^6 3d^7 \xrightarrow{+h\nu} 2p^5 3d^8 \rightarrow 2p^6 3d^6 + e^-$, see Sec. 3.3.5.

ARPES band maps at an off-resonance and an on-resonance photoexcitation condition resolve this behavior in k-space and are plotted in Figs. 5.5**h, i**, respectively. These maps are each an average of the respective photoemission signal over the range of photon energies marked by the respective marker in Fig. 5.5**g**. When the off-resonance condition is met the photoemission intensity in the range $0\,\mathrm{eV} \leq E \leq 1\,\mathrm{eV}$ is faint and a dispersion is hardly detected. This changes drastically when the on-resonance condition is met, which is accompanied by a clear enhancement of dispersive states in the mentioned low-energy sector. Overlaying the suggested electron pocket derived states $S0$ from Fig. 5.5**d** shows that they are in good qualitative agreement with the ARPES signal.

Finally, the k_x-averaged EDCs in Fig. 5.5**j**, which are normalized to the depicted high-energy onset, prove the resonant photoemission enhancement in the energy region of the $S0$ state convincingly. As a conclusion, the valence band state $S0$ in the low-energy sector of Bi/Co-alloy samples is related to electron pockets originating from the Co atomic species.

5.2.3 Tunneling spectroscopy at the bismuthene – Bi/Co-alloy interface

The Bi/Co-alloy forms islands in coexistence with pristine bismuthene in the inital stage of growth, see Sec. 5.2.1. An atomically precise interface appears between these islands and bismuthene, similar to what has been observed for the Bi/Mn-alloy at sub-monolayer coverage in Sec. 5.1.3. In particular, these interfaces are oriented along the bismuthene armchair edge lattice termination. Figure 5.6**a** shows such an interface with bismuthene on the left half and the Bi/Co-alloy on the right half of the image. Spatially resolved differential conductivity measurements in the depicted area resolve its electronic structure.

First, the evolution of the differential conductivity ($\mathrm{d}I/\mathrm{d}V$) spectra, starting from the bulk of bismuthene, across the interface and into the Bi/Co-alloy (along the x-direction), is discussed. These spectra are shown in Fig. 5.6**b** and they reflect the mean of 23 single-point spectra averaged along the y-direction in the indicated "avg." region. Colored markers in Fig. 5.6**a, d**, and Fig. 5.6**f** indicate the corresponding position in x-direction. Gray spectra are measured equally spaced in x-direction, and the direction of the black arrows in Fig. 5.6**a** corresponds to the ordering of the spectra in Fig. 5.6**b**. The main finding is that the bismuthene bulk energy gap, which is clearly seen for the blue spectrum, is continuously filled when approaching the interface. Moreover, the tunneling conductivity for energies of the bismuthene bulk gap takes the largest values when measured directly at the interface represented by the green spectrum and drops again (but not to zero) within the Bi/Co-alloy, see the red spectrum.

Spatially resolved $\mathrm{d}I/\mathrm{d}V$ maps in Figs. 5.6**c**–**e** complement the discussion about the $\mathrm{d}I/\mathrm{d}V$ spectra. Here, Fig. 5.6**d**, which reflects the $\mathrm{d}I/\mathrm{d}V$ map at energies within the bismuthene bulk energy gap, is of special interest. This measurement highlights that indeed the largest LDOS is located directly in between the bismuthene and the Bi/Co-alloy. The pronounced $\mathrm{d}I/\mathrm{d}V$ signal constitutes a quasi-1D edge channel that extends along the inter-

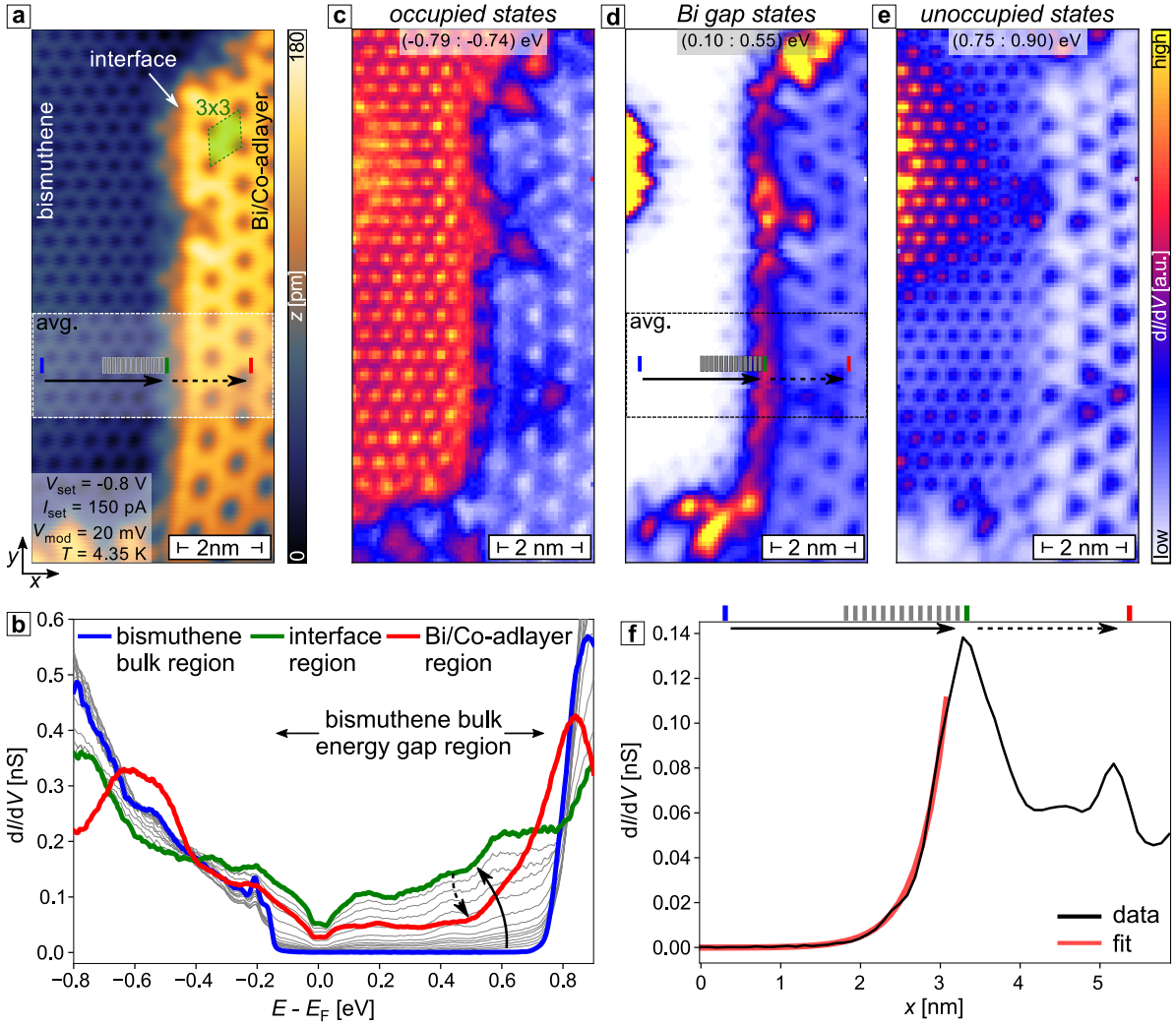

Figure 5.6: Atomically resolved spectroscopy at the bismuthene – Bi/Co-alloy interface. **(a),** Constant current image corresponding to a grid spectroscopy over the depicted interface area between bismuthene (left) and the Bi/Co-alloy (right). The colored marks indicate the x-positions of the differential conductivity spectra in **e**. **(b),** Differential conductivity spectra across the bismuthene – Bi/Co-alloy interface at x-positions indicated by colored marks in **a**. The gray spectra are measured at equally spaced positions along the gray arrow in **a**. Each spectrum is an average of 23 single-point spectra along the y-direction in **a**. **(c) – (e),** Spatially resolved differential conductivity maps averaged over the energy range indicated at the top of the respective image. **(f),** Spatially dependent differential conductivity amplitude across the bismuthene – Bi/Co-alloy interface at $E - E_F = 0.4\,\text{eV}$. An exponential fit (red line) to the differential conductivity from the interface towards the bismuthene bulk yields a $1/e$-decay constant of $(3.5 \pm 0.1)\,\text{Å}$.

face and, importantly, is clearly distinguishable from the metallic LDOS of the Bi/Co-alloy itself. This is in contrast to what has been observed at the interface of bismuthene to the Bi/Mn-alloy in Sec. 5.3, where no pronounced interface state was detected.

The last remark concerns the x-dependent $\mathrm{d}I/\mathrm{d}V$ amplitude across the interface at $E - E_\mathrm{F} = 0.4\,\mathrm{eV}$ in Fig. 5.6**f**. A least-squares fit with an exponential function yields a $1/e$-decay constant of $(3.5 \pm 0.1)\,\text{Å}$, which is close to the value of $(4.1 \pm 0.3)\,\text{Å}$ found for metallic edge states of pristine bismuthene films terminated at SiC(0001) substrate steps in armchair configuration in Ref. [6].

5.3 Discussion

Studying the interplay between magnetism and topology in the 2D TI bismuthene deserves further experimental and theoretical continuation in the future. Especially resolving the magnetic properties of the Bi-Mn/Co alloys is an important experimental task. This could be accomplished, e.g., by X-ray magnetic circular dichroism measurements or spin-polarized STM, but which was beyond the scope of this thesis.

As a first step towards such studies, however, the presented work demonstrates that magnetic transition metals, such as Mn and Co, deposited on a bismuthene surface followed by an annealing step at elevated temperatures reproducibly form surface alloys. STM constant current measurements could resolve their formation at an initial stage of growth, where the alloy forms less than a monolayer. In that case the formation of islands within the bismuthene film is accompanied by the formation of atomically sharp and straight interfaces of bismuthene with the transition metal alloy island. These interfaces establish a unique experimental setting for the study of helical edge states in closest proximity to a magnetic transition metal alloy. This scenario was proved to be accessible with STM/STS. Interestingly, while tunneling spectroscopy at the bismuthene – Bi/Mn-alloy interface does not lead to a clear identification of a distinct (quasi-1D) state residing at the interface, tunneling spectroscopy at the bismuthene – Bi/Co-alloy *is* showing clearly a quasi-1D state at the interface.

Moreover, the electronic structure of both the Bi/Mn-alloy and Bi/Co-alloy was resolved for a (close to) monolayer coverage. Apparently, characteristic features in the ARPES band structure point to the fact that strong SOC is shaping the low-energy electronic states. In the case of the Bi/Mn-alloy, a pronounced metallic band residing at the Γ-points of the (3×3) surface BZ shows a splitting that could be explained in terms of the linear Rashba model with a Rashba parameter $\alpha_\mathrm{R} = 1.19\,\mathrm{eV}\,\text{Å}$ and an effective mass $m^* = 0.23 m_\mathrm{e}$. Moreover, hole-like bands at the K/K'-points of the (3×3) surface BZ also show a strong energy splitting of 0.19 eV. In the case of the Bi/Co-alloy, split bands with a crossing point at the M-point of the (3×3) surface BZ and large metallic electron pockets ($S0$) centered around the Γ-points of the (3×3) surface BZ were observed. The ResPES measurements resolved that the metallic electron pockets $S0$ are essentially connected to the Co-species in the alloy, as they show a pronounced resonant enhancement of photoemission intensity

when the photon energy is equal to the Co L_3 X-ray absorption edge.

The presented observations of bismuthene – Bi/TM-alloy interfaces (where TM is Mn and Co in this case, but could be exchanged by other transition metals) stimulate a plethora of future investigations. Specifically, they provide an unprecedented study case of the interplay between magnetism and helical topological edge states of a large gap 2D TI. As an alternative of using $3d$ transition metals, also $4f$ rare earth metals might be used instead. These have been used to form few-layer silicides and can exhibit ferromagnetism down to the monolayer thickness [157, 158].

CHAPTER 6

Coupling of topological edge states in 1D line defects of bismuthene

Parts of this chapter were published as a research article [159]:
R. Stühler, A. Kowalewski, F. Reis, D. Jungblut, F. Dominguez, B. Scharf, G. Li, J. Schäfer, E. M. Hankiewicz, and R. Claessen, "Effective lifting of the topological protection of quantum spin Hall edge states by edge coupling", *Nat Commun* **15**, 3480 (2022). DOI: 10.1038/s41467-022-30996-z

In what follows, D. Jungblut, F. Dominguez, and B. Scharf have performed the tight binding calculations.

Overview

Extended defects, e.g., quasi-1D line defects, can significantly impact the properties of a 2D material. To date, a variety of phenomena related to such line defects have been reported. For example, Lahiri *et al.* [160] observed an enhanced conductance at line defects of graphene. Another example is the observation of charge modulations in line defects with finite length of (topologically trivial) monolayer transition metal dichalcogenides (TMDs). Here, different conclusions concerning their physical origin have been reached by different research groups. On one side, Barja et al. [139] and Wang et al. [161] attributed the charge density modulations to the formation of a 1D Peierls-type charge density wave in the materials $MoSe_2$ and $MoTe_2$, respectively. On the other side, Jolie et al. [65] ruled out the charge density wave scenario in line defects of MoS_2 and explained the observed charge modulations by a Tomonaga-Luttinger liquid ground state showing separated spinon and holon modulation branches instead. The above cited examples emphasize that the study of quasi-1D line defects in 2D materials continues to be an active research field.

It must further be emphasized that the presence of quasi-1D line defects in a 2D topological insulator represents an intriguing situation different from the ones mentioned above. This can be seen by the theoretical work of Lima *et al.* [162] who studied an extended line defect placed within a *topological* freestanding buckled bismuthene monolayer. The authors showed that two pairs of topological edge states appear at either side of the line defect as a result of the bulk-boundary correspondence. Interestingly, the two pairs of helical edge states hybridize across the line defect due to the close spatial proximity of their wave functions. This mutual edge coupling has two effects. First, it opens an energy gap in the spectrum of the coupled topological states. Second, the right(left)-moving electrons on one side of the line defect will encounter a single-particle backscattering channel because of the spatial

proximity of the left(right)-moving electrons of like spin character on the other side of the line defect. The latter implies that the property of spin-momentum locking becomes lifted *without* the need to break time-reversal symmetry.

While numerous theoretical proposals along this line have been put forward [29,163–169], there exist surprisingly few experimental studies on edge coupling in a QSH insulator. Strunz *et al.* [170] have recently studied the effect of Coulomb interaction between 2D TI edges in spatial proximity. Another work by Jung *et al.* [171] focused on the tunneling-induced gap opening in the 1D edge states of a topological crystalline insulator. The work in this chapter substantially extends the existing understanding of such a peculiar situation. Section 6.1 presents an investigation of the structural properties of quasi-1D line defects, so called domain boundaries (DBs), in the 2D topological insulator bismuthene on SiC(0001). This includes a formal classification and an experimental study based on STM measurements. Section 6.2 then concentrates on the electronic properties of these DBs and scrutinizes the intriguing observation of Fabry-Pérot oscillations. It will be shown that this phenomenon is connected to an effective lifting of the topological protection of helical edge states as a result of hybridization across the DB.

6.1 Structural properties of bismuthene domain boundaries

6.1.1 Formal classification and topographic characterization

Domain boundaries in bismuthene on SiC(0001) can *not* arise as a result of a rotational misalignment of single domains with respect to each other, because all bismuthene domains adopt the same single orientation of the substrate. Instead, DBs form as a consequence of bismuthene being a $(\sqrt{3}\times\sqrt{3})R30°$ reconstruction on the substrate. Therefore, bismuthene domains can have a translational offset, i.e., an integer multiple of the in-plane SiC(0001) lattice constant, with respect to other domains.

The formation of DBs in bismuthene is schematically visualized in Fig. 6.1 for the case of zigzag edge terminated bismuthene domains. Here, domains are categorized into groups named A, B, and C (indicated by different colors). Domains that fall within one group are related to domains that fall into another group by a translational offset of one or two multiples of the in-plane SiC(0001) lattice constant. It can be easily seen that the coalescence of two domains that belong to different groups, i.e., A/B, A/C, or B/C, only gives rise to two distinct types of DBs, which are referred to as "type-I" and "type-II" DB, see Fig. 6.1. It must be noted that without exception, only type-I DBs have been observed in STM experiments. They are identified by measuring the relative distance of the bismuthene honeycombs perpendicularly across the DB (see caption in Fig. 6.1 for details). A probable reason might be that type-II DBs (and also DBs not oriented along the bismuthene zigzag edge) are energetically unstable and therefore do not grow during the epitaxial process.

Figures 6.2**a0**–**a9** represent a bias dependent constant current STM measurement series in order to resolve the "topography" of the type-I DB. As can be seen, the apparent structure and height of the DB strongly depend on the applied bias voltage (see also line profiles

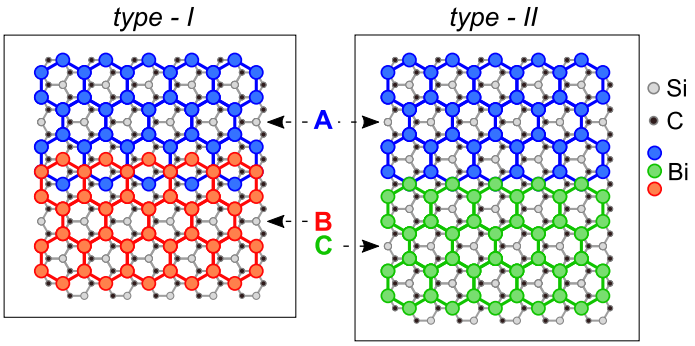

Figure 6.1: Schematic of DB formation. The type-I DB between A/B domains and the type-II DB between A/C domains are discerned by the spatial distance of two Bi hexagon ring centers measured perpendicularly across the DB, which either yields $(3n+1)a_{\mathrm{SiC}}$ for type-I or $(3n+2)a_{\mathrm{SiC}}$ for type-II with $n \in \mathbb{N}_0$. This distance can directly be inferred from STM measurements.

in Fig. 6.2**b**). Specifically, the apparent height of the DB is up to $\sim 2\,\text{Å}$ higher than the bismuthene film in the range $V_{\mathrm{set}} < 1.9\,\mathrm{V}$, but up to $\sim 1\,\text{Å}$ lower than the bismuthene film in the range $V_{\mathrm{set}} > 1.9\,\mathrm{V}$. The strong bias dependence of the apparent height in the STM measurement is a result of local variations of the DB LDOS relative to the bismuthene LDOS. The "real" height difference, i.e., the height difference of the atoms in the DB and the atoms in the bismuthene film, can thus not be deduced from the constant current STM scans alone. Atomically resolved non-contact atomic force microscopy measurements could help to resolve this issue [139].

The STM measurements definitely reveal, however, that the DB always exhibits a well-defined longitudinal periodicity which is independent of the bias voltage. The periodicity amounts to 10.9 Å (cf. Fig. 6.2**b**), which is in excellent agreement with the double length of the bismuthene unit cell $2a_{\mathrm{Bi}} = 10.6\,\text{Å}$.

Moreover, the x-, y-resolved inner structure of the DB features prominent bias voltage dependent topographic patterns, as seen in the false color plots in Figs. 6.2**a0**–**a9**. These are an arrow-shaped pattern in the range between $V_{\mathrm{set}} = 0.9\,\mathrm{V}$ and $1.6\,\mathrm{V}$, a bone-shaped pattern between $V_{\mathrm{set}} = 1.8\,\mathrm{V}$ and $1.9\,\mathrm{V}$, and an almost featureless groove at $V_{\mathrm{set}} = 2.4\,\mathrm{V}$. Interestingly, in the bias voltage range between $V_{\mathrm{set}} = 0.9\,\mathrm{V}$ and $1.6\,\mathrm{V}$ the arrow-shaped segments exhibit a longitudinal directionality which is marked with a white arrow in Fig. 6.2**a3**. This direction is parallel to the $[1\bar{1}00]$ direction of the underlying SiC(0001) surface. At all other bias voltages the DB appears fully symmetric. In the following, a possible origin of the observed directional asymmetry inside the DB is discussed and a candidate atomic structure model of the DB itself is proposed.

6.1.2 Origin of internal asymmetry and candidate atomic structure models

The directional asymmetry observed in the DB is surprising, considering the C_6 symmetry of a Bi honeycomb lattice. However, the SiC substrate can be a possible origin of the asymmetry, as the Si- and C-atoms of every buckled bi-layer of SiC are located on different sublattice sites (cf. Figs. 2.1**a, b**). If one considers only the topmost C-sublattice, one recognizes that it induces a symmetry breaking $C_6 \rightarrow C_3$ to the combined bismuthene monolayer substrate system (see schematic of bismuthene honeycomb on top of a portion

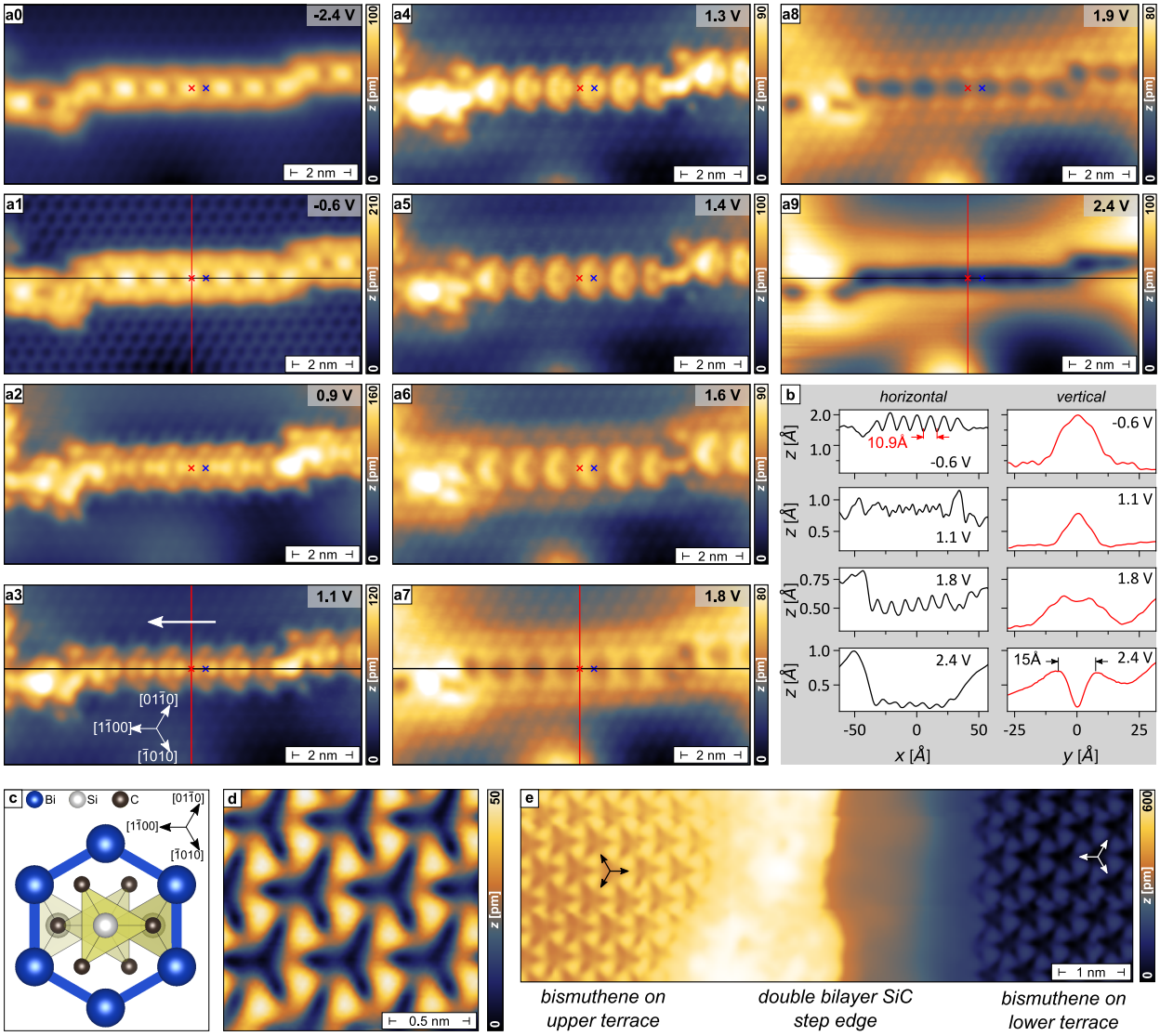

Figure 6.2: STM characterization of a domain boundary. **(a0) – (a9),** STM constant current measurements of a type-I DB at the setpoint bias voltages (V_{set}) indicated in the respective image. ($I_{\mathrm{set}} = 100\,\mathrm{pA}$, $T = 4.35\,\mathrm{K}$). Blue and red crosses mark the same position in each image to facilitate orientation between the different false color plots. High symmetry directions of the SiC(0001) substrate are indicated by arrows in **a3**. **(b),** Constant current STM line profiles at the setpoint bias voltages (V_{set}) indicated in the respective image. The line profiles were measured along the black and red lines indicated in **a1, a3, a7,** and **a9**, respectively. **(c),** Top-view illustration of bismuthene on SiC(0001). For simplicity, only one bismuthene honeycomb placed on top of a portion of four Si-C bi-layers is shown. The topmost C-atoms break the C_6 symmetry of the honeycomb and give rise to an overall C_3 symmetry. High symmetry directions of the SiC(0001) substrate are indicated by arrows. **(d),** The STM constant current image of bismuthene ($V_{\mathrm{set}} = -1\,\mathrm{V}$, $I_{\mathrm{set}} = 10\,\mathrm{pA}$, and $T = 4.35\,\mathrm{K}$) shows a C_3 symmetric distortion imprinted on the Bi hexagon rings. **(e),** STM constant current image ($V_{\mathrm{set}} = -1\,\mathrm{V}$, $I_{\mathrm{set}} = 10\,\mathrm{pA}$, $T = 4.35\,\mathrm{K}$) of bismuthene at a double bi-layer SiC step. The arrows indicate the orientation of the C_3 symmetry of the Bi honeycombs, which flips after traversing the double bi-layer SiC step.

of four Si-C bi-layers in Fig. 6.2**c**). This symmetry breaking effect is also observed in STM constant current measurements in Fig. 6.2**d**. The bismuthene honeycomb lattice is distorted in a way in which only every other interstitial space (Bi-Bi bond) between the Bi positions protrudes further into the center of the hexagon. The larger apparent height of every other interstitial space between the Bi positions in the honeycomb lattice originates from the position of the uppermost C-atoms, a conjecture supported by calculations of the iso-charge surface of bismuthene on SiC from DFT [7].

An experimental consistency check is presented by the constant current STM measurement of a bismuthene film at an upper and lower SiC terrace separated by a double Si-C bi-layer step in Fig. 6.2**e**. As a consequence of using the 4H-polytype of SiC, traversing this terrace step is necessarily accompanied by the change of the in-plane orientation of the top-most C-sublattice by 180°. The arrows in Fig. 6.2**e** indicate that this flip of the C_3 asymmetry is indeed observed in the bismuthene film. As a conclusion, already the bismuthene film exhibits a $C_6 \rightarrow C_3$ symmetry breaking due to the SiC substrate. Therefore, a possible conjecture is that the observed directionality within the DBs is also due to the $C_6 \rightarrow C_3$ symmetry breaking induced by the SiC substrate.

No realistic atomic structure model of the DB in bismuthene has so far been proposed, because a suitable model must take into account the clearly resolved doubled periodicity of the DB with respect to the bismuthene honeycomb lattice. The scientific literature about other 2D honeycomb systems offers examples for known line defects. For example, Lahiri *et al.* [160] observed that zigzag edges of a graphene film on Ni(111) tend to reconstruct into a so-called 57-edge consisting of a periodic formation of pentagon and heptagon C-rings in each unit cell. This edge reconstruction was found to be energetically more favorable than the zigzag edge [172–174]. Eventually, the merging of two 57-edges naturally transforms into a so called 558-DB upon the coalescence of two graphene domains with a translational offset relative to each other. The translational offset results from the possibility of having different registries of the graphene film with respect to the substrate. Because a 558-DB is a periodic arrangement of two pentagon and one octagon C-rings in each unit cell, it has a doubled periodicity compared to the pristine graphene lattice along the zigzag termination. This scenario could therefore also apply to the formation of bismuthene DBs.

Figure 6.3 schematically presents the analogous situation of the formation of a 558-DB in the case of bismuthene on SiC. The left image in Fig. 6.3 shows bismuthene edges that have reconstructed from the zigzag- to the 57-edge similar to the case observed for graphene on Ni(111) [160]. These edges merge and form a 558-DB upon coalescence of both domains (right image in Fig. 6.3). The pentagon Bi-rings of both domains are connected by sharing two Bi atoms, whereas the heptagon Bi-rings of both domains combine to form a single octagon Bi-ring. The 558-structure (or slight modifications of it) could explain the observed topographic period doubling with respect to the bulk bismuthene lattice which is seen in Fig. 6.2. Concerning the observed directionality in bismuthene DBs at certain tip bias voltages (cf. Fig. 6.2**a3**), one explanation could be an additional substrate induced structural shift of the Bi-dimers of connected pentagon Bi-rings along the longitudinal direction.

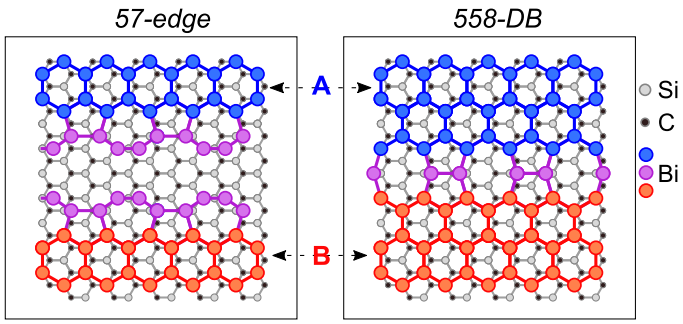

Figure 6.3: 57-edge and 558-DB. (left) A schematic image illustrating the merging of *A* and *B* bismuthene domains each terminated with a 57-edge reconstruction. (right) Two 57-edges have merged to form a 558-DB. The 558-DB is build from periodically repeating units of a pair of pentagon Bi-rings and one octagon Bi-ring. This situation is similar to line defects observed in graphene on Ni(111) in Ref. [160].

Non-contact atomic force microscopy measurements could possibly resolve the inner atomic structure of the DB, as this technique is not primarily sensitive to the electronic charge density and able to resolve more structural details than STM in some cases [139].

6.2 Proximity induced lifting of topological protection in bismuthene domain boundaries

This section presents experimental scrutiny of topological edge coupling in bismuthene on SiC by STM/STS experiments. Importantly, in the course of the following investigation, the discussion is not limited to the electronic phenomena observed in DBs, but these observations and discussions are compared side by side with the situation of 1D metallic states at free zigzag edges in bismuthene. As discussed above, DBs in bismuthene have formed upon the coalescence of two bismuthene domains terminated along the zigzag direction of the honeycomb lattice. Therefore, a direct comparison of the situation of a single, i.e., "free" zigzag edge with a DB is particularly adequate to study the influence of precisely the coupling between edges.

6.2.1 Concept of inter-edge coupling: the free bismuthene edge vs. the domain boundary

As a first step, it is insightful to discuss edge coupling on a phenomenological basis. At a free, i.e., not coupled, edge of bismuthene the bulk-boundary correspondence enforces the existence of helical edge states that have their spin rigidly locked to the electron's momentum [11]. These states are confined to the edge of the material to form a quasi 1D metallic state that spans the bulk energy gap. Because of their helical nature, the edge states can not exhibit single-particle backscattering by any non-magnetic defects, as schematically depicted in Fig. 6.4**a**.

If, however, two pairs of helical edge states are being brought together into close spatial proximity, such that their wave functions overlap, an electronic tunneling between opposite edges is achieved and the respective wave functions hybridize. This scenario generally applies to the edge states of 2D topological insulators and has been covered extensively in

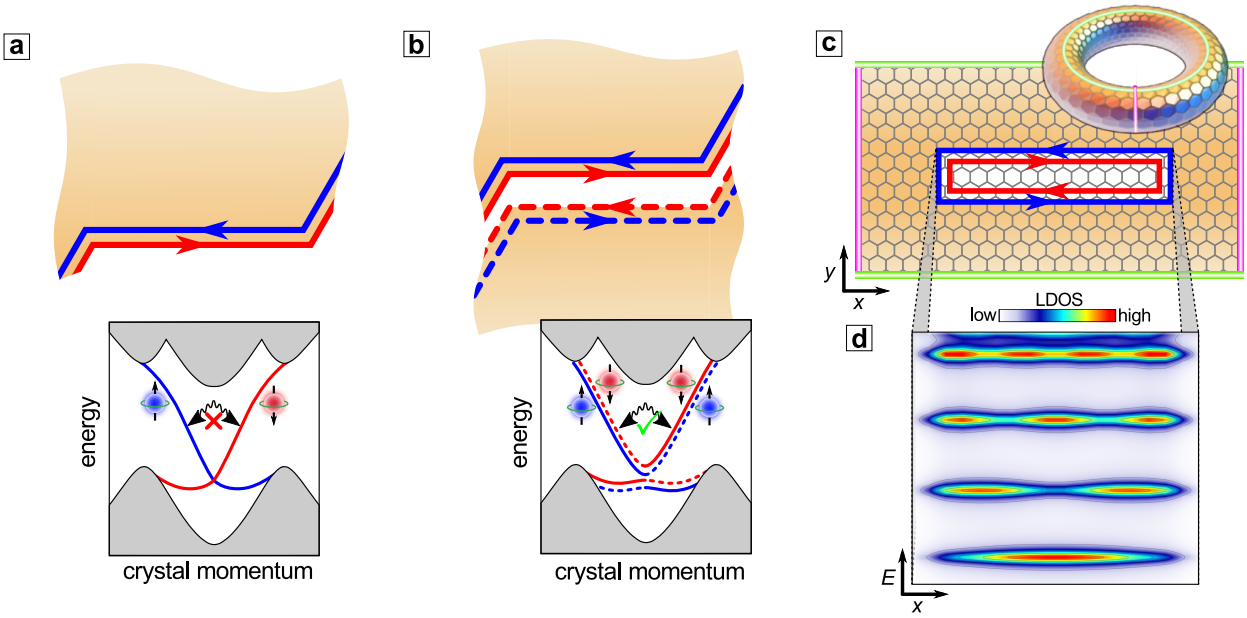

Figure 6.4: Free vs. coupled helical edge states. **(a)**, Edge segment of a generic 2D TI material. A pair of helical edge states is bound to the edge. Back-scattering from defects such as the edge kinks is impeded by topologically protected spin-momentum locking, i.e., left-moving spin-up states (blue) cannot be scattered into right-moving spin-down states (red). The corresponding one-dimensional band structure is schematically depicted below. **(b)**, Two opposing edge segments in close proximity. Spatial overlap of both pairs of helical edge states induces hybridization (or tunneling) between both edges, thereby allowing inter-edge scattering from one segment to the other across the boundary. Strikingly, this opens a channel for back scattering from the edge kinks, i.e., the topological protection becomes partially lifted due to inter-edge hybridization. The corresponding band structure is depicted below. **(c)**, Tight-binding model of coupled edge states in the 2D TI bismuthene. The white area indicates a topologically trivial line defect along the x-direction embedded in the topological bulk (light brown). The green and pink boundaries of the finite-size bulk are connected via periodic boundary conditions, resulting in the depicted torus. The trivial line defect connects two opposite edges; the resulting wave function overlap between both sides induces hybridization of like-spin edge states across the line defect (y-direction) as in **b**. **(d)**, Energy-dependent LDOS of the tight-binding model along the line defect in **c** (integrated across its y-width). The line defect induces standing wave excitations bound to its longitudinal extent (along x) and, as the underlying helical states of bismuthene exhibit an approximate linear dispersion, are linearly quantized in energy E. *Figure reprinted and adapted from Ref. [159] under a Creative Commons Attribution 4.0 International (CC BY 4.0) License.*

many theoretically works [29, 163–169]. It is generally found that the hybridization between right(left)-moving electrons on one edge with their left(right)-moving counterparts of like spin on the opposite edge opens an energy gap at the Dirac point, as depicted in Fig. 6.4**b**. The size of the gap can be small and generally depends on the inter-edge distance involved. For what follows it is more important to emphasize that with the inter-edge hybridization a channel for electron single-particle backscattering is provided without the need to break time-reversal symmetry.

As a starting point, a tight-binding approach was applied based on first-principles calculations [6, 9] to study a model system for the described inter-edge hybridization scenario in bismuthene on SiC.[9] Therefore, a line defect, consisting of a stripe-like region of topologically trivial material, is placed into the bismuthene bulk as depicted in Fig. 6.4**c**. The tight-binding calculations are based on an effective low-energy Hamiltonian derived from a standard "down folding" procedure of the s- and p_z-orbitals from DFT calculations as presented in Sec. 2.3 and in Ref. [6]. Within the tight-binding formalism the trivial stripe-like region is embedded between the topological regions by simply tuning the involved Slater-Koster parameters locally to values which tune this region into a topologically trivial phase. The reader is referred to the Supplementary information of Ref. [159] for details of the calculation.

The tight-binding approach of the scenario depicted in Fig. 6.4**c** predicts the formation of helical edge states along both edges of the trivial line defect, which counterpropagate with opposite helicity. Because the line defect is narrow enough to generate a spatial overlap of the edge state wave functions across the defect (i.e., in y-direction), the wave functions of like spin at opposite edges hybridize. The local density of states along the line defect (i.e., in x-direction) is depicted in Fig. 6.4**d**. It exhibits the formation of standing wave patterns. Because the energy separation of the standing wave excitations are linearly spaced, these states are reminiscent of the behavior of light waves in an optical resonator [175, 176], so called Fabry-Pérot oscillations. The linearly spaced resonance levels are a direct consequence of the linear dispersion relation of the underlying bismuthene edge states. It is conceptually inherent that these Fabry-Pérot oscillations are only observed due to the finite hybridization of helical edge states across the narrow line defect from which the possibility of single-particle backscattering at its two terminations follows. The tight-binding approach thus shows that the nanoribbon with embedded line defect can effectively be thought of as two finite-length edges of bismuthene coupled across the quasi-1D line defect.

Structural comparison of free zigzag edges and domain boundaries

The following analysis investigates the structural properties of free zigzag edges and DBs in bismuthene side by side. The occurrence of both can be seen in an overview constant current STM measurement in Fig. 6.5**a**. The bismuthene film (blue regions) is subdivided into domains by a meandering network of DBs. One of the atomically ordered and straight type-I DBs (as discussed in Sec. 6.1) is indicated by window 1. While this DB is relatively short, a wide distribution of lengths up to $\sim 25\,\mathrm{nm}$ is generally observed (see Appendix Fig. E.1). Window 2 highlights a bismuthene domain with an edge that is not connected to another domain because the film growth is locally incomplete. These edges appear frequently terminated in zigzag direction, and thus establish the case of a free zigzag edge. Figure 6.5**b** and Fig. 6.5**c** compare bias voltage dependent STM constant current measurements of a DB

[9] The tight-binding calculations have been performed by D. Jungblut, F. Dominguez, and B. Scharf in the group of E. M. Hankiewicz.

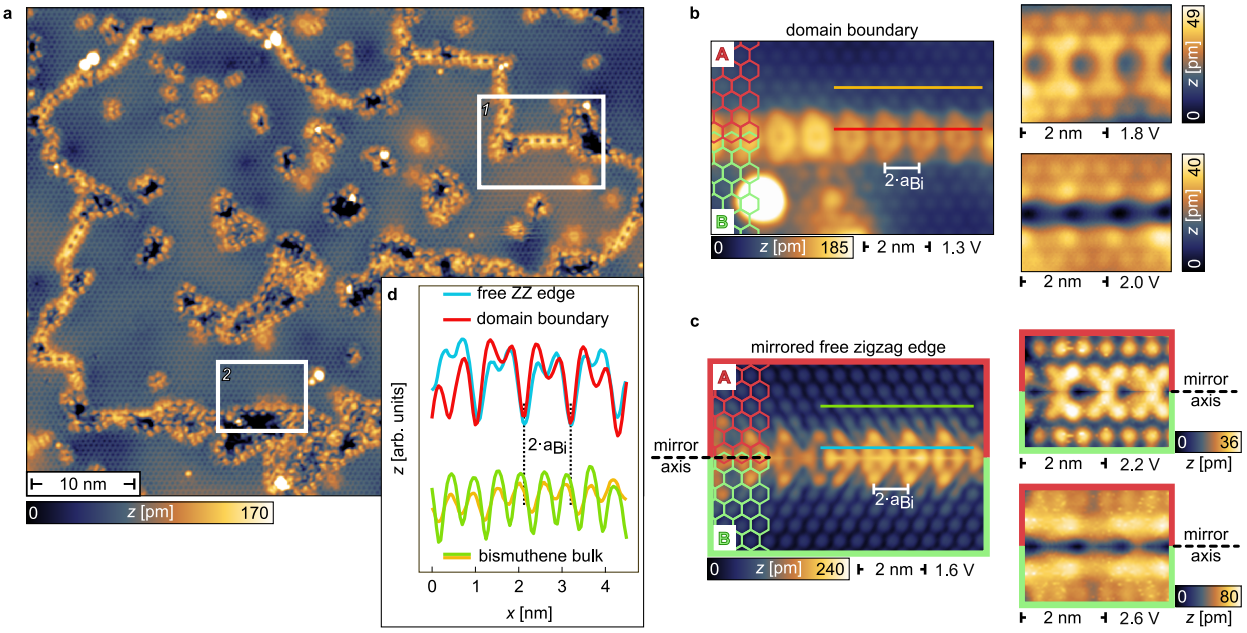

Figure 6.5: Domain boundary and zigzag edge topography. **(a)**, STM constant current map showing a topographic overview of bismuthene. Its $\sqrt{3}\times\sqrt{3}R30°$ superstructure with respect to the SiC(0001) substrate surface results in the formation of three distinct phase domains. The meandering network of line defects are DBs separating the domains from each other. Window 1 marks a particularly well-ordered straight DB section. The map also shows free zigzag edges encircling uncovered substrate surface due to incomplete monolayer growth, see window 2. $V_{\mathrm{set}} = -1.0\,\mathrm{V}$, $I_{\mathrm{set}} = 10\,\mathrm{pA}$. **(b)**, STM topography of a DB recorded at different set-points ($V_{\mathrm{set}} = [1.3\,\mathrm{V}, 1.8\,\mathrm{V}, 2.0\,\mathrm{V}]$), revealing bias-dependent structural features. $I_{\mathrm{set}} = [50\,\mathrm{pA}, 50\,\mathrm{pA}, 50\,\mathrm{pA}]$. **(c)**, STM topography of a free zigzag edge recorded at $V_{\mathrm{set}} = [1.6\,\mathrm{V}, 2.2\,\mathrm{V}, 2.6\,\mathrm{V}]$. The images show the free zigzag edge mirrored at the marked mirror axis such that domain 'A' is mirrored into domain 'B' to properly generate an adsorption site shift to mimic the situation at a DB. The registry mismatch between both domains can be seen in the respective hexagonal lattices. $I_{\mathrm{set}} = [70\,\mathrm{pA}, 100\,\mathrm{pA}, 100\,\mathrm{pA}]$. The procedure of mirroring is exemplified for one zigzag edge in the Appendix Sec. E.2 Fig. E.2. **(d)**, STM constant current line profiles from the STM topographies in **b** and **c**, highlighting the similarly doubled periodicities of free zigzag edge and DB with respect to the bismuthene bulk. *Figure reprinted from Ref. [159] under a Creative Commons Attribution 4.0 International (CC BY 4.0) License.*

and a free zigzag edge. The free zigzag edge is mirrored at an appropriate mirror axis to mimic the coalescence of bismuthene domains 'A' and 'B' as in the case of the formation of a type-I DB. This procedure facilitates the comparison with the DB and the details of the mirror operation are explained in the Appendix Fig. E.2.

Although at slightly shifted bias voltages all characteristic topographic features of the original DB in Fig. 6.5**b** are also found for the mirrored free zigzag edge in Fig. 6.5**c**, i.e., arrow-shaped and bone-shaped segments, and the topography of a groove. Overall the topography shows an excellent structural correspondence. Figure 6.5**d** shows line profiles of both the DB and the free zigzag edge at the bias voltages that lead to the arrow-shaped segments. The line profiles further indicate the close structural similarities of both struc-

tures. In both cases the line profile along the DB (red) and along the free zigzag edge (blue) reveal a period doubling of ($2a_{\mathrm{Bi}} = 10.7\,\text{Å}$) with respect to the lattice constant a_{Bi} of bulk bismuthene (green, yellow). The observed agreement motivates the assumption that DBs in bismuthene stem from the coalescence of two free zigzag edges, or, more precisely zigzag edges that are subject to an edge reconstruction that gives rise to the observed period doubling as described in detail in Sec. 6.1. In fact, this behavior is strongly reminiscent of the 57-reconstruction reported for graphene zigzag edges [172–174] discussed in Sec. 6.1.2 in connection with Fig. 6.3 and the observed 558-DBs in graphene/Ni(111) that form from the merging of two 57-reconstructed zigzag edges [160].

6.2.2 Lifting of topological protection by proximity induced coupling of helical edge states

The following now elucidates the electronic properties of the quasi 1D states confined to the free zigzag edge and compares them with the electronic properties of quasi 1D states confined to the DB. Although the free zigzag edges share obvious structural similarities with DBs as if these can be understood as coupled zigzag edges (possibly in a 57-reconstruction), the following experiments will show that their electronic properties differ considerably.

Absence of single-partice backscattring in free zigzag edges

First, Fig. 6.6**a** considers the situation of a free zigzag edge that terminates the bismuthene domain in the upper half of the image. Important for the following discussion is the observation that the edge contour is not just one continuous straight line, but consists of several straight segments, which are interconnected by kinks. Each intersection at kinks is such that the straight segments each correspond to free zigzag edges aligned in parallel. The electronic properties of bismuthene edges have already been studied in Refs. [6, 8]. These focused on bismuthene armchair edges that arise at SiC substrate terrace steps, and showed that quasi 1D metallic states are strictly localized to these edges. A corresponding scheme now probes the electronic behavior at free zigzag edges by STS differential conductivity ($\mathrm{d}I/\mathrm{d}V$) measurements the results of which are shown in Fig. 6.6**b**. The gray-shaded curve reflects the $\mathrm{d}I/\mathrm{d}V$ spectrum in the bulk bismuthene region marked with a gray square in Fig. 6.6**a** and reveals the expected large electronic band gap of bismuthene. In contrast thereto, the red and green $\mathrm{d}I/\mathrm{d}V$ spectra which were measured immediately at the free zigzag edge (positions marked by red and green squares in Fig. 6.6**a**, respectively) consistently show a filling of the entire bulk gap with spectral weight. In full correspondence to what has been observed for armchair edges at SiC substrate steps in Ref. [8], the spectra at the free zigzag edge also reveal a metallic and overall smooth LDOS. From a spatial mapping of the in-gap local density in Fig. 6.6**c** the metallic edge channel (bluish $\hat{=}$ high LDOS) is seen to extend along the circumference of the bismuthene domain (white $\hat{=}$ low LDOS), rendering the metallic LDOS strictly confined to the very edge.

The free zigzag edge in Fig. 6.6**a** consists of interconnected straight segments that are sep-

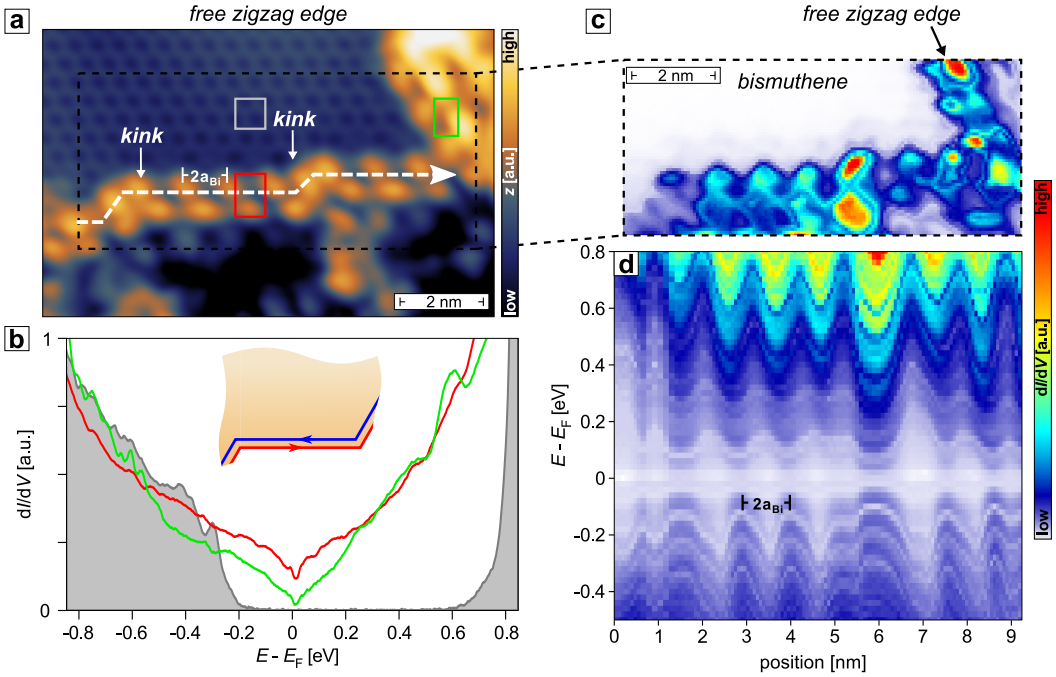

Figure 6.6: Electronic properties of free zigzag edge states. **(a)**, Constant current STM topography of a free zigzag edge ($V_{\mathrm{set}} = -1.2\,\mathrm{V}$, $I_{\mathrm{set}} = 20\,\mathrm{pA}$, $T = 4.35\,\mathrm{K}$). The edge is divided into straight edge segments of variable length separated by kinks. The colored squares mark the positions, where the spectra in **b** are taken. **(b)**, $\mathrm{d}I/\mathrm{d}V$ tunneling spectra in the bulk of bismuthene and at the free bismuthene zigzag edge. The positions are marked in **b**. While the bulk spectrum (gray) shows a clear insulating band gap, the $\mathrm{d}I/\mathrm{d}V$ spectra taken on the edge (red, green) verify the existence of a metallic edge channel smoothly filling the gap. **(c)**, Constant-energy $\mathrm{d}I/\mathrm{d}V$ map within the bulk band gap of bismuthene at $E - E_{\mathrm{F}} = 0.422\,\mathrm{eV}$ (averaged over $\pm 20\,\mathrm{mV}$). The region for the spatially resolved $\mathrm{d}I/\mathrm{d}V$ mapping is indicated by the dashed black box in **a**. **(d)**, False color plot of $\mathrm{d}I/\mathrm{d}V$ signal as a function of energy and position along the white-dashed path marked in **a**. The periodic modulations are energy independent and correspond to the structural edge periodicity $2a_{\mathrm{Bi}}$. Scan parameters in **b, c,** and **d**: $V_{\mathrm{set}} = -1.0\,\mathrm{V}$, $I_{\mathrm{set}} = 250\,\mathrm{pA}$, $V_{\mathrm{mod}} = 10\,\mathrm{mV}$, $T = 4.35\,\mathrm{K}$. *Figure reprinted and adapted from Ref. [159] under a Creative Commons Attribution 4.0 International (CC BY 4.0) License.*

arated from each other by kinks which break the zigzag edge periodicity along the contour of the edge. If lattice imperfections are present, they can give rise to a modulation of the LDOS different from the bare lattice periodicity, which is a manifestation of quasi-particle interference (QPI), i.e., the interference between incoming and elastically scattered electron wave at the lattice imperfection. The detected modulation wavelength is then given by $\lambda(E) = \pi/k(E)$, where E and k are energy and momentum of the electron, respectively. This technique was used before to study the metallic states at bismuthene armchair edges in Ref. [8]. There, these states showed no quasi-particle backscattering from kinks in the SiC substrate steps. The spatial LDOS was modulated only according to the lattice periodicity. The absence of QPI at the kinks was attributed to an absence of single-particle backscattering and the manifestation of the predicted topological protection of edge states

in bismuthene. For trivial metallic edge channels, on the other hand, that are not topologically protected from single-particle backscattering only a perfectly periodic lattice without lattice imperfections would be expected to show no QPI.

The detection of QPI in the case of the metallic edge channel at a free zigzag edge is approached in the same way. Therefore Fig. 6.6**d** shows the spatially resolved $\mathrm{d}I/\mathrm{d}V$ spectroscopy along the edge contour marked with a white dashed line in Fig. 6.6**a**. It can be seen that the $\mathrm{d}I/\mathrm{d}V$ is spatially modulated only according to a $2a_{\mathrm{Bi}}$-periodicity ($2a_{\mathrm{Bi}} = 10.7\,\text{Å}$). This periodicity arises purely from the atomic structure of the zigzag edge which is $2a_{\mathrm{Bi}}$. The structural origin of the observed $\mathrm{d}I/\mathrm{d}V$ modulation is corroborated by its energy independence. No additional and, in particular, energy-dependent modulations are seen that would reflect any QPI. To conclude, no backscattering occurs at the kinks between the piecewise straight edge segments. This observation is thus consistent with a topological protection of the helical edge states at the free zigzag edges in full agreement to what was observed for bismuthene armchair edges at SiC substrate steps [8].

Presence of single-particle backscattering in domain boundaries

The prior section suggested that the DBs and the free zigzag edges share characteristic structural properties which led to the conclusion that DBs stem from the coalescence of two free zigzag edges. Such a scenario is reminiscent of the presented coupling of helical edge channels depicted in Fig. 6.4. The following contrasts the observations for a free zigzag edge with an investigation of the electronic structure of a DB. The DB depicted in Fig. 6.7**a** is separating a first bismuthene domain in the upper half from a second domain in the lower half of the image. Like the free zigzag edge, the DB is not straight throughout, but consists of three adjacent straight segments interrupted from each other by kinks. Important for the side by side comparison, the depicted DB exhibits a similar interrupted lattice periodicity as was discussed for the free zigzag edge in Fig. 6.6**a**.

First, local tunneling spectra are measured on and off the DB, see Fig. 6.7**b**. The positions where spectra were measured are marked by the colored squares in Fig. 6.7**a**. The $\mathrm{d}I/\mathrm{d}V$ spectrum (gray) of the bismuthene bulk is practically unchanged to what was observed for bismuthene bulk in the vicinity of a free zigzag edge. However, as a striking contrast the $\mathrm{d}I/\mathrm{d}V$ spectra from inside the DB (green, blue, and red curves) differ significantly from what has been observed at the free zigzag edge in Fig. 6.6**b**. Instead of showing a smooth gap filling as in the case of a free zigzag edge, the $\mathrm{d}I/\mathrm{d}V$ spectra measured inside the DB exhibit distinct peaks as a function of energy. Some of these peaks are labeled by E_1 – E_4 in Fig. 6.7**b**. Interestingly, the green and blue spectrum are measured at topographically equivalent positions. Yet, the observed peak intensities differ in both cases. Overall the $\mathrm{d}I/\mathrm{d}V$ spectra display strong spatial modulations which already points towards the possibility of a non-structural origin, as would be the case for QPI.

Figure 6.7**c** presents the full energy and position dependent $\mathrm{d}I/\mathrm{d}V(E, x)$ measurement along the domain boundary in order to elucidate this question. At energies $E - E_F > 0.6\,\mathrm{eV}$,

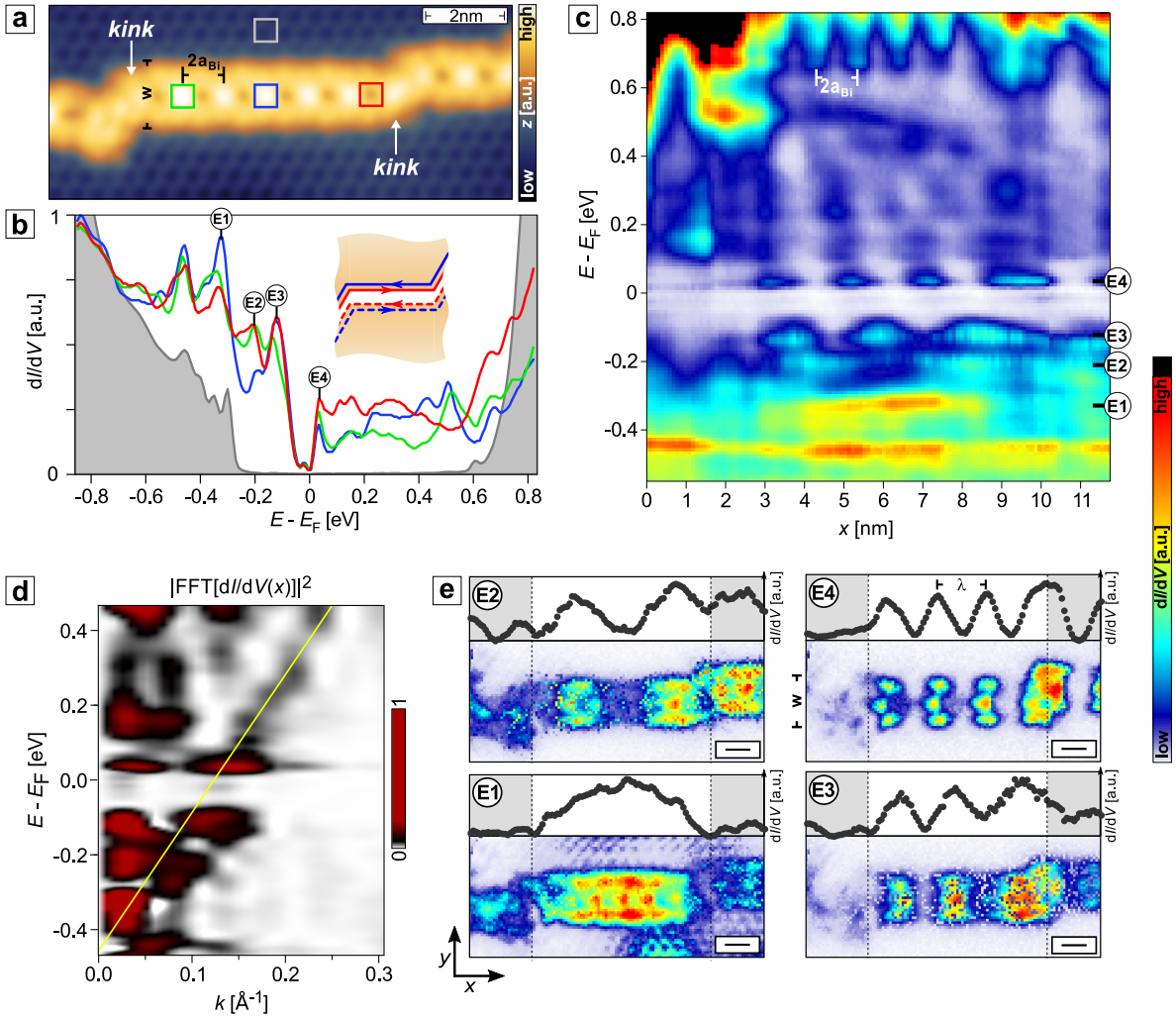

Figure 6.7: Electronic properties of a domain boundary. **(a)**, STM topography of a DB ($V_{\mathrm{set}} = -0.85\,\mathrm{V}$, $I_{\mathrm{set}} = 80\,\mathrm{pA}$, $T = 4.35\,\mathrm{K}$). Similar to the free zigzag edge, the DB consists of piecewise straight sections connected by kinks. The colored squares mark the positions, where the spectra in **b** are taken. **(b)**, $\mathrm{d}I/\mathrm{d}V$ spectra on and off a bismuthene DB, taken at the positions marked in a. The bulk spectrum (gray) agrees with the one in 6.6 **b**. The spectra taken on the DB (green, blue, red) (nearly) fill the band gap and are characterized by the presence of intense peaks at discrete energies, in remarkable contrast to the zigzag edge spectra in 6.6 **b**. **(c)**, Energy-dependent $\mathrm{d}I/\mathrm{d}V$ signal versus position along the DB in **a**, integrated over the DB width w. Energy-dependent standing wave excitations are observed at the marked energies E_1 to E_4, additionally to the structural $2a_{\mathrm{Bi}}$ modulation. **(d)**, Power spectrum ($|\mathrm{FFT}\,[dI/dV(E;x)]\,(k)|^2$) of the $\mathrm{d}I/\mathrm{d}V$ map in **c**. The yellow line is a guide to the eye with a slope of 3.6 eV Å. **(e)**, Two-dimensional $\mathrm{d}I/\mathrm{d}V$ maps of the DB in **a**, taken at the discrete energies E_1 to E_4 defined in **c**. The corresponding $\mathrm{d}I/\mathrm{d}V$ profile along the DB (integrated over its width w) is shown above each map. The modulation wavelength λ can be extracted from the $\mathrm{d}I/\mathrm{d}V$ profiles. As guide to the eye, the extension of the effective resonator is marked by the limiting grey-shaded regions. The scale bar is 1 nm. Scan parameters in **b, c,** and **e**: $V_{\mathrm{set}} = -0.85\,\mathrm{V}$, $I_{\mathrm{set}} = 250\,\mathrm{pA}$, $V_{\mathrm{mod}} = 12\,\mathrm{mV}$, $T = 4.35\,\mathrm{K}$. *Figure reprinted and adapted from Ref. [159] under a Creative Commons Attribution 4.0 International (CC BY 4.0) License.*

i.e., for energies within the bulk CB states of bismuthene, the LDOS clearly reflects the DB's morphological periodicity of $2a_{\mathrm{Bi}} = 10.7\,\text{Å}$. For energies predominantly within the gap, however, the spatial $\mathrm{d}I/\mathrm{d}V(E,x)$ dependence features additional periodic modulations, some of which appear at the marked discrete energies E_1 – E_4 that correspond to the spectral peaks in Fig. 6.7**b**. The wavelength of the modulations decreases towards higher energies, reminiscent of standing waves in a resonator, and are a clear indication of the presence of quasi-particle backscattering. A Fourier transform (FFT) of the differential conductivity map $\mathrm{d}I/\mathrm{d}V(E,x) \rightarrow \mathrm{d}I/\mathrm{d}V(E,k)$ can provide a complementary view on any underlying dispersion relation. The corresponding power spectrum, i.e., $|\mathrm{FFT}\left[\mathrm{d}I/\mathrm{d}V(E;x)\right](k)|^2$, of the $\mathrm{d}I/\mathrm{d}V$ map in Fig. 6.7**c** is shown in Fig. 6.7**d**. In the Fourier transformed signal one can observe a branch that is highlighted by a yellow line as a guide to the eye. Thus notably, the observed QPI roughly follows a linear dispersion relation.

Analysing the $\mathrm{d}I/\mathrm{d}V$ at discrete resonance energies, spatially resolved in both the x- and y-coordinate across the DB, provides a complementary view on the observed quasi-particle backscattering. Figure 6.7**e** shows $dI/dV(x,y)|_{E_i}$, $i = 1,...4$, i.e., the resonance levels that correspond to energies E_1 – E_4. The modulations observed in the LDOS maps are indeed wave-like along the direction of the DB. They are spatially constraint to the DB and corroborate the interpretation that these modulations are not of structural origin, but originate from QPI due to backscattering off the kinks that terminate the DB. The wavelength λ can directly be inferred from the width-integrated $\mathrm{d}I/\mathrm{d}V$ line profiles also contained in Fig. 6.7**e**. As the observed resonances in the LDOS are roughly separated linear in energy they are strongly reminiscent of the formation of electronic Fabry-Pérot states [176]. The combined data thus provides clear evidence that the protection against backscattering observed for the free zigzag (and armchair [8]) edge is lifted for the metallic DB states, at least partially. What remains to be shown is that the Fabry-Pérot states in the DBs are composed of coupled topological edge states and not just caused by QPI of trivial boundary states. The fact that the standing wave excitations carry information on the $E(k)$ dispersion of the underlying electronic states is used for this purpose. A first hint of the underlying dispersion can already be inferred from the FFT of the STS measurements into reciprocal space shown in Fig. 6.7**d** where the Fabry-Pérot modulations generate a roughly linear $E(k)$ dependence (marked by the yellow line), as expected for a Dirac-like topological edge state.

6.2.3 Linear dispersion relation of electronic Fabry-Pérot states

Standing wave excitations in the $\mathrm{d}I/\mathrm{d}V$ maps of many different straight DB sections with lengths ranging from 3.2 nm to 8.6 nm have been analyzed to allow a more systematic determination of the dispersion.[10] At all resonance energies of each DB the wavelength λ of the standing wave excitation was determined. In order to correct for extrinsic energy shifts due to local variations of the chemical potential, all energies are referred to the bulk valence band

[10]The Appendix Fig. E.3 is a compilation of all analyzed DBs.

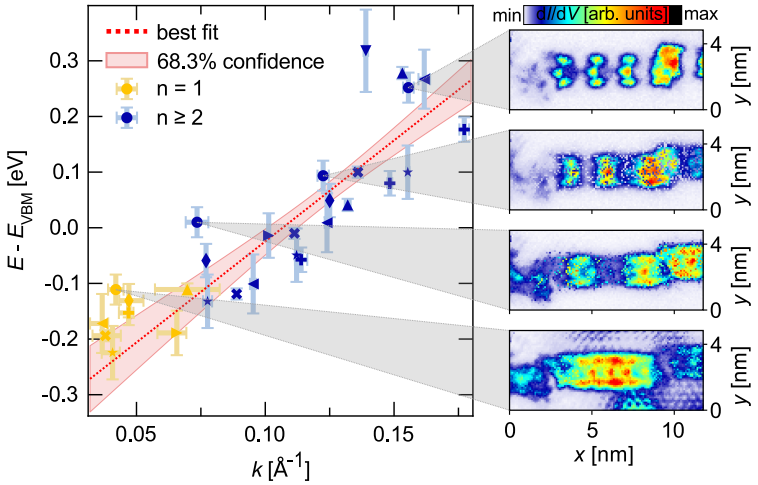

Figure 6.8: Linear dispersion of Fabry-Pérot states. Fabry-Pérot resonator modes labeled by index n as a function of $k = \pi/\lambda$. The modes of equal DBs are assigned equal marker symbols. Red dotted line: Least squares fit to the data for n $\geq$ 2 (see Methods for details). Red shaded region: 68.3% confidence bands of the fit. The constant energy dI/dV maps on the right-hand side (taken from Fig. 6.7e) are assigned to the respective data points. The energy error bars reflect the standard deviation related to the valence band onset (E_{VB}) determination, see Fig. E.4. The k error bars for n $\geq$ 2 relate to the standard deviation in determining λ. The k error bars for n = 1 relate to the estimated error in determining the length of the specific DB. *Figure reprinted from Ref. [159] under a Creative Commons Attribution 4.0 International (CC BY 4.0) License.*

onset E_{VB}, individually measured in the local vicinity of each DB (cf. Appendix Fig. E.4). The standing wave energies thus obtained are plotted in Fig. 6.8 as function of $k = \pi/\lambda$. The important result is that the data points are clearly consistent with a linear dispersion relation of the form

$$E - E_{\mathrm{VB}} = E_{\mathrm{D}} + \hbar v_{\mathrm{F}} k, \tag{6.1}$$

where E_{D} is the Dirac point energy relative to E_{VB} and v_{F} the Fermi velocity. A possible small hybridization gap due to inter-edge tunneling (cf. Fig. 6.4**b**) is not resolved here. A numerical fit of the data with the dispersion of equation (6.1) yields $E_{\mathrm{D}} = (-0.39 \pm 0.08)\,\mathrm{eV}$ and $\hbar v_{\mathrm{F}} = (3.6 \pm 0.6)\,\mathrm{eV\,Å}$. For comparison, the theoretical Fermi velocity predicted for the bismuthene zigzag edge is $\hbar v_{\mathrm{F}} = 4.3\,\mathrm{eV\,Å}$. Density-functional theory (DFT) predicts for the topological state at a bismuthene zigzag edge a bare Fermi velocity of 2.6 eV Å [6]. However, this DFT calculation (using a PBE exchange-correlation potential) strongly underestimates the indirect band gap ($E_{gap}^{DFT} = 0.48\,\mathrm{eV}$) spanned by the edge state. Its actual experimental value is $E_{gap}^{exp} = 0.80\,\mathrm{eV}$ [6, 177]. Renormalizing v_F by the factor $E_{gap}^{exp}/E_{gap}^{DFT}$ yields the value given above. This good correspondence provides smoking gun evidence that the Fabry-Pérot states observed in the bismuthene DBs are indeed derived from pairs of topological edge states, and that their coupling opens a channel for single-particle backscattering, i.e., that their topological protection is lifted.

It is interesting at this point to compare the presented results with related recent work performed on different topological material systems. Pedramrazi *et al.* [178] have conducted

STM/STS on similar DBs in the 2D TI $1T'$-WSe_2. While they report qualitative differences in the spectral line shape for DBs versus interfaces between topological and trivial phases, no backscattering-induced QPI could be detected. Furthermore, Howard *et al.* [179] do observe QPI at step edges of the quantum anomalous Hall material $Co_3Sn_2S_2$ induced by random local impurities and relate their findings to the coupling of chiral edge states in this material system with broken time-reversal symmetry.

6.2.4 Coupling between two Fabry-Pérot resonators

At the origin of referring to the observed charge modulations as "Fabry-Pérot resonances" instead of "quantum well states" lies the idea that the scattering centers exhibit a finite transmission probability, which implies that the coupled edge states at the DB possess a finite probability of not being back-scattered. This property is exemplified for the special case of two *coupled* Fabry-Pérot resonators. This experimental situation is seen in the STM constant current image in Fig. 6.9**a**. A point defect (marked by an arrow) is located inside the long DB and separates a left DB segment from a right DB segment. The left and the right segments have lengths L_1 and L_2, respectively, as indicated. A full spatially resolved STS differential conductivity measurement was conducted within the region indicated by a red rectangle in Fig. 6.9**a**. The energy resolved and DB width-integrated $\mathrm{d}I/\mathrm{d}V$ spectrum is shown in Fig. 6.9**b**. Moreover, spatially resolved $\mathrm{d}I/\mathrm{d}V$ maps at certain resonance energies are depicted in Fig. 6.9**c**.

In Fig. 6.9**b**, it can be clearly seen that charge modulations are present both to the left and to the right of the defect. Moreover, the modulations in the left DB segment (the longer one) set in at lower energies and feature smaller energy separations compared to the modulations in the right DB segment (the shorter one). As already mentioned in connection to Fig. 6.7, the charge modulations can even better be visualized in the spatially resolved $\mathrm{d}I/\mathrm{d}V$ maps plotted in Fig. 6.9**c**. The corresponding energies are indicated by the arrows pointing from Fig. 6.9**c** to the energy scale of Fig. 6.9**b**. Here the lowest image shows the charge modulation that corresponds to the first Fabry-Pérot resonance in the left DB segment. The $\mathrm{d}I/\mathrm{d}V$ in the right DB segment, on the other hand, is rather featureless at this energy. In the second-to-lowest panel in Fig. 6.9**c** the second Fabry-Pérot resonance is seen in the left DB segment, whereas the first Fabry-Pérot resonance is seen in the right DB segment. At higher energies, the subsequent Fabry-Pérot resonances appear both in the left and right DB segments.

Figure 6.9**d** introduces a coupled double Fabry-Pérot resonator model for the qualitative interpretation of the data. It is an extension to the model by Seo *et al.* [176] who studied electronic Fabry-Pérot oscillations in topological surface states of a 3D TI at substrate steps by STM. According to the observed topography of the DB in Fig. 6.9**a**, the left resonator (1) has a length L_1 and the right resonator (2) a length L_2. The model in Fig. 6.9**d** exhibits a left, middle, and right barrier depicted by gray dashed lines to simulate back-scattering off from point scatterers with finite reflectivities $R_p = |R_p|e^{i\arg(R_p)}$, with $p \in 0, 1, 2$. In a plane wave scattering approach charge carriers with an energy-momentum dispersion $E(k_L, k_R)$,

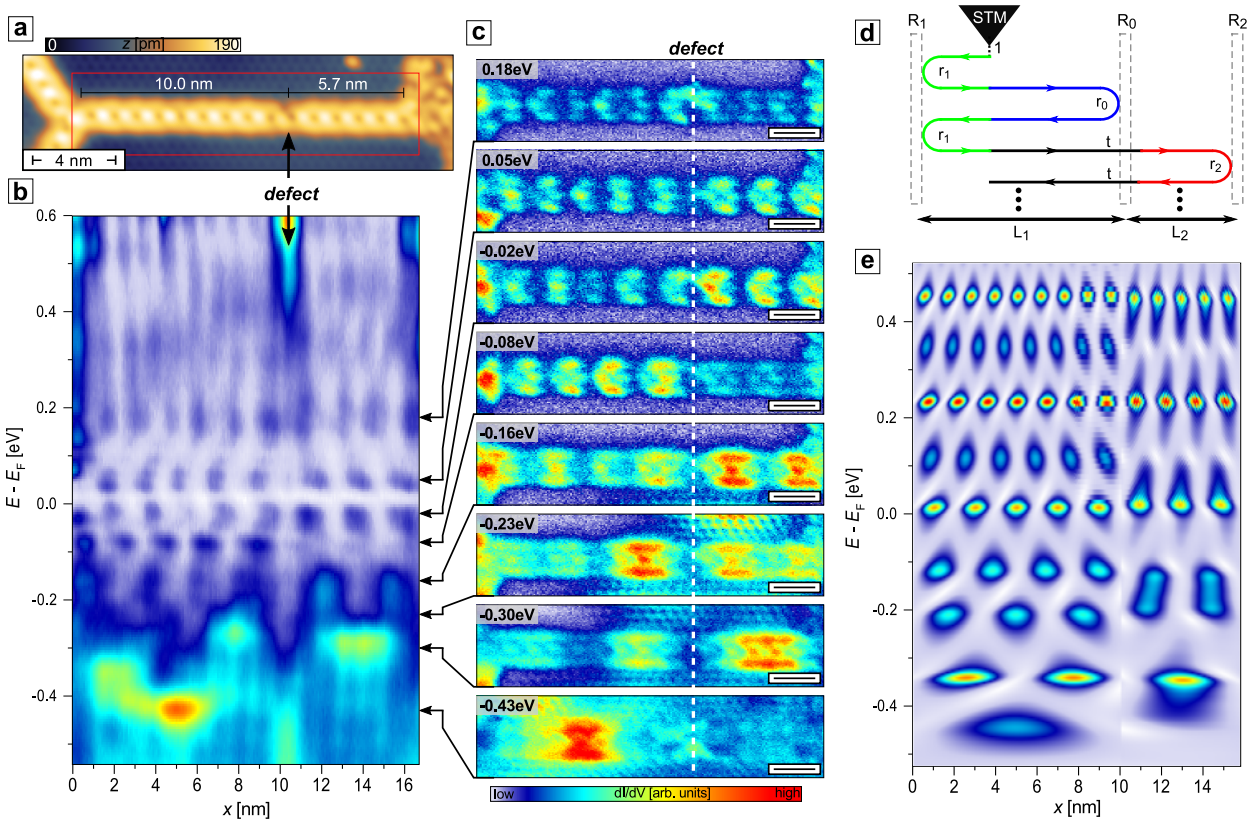

Figure 6.9: Spectroscopy of a coupled Fabry-Pérot resonator. (a), Constant current STM measurement ($V_{\mathrm{set}} = -1.2\,\mathrm{V}$, $I_{\mathrm{set}} = 10\,\mathrm{pA}$, $T = 4.35\,\mathrm{K}$) of a DB with a defect that splits the DB into two straight DB segments with different lengths. The red rectangle indicates the region for spatially resolved $\mathrm{d}I/\mathrm{d}V$ mapping. **(b),** $\mathrm{d}I/\mathrm{d}V$ (integrated over the width of the DB) as a function of longitudinal position x. The wavelengths of the energy dependent charge modulations in both the left and right DB segment shorten with increasing energies. The situation is reminiscent of a coupled double Fabry-Pérot resonator, see **d, e** for qualitative modelling. ($V_{\mathrm{set}} = -0.8\,\mathrm{V}$, $I_{\mathrm{set}} = 180\,\mathrm{pA}$, $V_{\mathrm{mod}} = 10\,\mathrm{mV}$, $T = 4.35\,\mathrm{K}$) **(c),** $\mathrm{d}I/\mathrm{d}V$ maps at constant energy marked with arrows in **b**. For certain energies the charge modulations are mainly confined within the left DB segment and for other energies mainly confined within the right DB segment. Scale bar: 2 nm. **(d),** Schematic of coupled double Fabry-Pérot resonator composed of a first resonator with length $L1$ and a second resonator with length $L2$. Both resonators are coupled with a partially reflective wall R_0. For the qualitative modelling of the experimentally observed charge modulations it is assumed that charge carriers injected into the resonator by the STM tip are reflected/transmitted multiple times at the resonators walls characterized by a reflectivity $R_i = |R_i|e^{i\mathrm{arg}(R_i)}$, where $i \in 0, 1, 2$. In a plane wave scattering approach the electronic wave function ψ at position x can be modelled by summing over all possible scattering paths, see Eqs. (6.2)–(6.9) (the initial amplitude of the injected carrier is set to 1). **(e),** Simulation of charge modulations in a coupled double Fabry-Pérot resonator in **d**. The false color plot shows $|\psi|^2$ from Eq. (6.2) for model parameters: $L_1 = 10.0\,\mathrm{nm}$, $L_2 = 5.7\,\mathrm{nm}$, $R_0 = 0.7e^{i\pi}$, $R_1 = R_2 = 0.5e^{i\pi}$, and $E_{R/L} - E_F = \hbar v_F k_{R/L} + \mu$, where $\hbar v_F = 3.6\,\mathrm{eV\,Å}$ and $\mu = -0.56\,\mathrm{eV}$. The infinite sums in Eqs. (6.3), (6.4) were evaluated up to $j_F = 5$ and $m_F = 2$. *Figure reprinted from Ref. [159] under a Creative Commons Attribution 4.0 International (CC BY 4.0) License.*

where $k_L(k_R)$ describes the wave vector for left(right) moving carriers, are injected from the STM tip at position x. They can experience reflection off or transmission through the barriers and eventually return to position x. Then, the electronic wave function ψ at position x can be modelled by summing over all possible scattering paths. Setting the initial amplitude of the injected carrier to 1, a series expansion for the electronic wave function ψ reads:

$$\psi = \begin{cases} \psi_1^{\mathrm{L}} + \psi_1^{\mathrm{R}} & -L_1 \leq x < 0 \\ \psi_2^{\mathrm{L}} + \psi_2^{\mathrm{R}} & 0 \leq x \leq L_2 \end{cases} \tag{6.2}$$

$$\psi_1^{\mathrm{L}} = \sum_{j=0}^{\infty} \sum_{k=0}^{j} \sum_{n=0}^{k} \binom{j}{k} \binom{k}{n} \left[r_0^j + r_0^{j+1} \right] \times r_1^{j-k} \times t^k \times r_2^{k+n} \times R_0^n \tag{6.3}$$

$$\psi_1^{\mathrm{R}} = 1 + \left(r_1 + t \sum_{m=0}^{\infty} r_2^{1+m} \times R_0^m \right) \psi_1^{\mathrm{L}} \tag{6.4}$$

$$\psi_1^{\mathrm{L/R}} \mapsto \psi_2^{\mathrm{L/R}} : \{ R_1 \leftrightarrow R_2,\, L_1 \leftrightarrow L_2,\, k_L \leftrightarrow k_R \} \,, \tag{6.5}$$

with the following definitions:

$$r_0 := e^{i(k_L+k_R)(L_1-|x|)} R_1 \tag{6.6}$$

$$r_1 := e^{i(k_L+k_R)|x|} R_0 \tag{6.7}$$

$$t := t_R t_L := e^{i(k_L+k_R)|x|} \underbrace{\left[1 + |R_0| e^{i \arg(R_0)} \right]^2}_{T_0^2} \tag{6.8}$$

$$r_2 := e^{i(k_L+k_R)L_2} R_2 \,. \tag{6.9}$$

Here $\psi_{1/2}^{\mathrm{L/R}}$ describe wave functions of initially left (L) and right (R) moving carriers in the first (1) and second (2) resonator, respectively.

The above modelling assumes a complex reflectively $R = |R| e^{i \arg(R)}$, whose amplitude will generally be less than unity ($|R| < 1$). It therefore expands the qualitative explanation of the observed Fabry-Pérot-like charge modulations by taking into account that the edge state electrons are not perfectly reflected by the scattering centers, just as in an optical Fabry-Pérot interferometer. Although, one can only infer the microscopic details of R from ab-initio atomistic calculations capturing the respective scattering potential (which is not addressed here), already the presented qualitative modeling ($|R| = \text{const.} < 1$ and $\arg(R) = \pi$) is able to explain characteristic features of the measured $\mathrm{d}I/\mathrm{d}V$ spectra seen for the DBs in Fig. 6.9 (and Fig. 6.7), namely: (1) a rather smooth background signal associated with the unscattered, i.e., transmitted part of the propagating edge state, and (2) the strongly modulated (along the DB) and peaky (in energy) component resulting from the backscattering-induced interference. For the specific qualitative modelling of the data in Figs. 6.9**b, c** that reflects the LDOS in the system, the following parameters for the calculation of $|\psi|^2 \propto$ LDOS in Fig. 6.9**e** have been used: $L_1 = 10.0\,\mathrm{nm}$, $L_2 = 5.7\,\mathrm{nm}$,

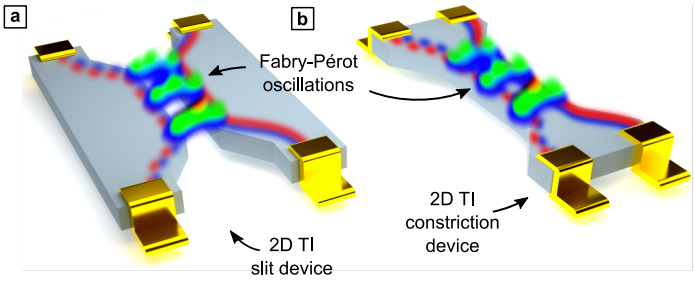

Figure 6.10: 2D TI Fabry-Pérot devices. Schematic four-terminal devices for electronic Fabry-Pérot interferometry based on a QSH insulator in slit or, alternatively, constriction geometry. *Figure reprinted from Ref. [159] under a Creative Commons Attribution 4.0 International (CC BY 4.0) License.*

$R_0 = 0.7e^{i\pi}$, $R_1 = R_2 = 0.5e^{i\pi}$, and $E_{R/L} - E_F = \hbar v_F k_{R/L} + \mu$, where $\hbar v_F = 3.6\,\text{eV Å}$ and $\mu = -0.56\,\text{eV}$. The infinite sums in Eqs. (6.3), (6.4) were evaluated up to $j_F = 5$ and $m_F = 2$. A good qualitative agreement with the measurement is reached, which underpins the assignment of the LDOS modulations in DBs with Fabry-Pérot oscillations.

6.3 Discussion

The work of this chapter scrutinized the intrinsic DBs in the 2D TI material bismuthene on SiC(0001) and revealed that these extended line defects realize the direct coupling between spin-momentum locked edge states on either side of the DB. Since a mutual edge coupling offers the possibility for right(left)-moving electrons on one edge to scatter into left(right)-moving electrons of spin like character on the coupled edge, spin-momentum locking for the participant edge states is (partially) lifted. As an important consequence, a backscattering channel is enabled without the need to break time-reversal symmetry. The loss of their topological protection against single-particle back-scattering ultimately manifests itself in QPI reminiscent of electronic counterparts of Fabry-Pérot states.

As an outlook, the phenomenon of Fabry-Pérot interference in a 2D TI is discussed from a broader perspective. The underlying coupling of topological edges encourages the generally applicable strategy of controlling and eventually lifting topological protection by the inter-edge hybridization of two pairs of edge states [29,163–169]. This can be used to implement a so called electronic Fabry-Pérot interferometer in 2D TI materials.[11] Here, if narrow enough a simple slit or constriction nanopatterned into a QSH insulator suitable for nanolithography, as schematically depicted in Figs. 6.10**a, b**, is sufficient to generate coupling between the helical QSH states on its outer edges, similar to the situation in bismuthene DBs. Additionally, suitable gate electrodes could be used to tune the effective length and edge coupling strength of the constriction and hence provide wide control of its electronic transmission, e.g., for a separate control of charge and spin transport [29,164,165]. Moreover, the idea of switching on and off the topological protection of the helical edge states was suggested as the basis for an on/off functionality in a field-effect transistor based on a 2D topological insulator [180–182]. The presented microscopic study of edge coupling in a QSH insulator hopefully fertilizes the realization of such quantum transport experiments and novel device concepts for 2D TI-based electronics.

[11] Related implementations in topologically trivial materials have been realized, e.g., in carbon nanotubes [175].

CHAPTER 7

Optical spectroscopy of bismuthene and the detection of excitons

Parts of this chapter were published as a research article [124]:
M. Syperek†, R. Stühler†, A. Consiglio†, P. Holewa, P. Wyborski, Ł. Dusanowski, F. Reis, S. Höfling, R. Thomale, W. Hanke, R. Claessen, D. Di Sante, and C. Schneider, "Observation of room temperature excitons in an atomically thin topological insulator", *Nat Commun* **13**, 6313 (2022). DOI: 10.1038/s41467-022-33822-8
†These authors contributed equally.

The optical spectroscopy measurements shown and discussed in the following were performed and provided by M. Syperek, P. Holewa, P. Wyborski, and Ł Dusanowski. All DFT, *GW* and Bethe-Salpeter equation calculations were performed and provided by A. Consiglio and D. Di Sante.

Overview

Whereas the one-particle spectral properties are experimentally accessible via spectroscopic probes such as STS and PES as they involve the removal or addition of an electron, the two-particle spectral properties are experimentally accessible via optical spectroscopy which involves the simultaneous creation of an electron and a hole. This chapter examines the optical response of bismuthene. Specifically, the electronic band gap of bismuthene measured by STS is compared with the optical band gap of bismuthene measured by photo-modulated reflectivity (PR). These measurements are complemented by ab-initio *GW* and Bethe-Salpeter equation calculations which account for the electronic Coulomb interactions [55, 183, 184]. Moreover, the presented work relates to the first observation of excitons in bismuthene, and in a large-gap QSH insulator in general. On a broader perspective, the presented findings relate to a new aspect of combining non-trivial global band topology and multi-particle physics (here in the form of excitons stimulated by the light-matter interaction), for which to date experimental scrutiny has so far been largely hampered by the lack of suitable 2D TIs with a sufficiently wide band gap that allows coupling to high-energy photons.

7.1 Single-particle band gap: Experiment vs. theory

A first step is to develop a good understanding of the underlying single-particle electronic properties of bismuthene. To this end, the direct experimental access to the single-particle spectral function in both the occupied and unoccupied states via tunneling spectroscopy is exploited.

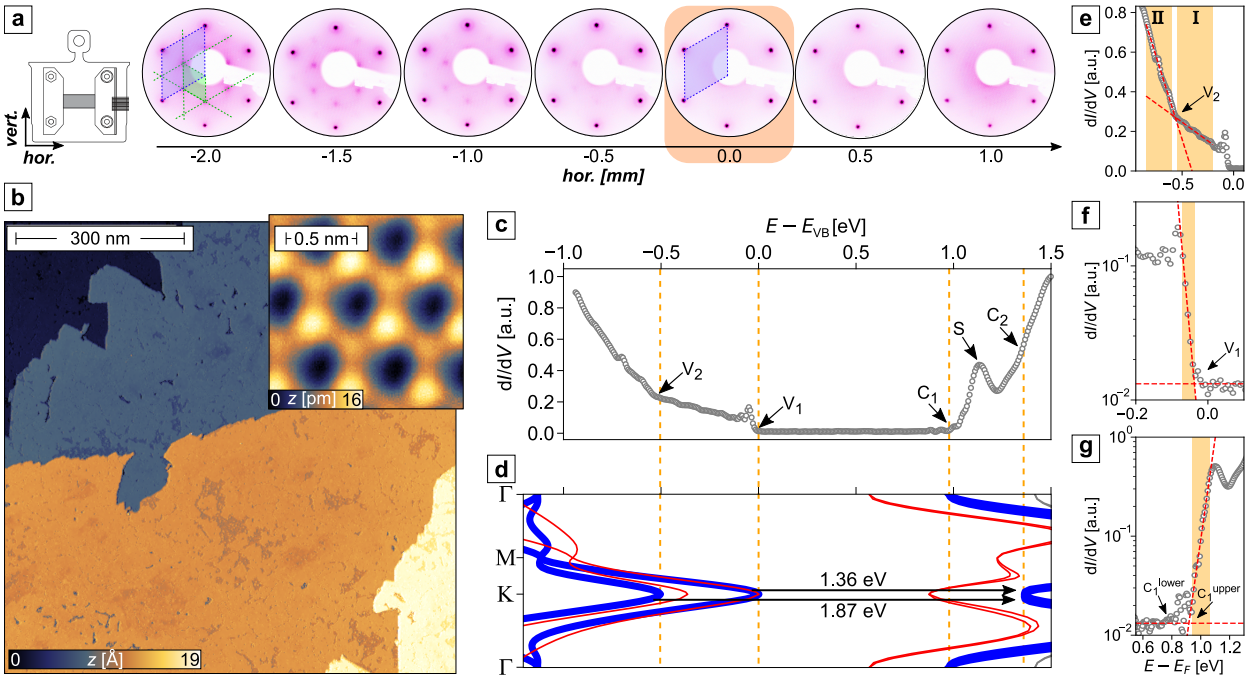

Figure 7.1: Bismuthene sample characterization. (a), LEED series ($E_{\mathrm{kin}} = 40\,\mathrm{eV}$, $T = RT$) along the horizontal direction of the bismuthene sample (cf. schematic drawing of the bismuthene sample (gray strip) mounted on a *ScientaOmicron* DC sample holder). The blue-shaded rhombs indicate the surface Brillouin zone defined by the Bragg peaks of the intrinsic bismuthene ($\sqrt{3} \times \sqrt{3})R30°$ reconstruction on the SiC(0001) surface. Towards the left side of the sample additional Bragg peaks are seen to appear, resulting in a new $(2\sqrt{3} \times 2\sqrt{3})R30°$ reconstruction, which is associated with a different (non-bismuthene) phase induced by the local growth temperature having exceeded its optimum value during growth as described in Sec. 4.2.3. The green-shaded rhomb marks the corresponding surface Brillouin zone. In comparison, the right-hand side of the film displays only intrinsic bismuthene Bragg spots which are however accompanied by a strong diffusive background indicating a highly defective film. The optimal bismuthene coverage is thus located at the center of the film (horizontal position 0.0 mm). **(b),** Constant current STM image of bismuthene at the horizontal spot of best sample quality as indicated by the orange background in **a**. The topographic map displays the high coverage ($\sim 87\%$) of the epitaxially grown bismuthene monolayer and the terrace structure of the underlying SiC substrate. ($T = 4.2\,\mathrm{K}$ and $V_{\mathrm{set}} = 2.6\,\mathrm{V}$, $I_{\mathrm{set}} = 50\,\mathrm{pA}$.) Inset: A high-resolution measurement reveals the bismuthene honeycomb lattice. ($T = 4.2\,\mathrm{K}$ and $V_{\mathrm{set}} = -0.4\,\mathrm{V}$, $I_{\mathrm{set}} = 200\,\mathrm{pA}$.) **(c),** Differential tunneling conductivity ($\mathrm{d}I/\mathrm{d}V$) spectrum, locally measured in the center of the bismuthene film ($T = 4.2\,\mathrm{K}$ and $V_{\mathrm{set}} = -0.4\,\mathrm{V}$, $I_{\mathrm{set}} = 200\,\mathrm{pA}$, $V_{\mathrm{mod}} = 10\,\mathrm{mV}$). The origin of the peak labeled S is explained in the main text. **(d),** *GW* band structure calculation (blue curves) for bismuthene. The direct optical transitions at the K-point are indicated by arrows. Also shown is the DFT band structure obtained with the HSE hybrid functional (red curves) [6], illustrating the propensity of DFT to underestimate the band gaps. Characteristic points in the spectrum that correspond to the valence band onsets (V_1, V_2) and the conduction band onsets (C_1, C_2) are marked with orange dashed lines. **(e) – (g),** Detailed plots of the dI/dV in **c** around V_2 (onset of the lower valence band), V_1 (onset of the upper valence band), and C_1 (onset of the conduction band), respectively. Red dashed lines mark best fits to the spectrum for the determination of the onsets (see text for details). *Figure reprinted and adapted from Ref. [124] under a Creative Commons Attribution 4.0 International (CC BY 4.0) License.*

Sample preparation and tunneling spectroscopy

The bismuthene samples used for the STS experiments, as well as for the optical experiments described below, were prepared as described in Ch. 4. After molecular beam epitaxy the sample quality was checked on a macroscopic scale by performing LEED measurements across the full extent of the SiC substrate, see Fig. 7.1**a**. This step will be important for later correlation of the bismuthene film quality with optical measurements. Clearly, at the center of the sample, i.e., at position $\sim 0.0\,\mathrm{mm}$, the bismuthene film quality reaches its maximum (the corresponding LEED image is highlighted by an orange background). This spot on the sample reveals the highest intensity of the $\sqrt{3} \times \sqrt{3}$ Bragg peaks (marked by a blue shaded rhomb) associated with the bismuthene reconstruction on SiC(0001), as well as the lowest diffuse background intensity. The LEED images also show that the film quality is inhomogeneous on a millimeter scale along the horizontal (i.e., longitudinal) direction of the substrate. This effect is caused by a temperature gradient due to the DC resistive heating method used with the *ScientaOmicron*-type sample holder (see schematic image in Fig. 7.1**a**). Therefore, the left edge of the sample exhibits an additional $(2\sqrt{3} \times 2\sqrt{3})R30°$ surface reconstruction with weak indications of stripes (marked by a green shaded rhomb and green dashed lines). This surface reconstruction is characteristic for a locally too high growth temperature during growth, as described in Sec. 4.2.3 in Fig. 4.9**d, e**. It is also known from previous STM experiments that at such spots the bismuthene coverage is lower compared to a growth with optimal growth temperature.

STM and STS measurements are conducted on the sample spot with the highest film quality. Figure 7.1**b** shows an STM constant current overview scan which confirms the excellent bismuthene coverage ($\sim 87\%$) at this spot on the sample. The detailed view on the honeycomb arrangement of the bismuthene atoms in the inset figure ultimately confirms the successful growth. Both the occupied and unoccupied states and their relative energy separation, which is relevant for the optical transitions, can be resolved by STS. Figure 7.1**c** displays the STS spectrum measured at a position of highest structural film quality as in Fig. 7.1**b**. The most prominent feature of the spectrum is the vanishing LDOS between the energy positions marked by V_1 and C_1. This region is identified as the fundamental single-particle electronic band gap, with the spectral onsets V_1 and C_1 representing the valence band maximum (VBM) and conduction band minimum (CBM), respectively. Overall, the dI/dV spectrum in Fig. 7.1**c** displays four characteristic points named V_1, V_2, C_1, and C_2. The energy positions of these points will be analyzed in the following.

Figure 7.1**e** is a detailed plot of the dI/dV spectrum in Fig. 7.1**c** in the vicinity of V_2. This feature, which is related to a prominent kink in the spectrum, can be attributed to the onset of the lower Rashba band in the bismuthene VB states. The red dashed lines in Fig. 7.1**e** are two linear functions fitted to the data within the regions I and II. The intersection point of these two fitting lines yields the energy position of the kink and gives $V_2 = -0.57\,\mathrm{eV}$.

Moreover, Fig. 7.1**f** is a detailed log-plot of the dI/dV of Fig. 7.1**c** in the vicinity of V_1. The red dashed lines indicate on the one hand the mean tunneling intensity within the

single-particle gap of bismuthene, which relates to the noise level of the measurement, and on the other hand the result of fitting a linear function to the data in the orange shaded region, i.e., around the VB edge. The intersecting point of the two red dashed lines yields the energy position of the VBM and is given by $V_1 = -0.04\,\mathrm{eV}$.

The same procedure as for the determination of V_1 is also applied for the determination of the CBM in Fig. 7.1**g**. This yields an upper limit for the energy position of the related spectral feature $C_1^{\mathrm{upper}} = 0.92\,\mathrm{eV}$. A lower limit of the CBM is defined as the low energetic end of a hump in the dI/dV marked by C_1^{lower}. It lies energetically just below the steep onset of the CB and is frequently observed in bismuthene tunneling spectra. Its energetic position together with an estimated error is $C_1^{\mathrm{lower}} = (0.80 \pm 0.05)\,\mathrm{eV}$, which is in good agreement with the work of Ref. [6].

Finally, the energy separation of C_1 and V_1 defines the experimental single-particle band gap, i.e., the indirect band gap from the VBM at K to the CBM at Γ, and yields $0.80\,\mathrm{eV} \leq E_{\mathrm{ind}} \leq 0.96\,\mathrm{eV}$. This value is in accordance with prior STS results in Refs. [6,7]. Notably, the gap is also in accordance with the extracted electronic band gap from pump-probe ARPES measurements, which will be presented in Ch. 8.

Apart from the spectral features discussed above, the STS spectrum in Fig. 7.1**c** also exhibits a peak S located between the features C_1 and C_2, which has already been reported in the work by Reis *et al.* [6], see dark red spectrum in Fig. 4A in Ref. [6]. However, it has not been discussed any further there. Therefore, the Appendix Fig. F.1 shows STS spectra recorded on an extended spatial area of the bismuthene surface containing multiple bismuthene unit cells as a comparison to the single-point $\mathrm{d}I/\mathrm{d}V$ spectrum in Fig. 7.1**c**. This extended measurement shows that the intensity of this tunneling peak S between features C_1 and C_2 varies strongly on length scales of several nanometers and is even absent in some probed areas, see Appendix Fig. F.1**a**. Interestingly, the bismuthene surface topography map remains at the same time homogeneous, i.e., the bismuthene lattice displays no anomalies such as bismuthene lattice defects correlating with the S peak intensity, see Appendix Fig. F.1**b**. In addition to this experimental observation it is noted that the total (i.e., momentum-integrated) joint-DOS obtained from GW calculations does likewise not exhibit any such peak S (see Fig. 7.5**a**) suggesting that its appearance in the STS spectra cannot be an intrinsic band structure feature. The collected experimental and theoretical findings lead to the conclusion that the peak S located between the features C_1 and C_2 in Fig. 7.1**c** is not related to the bismuthene monolayer, but rather to the SiC substrate instead. Obvious candidates are the nitrogen donor level of the n-doped SiC substrate (doping concentration between $5 \times 10^{18}\,\mathrm{cm}^{-3}$ and $1 \times 10^{19}\,\mathrm{cm}^{-3}$) and/or localized SiC lattice defect states.

Comparison to quasi-particle band structure from GW calculations

So far, Sec. 2.2.2 has discussed the electronic band structure of bismuthene on SiC(0001) based on the DFT approach. However, DFT-based approaches are only designed to yield accurate total ground-state energies, but they are not devised for extracting single-particle

energies [52]. Typically they tend to underestimate electronic band gaps as for example measured by STS or PES and inverse PES experiments due to the well known problem of handling the derivative discontinuity in implementations of DFT [54,185–188] (cf. Appendix Sec. A.2 Eq. (A.9)). In order to calculate electronic quasi-particle spectra, a diagrammatic perturbation theory developed by Hedin [55, 184, 189–191], the so called *GW* method, has become a standard technique. It can cope with this problem by perturbatively calculating corrections to the self-energy (Σ) that result from removing or adding an electron from the ground state system. Within Hedin's approximation the electronic self-energy is given by $\Sigma = i\hbar GW$ [55, 184, 190], where G is the electron propagator of the interacting system, and $W(\mathbf{k}, \omega)$ the screened Coulomb interaction (cf. Appendix Sec. A.3). The self-energy takes into account all scattering processes, and thus the feedback to the added electron or hole as it interacts with its surrounding. This is essential, since clearly the added electron (or hole in the case of electron removal) interacts via the Coulomb interaction with the remaining electrons of the system and, therefore, driving it out of its ground state. Overall the *GW* approach has proved to be very successful in predicting electronic band gaps [192–194].

The calculation of the *GW* band structure for bismuthene starts from DFT single-particle eigenenergies and uses a single shot G_0W_0 approximation.[12] The thus calculated quasi-particle bands are shown in Fig. 7.1**d** as solid blue lines. First and foremost, they exhibit a substantially larger electronic band gap than the DFT band structure (red lines). Specifically, the quasi-particle band structure has an indirect electronic band gap between the VBM at K and the CBM at Γ of $E_{\text{ind}} = 0.97\,\text{eV}$, which is in excellent agreement with the experimental gap value from STS. The *GW* band structure accounts also for other features in the experimental data and are indicated by the dashed orange lines connecting Fig. 7.1**c** and Fig. 7.1**d**. For instance, the kink in the measured LDOS at approximately $-0.5\,\text{eV}$ (marked by V_2) matches closely with the maximum of the lower Rashba-split *GW* valence band. Likewise, the experimental kink feature C_2 agrees well with the K-point minimum of the *GW* conduction band. Finally, and as of immediate relevance for the optical transitions, the direct single-particle gap at the $K(K')$ valley amounts to $E_{\text{direct}} = 1.36\,\text{eV}$ in the *GW* calculation. This giant topological band-gap of bismuthene is opened by the sizable SOC and the orbital filtering from covalent bonding of Bi atoms to the substrate, as discussed in detail in Sec. 2 (cf. Ref. [9]).

7.2 Optical spectroscopy, optical gap and excitonic resonances

To date optical spectroscopy conducted on a 2D TI in the near infrared optical range have so far been hampered by the lack of materials with sufficiently wide band gap to allow coupling to high-energy photons. Bismuthene is ideally suited in this regard, due to its

[12] The DFT calculations were performed with the Quantum Espresso simulation package [195]. Here, norm-conserving pseudo-potentials were used to quantify the electron-ion interactions and the Perdew-Burke-Ernzerhof (PBE) functional [48] was used for the exchange-correlation potential. Spin-orbit coupling is included self-consistently. The structure that was simulated contained four Si-C bi-layers for the substrate and the bismuthene monolayer placed on top. The interactions with phonons were neglected here.

electronic band gap on the order of 1 eV, as discussed in the previous section. This chapter presents photo-modulated reflectivity (PR) measurements (see Sec. 3.4 for technical details) and thereby expands the electronic structure investigations of bismuthene to optical two-particle excitations. Before the discussion of the optical experiments in Sec. 7.2.2, the following first describes how a protection of the bismuthene film from oxidation has been achieved. It is crucial for the reliable interpretation of the optical measurements, since the PR setup offers no UHV conditions.

7.2.1 Protection of bismuthene against oxidation for optical experiments

It is known that bismuthene must be carefully isolated from ambient air and oxygen in general, because it is highly sensitive to oxidation (cf. XPS measurements in Appendix Sec. D.3). Concerning the growth and surface analysis of bismuthene, oxidation is excluded since at this stage the samples have never left UHV-conditions ($p \sim 5 \times 10^{-11}$ mbar to 5×10^{-10} mbar).[13] The PR setup that is used for optical spectroscopy (see Fig. 3.6), however, does not allow to keep bismuthene under UHV conditions anymore. Therefore, a protection from oxidation by other means needs to be realized for transferring the samples to the PR measurement setup. The following shows how this is achieved by keeping bismuthene under a protective inert gas atmosphere at atmospheric pressure anytime after the sample preparation and surface analysis experiments. It involves that the samples are transferred with a UHV suitcase ($p \approx 5 \times 10^{-10}$ mbar) into a glovebox filled with N_2 gas (< 0.1 ppm H_2O; < 0.1 ppm O_2). Then, the samples are sealed inside the glovebox into a CF-flange metal container. In this way the samples are enclosed in the inert gas atmosphere. Importantly, the CF-flange metal container is equipped with a window (alkali borosilicate, a.k.a. "kodial" glass) which is transparent in a suitable optical range for the optical spectroscopy measurements. The container is also small enough to be transferred into the PR setup.

The effect of the N_2 inert gas atmosphere on the electronic structure of bismuthene

ARPES and XPS measurements can elucidate if storing bismuthene in the N_2 inert gas atmosphere has a detrimental effect on its electronic structure. First, Fig. 7.2**a** shows an ARPES band map of an as-grown bismuthene film which never left the UHV conditions ($p \sim 5 \times 10^{-11}$ mbar to 5×10^{-10} mbar). The spectrum stems from photoelectrons of bismuthene in the vicinity of the K-point of the 1$^{\text{st}}$ BZ (cf. inset) and it shows the characteristic Rashba-split valence bands [6]. The corresponding GW quasi-particle band structure from Fig. 7.1**d** is depicted as green curves and is in excellent agreement with the measured dispersion. Figure 7.2**b** shows an APRES spectrum of a bismuthene sample that has been stored at atmospheric pressure in the N_2 inert gas atmosphere (< 0.1 ppm H_2O; < 0.1 ppm O_2)

[13] Bismuthene samples can be stored under these conditions in the used UHV chamber for weeks without substantial degradation.

for 90 min and subsequently transferred back to UHV. Prior to the ARPES measurement, a standard temperature annealing process (250 °C for 10 min) has been applied, which is known to leave the bismuthene film unchanged, but removes physisorbed adsorbates from the surface. Importantly, this treatment is not capable of reversing any chemisorption of oxygen, i.e., once the bismuthene has been oxidized it is not possible to recover intact bismuthene with a thermal treatment. Instead, in the case of oxidation the film is left with large defective areas as verified by STM (cf. Appendix Fig. D.3**b**). The ARPES spectrum in Fig. 7.2**b** reveals basically the same characteristic Rashba-split VB dispersion as the spectrum from the pristine bismuthene film in Fig. 7.2**a**. This demonstrates that even extended exposure to the N_2 inert gas atmosphere at atmospheric pressure does not deteriorate the electronic structure of a bismuthene monolayer. The van-der-Waals nature of the bismuthene surface is the reason for its inertness.

XPS measurements of a bismuthene sample grown under UHV conditions and subsequently stored in the N_2 inert gas atmosphere (< 0.1 ppm H_2O; < 0.1 ppm O_2) for 300 min before being transferred back into the UHV analysis chamber for recording the XPS spectra provide chemical information to complement the ARPES data. The reader is referred to Appendix Fig. D.2 for the full XPS survey. The key insight from Fig. 7.2**c** is that after the exposure to the protective atmosphere, the spin-orbit split Bi4f core levels exhibit no spectral contribution from oxidation states. Specifically, the core level spectrum contains only a single 4f-doublet, indicative of pristine, i.e., non-oxidized Bi[14]. For comparison, the XPS spectrum after exposure to ambient air for only 5 min in Fig. 7.2**d** already shows clear Bi oxidation which can be deduced from the dominating appearance of an additional 4f-doublet chemically shifted by ≈ 2.4 eV to higher binding energy with respect to the intrinsic Bi4f-doublet. This component is known to be a clear indicator for oxidized Bi. The full XPS survey of bismuthene exposed to air can be found in the Appendix Fig. D.3.

The ARPES and XPS measurements lead to the conclusion that bismuthene suffers no measurable oxidization if kept under the used inert gas atmosphere at atmospheric pressure. On the other hand only a short exposure to ambient air is sufficient to fully oxidize the Bi monolayer (BiO_x) and thus destroy the monolayer bismuthene. What is left to examine is, what effect the bismuthene oxidation has on the optical response. It is reasonable to assume that the PR spectra of an oxidized sample can no longer reflect the intrinsic optical response of the bismuthene film, because oxidation severely damages the monolayer, see Appendix Fig. D.3**b**. A direct comparison of PR measurements on a bismuthene sample kept in the inert gas atmosphere at atmospheric pressure inside the CF-flange sealed container and PR measurements on the same sample directly after exposure to ambient air tests this hypothesis explicitly, see Appendix Fig. F.2. Only minutes after opening the CF-flange sealed container filled with the inert gas atmosphere and thus exposing the bismuthene sample to ambient air triggers the rapid extinction of bismuthene's optical response. However, keeping the sample in the inert gas atmosphere at atmospheric pressure in the container preserves the optical

[14] c.f. Appendix Fig. D.1 for XPS on a pristine bismuthene sample that was always kept under UHV conditions.

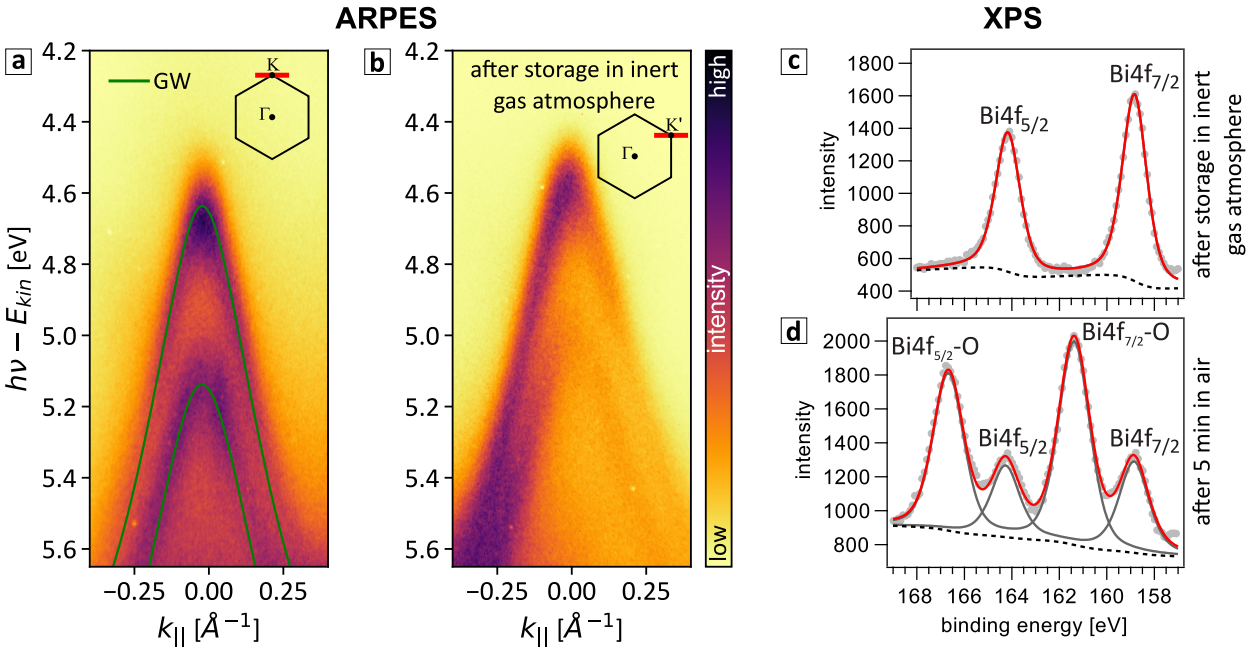

Figure 7.2: Protection of bismuthene by inert gas atmosphere. **(a),** ARPES spectrum ($h\nu = 21.2\,\text{eV}$ (He I α) and $T = 10\,\text{K}$) of the bismuthene valence band maximum at the K-point (see inset for the measured k-space path and its location relative to the Brillouin zone). The overlaid green curves represent the theoretical band structure from the GW calculation. **(b),** ARPES spectrum ($h\nu = 21.2\,\text{eV}$ (He I α) and T =RT) after storage of the bismuthene sample at atmospheric pressure in an N_2 inert gas atmosphere (< 0.1 ppm H_2O; < 0.1 ppm O_2) for 90 min and reinsertion into the UHV analysis chamber followed by a standard surface cleaning procedure for bismuthene samples by annealing at 250 °C for 10 min. **(c),** XPS spectrum (T = RT and Al K_α line) of the spin-orbit split Bi4f core levels. The spectra were measured after storage of the bismuthene sample at atmospheric pressure in an N_2 inert gas atmosphere (< 0.1 ppm H_2O; < 0.1 ppm O_2) for 300 min. Red lines: best fits to the data using a Shirley background (dashed line) and pseudo-Voigt profiles, see Appendix Fig. D.2 for details. No relevant contributions due to Bi oxidation are observed. **(d),** XPS spectrum (T = RT and Al K_α line) of the spin-orbit split Bi4f core levels. The spectra were measured after the bismuthene sample has been transferred into air for 5 min. Red lines: best fits to the data using a Shirley background (dashed line) and pseudo-Voigt profiles, see Appendix Fig. D.3 for details. Large contributions due to Bi oxidation are observed. *Figure reprinted and adapted from Ref. [124] under a Creative Commons Attribution 4.0 International (CC BY 4.0) License.*

response over weeks. Thus it is proved that the PR spectra from a bismuthene sample kept at atmospheric pressure under inert gas atmosphere indeed reflect the true optical response from an intact bismuthene monolayer.

7.2.2 Optical response of the bismuthene monolayer

The following covers PR measurements for the optical characterization of bismuthene. All measurements were performed at room-temperature and with the sample kept at atmospheric pressure under the N_2 inert gas atmosphere (< 0.1 ppm H_2O; < 0.1 ppm O_2) as presented above to prevent bismuthene from oxidation. For the spectral range of 0.9 µm–1.5 µm,

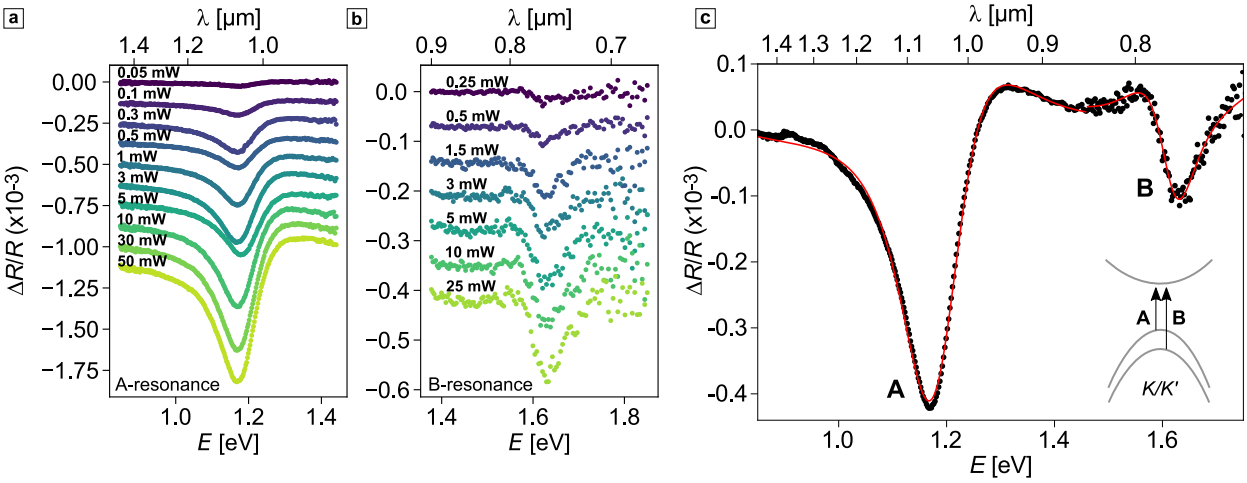

Figure 7.3: PR measurements on a bismuthene monolayer. (a), (b), Evolution of the A- and B-resonance with average pumping power, respectively. The photon source is a chopped continuous-wave neodymium-doped yttrium aluminum garnet laser emitting at 532 nm in **a** and a synchronously pulse pumped optical parametric oscillator emitting at 650 nm in **b**. **(c),** The combined fundamental excitation spectrum of bismuthene measured in the PR experiment ($T =$ RT, CW excitation, $E_{\text{laser}} \sim 2.33\,\text{eV}$, $P_{\text{ave}} \sim 0.5\,\text{mW}$). A and B are exciton-like PR features centred at $E_{\text{A}} \approx 1.19\,\text{eV}$ and $E_{\text{B}} \approx 1.63\,\text{eV}$, respectively. The solid red curve represents a numerical fit with the expression from Eq. 7.1. Inset: sketch of the fundamental exciton-like optical transitions at the K/K' points of bismuthene. *Figure reprinted and adapted from Ref. [124] under a Creative Commons Attribution 4.0 International (CC BY 4.0) License.*

an InGaAs photo-receiver was used. For covering the spectral range of 0.3 µm–1.0 µm, the detector was changed to a Si diode. The modulation in the spectral range of 0.9 µm–1.5 µm is provided by a continuous-wave neodymium-doped yttrium aluminum garnet laser emitting at 532 nm, and for the spectral range of 0.6 µm–0.9 µm by an optical parametric oscillator with an emission wavelength of 650 nm. In this way, Figs. 7.3**a, b** show power dependent PR spectra recorded at the highest quality bismuthene area, i.e., at 0 mm horizontal position according to Fig. 7.1**a**.

Most prominently, a PR resonance peak is observed in each spectrum in Figs. 7.3**a, b**. These peaks have an amplitude that increases monotonically with the average modulation power tuned over a few orders of magnitude. For now, the lower and higher energy peak are referred to as A- and B-peak, respectively. Figure 7.3**c** shows the total range spectrum recoreded with a moderate average modulation power of 0.5 mW. This spectrum is again fully dominated by the two distinct PR peaks A and B. The following quantitative line shape analysis uses the expression derived for exciton resonances in the PR spectrum (Sec. 3.4.2 Eq. (3.34)), i.e.:

$$\frac{\Delta R}{R} = \text{Re}\left(C_{\text{j}} e^{i\theta_{\text{j}}} (E - E_{\text{j}} + i\Gamma_{\text{j}})^{-2}\right) , \tag{7.1}$$

where C_{j} and θ_{j} are the resonance amplitude and phase, and where E_{j} and Γ_{j} are the energy and broadening parameters of the $j \in A, B$ optical transition, respectively. The fitting proce-

dure to the PR spectrum in Fig. 7.3**c** yields $E_A = (1.191 \pm 0.004)$ eV, $E_B = (1.625 \pm 0.004)$ eV, $\Gamma_A = (100 \pm 4)$ meV, and $\Gamma_B = (60 \pm 4)$ meV. It is worth noting that both the A- and B-transition show substantial spectral broadening, which can be attributed to effects arising from, e.g., sample inhomogeneity within the probed area and interaction between photo-excited electron-hole pairs and phonons in these room-temperature measurements [196,197].

In analogy to other 2D semiconducting materials, in particular TMDs [198], and by taking into account the aforementioned agreement between theoretical *GW* calculations and experiment concerning the single-particle properties, it appears reasonable already at this stage to assign the captured optical transitions to Coulomb-interacting electron-hole excitations in the vicinity of K and K' points of the Brillouin zone, see inset in Fig. 7.3**c**. Importantly, the *GW* method is only devised to take into account the many-body effects relevant for corrections to the self-energy of the single-particle excitations. This is suited to calculate for example the single-particle band gap (E_{gap}). However, the many-body effects contained in an optical excitation (and the optical gap E_{opt}) are of different nature, as the optical spectrum is additionally affected by the Coulomb coupling between electrons and holes simultaneously generated by the photo-excitation. This is essential for describing the optical response and lies at the very heart of exciton physics. To this end the absorption spectrum of bismuthene was directly calculated by A. Consiglio and D. Di Sante based on solving the Bethe-Salpeter equation that takes into account the electron-hole interaction. It will be presented in Sec. 7.2.3.

Variation of optical response with bismuthene film quality

The investigated sample (see Fig. 7.1) showed a high quality bismuthene film, i.e., a coherent crystal regime, around the center of the substrate strip on a mm range, and exhibited a more disordered regime at its edges. The following is an analysis of the effect of crystal film quality on the optical response of the sample and uses a comparison of spatially dependent PR measurements with the spatially dependent LEED characterization of the sample (see Fig. 7.1**a**).

Figure 7.4**a** is a schematic that visualizes the scanning along the vertical and horizontal direction performed for the following PR measurements. These now focus exclusively on the evolution of the A-peak as a function of the spatial position on the sample and are shown in Figs. 7.4**b, c**. Applying the same fitting procedure as before provides the transition energy E in Fig. 7.4**d**, broadening Γ in Fig. 7.4**e**, and the PR amplitude C in Fig. 7.4**f**. These parameters indeed vary only weakly along the 2 mm-long scanning line in horizontal and vertical direction around the center, which suggests a still fairly good quality of the bismuthene layer over a macroscopically large spatial extension. However, the layer quality deteriorates close to the bismuthene edges especially in horizontal direction, which is clearly reflected by the diminishing PR amplitude as well as the increased spectral broadening of the resonance peak. Independent of the detailed mechanism, the described correlation between PR signal of the A-peak and the local bismuthene film quality is a clear evidence that the

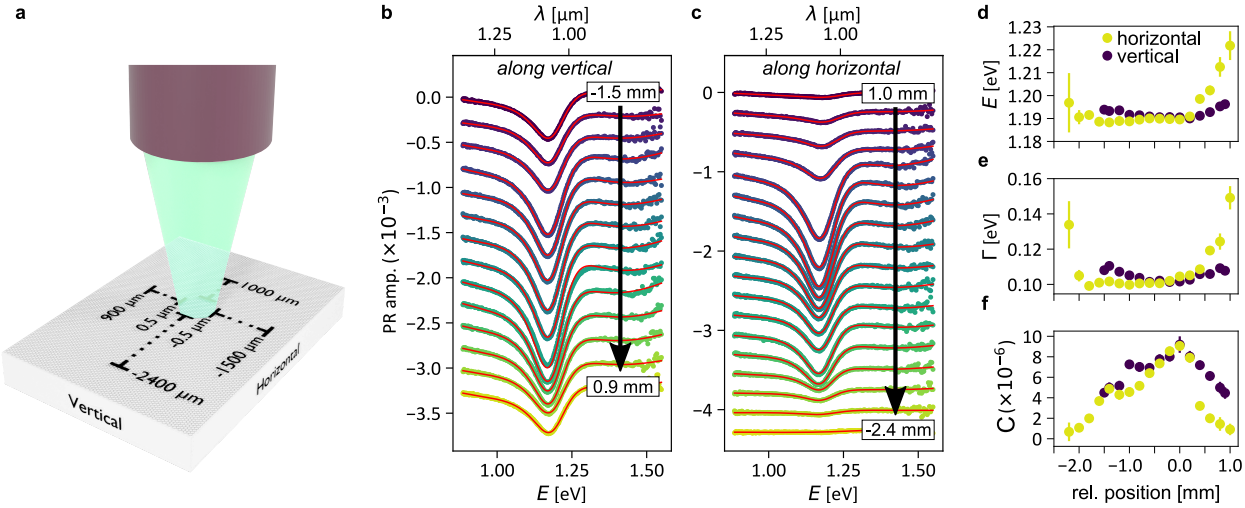

Figure 7.4: Spatial modulation of the optical response of bismuthene. **(a),** Sketch of the scanning movement along a vertical and horizontal line on bismuthene. **(b), (c),** Evolution of the PR resonance of the A-peak along the vertical and horizontal scanning line, respectively. Solid red lines represent the fitting curves (Eq. 7.1). **(d), (e), (f),** The energy, broadening, and PR amplitude of the A-transition, respectively. (Pulsed laser source, $E_{\text{laser}} \sim 1.65\,\text{eV}$, pump fluence: $\sim 1.67\,\text{mJ}\,\text{cm}^{-2}$). The PR amplitude in horizontal direction correlates well with the bismuthene sample quality (cf. Fig. 7.1a). *Figure reprinted and adapted from Ref. [124] under a Creative Commons Attribution 4.0 International (CC BY 4.0) License.*

optical response is indeed intrinsic to the pristine bismuthene monolayer.

7.2.3 Interpretation of the A- and B-peak in photo-reflectance as excitons based on Bethe-Salpeter equation calculations

Simulating absorption spectra involves calculating the imaginary part of the dielectric function ($\text{Im}(\epsilon)$) while taking into account electron-hole interactions. This was done by A. Consiglio and D. di Sante in a theoretical approach of solving the Bethe-Salpeter equation (cf. Appendix Sec. A.4) based on the aforementioned GW quasi-particle calculations and with the computational package YAMBO [199, 200]. The result is the absorption spectrum for bismuthene on SiC(0001) displayed as solid line in Fig. 7.5**a**. Most predominantly it features two sharp peaks (A and B), which stem from bound electron-hole pairs at discrete resonance energies, i.e., excitons.[15] The excitonic binding energy, i.e., the energy difference between the independent particle GW absorption gap E_{direct} (indicated by the arrow) and the energy position of exciton peak A yields $E_{\text{X}} \sim 0.15\,\text{eV}$. Moreover, the B-peak is shifted by an energy comparable to the Rashba splitting ($\approx 0.5\,\text{eV}$) of the valence states at the K and K' valleys. This results in a merging with the continuum of electron-hole excitations. Therefore, depending on coupling strength between the B related exciton and the continuum excitations, it might be more adequate to identify the absorption peak B with a Fano-type

[15] The reason for the smooth slope for $E \to 0\,\text{eV}$ is that a Lorentzian broadening of 0.1 eV was added to the discrete absorption peaks.

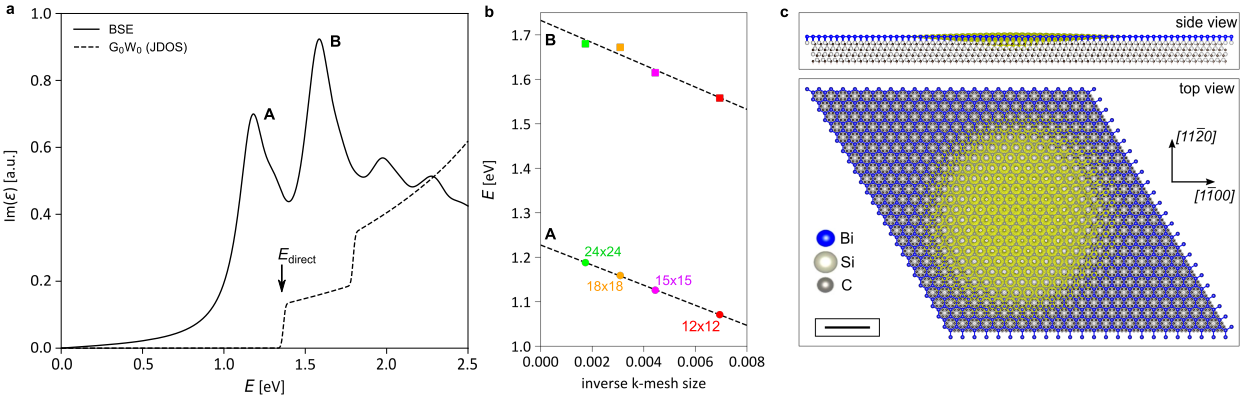

Figure 7.5: Ab-initio *GW*+BSE results. (a), The solid line displays the absorption spectrum of Bi/SiC inferred from the imaginary part of the dielectric function from the BSE calculation. The dashed line displays the joint density of states from the *GW* calculation, where the electron-hole interaction is neglected. **(b),** Convergence of the A and B exciton peaks, as a function of the inverse of the number of k-points. The intersection of the gray dashed line with the y-axis gives the result ideally obtained from an infinitely dense k-mesh. **(c),** Side and top views of the A exciton wave-function (yellow). The radius of the exciton is $\sim 3\,\mathrm{nm}$. The scale bar amounts to 2 nm. *Figure reprinted and adapted from Ref. [124] under a Creative Commons Attribution 4.0 International (CC BY 4.0) License.*

resonance.

Importantly, special care has been taken to assure a proper convergence of the calculation of $\mathrm{Im}(\epsilon)$ in Fig. 7.5**a**. In this context it was found that the position of the theoretical A and B peaks scales linearly as a function of the inverse number of k-points employed in the BSE calculation as seen from Fig. 7.5**b**. This observation allows to conduct an extrapolation towards $E_\mathrm{A} \approx 1.23\,\mathrm{eV}$ for an infinitely dense sampling. The extrapolated value is in excellent agreement with its measured value (1.19 eV). For exciton peak B, the extrapolation yields a theoretical value of $E_\mathrm{B} \approx 1.73\,\mathrm{eV}$, still satisfyingly close to the experimental result (1.63 eV).

Figure 7.5**c** presents the side and top view of the Wannier-Mott type excitonic wave-function connected to the A peak obtained from the calculations. The exciton radius of $\sim$3 nm extends over several lattice constants, resulting from the strong localization in reciprocal space around the K and K' valleys. This, in turn, requires a dense k-mesh to reduce the spurious Coulomb repulsion between periodic excitons, and explains the aforementioned convergence issue. Remarkably, Fig. 7.5**c** shows also how the exciton wave-function is not strictly localized inside the bismuthene monolayer, but rather extends for at least two atomic layers into the SiC substrate. This further evidences the pivotal role played by the substrate in bismuthene at the single- and two-particle levels: SiC is not only responsible for the orbital filtering mechanism and the huge topological gap [6,9], but also provides an important screening channel for the Coulomb interaction.

7.3 Discussion

The knowledge about the single-particle and two-particle electronic excitations of a material is of fundamental importance. Performing the first ever optical measurements on bismuthene greatly advanced the understanding of its two-particle electronic properties. The first step in order to be able to perform the PR experiments in the first place was to effectively protect bismuthene from oxidation, which was achieved by introducing it into an N_2 inert gas atmosphere at atmospheric pressure. As a consequence of enhanced electron-hole Coulomb interactions and reduced electrostatic screening in 2D, monolayer bismuthene still shows a clear optical response. The presented combined experimental and theoretical approach allows to draw the conclusion that the two prominent optical transitions ("A" and "B") are associated with excitonic transitions derived from the Rashba-split valence bands. Notably, the experimental excitonic resonance energies are well reproduced by many-body calculations in the GW+BSE framework also on a quantitative level [191, 201–204].

It must be emphasized that the many-particle response of bismuthene differs fundamentally from what is known from the vastly studied 2H-TMDs. First, whereas in the latter materials the low-energy interband transitions are captured by two decoupled so called *gapped chiral Dirac fermion* models [205, 206] with the same winding number in each valley (with opposite sign between K/K'-valley), in bismuthene, low-energy interband transitions are described by chiral models with different winding numbers in each valley. Therefore, in contrast to the strict valley-locked optical selection rules that govern 2H-TMDs, bismuthene could be sensitive to controlling the coupling to σ^+- and σ^--polarized light by reordering electronic bands with external electric and magnetic fields, as proposed in Refs. [207, 208]. The latter provides a possible technological advantage over TMDs for engineering electro-optical devices based on atomically thin materials. Second, in bismuthene the excitonic *and* the topological physics originate from the very same electronic states, i.e., they establish a direct link between excitonic physics and *global* topology, which has only been proposed theoretically so far (see, e.g., Ref. [209–215]). The presented findings may trigger a plethora of more experimental investigations in the future which could for example be related to the helical excitonic transport in topological edge modes [216], finding and assessing *global* topological properties of the QSH phase via optical band-to-band transitions and selection rules, topological polaritonics [217].

CHAPTER 8

Mapping the excited state gap and temporal dynamics of transiently occupied charge carriers in bismuthene

Parts of this chapter are the basis for a published research article [218]:
J. Maklar, R. Stühler, M. Dendzik, T. Pincelli, S. Dong, S. Beaulieu, A. Neef, G. Li, M. Wolf, R. Ernstorfer, R. Claessen, and L. Rettig, "Ultrafast Momentum-Resolved Hot Electron Dynamics in the Two-Dimensional Topological Insulator Bismuthene", *Nano Lett.* **22**, 5420 – 5426 (2022). DOI: 10.1021/acs.nanolett.2c01462

The theoretical band structure calculations that are shown and discussed in the following were performed by A. Consiglio and D. Di Sante. The trARPES measurements were performed together with J. Maklar, M. Dendzik, and L. Rettig.

Overview

Conventional ARPES (cf. Sec. 3.3) is a powerful technique to probe the occupied electronic structure, or more precisely, the one-particle removal spectral function, in momentum and energy space [85]. In order to reveal a more complete picture of the electronic structure of a material, it is mandatory to also map the electronic excitations between Fermi and vacuum level that are unoccupied in the ground state. This chapter covers experiments that leverage a pump-probe approach as an extension of conventional APRES to map transiently occupied excited electronic states of bismuthene with energy and momentum resolution. In addition, the femtosecond temporal pump-probe cross-correlation enables to trace the dynamic evolution of photo-ionization and subsequent relaxation of the electronic system. These ultra-fast time- and angle-resolved photoemission spectroscopy (trARPES) measurements are used to probe the excited state electronic band structure of bismuthene in Sec. 8.1. Then, Sec. 8.2 covers the effect of a time-dependent band-gap renormalization due to a modified excitation driven charge carrier screening. Moreover, Sec. 8.3 scrutinizes the ultra-fast relaxation pathway of excited charge carriers. Overall, the conducted trARPES experiments constitute a substantial contribution to the mapping of the complete electronic structure of bismuthene.

8.1 Excited state electronic structure mapping

So far, only few studies have demonstrated trAPRES with a monolayer material, due to the difficulties in preparing high quality samples that suit the demands for generating high enough count rates from excited state carriers. These exclusively include measurements

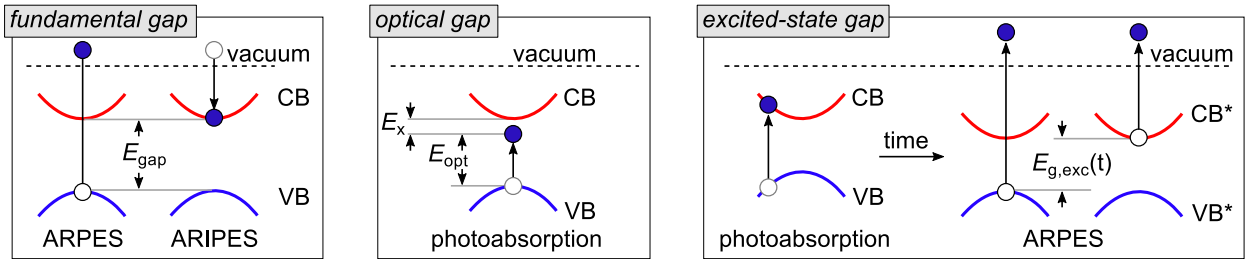

Figure 8.1: Pictorial illustration of the fundamental, optical, and excited state gaps of a direct gap semiconductor as measured by ARPES/ARIPES, optical spectroscopy, and trARPES, respectively. See main text for detailed description. *Figure reprinted and adapted from Ref. [231] under a Creative Commons Attribution 4.0 International (CC BY 4.0) License.*

performed with van-der-Waals materials like graphene [219], WSe_2 [220–222], WS_2 [223–225], MoS_2 [226–229], and a WSe_2/MoS_2 heterostructure [230]. The rapid evolution in this field is triggered by the expectation to observe emergent correlated electron phenomena in the excited state spectra, due to a general poor screening of Coulomb interactions in 2D semiconductors. Studying bismuthene with trARPES is additionally motivated by a hitherto experimentally unexplored physical aspect, namely resolving the transient charge carrier dynamics of a 2D TI in the presence of its metallic topological boundary states which have been proved by local STS measurements at film terminations [6,8], as well as at domain boundaries (here in the form of coupled helical edge states, cf. Ch. 6). Before addressing the temporal dynamics of the transiently occupied charge carrier population and discussing the role of the metallic topological edge states in Sec. 8.3, this section first maps the excited bulk conduction band states of bismuthene, which allows to directly probe a direct and indirect energy gap in the excited state band structure.

It is instructive to shortly review the conceptual determination of electronic band-gaps, and contrast the band-gap observed in trARPES, which is sometimes called the excited state band-gap $E_{g,exc}$ [231], with band-gaps determined by other experimental techniques along the illustration in Fig. 8.1.

The **fundamental band-gap** (E_{gap}) is the difference between the electron affinity and the ionization energy [54, 185, 232]. While the electron affinity is the energy involved in the one-particle excitation process of adding an electron to a system of N electrons, i.e., $|N\rangle \xrightarrow{+e^-} |N+1\rangle$, the ionization energy is the energy involved in the one-particle excitation process of removing an electron from the system, i.e., $|N\rangle \xrightarrow{-e^-} |N-1\rangle$. These quantities can be obtained by a combination of (angle-resolved) direct and inverse PES. In the latter, an electron is added to the system and therefore the one-electron-addition spectral function $A^+(k,E)$ is probed [233], complementary to the one-electron-removal spectral function $A^-(k,E)$ in the case of direct PES (cf. Sec. 3.3.1).

The **optical band-gap** (E_{opt}) is the energy that is required for an electronic transition by optical absorption. It involves a neutral two-particle excitation process $|N,0\rangle \xrightarrow{+h\nu} |N,S\rangle$ that conserves the number of electrons N and excites a Coulomb correlated electron-hole

pair $|S\rangle$ [234]. Typically, these excitonic resonances appear energetically below the energy onset of the single-particle CB states and are particularly strong in 2D materials. In Ch. 7, the optical band-gap E_{opt} of bismuthene was determined.

The **excited state band-gap** ($E_{\mathrm{g,exc}}$) measured in trARPES is a result of a two step process (cf. Ref. [231]). First, it involves a neutral optical excitation by the pump pulse in which photons with the energy of the pump pulse excite charge carriers above the direct band-gap of the material. Then a probe pulse follows that triggers the photo-ionization process.[16] It is important to bear in mind that the VB and CB states defined in the ground state of the material can be significantly re-normalized, as a significant amount of charge carriers is excited with the pump pulse which leads to Coulomb interactions of photo-electrons and photo-holes. Electronic states after photo-excitation are thus called excited state valence band (VB*) and excited state conduction band (CB*) states, respectively, which gives rise to the definition of the excited state band-gap ($E_{\mathrm{g,exc}}$) as the energy difference between CB* and VB* states.

Note that the simplistic depicted picture of the trARPES process in Fig. 8.1 does not account for momentum re-distribution of charge carriers by scattering processes to other valleys in k-space as would be present in the indirect band-gap semiconductor bismuthene. Moreover, in certain cases it is reasonable to make a phenomenological distinction for pump pulse excitations at energies well above vs. excitations at energies in-resonance with strongly bound electron-hole pair excitations. In the first case, the excitations can be thought of as an electron-hole plasma, where electrons and holes move in a dynamically screened "background". The dynamically screened self-energy can then be theoretically captured within Hedin's perturbative *GW* formalism if the density of excited charge carriers is not too large [55, 184, 190, 235]. In the second case, the formation of correlated electron-hole pairs (excitons) must be captured by an additional two-particle formalism within the so called Bethe-Salpeter equation [204, 236].

8.1.1 Excitation with $h\nu_{\mathrm{pump}} = 1.55\,\mathrm{eV}$

TrARPES measurements were performed with the setup described along Fig. 3.5 in Sec. 3.3.3. First, we examine the experiments using a pump-pulse with $h\nu_{\mathrm{pump}} = 1.55\,\mathrm{eV}$ (FWHM bandwidth of 80 meV [101]). Figure 8.2 summarizes the photoelectron intensity $I(E_{\mathrm{kin}}, k_{\mathrm{x}}, k_{\mathrm{y}}, \Delta t)$ as a function of photo-electron kinetic energy (E_{kin}), 2D in-plane momentum components (k_{x}, k_{y}), and pump-probe delay time (Δt) probed with a time-of-flight momentum microscope (*SPECS METIS 1000*). In Sec. 8.2, these measurements are complemented with trARPES using an hemispherical electron energy analyzer for a detailed quantitative analysis of the global excited state band-gap.

First, the constant energy maps at the time of optical excitation, i.e., $\Delta t = 0\,\mathrm{fs}$, across the full 1st and parts of the 2nd BZs of bismuthene are given in Fig. 8.2**a**. These maps are

[16] The temporal difference of pump- and probe-pulse defines the probing delay time Δt. The temporal resolution is given by the temporal cross-correlation of pump- and probe-pulse.

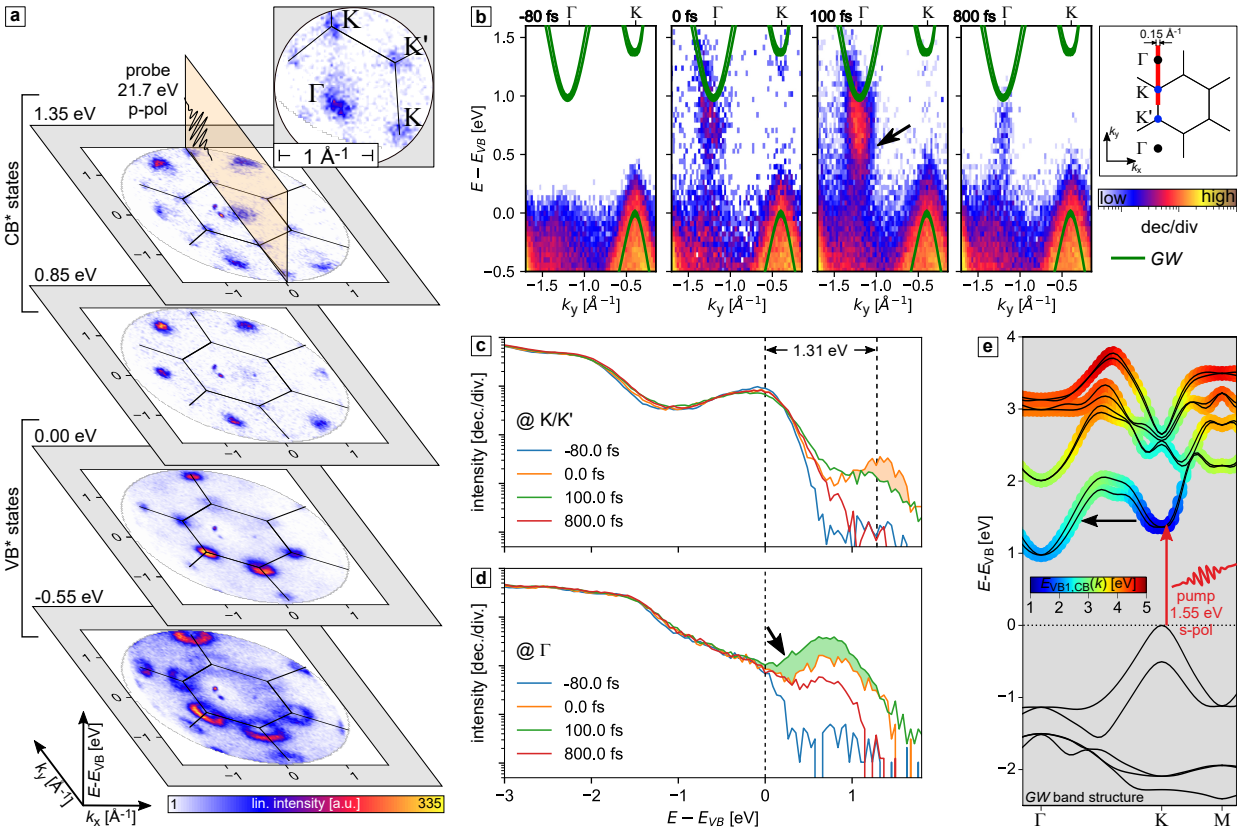

Figure 8.2: Mapping of the excited charge carriers in bismuthene with $h\nu_{\mathbf{pump}} = 1.55\,\mathrm{eV}$. **(a),** Constant energy 2D momentum space maps (p-polarized probe pulse incident 65° from surface normal, $h\nu_{\mathrm{probe}} = 21.7\,\mathrm{eV}$, $h\nu_{\mathrm{pump}} = 1.55\,\mathrm{eV}$, $T = \mathrm{RT}$) of the excited states across the 1st and 2nd BZs (indicated by black lines) of a planar bismuthene sample at delay time $\Delta t = (0 \pm 50)\,\mathrm{fs}$ and energies $E - E_{\mathrm{VB}} = (-0.55 \pm 0.05)\,\mathrm{eV}$, $E - E_{\mathrm{VB}} = (0.00 \pm 0.10)\,\mathrm{eV}$, $E - E_{\mathrm{VB}} = (0.85 \pm 0.10)\,\mathrm{eV}$, and $E - E_{\mathrm{VB}} = (1.35 \pm 0.30)\,\mathrm{eV}$. Upper right inset: Zoom-in into a 2nd BZ at $E - E_{\mathrm{VB}} = (1.35 \pm 0.30)\,\mathrm{eV}$. **(b),** trARPES maps at different delay times along the $\Gamma - K$ direction as indicated in the schematic of the surface BZ on the right. The spectra are from the same measurement as in **a**. The corresponding delay time is indicated above each image and is always an average over a ±50 fs delay time window. (cf. Appendix Fig. G.2 for trARPES maps plotted in a larger energy and momentum region.) **(c), (d),** EDCs at the K/K'-points (averaged over discs with radius $0.10\,\mathrm{Å}^{-1}$) and Γ-points (averaged over discs with radius $0.05\,\mathrm{Å}^{-1}$) in the 2nd BZs, respectively. The EDCs were extracted from the measurement in **a** at different delay times as indicated in the figure legend. The least-square fit to the orange spectrum in **c** is shown in Fig. G.1. **(e),** Black lines: *GW* band structure of bismuthene on SiC(0001). The color code corresponds to $E_{\mathrm{VB1,CB}}(k) = E_{GW,\mathrm{CB}}(k) - E_{GW,\mathrm{VB1}}(k)$, where $E_{GW,\mathrm{VB1}}$ is the topmost *GW* VB. $E_{\mathrm{VB1,CB}}(k)$ is the relevant quantity to indicate the possibility for photo-excitation across the band gap by a pump pulse. The only possible photo-excitation with $h\nu_{\mathrm{pump}} = 1.55\,\mathrm{eV}$ is a direct transition at the K/K'-points according to *GW* (red arrow). Photo-electrons may re-distribute to the Γ-valley by scattering events (black arrow).

plotted at discrete constant energies relative to the VB maximum (E_{VB}, determined before the pump-pulse) and with a time integration window of ±50 fs. While in the constant energy maps for $E - E_{\mathrm{VB}} \leq 0\,\mathrm{eV}$ only VB* states that are centered around the K/K'-points are observed (they are related to the VB states measured by conventional ARPES, see Fig. 7.2 and Ref. [6]), it can be seen that in the constant energy maps at $E - E_{\mathrm{VB}} \geq 0\,\mathrm{eV}$ the optical excitation has excited a considerable amount of charge carriers into the otherwise unoccupied conduction band states, i.e., the CB* states (note that the color scale is linear and is the same for all maps). Specifically, at $E - E_{\mathrm{VB}} = 0.85\,\mathrm{eV}$ excited charge carriers are almost exclusively observed at the Γ-points of the 2D BZ, but both at the Γ-points *and* the K/K'-points of the 2D BZ at $E - E_{\mathrm{VB}} = 1.35\,\mathrm{eV}$ [17]. Moreover, the photoemission intensity of CB* states is strongly asymmetric about the Γ-points for $E - E_{\mathrm{VB}} = 1.35\,\mathrm{eV}$. This effect is indicative of photoemission matrix elements which can be captured qualitatively within an ARPES simulation that only takes into account the measurement geometry and the bismuthene band structure in a tight-binding approximation presented in Appendix Sec. G.3. The following discusses the excited states around the K/K'- and Γ-points in more detail alongside Figs. 8.2**b, c**, and **d**.

Figure 8.2**b**, which depicts time-dependent band maps along a path in reciprocal space connecting the Γ- and K-points of the $(\sqrt{3}\times\sqrt{3})R30°$ 2D BZ of bismuthene (cf. schematic on the right side), together with Figs. 8.2**c, d**, which depict the time-dependent EDCs at the K/K'- and Γ-points, respectively, reveal that only VB states are occupied before photo-excitation, i.e., at $\Delta t = -80\,\mathrm{fs}$. Then, a strong photoemission intensity from CB* states around the Γ-point, and a weaker photoemission intensity from CB* states around the K-point appears at the pump-probe overlap, i.e., at $\Delta t = 0\,\mathrm{fs}$. Notably, the orange spectrum in Fig. 8.2**c** clearly indicates a pronounced photoemission peak at energy $E - E_{\mathrm{VB}} = 1.31\,\mathrm{eV}$ and at the $K(K')$-point (see Appendix Fig. G.1 for a least-square fit). The orange spectrum in Fig. 8.2**d** reveals yet another photoemission peak of the CB* states at the Γ-point at about $E - E_{\mathrm{VB}} \approx 0.85\,\mathrm{eV}$ which will be more precisely evaluated in Sec. 8.2. Importantly, however, this observation already proves that the *global* conduction band minimum of bismuthene indeed resides at the Γ-points, and that the *local* CB minima are located at the $K(K')$-points. This marks the first direct experimental verification that bismuthene is indeed an indirect semiconductor as anticipated by first-principles calculations [6].

At delay time $\Delta t = 100\,\mathrm{fs}$ the CB* photoemission intensity around the Γ-valley is further enhanced, while the CB* photoemission intensity around the K-valley decreases (see band map in Fig. 8.2**b** and green EDCs in Figs. 8.2**c, d**). Since this delay time is already considerable larger than the FWHM of 40 fs of the temporal pump-probe cross-correlation, the increase in intensity at the Γ-point can not be induced by further pump-pulse induced photo-excitation, but indicates that excited charge carriers must have relaxed from other

[17] The photoemission intensity from a small area ($\sqrt{k_{\mathrm{x}}^2 + k_{\mathrm{y}}^2} \approx \pm 0.5\,\mathrm{\AA}^{-1}$) which relates in this measurement to the region around Γ-point of the 1st BZ must be taken with caution, since the photoelectron detector is damaged in this specific area.

regions of the BZ to the CB* Γ-valley. In combination with the immediate decrease of intensity of the CB* states at K/K'-valleys, the increase of photoemission intensity at the CB* Γ-valley is attributed to the scattering of excited charge carriers at the CB* K-valley towards the CB* Γ-valley within a time scale of $\lesssim 100\,\mathrm{fs}$. Moreover, the CB* peak position has slightly moved to lower energies as seen from the comparison of the orange and green spectra in Fig. 8.2**d**. This behavior can be related to an energy gap re-normalization and will be studied in detail in Sec. 8.2.

Figure 8.2**b** compares the trARPES measurements with the *GW* band structure of bismuthene shown as green lines. The calculation of the *GW* band structure for bismuthene is the same as shown in Ch. 7. Calculations were performed by A. Consiglio and D. Di Sante using the Quantum Espresso simulation package [195] using norm-conserving pseudopotentials to quantify the electron-ion interactions and the PBE functional [48] for the exchange-correlation potential. Spin-orbit coupling is included self-consistently. The structure that was simulated contained four Si-C bi-layers as substrate and the bismuthene monolayer placed on top. The *GW* band structure in Fig. 8.2**b** has been aligned in energy to match the experimental VB onset (E_{VB}). An extended view of the *GW* quasi-particle band structure is also shown in Fig. 8.2**e**. On the one hand, the measured photoemission intensity of the CB* states at the Γ-valley minimum lies energetically below the *GW* bands at all probed delay times. On the other hand, the dispersion of the CB* states from the Γ-valley minimum towards more negative k_{y}-values fits very close to the *GW* bands. Whereas a re-normalization of excited bands in the trARPES measurements may account for a certain amount of this effect (which will be quantitatively studied in Sec. 8.2), another very surprising observation can be made. The photoemission intensity from the CB* states at the Γ-valley shows a strongly elongated shape marked by an arrow in Fig. 8.2**b**. It is readily apparent from the green EDC in Fig. 8.2**d** that this intensity extends from the CB* valley minimum at Γ to $E - E_{\mathrm{VB}} = 0\,\mathrm{eV}$ (marked by black arrow). This in-gap intensity clearly remains even after a large part of the CB* peak intensity at the Γ-point already decayed, see Fig. 8.2**b** at $\Delta t = 800\,\mathrm{fs}$. The *GW* calculations of 2D bulk bismuthene do not anticipate this in-gap intensity. The following considerations provide possible microscopic causes of the observed in-gap intensity.

① One source for an in-gap photoemission signal could be random impurities and lattice defects in bismuthene. However, such states result in a diffuse photoemission background. The observed confinement only to the momentum-region around the Γ-point thus rules out random impurities and defects as predominant origin.

② Local STS measurements proved the existence of metallic edge states at bismuthene film terminations (see Refs. [6, 8]) and they were identified with the topological boundary modes of the system. As these states are intrinsically metallic and quasi-1D, they contribute to an in-gap photoemission intensity around the Γ-point. However, since their density is very low in the case of bismuthene grown on a planar SiC sample (cf. Fig. 4.10**b**) it is unlikely that they can amount to a significant portion of the observed in-gap photoemission intensity.

③ Another microscopic source for an in-gap DOS in bismuthene is the metallic coupled topological states at domain boundaries (DBs) which Ch. 6 covered in detail. Domain boundaries consist of partially straight segments with varying lengths that meander with different orientations in a dense network across the bismuthene film. Thus, their density is considerably larger than the density of free edges found almost exclusively at SiC terrace steps. As the metallic DB states originate from the 1D topological edge states, but the length and the direction of the DB segments are distributed randomly, it is expected that these states give rise to an isotropic and gap-filling photoemission signal centered around the Γ-point. As a conclusion, the DB states are thus considered the most probable origin of the observed in-gap feature.

8.1.2 Excitation with $h\nu_{\mathrm{pump}} = 3.10\,\mathrm{eV}$

The pump-pulse with energy $h\nu_{\mathrm{pump}} = 1.55\,\mathrm{eV}$ used in the last section provided only enough energy to excite charge carriers in the direct vicinity of the K/K'-points. These charge carriers then scattered across the 2D BZ to finally accumulate at the global CB* minimum at the Γ-point. Here, the pump-pulse energy is increased to $h\nu_{\mathrm{pump}} = 3.10\,\mathrm{eV}$ to also access energetically higher lying CB* states. The energetic bandwidth of this higher energy pump pulse is not affected and its FWHM still remains at 80 meV [101]. Recording the excited state spectra now with an hemispherical electron energy analyzer (*SPECS Phoibos 150*) along paths in the 2D BZ that encounter high-symmetry points Γ, $K(K')$, and M provides better momentum resolution for these measurements, see Fig. 8.3**a**. This trARPES map was recorded at $\Delta t = 0\,\mathrm{fs}$ using an integration window of $\pm 50\,\mathrm{fs}$. The failure to reliably determine the VB onset for these spectra motivated the adaption of the experimental energy scale so that the minimum of the experimentally determined CB* states at the Γ-valley coincides with the onset of the calculated *GW* CB states at Γ (cf. Appendix Sec. G.4 and Fig. G.4**b** for EDC fits). The energy onset of the *GW* VB maximum at the K-point, i.e., $E_{GW,\mathrm{VB}}$, is set as zero reference energy.

The photoemission signal in Fig. 8.3**a** reveals clear band dispersions around the Γ-point, K-point, and M-point. While the dispersion of the measured CB* states at Γ matches very well with the *GW* quasi-particle bands (blue lines), the energetic position of the dispersive feature $S1$ around the M-point (marked with an arrow) deviates severely from the calculated quasi-particle energy. Notably, a "below-the-gap" photo-excitation condition holds around the M-point, which means that according to the *GW* bandstructure the pump photon energy would not be large enough to excite charge carriers at this area in momentum space, i.e., $E_{\mathrm{VB1,CB}}(k) > h\nu_{\mathrm{pump}}$ (see Fig. 8.3**c** and Tab. 8.1). In other words, the *GW* calculations imply the inability of direct optical VB → CB excitations around the M-point. This is, however, opposing the experimental outcome.

The quantitative analysis of the CB* states involves fitting the EDCs from the photoemission spectrum in Fig. 8.3**a**. Figure 8.3**b** depicts these EDCs on a logarithmic energy scale in the waterfall plot. Each EDC is E-binned over 150 meV and k-binned over $\pm 0.05\,\mathrm{\AA}^{-1}$ (cf. complementary evaluation of EDCs at certain momenta in Appendix Fig. 8.3). The red

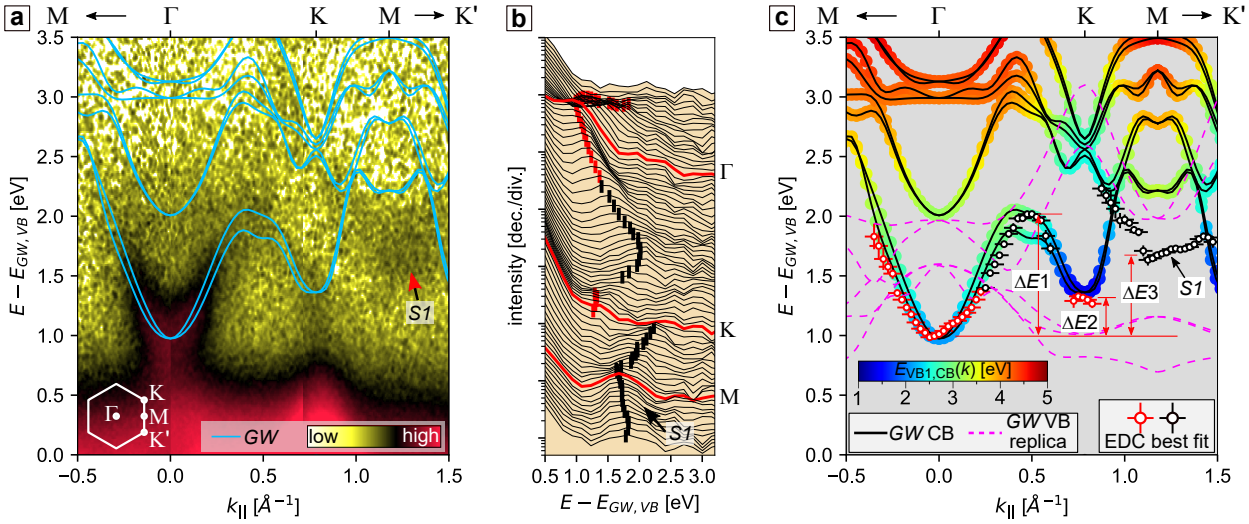

Figure 8.3: Mapping of the excited charge carriers in bismuthene with $h\nu_{\mathrm{pump}}$ = 3.10 eV. **(a),** Excited state trARPES map ($h\nu_{\mathrm{pump}} = 3.10\,\mathrm{eV}$, $h\nu_{\mathrm{probe}} = 21.7\,\mathrm{eV}$, T = RT, $\Delta t = (0 \pm 50)\,\mathrm{fs}$, $F = 0.03\,\mathrm{mJ\,cm^{-2}}$). Blue lines: *GW* quasi-particle conduction bands. The experimental energy scale was shifted such that the minimum of the CB* states at the Γ-valley matches the minimum of the *GW* quasi-particle band at the Γ-valley. The energy onset of the *GW* quasi-particle VB at the *K*-point ($E_{GW,\mathrm{VB}}$) is used as zero reference energy. **(b),** Logarithmic waterfall plot of EDCs from **a**. Each EDC is E-binned over $E_{\mathrm{bin}} = 150\,\mathrm{meV}$ (corresponds to 11 data points in **a**) and k-averaged over $\pm 0.05\,\mathrm{Å}^{-1}$. The red and black vertical line markers indicate the fitted peak positions in **c** (cf. Appendix Fig. G.4**b** for complementary EDCs). **(c),** The red and black data points are fitted peak positions to the EDCs in **b**. Red markers: a Gaussian tail + linear function for the background + a Gaussian peak for the dispersive CB* feature was used for the least-square fit. Black markers: a linear function for the background + a Gaussian peak for the dispersive CB* feature was used for the least-square fit. In all cases the error bars in energy correspond to the standard deviation obtained from the square-root of the estimated covariance in the least-square fit, and error bars in $k_{||}$ correspond to the k-averaging window used for the EDCs. The black lines indicate the *GW* conduction bands. They are colored according to $E_{\mathrm{VB1,CB}}(k) = E_{GW,\mathrm{CB}}(k) - E_{GW,\mathrm{VB1}}(k)$, where $E_{GW,\mathrm{VB1}}$ is the topmost *GW* VB, to indicate the possibility for photo-excitation with the pump pulse. Purple dashed lines: replica of *GW* quasi-particle valence band shifted in energy by $h\nu_{\mathrm{pump}} = 3.10\,\mathrm{eV}$. The values for $\Delta E1$, $\Delta E2$, $\Delta E3$ are listed in Tab. 8.1.

momentum k in Fig. 8.3	0 Å^{-1}	0.48 Å^{-1}	0.80 Å^{-1}	1.18 Å^{-1}
GW: $E - E_{GW,\mathrm{VB}}$	0.97 eV	1.82 eV; 2.02 eV	1.36 eV	2.22 eV
fit: $E - E_{GW,\mathrm{VB}}$	–	(2.02 ± 0.03) eV	(1.30 ± 0.02) eV	(1.67 ± 0.02) eV
GW: $E - E(k = 0\,\mathrm{Å}^{-1})$	–	$\Delta E1$: 0.85 eV ; 1.05 eV	$\Delta E2$: 0.39 eV	$\Delta E3$: 1.25 eV
fit: $E - E(k = 0\,\mathrm{Å}^{-1})$	–	$\Delta E1$: (1.05 ± 0.03) eV	$\Delta E2$: (0.33 ± 0.02) eV	$\Delta E3$: (0.70 ± 0.02) eV
GW: $E_{\mathrm{VB1,CB}}(k)$	2.11 eV	2.70 eV; 2.90 eV	1.36 eV	3.33 eV

Table 8.1: From top to bottom: *GW* quasi-particle energies; fitted peak positions; energy offset from the *GW* quasi-particle energy at $k = 0\,\mathrm{Å}^{-1}$ (cf. $\Delta E1$, $\Delta E2$, $\Delta E3$ in Fig. 8.3**c**), and $E_{\mathrm{VB1,CB}}(k) \equiv E_{GW,\mathrm{CB}}(k) - E_{GW,\mathrm{VB1}}(k)$, where $E_{GW,\mathrm{VB1}}$ is the topmost *GW* VB (cf. color code of *GW* bands in Fig. 8.3**c**). Errors are the square-root of the estimated covariance in the least-square fit.

and black vertical line markers in Fig. 8.3**b** are the fitted peak positions from least-square fits. Whereas, red markers indicate the use of a Gaussian tail in combination with a linear function for the background, black markers indicate that a linear function was used for the background. In both cases an additional Gaussian peak was used to fit the dispersive CB* feature.

Figure 8.3**c** compares these fitted peak positions (red and black colored dots) with the *GW* conduction band structure (black lines). The dispersion is in notably good agreement with the calculated band dispersion in a range of $\pm 0.35\,\text{Å}^{-1}$ around the Γ-point.[18] In addition, Fig. 8.3**c** includes three energy offsets from the CB* minimum ($\Delta E1$, $\Delta E2$, and $\Delta E3$) defined at three distinct momenta. Their corresponding numerical values are listed in Tab. 8.1. $\Delta E1$, defined at a momentum approximately half way between Γ- and K-point, is in very good correspondence with the quasi-particle energy of the second lowest CB from the *GW* calculations. $\Delta E2$, taken directly at the K-point, lies $(60 \pm 20)\,\text{meV}$ below the quasi-particle energy of the lowest lying *GW* band at the K-point. Lastly, $\Delta E3$ indicates a $(550 \pm 20)\,\text{meV}$ offset of the dispersive feature $S1$ from the lowest lying *GW* band at the M-point. This discrepancy is too large to be an artefact of the fitting procedure and, moreover, it is also clearly seen in the false color plot in Fig. 8.3**a**. Yet, another apparent discrepancy with the *GW* quasi-particle calculation is the fact that any direct photo-excitation across the band-gap at the M-point by a pump-pulse with energy $h\nu_{\text{pump}} = 3.10\,\text{eV}$ should be prohibited. This is encoded in the color code of the quasi-particle bands in Fig. 8.3**c** which indicates the quantity $E_{\text{VB1,CB}}(k) \equiv E_{GW,\text{CB}}(k) - E_{GW,\text{VB1}}(k)$, where $E_{GW,\text{VB1}}$ is the highest VB. The exact value at the M-point is listed in Tab. 8.1 and is $E_{\text{gap}}(k = 1.18\,\text{Å}^{-1}) = 3.33\,\text{eV}$, which is larger than the pump-pulse by 230 meV (i.e., ≈ 2.9 times the FWHM band-width of the pump-pulse).

The following provides possible explanations for the observed discrepancy of the presented measurements with the *GW* calculation, in particular for the feature $S1$ in the photoemission spectrum.

① **Photon-dressed bands:** A very short-lived signal at temporal pump-probe overlap and energies within the gap can be a sign of Floquet-Bloch states, a.k.a. "photon-dressed" bands, as a result of coherent interaction between the strong pump pulse light-field and the electronic system [237]. Such states can be observed in the photoemission spectrum as a replica of the VB shifted in energy by multiples of the pump pulse energy ($h\nu_{\text{pump}} = 3.10\,\text{eV}$) [237–239]. Figure 8.3**c** includes the *GW* VBs shifted accordingly in energy as purple dashed lines to visualize possible VB replicas. At the M-point, the VB replica closest in energy to the observed photoemission signal $S1$ appears at $E - E_{GW,\text{VB}} = 1.98\,\text{eV}$, and thus still 310 meV above $S1$, which renders this scenario rather unlikely.

② **Band re-normalization:** The observed discrepancy can be a result of a strong and, in

[18] A possible energy offset between fitted peak positions and *GW* band structure can not be excluded, since the energy onset of the experimental data at Γ was adapted to coincide with the band onset from the *GW* calculation.

particular, k-dependent re-normalization of the CB* states originating from strong Coulomb interactions between photo-electrons and photo-holes. This effect would be promoted by a large excited charge carrier density during the measurement, which is not taken into account in the GW calculations. Instead, it is known that the inclusion of large excited charge carrier densities is a challenge for realistic theoretical modelling of trARPES spectra [235].

③ **Excitons:** Another possibility is that $S1$ points to the formation of excitons in bismuthene. Several theoretical works have been devoted to the prediction of signatures of excitons in trARPES [240–246]. It can be summarized, that the signature of (direct) excitons in trARPES is the appearance of a band at an energy which lies about an amount of E_X above the VB. Here, E_X denotes the energy position of the (bright) exciton in the photo-absorption spectrum as inferred from optical spectroscopy. The dispersion of this exciton-derived band can appear in either of two ways (see Ref. [246]). In the case of a resonant photo-excitation by the pump pulse into the exciton state and subsequent photo-ionization by the probe pulse, the dispersion is expected to be a replica of the VB to which the left-over hole of the exciton belonged. In case of a non-resonant photo-excitation by the pump pulse and a subsequent exciton formation via photo-electron and photo-hole interaction, the probed dispersion is expected to be a replica of the CB to which the electron of the exciton belonged. In both cases, the dispersion can be additionally affected by electron-phonon scattering, but this effect is only relevant on much larger time scales of several hundreds of femtoseconds [246].

Only recently, have signs of excitons been observed in trARPES experiments performed with transition metal dichalcogenides. The 2D nature that leads to a weak Coulomb screening and the large electronic band gap are essential in rendering these materials optimal candidates in which strong excitonic effects are expected to be observed [221, 222, 225, 230, 239]. Specifically, peaks in the photoemission spectrum of a WSe_2 monolayer appeared at resonance energies of both direct and indirect excitons. Here, a giant exciton binding energy of $\approx 400\,\mathrm{meV}$ could be inferred [221, 222]. In the case of a WSe_2/MoS_2 heterostructure, the authors observed a photoemission intensity that was assigned to the electron that belonged to inter-layer excitons forming across the WSe_2/MoS_2 interface. The observed dispersion appeared as a replica of the VB of WSe_2 in accordance with the theoretical picture described above.

The fact that bismuthene is a monolayer material with poor Coulomb screening generally supports the possibility of large exciton binding energies. Therefore, it is not a-priori far-fetched to identify the large discrepancy of 550 meV, i.e., the energetic difference of the observed $S1$ feature and the energy position of the GW CB at the M-point (cf. Fig. 8.3 and Tab. 8.1), with an exciton binding energy. A possibility to clarify if the exciton scenario is indeed a valid explanation for our observations, explicit Bethe-Salpeter equation calculations that cover finite composite electron-hole momenta are needed but are not available at present. So far, the work presented in Ch. 7 only covered the observation of direct (i.e., K–K) excitons in bismuthene.

④ **Spurious effect from considering only four Si-C bi-layers as substrate in the *GW* calculation:** The *GW* band structure calculation for bismuthene on SiC(0001) was performed using four Si-C bi-layers as substrate and the bismuthene monolayer placed on top. The quasi-particle energies that are strongly related to the Si- and C-orbitals of the SiC substrate could be strongly affected by the circumstance that no quasi semi-infinite substrate is taken into account. Including more Si-C bi-layers in the *GW* calculations, however, would have been computationally too demanding and could not be afforded at this stage. However, the influence of the number of included Si-C bi-layers was tested based on DFT band structure calculations, see Appendix Sec. G.5. Projecting the weight of the Bi-, Si-, and C-atom orbital character onto the DFT band structure indicates that the lowest CB states around the M-point relate almost exclusively to the substrate atoms. Interestingly, the more Si-C bilayers are included in the calculation, the more these states shift to lower energies. Both aspects can be assumed to qualitatively also hold true for *GW* quasi-particle calculations. Therefore, it can not be excluded that the observed deviation of the feature $S1$ in trARPES and the *GW* band structure is a result of a spurious effect from considering only four Si-C bi-layers in the *GW* calculation.

8.2 Determination of the excited state band-gap

As outlined in the beginning of this chapter, trARPES probes the system under out-of-equilibrium conditions. Therefore, the trARPES photoemission intensity relates to excited state bands CB* and VB* and not to equilibrium quasi-particle bands CB and VB. In general, the deviation to the equilibrium spectral function largely depends on the amount of excited charge carriers [231,235]. In particular, an accompanying band-gap re-normalization has already been observed to be particularly strong in 2D materials [227, 228], since charge screening of excited charge carriers is strongly diminished as compared to 3D materials. The screening of the Coulomb interaction by excited carriers is the dynamical adaptation of the Coulomb force that the charge carriers "feel" due to the changed electrostatic environment caused by photo-excitation of charge carriers. This applies in particular to free charge carriers, i.e., electrons and holes that "move" independently from each other, but also to strongly bound charge carriers, i.e., electrons and holes that form strongly bond electron-hole complexes such as excitons. The bottom line consequence for deriving a value for the fundamental energy gap (E_{gap}) from trARPES is that special care has to be devoted to band gap re-normalization effects that can accompany trARPES experiments as a consequence of a considerable density of charge carriers being excited [226, 231]. The density of excited charge carriers is clearly changing with the delay time during a trARPES measurement (cf. Fig. 8.2). This motivates to trace the time evolution of the excited state gap ($E_{\mathrm{g,exc}}(t)$), which has been similary done for a TMD material in Ref. [226]. The objective here is to extrapolate or at least to infer a lower limit for the fundamental energy gap (E_{gap}) from the temporally evolving excited state band-gap ($E_{\mathrm{g,exc}}(t)$).

The trARPES spectra in Fig. 8.4 were recorded with an hemispherical electron energy analyzer (*SPECS Phoibos 150*) along a path in k-space connecting the Γ- and K-point in the

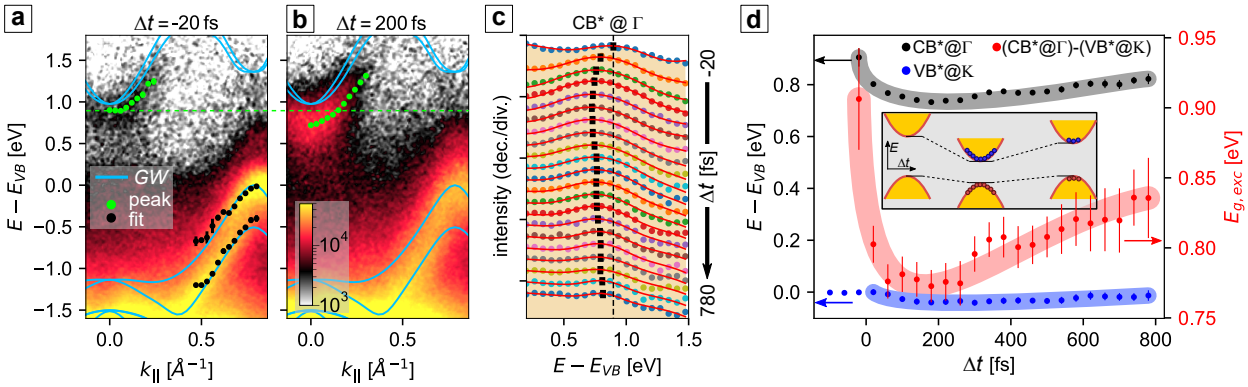

Figure 8.4: Time-resolved band gap renormalization. **(a), (b),** Energy- and momentum-resolved photoemission spectra ($h\nu_{\mathrm{pump}} = 1.55\,\mathrm{eV}$, incident fluence $F = 0.50\,\mathrm{mJ\,cm^{-2}}$, $T = \mathrm{RT}$) along Γ–K direction at two different delay times Δt (delay time averaging window of $\pm 40\,\mathrm{fs}$). The spectrum in a is set to trace the very onset of the pump-probe cross-correlation, where the pump pulse has already excited a low density of charge carriers. At the later delay time ($\Delta t = 200\,\mathrm{fs}$) in **b**, the photoemission intensity of the CB* Γ-valley states increased by a factor of ≈ 7, which points to an increased density of excited charge carriers. The black (green) dots in **a, b** correspond to peak positions for the VB*- (CB*-)states from best fits to EDCs (cf. Appendix Fig. G.6). Blue lines indicate *GW* bands. **(c),** Logarithmic waterfall plot of EDCs at $k_{\parallel} = 0\,\mathrm{Å}^{-1}$ showing the temporal evolution of the CB* minimum. Each EDC is E-binned over $E_{\mathrm{bin}} = 67\,\mathrm{meV}$ (corresponds to 5 data points in **a, b**), k-averaged over $\pm 0.04\,\mathrm{Å}^{-1}$, and Δt-averaged over $\pm 40\,\mathrm{fs}$. Red lines: least-square fits to EDCs. The fit function is a Gaussian tail + linear function for the background + Gaussian peak for the CB* state. Black markers: CB* (Gaussian) peak position from fits to the EDCs. **(d),** Left axis: Fitted VB* maxima (blue) and CB* minima (black) as a function of delay time Δt. The EDCs for fitting the VB* maximum and the CB* minimum were taken at momentum $k_{\parallel} = (0.815 \pm 0.035)\,\mathrm{Å}^{-1}$ and $k_{\parallel} = (0.00 \pm 0.40)\,\mathrm{Å}^{-1}$, respectively, and Δt-averaged over $\pm 40\,\mathrm{fs}$. Right axis: Excited state gap (red) obtained from the difference of VB* maxima (blue) and CB* minima (black). Error bars in energy correspond to the standard deviation obtained from the square-root of estimated covariance of the least-square fit. The black, blue, and red shaded bands are guides to the eye. Inset: Schematic of temporal evolution of the energy gap as a result of the temporal change of the screening environment due to excited hole (red circles) and electron (blue circles) carriers. The case of a direct band gap semiconductor is chosen for simplicity. The energy scale is set relative to the VB maximum (E_{VB}) in equilibrium conditions in all cases.

first 2D BZ of bismuthene. Figures 8.4**a, b** show the excited state spectrum at $\Delta t = -20\,\mathrm{fs}$ and at a later delay time $\Delta t = 200\,\mathrm{fs}$, respectively, and both are time averaged around $\pm 40\,\mathrm{fs}$. The delay time $\Delta t = -20\,\mathrm{fs}$ was chosen to infer the excited spectrum at the very onset of the pump-probe overlap, as the FWHM of the pump-probe cross-correlation is 40 fs [101]. The data points that are overlaid onto the false color plots mark peak positions from least-square fits to EDCs in the CB* Γ-valley (green dots), and in the VB* K-valley (black dots), see Appendix Fig. G.6 for the EDCs and fits. It can be seen that the Rashba splitting in the VB* states is nicely recovered by the fitted peak positions (black dots) and overall matches closely with the quasi-particle *GW* bands (blue lines). In turn, a comparison of Fig. 8.4**a**

with Fig. 8.4**b** reveals that the fitted peak positions of the CB* states at the Γ-valley change strongly as a function of delay time. While at $\Delta t = -20\,\mathrm{fs}$ the fitted minimum of CB* states is located $\approx 100\,\mathrm{meV}$ below the *GW* bands, it drops to lower energies at $\Delta t = 200\,\mathrm{fs}$, which is indicated by a green dashed line as guide to the eye. The change is also connected to a drastically increased CB* photoemission intensity from Fig. 8.4**a** to Fig. 8.4**b** which originates from a substantial increase of the excited charge carrier density.

This change can be traced even better in the time evolution of EDCs at $k_{\parallel} = 0\,\mathrm{\mathring{A}}^{-1}$ and at energies close to the CB* minimum depicted in the waterfall plot in Fig. 8.4**c**. The photoemission peak of the CB* minimum (black markers) first shifts to lower energies within the first $\approx 200\,\mathrm{fs}$, and then shifts to higher energies again at progressing delay times. Figure 8.4**d** summarizes this behavior. Here, black dots belong to the peak positions of the minimum of the CB* states at Γ from Fig. 8.4**c**. Blue dots belong to the fitted maximum of the VB* at *K* as a function of the delay time. The data points reach to 780 fs, since at later delay times the observed photoemission intensity of the excited charge carriers in the vicinity of the Γ point is too weak to be fitted reliably. The excited state gap ($E_{\mathrm{g,exc}}$) (red dots) is then calculated by subtracting the maximum of the VB* at *K* (blue dots) from the minimum of the CB* at Γ (black dots). After a fast initial drop from $E_{\mathrm{g,exc}} = (0.91 \pm 0.04)\,\mathrm{eV}$ at $\Delta t = -20\,\mathrm{fs}$ to $E_{\mathrm{g,exc}} \approx (0.77 \pm 0.01)\,\mathrm{eV}$ at $\Delta t = 180\,\mathrm{fs}$, the energy $E_{\mathrm{g,exc}}$ increases again for later delay times until it reaches $E_{\mathrm{g,exc}} = (0.84 \pm 0.03)\,\mathrm{eV}$ at $\Delta t = 780\,\mathrm{fs}$. The black, blue, and red shaded bands highlight this behavior and serve to guide the eye.

A possible explanation for the observed band gap shrinkage followed by a partial recovery to its initial value is band re-normalization as a function of temporally varying excited charge carrier density. The corresponding process is schematically depicted in the inset of Fig. 8.4**d**, which for simplicity, however, relates to the scenario of a direct band-gap. TrARPES experiments performed on the monolayer system MoS_2 made a similar observation. Accordingly, the authors of Ref. [226] reported on a dynamical band-gap reduction as a function of the delay time which amounts to nearly 400 meV only $\approx 200\,\mathrm{fs}$ after photo-excitation. Then the very-fast band-gap shrinkage gradually recovered to nearly the equilibrium value as the excited charge carriers relax over time. The authors concluded that the driving force behind the observed large band-gap re-normalization in the presence of excited charge carriers is sizable Coulomb interactions.

The presented investigations of bismuthene are therefore suited to extract a lower limit of the fundamental quasi-particle band gap (E_{gap}) by taking the initial value of the excited state gap, i.e., $E_{\mathrm{g,exc}} = (0.91 \pm 0.04)\,\mathrm{eV}$ at $\Delta t = -20\,\mathrm{fs}$. Moreover, they also indicate a sizable band-gap re-normalization on the order of $\Delta E_{\mathrm{g,exc}} = (0.14 \pm 0.04)\,\mathrm{eV}$.

8.3 Energy and momentum resolved relaxation of excited charge carriers

The following section analyzes the relaxation dynamics of excited charge carriers in bismuthene, contrasting the case of a planar sample with the case of a stepped sample. This

sample	valley	decay time τ [fs]	arrival time $t_{\max}$ [fs]	spectrum in Fig. 8.5**e**
planar	K	(139 ± 11) fs	(25 ± 10) fs	red
	Γ	(365 ± 7) fs	(72 ± 10) fs	green
stepped	K	(129 ± 8) fs	(24 ± 10) fs	yellow
	Γ	(301 ± 7) fs	(48 ± 10) fs	blue

Table 8.2: Best fit results of decay spectra in Fig. 8.5**e**. The errors for τ represent the square root of the estimated covariance from the least-square fit and the errors of $t_{\max}$ are given as the temporal resolution of the data.

aspect is particularly interesting with respect to the role of the metallic DOS found by STS measurements at bismuthene film terminations (cf. Refs. [6, 8]) and at domain boundaries (cf. Ch. 6), because the incorporation of metallic DOS in a semiconductor can strongly affect the lifetimes of excited charge carriers and facilitate efficient carrier relaxation process that are driven, e.g., by electron-electron and/or electron-phonon scattering. Specifically, the excited carrier dynamics is resolved using the energy-, momentum- and time-dependent trARPES maps that were recorded with a hemispherical electron energy analyzer along a path from bismuthene's Γ- to K-point in the 2D BZ. These maps enable to extract time-dependent traces of photoemission intensity at certain momenta and energies, i.e., $I(\Delta t)|_{k_\parallel,E}$, and to individually fit these with decay functions that are composed of a single-exponential convolved with a Gaussian. The parameters that characterize the decay function are thus the $1/e$ decay time τ [19], the delay time at which the photoemission intensity reaches its maximum (a.k.a "arrival time") $t_{\max}$, and the FWHM of the Gaussian. This way, momentum and energy resolved maps of the $1/e$ decay time, i.e., $\tau(k_\parallel, E)$, are obtained both for a bismuthene sample on a planar and on a stepped SiC substrate in Figs. 8.5**a, c**, respectively. In the same way, momentum and energy resolved maps of the arrival time, i.e., $t_{\max}(k_\parallel, E)$, are obtained for both a bismuthene sample on a planar and on a stepped SiC substrate in Figs. 8.5**b, d**, respectively. The validity of the fitting procedure can be explicit seen for the examples of fitted photoemission intensity time-traces in Fig. 8.5**e**. These show the photoemission intensity integrated over energy and momentum space regions in the vicinity of the CB* minima at the Γ- and K-point as indicated by dashed boxes in Figs. 8.5**a**–**d**. The close matching of the best fit function with the data in Fig. 8.5**e** underpins that a single-exponential is sufficient to describe the observed decay dynamics reasonably well. The following first considers the decay times of excited charge carriers for both planar and stepped sample, before the comparison of the arrival times follows afterwards.

[19] The extracted decay times (τ) of the excited charge carriers are not equal to single-particle lifetimes (τ_{SP}) derived from the self-energy and inferred, e.g., from conventional ARPES under equilibrium conditions ($\tau_{\mathrm{SP}}(\epsilon) = \hbar/(2\mathrm{Im}[\Sigma(\epsilon)])$ [85]. Yang et al. [247] showed that in the studied case of a cuprate superconductor at low temperatures and small excitations τ and τ_{SP} differed largely by a factor of $\sim 10 - 100$.

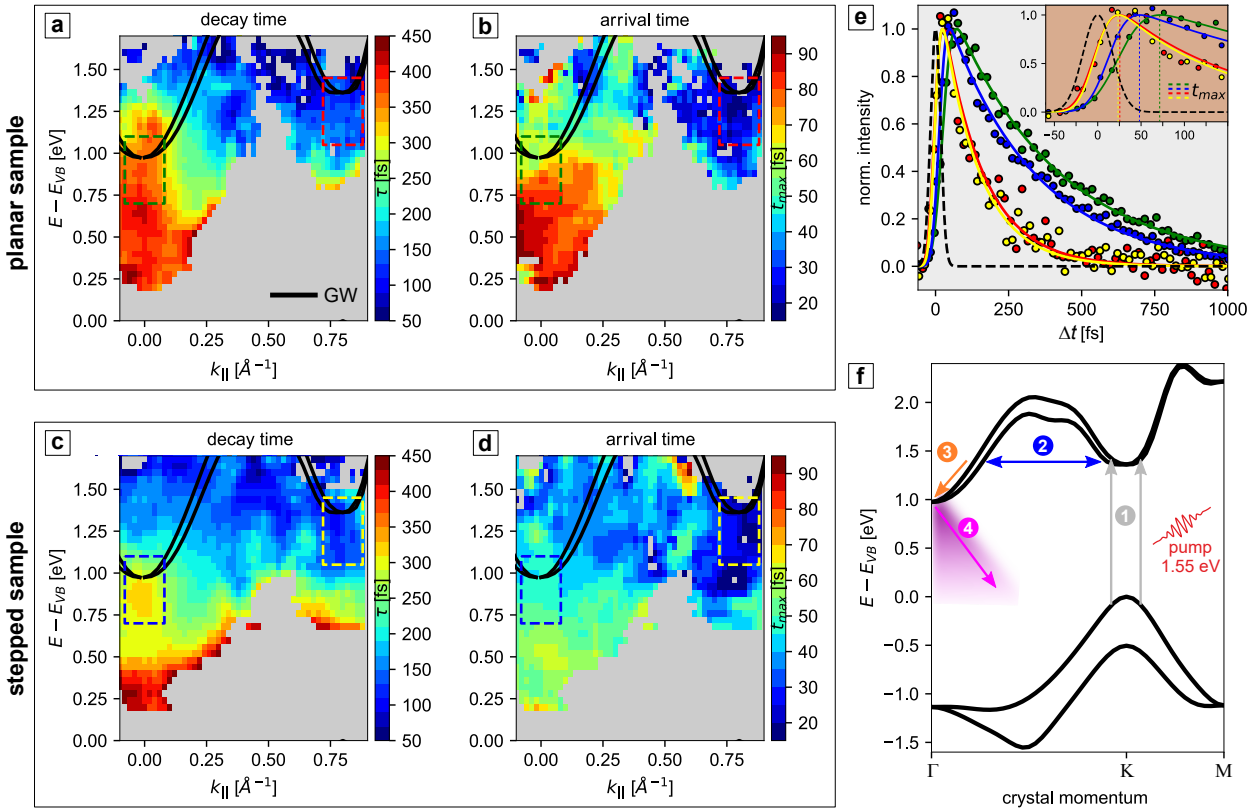

Figure 8.5: Excited charge carrier relaxation dynamics. **(a), (b),** Decay time ($1/e$ decay constant τ) and arrival time (temporal maximum $t_{\max}$) map, respectively, of the excited charge carriers measured on a *planar* bismuthene sample ($h\nu_{\text{pump}} = 1.55\,\text{eV}$, incident fluence $F = 0.52\,\text{mJ}\,\text{cm}^{-2}$, $T = \text{RT}$). The decay time (τ) in **a** was extracted from temporal decay fits with a single-exponential decay convolved with a Gaussian (see **e**) using sliding bin-wise energy and momentum integration windows of $\Delta E = 0.2\,\text{eV}$ and $\Delta k_{\parallel} = 0.1\,\text{Å}^{-1}$. Only fit results with a one standard deviation fit error $\sigma_\tau \leq 40\,\text{fs}$ are considered. The arrival time ($t_{\max}$) in **b** is extracted from the same fits as in **a**. The green and red dashed rectangles indicate averaging windows for the temporal decay fits explicitly shown in **e**. The black lines depict the *GW* band structure. **(c), (d),** Decay time ($1/e$ decay constant τ) and arrival time (temporal maximum $t_{\max}$) map, respectively, of the excited charge carriers measured on a *stepped* bismuthene sample ($h\nu_{\text{pump}} = 1.55\,\text{eV}$, incident fluence $F = 0.50\,\text{mJ}\,\text{cm}^{-2}$, $T = \text{RT}$). The decay time in **c** was extracted from temporal decay fits with a single-exponential decay convolved with a Gaussian (see **e**) using sliding bin-wise energy and momentum integration windows of $\Delta E = 0.2\,\text{eV}$ and $\Delta k_{\parallel} = 0.1\,\text{Å}^{-1}$. Only fit results with a maximum of one standard deviation fit error $\Delta\tau \leq 40\,\text{fs}$ are depicted. The arrival time ($t_{\max}$) in **d** is extracted from the same fits as in **c**. The blue and yellow dashed rectangles indicate averaging windows for the temporal decay fits explicitly shown in **e**. The black lines depict the *GW* band structure. **(e),** Excited state photoemission intensities as a function of delay time Δt. The spectra are averaged over the energy-momentum regions marked by the colored boxes in Figs. **a** – **d**. Solid lines are best fits to the data with a single-exponential decay convolved with a Gaussian from which the $1/e$ decay constant τ and the temporal intensity maximum $t_{\max}$ (arrival time) are extracted. The black dashed curve indicates the Gaussian temporal profile of the pump-pulse with a FWHM of 40 fs. The numerical values of τ and $t_{\max}$ of the best fit curves are given in Tab. 8.2. **(f),** Schematic of scattering pathway for excited charge carriers involving processes ①–④ described in the main text. The black lines depict the *GW* band structure.

8.3.1 Decay time: planar vs. stepped sample

Figures 8.5**a, c, e** and Tab. 8.2 provide the basis for a discussion of the decay times. The excited charge carriers at the CB* K-valley exhibit a significantly shorter decay time than excited charge carriers at the CB* Γ-valley for both the planar and stepped sample. This points to an inter-valley scattering of excited charge carriers from the CB* K-valley to the CB* Γ-valley at time scales of $\lesssim 100$ fs. For comparison, the studies of Refs. [221,248,249] on TMD materials have observed decay times on the same order of magnitude for the excited carrier redistribution across the BZ from local band minima to global band minima.

The excited charge carriers at the CB* minimum at Γ exhibit the longest decay times, with a 20% deviation between the decay time found for the stepped sample and the one for the planar sample. However, also these decay times found at the global CB minimum of bismuthene are very short (< 400 fs), wich is unexpected bearing in mind that bismuthene exhibits a large indirect fundamental band-gap ($E_{\mathrm{gap},GW} = 0.97$ eV from GW calculations). In fact, the relaxation in bismuthene happens one order of magnitude faster than in other monolayer wide band-gap semiconductors [221, 228, 249]. A likely explanation is that these short lifetimes in bismuthene are mediated by an in-gap DOS. Figure 8.2**b** indeed revealed such an in-gap DOS spectroscopically. In this context it was argued that the in-gap DOS originates from the metallic DOS at bismuthene domain boundaries. Thus, the short decay times could be an indication of the presence of the domain boundary states that facilitate a highly efficient carrier relaxation by electron-electron and/or electron-phonon scattering.

Another argument supports the latter assignment. The decay times of excited charge carriers are almost the same in the case of bismuthene grown on a planar SiC substrate and bismuthene grown on a stepped SiC substrate. The latter case, however, is characterized by having a much higher density of bismuthene film terminations at the SiC substrate steps. Specifically, the density of such states is larger by a factor of ≈ 13, because the amount of SiC substrate steps is large by the same factor (one step every 14 nm), see Fig. 4.2 and Appendix Fig. B.1. Accurately analyzing the bismuthene domain sizes of samples grown on planar SiC substrates, which is mainly limited by the dense network of the domain boundaries, revealed a median size of 23.5 nm (first quartile of 14.7 nm and third quartile of 33.7 nm), see Tab. 4.2 in Sec. 4.2.4. This means that bismuthene domains of films grown on the planar SiC substrate are characterized by a size on the *same* order of magnitude as bismuthene domains grown on the stepped SiC substrate. In the first case the domains are limited in size almost exclusively by domain boundaries, whereas in the latter case they are limited by domain boundaries and SiC step edges. This leads us to the conclusion, that the relaxation of excited state charge carriers is strongly facilitated by the quasi-metallic DOS observed at domain boundaries, as the decay times between both cases differs only slighly. However, any definite conclusion on the additional role of the metallic edge states at SiC substrate steps is difficult to draw at this point. Bismuthene films with significantly larger domain sizes need to be grown to clarify this question. Yet, also disentangling carrier relaxation on a quantitative level taking into account also competing processes that are expected to

be present in all bismuthene samples, such as non-radiative electron-hole recombination and carrier trapping at point-defects, is challenging and remains to be addressed in future experiments.

8.3.2 Arrival time: planar vs. stepped sample

The following concerns a discussion of the arrival times ($t_{\max}$) of excited charge carriers in conjunction with Figs. 8.5**b, d, e**. Again, the planar and stepped sample show very similar numerical values for $t_{\max}$. They have in common that $t_{\max}$ is smaller around the K-point than around the Γ point, which corresponds to a temporal order of the transient charge carrier population. Figure 8.5**f** summarizes the information from the momentum and energy resolved maps and sketches the charge carrier excitation and relaxation pathway. The individual steps indicated are connected to:

① The pump pulse with photon energy $h\nu_{\text{pump}} = 1.55\,\text{eV}$ excites charge carriers at $\Delta t = 0\,\text{fs}$ in an inter-band transition with $\Delta k \approx 0\,\text{Å}^{-1}$ at the K-point. This step is supported by the fact that a minimum of $t_{\max}$ is found at the CB* K-valley.

② Inter-valley scattering redistributes excited charge carriers from the CB* K-valley to the CB* Γ-valley and takes place on a timescale of $\lesssim 100\,\text{fs}$. This step is supported by the temporal order of $t_{\max}$ between excited charge carriers at the CB* K-valley and at the CB* Γ-valley. It is also supported by the decay times found at both valleys.

③ Charge carriers relax towards the minimum of the Γ-valley, which is also the global minimum of the CB* states, driven by electron-electron and electron-phonon scattering processes.

④ The excited charge carriers further relax via an in-gap DOS (diffuse purple background in Fig. 8.5**f**) at the Γ-valley. The measurements in Figure 8.2**b** actually resolved this DOS spectroscopically, and it could be argued that it originates largely from the metallic DOS at bismuthene domain boundaries.

8.4 Discussion

TrARPES was employed to access the transiently occupied excited electronic states in bismuthene and to resolve their dynamic relaxation. Thereby, the electronic structure characterization of bismuthene was extended to states between Fermi and vacuum level which are unoccupied in the ground state and have therefore not been accessible to previous studies that used conventional ARPES [6]. This work sets a benchmark for electronic structure investigations of 2D materials in general by combining trARPES, tunneling and optical spectroscopy measurements with ab-initio DFT, *GW* and BSE calculations which are all presented in this thesis.

The trARPES measurements presented in this chapter unambiguously verify for the first time that bismuthene is indeed an indirect semiconductor as predicted by first-principles calculations. The direct and indirect excited state band-gaps between K- and Γ-points in the 2D BZ of bismuthene were determined, i.e., $E_{\text{g,exc}}(K-K) = 1.31\,\text{eV}$ and $E_{\text{g,exc}}(K-\Gamma) =$

0.91 eV. These values are on the order of 0.1 eV smaller than the quasi-particle band-gaps calculated in the *GW* approach. A small, but finite excited charge carrier density induced band-gap renormalization effect could account for the observed deviations.

Moreover, the presented work described the observation of a band-gap renormalization of the indirect global gap as a function of pump-probe delay time and thus excited charge carrier density. The extracted value of renormalization amounts to $\Delta E_{\mathrm{g,exc}} = (0.14 \pm 0.04)\,\mathrm{eV}$ which is facilitated by a reduced Coulomb screening due to the 2D nature of the bismuthene monolayer.

In addition, a strong deviation was found between measured excited states and calculated quasi-particle states around the valley of the lowest unoccupied conduction band states at the M-point. So far, the origin of this observation can not be explained unambiguously, but we argue that it might point either to a band re-normalization that is particularly strong at the M-point, to the presence of excitons with a large binding energy, or to a spurious effect in the *GW* calculation which results from taking into account only four Si-C bi-layers as substrate in the computation. Future experiments that employ pump-pulses with a continuously varied energy should be used to shed light on the exciton scenario. In this case, a resonant pump-pulse energy could lead to the observation of a modified shape of the associated photoemission intensity. Moreover, *GW* calculations that take into account a larger unit cell by adding more Si-C bi-layers to the substrate might be indispensable in order to clarify the convergence of the substrate related quasi-particle of the lowest unoccupied conduction band states at the M-point.

Lastly, the presented work resolved the relaxation dynamics and pathway of excited charge carriers and found no drastic difference between bismuthene grown on a planar SiC substrate and bismuthene grown on a stepped SiC substrate. Both types of samples show the same exceptionally fast decay time τ. The short decay times can be explained by the presence of the in-gap DOS that facilitate carrier relaxation. Direct spectroscopic signatures of this in-gap DOS around the Γ point were identified and it was argued that it originates predominantly from the topological edge states coupled across domain boundaries in bismuthene. This assignment is substantiated by the observation that both types of bismuthene samples show qualitatively the same fast carrier decay time τ as the density of domain boundaries is by far the dominant size-limiting factor for the bismuthene films grown on planar SiC substrates.

CHAPTER 9

Conclusion

The specific objective of this work was to contribute to the fundamental research of bismuthene on SiC(0001), a recently discovered 2D TI. This material has attracted much attention because it shows one of the largest topological band gaps among all QSHIs synthesized to date. The presented thesis constitutes a step forward in promoting bismuthene with its superior material characteristics compared to other known 2D TI's for future applications that aim at leveraging a room-temperature QSHE. More specifically, this work advanced the material synthesis of bismuthene and could build a deeper understanding of its one-particle and two-particle electronic properties by applying spectroscopic techniques that go beyond previous works of Refs. [6–8]. In the following, a concluding summary of this work is given.

Optimization of bismuthene film epitaxy

Details about the formation of the bismuthene monolayer have been largely unknown before [7]. Here, bismuthene film growth was studied at different stages, which provided valuable insights into the early, intermediate, and late process of film formation. These studies enabled to understand how the main growth parameters influence bismuthene's film morphology. Eventually, an adapted growth recipe could be established that reached a considerably improved bismuthene film quality. This growth recipe sets the stage to reproducibly achieve bismuthene samples with near to complete surface coverage and domain sizes increased by a factor of $\approx 3.2 - 6.5$ compared to the previous work in Ref. [7].

Growth and spectroscopy of manganese- and cobalt-induced alloys on bismuthene

Motivated to study the interplay between topology and magnetism in the future, this work succeeded for the first time in preparing magnetic surface alloys in coexistence with bismuthene by deposition of magnetic transition metal adatoms, such as Mn and Co. Scanning tunneling microscopy experiments resolved the formation and structure of these novel surface alloys at the atomic scale. Local tunneling spectroscopy and photoemission spectroscopy experiments were employed to also reveal their electronic structure.

Atomically sharp and straight interfaces between pristine bismuthene and the Bi/Mn-alloy, as well as between bismuthene and the Bi/Co-alloy were identified by STM. Local STS experiments were performed which resolved a clear signature of an electronic state strictly localized to the interface between bismuthene and the Bi/Co-alloy. It was argued that this quasi-1D state might be connected to the topological boundary states of bismuthene, but

to resolve its detailed nature deserves further experimental and theoretical work. Overall, these interfaces provide a unique experimental setting for studying the impact of magnetism on the topological boundary states of bismuthene in the future.

Photoemission spectroscopy also resolved the intrinsic electronic band structure of both the Bi/Mn-alloy and the Bi/Co-alloy. In both cases, characteristic signatures of strong SOC were identified in the low-energy electronic states. Specifically, the Bi/Mn-alloy was characterized by a metallic band localized at the Γ-point which showed substantial band splitting. The band alignment and the characteristic splitting was in good correspondence with the linear Rashba model. The Rashba parameter and the effective mass could therefore be extracted from a model fit and yielded $\alpha_{\mathrm{R}} = 1.19\,\mathrm{eV\,\AA}$ and $m^* = 0.23 m_{\mathrm{e}}$, respectively. Moreover, hole-like bands at the K/K'-points were resolved. They were also characterized by a strong energy splitting of 0.19 eV.

The Bi/Co-alloy was on the one hand characterized by split bands crossing at the M-point, and on the other hand by large metallic electron pockets centered around the Γ-points. These electron pockets showed a pronounced resonant enhancement of photoemission intensity upon tuning the photon energy to the Co L_3 X-ray absorption edge in a ResPES experiment. The conclusion was drawn that these states are essentially connected to the Co-species in the alloy.

What is left for future studies is to identify the atomic structure models of the pristine Bi/Mn-alloy and Bi/Co-alloy. Especially, resolving the detailed magnetic properties of these materials is an important experimental task that could be accomplished, e.g., by X-ray magnetic circular dichroism, or spin-polarized STM measurements.

Coupling of topological edge states in 1D line defects of bismuthene

The structural and electronic properties of quasi-1D line defects in bismuthene, i.e., the domain boundaries, were scrutinized by STS and STM. With STS, QPI was observed within the DBs. Moreover, it was pointed out that the QPIs were reminiscent of Fabry-Pérot states characterized by a linear energy-momentum dispersion relation. Supported by a theoretical tight-binding model, this phenomenon could be explained by a direct coupling between spin-momentum locked edge states on either side of the DB. The Fabry-Pérot states are thus a direct consequence of the mutual edge coupling and the accompanying loss of the topological protection against single-particle back-scattering.

Two aspects gave rise to the assignment of the QPI to the formation of Fabry-Pérot states. The first is the linear energy-momentum dispersion relation, which is directly inherited from the linear dispersion relation of the helical edge states of bismuthene. The second is that a DB can be considered as a Fabry-Pérot resonator with reflective walls that have a reflection coefficient smaller than one. The latter could be experimentally observed with STS for the case of two coupled DBs. An effective model in terms of a double-well resonator could be provided.

The presented microscopic study of edge coupling in bismuthene on SiC(0001) encourages

future transport experiments in QSH insulators that are suitable for nano-lithography. Such experiments could leverage the strategy of lifting topological protection by the inter-edge hybridization of two pairs of edge states without the need to break time-reversal symmetry [29, 163–169]. The effect could be implemented in novel electronic device concepts, e.g., by using the on and off switching of the topological protection of the helical edge states for an on/off functionality in a 2D TI based field-effect transistor [180–182].

Optical spectroscopy of bismuthene and the detection of excitons

In a first crucial step to enable optical experiments with bismuthene, it was shown by ARPES and XPS that bismuthene can be effectively protected from oxidation by inserting it into an N_2 inert gas atmosphere. The protection of the monolayer samples was key to enable the optical photoreflectance measurements presented in this work.

In the PR experiments it was observed that the bismuthene monolayer exhibits two prominent optical transitions ("A" and "B"). The resonance energies of these transitions could be notably well reproduced on a quantitative level by many-body calculations in the GW+BSE framework. It allowed to conclude that these optical transitions are connected to excitons derived from the Rashba-split valence bands of bismuthene. Intriguingly, this establishes a direct link between excitonic physics and topology, since the excitonic *and* the topological physics originate from the very same electronic states.

Overall, the performed optical experiments greatly expanded the knowledge of bismuthene's electronic structure from the single-particle to the two-particle excitation level. They promote also a plethora of more experimental investigations in the future which could for example be related to the helical excitonic transport in topological edge modes [216], finding and assessing *global* topological properties of the QSH phase via optical band-to-band transitions and selection rules, topological polaritonics [217], and other exotic many-body quantum phases.

Mapping the excited state gap and temporal dynamics of transiently occupied charge carriers in bismuthene

Lastly, trARPES was successfully applied to access the transiently occupied excited electronic states in bismuthene and to resolve their dynamic relaxation. In this way, the electronic structure characterization of bismuthene was extended to states between Fermi and vacuum level which are unoccupied in the ground state and therefore not accessible to conventional ARPES.

The presented momentum resolved pump-probe band structure mappings unambiguously verified for the first time that bismuthene is indeed an indirect semiconductor as predicted by first-principles calculations [6]. Values for the direct and indirect excited state bandgaps were explicitely determined. Whereas the direct energy gap between states at the K/K'-points amounts to $E_{\mathrm{g,exc}}(K-K) = 1.31\,\mathrm{eV}$, the indirect energy gap between valence band states at the Γ-point and conduction band states at the K/K'-point amounts to

$E_{\mathrm{g,exc}}(K-\Gamma) = 0.91\,\mathrm{eV}$. These gaps are $50-60\,\mathrm{meV}$ smaller than the quasi-particle band-gaps calculated within the *GW* approach, which could be explained by a modified charge carrier screening in the presence of excited charge carriers. Moreover, a dynamic band-gap renormalization of the indirect global gap as a function of pump-probe delay time could be resolved. The maximum of the gap renormalization amounts to $\Delta E_{\mathrm{g,exc}} = (0.14 \pm 0.04)\,\mathrm{eV}$. This substantial effect is promoted by bismuthene's monolayer thickness and a reduced Coulomb screening in 2D.

Moreover, one excited state feature located around the M-point valley of the lowest conduction band states was observed that did not match the quasi-particle states calculated in the *GW* approximation. Three possible scenarios were discussed. It was argued that it could either point to a particularly strong band re-normalization at the M-point, to the presence of excitons with a large binding energy, or to a spurious effect in the *GW* calculation as a result of taking into account only four Si-C bi-layers as substrate. Future experiments employing pump-pulses with a continuously varied energy could be used to shed light on the exciton scenario. In this case, a resonant pump-pulse energy would be expected to lead to the observation of a modified shape of the associated photoemission intensity. Moreover, *GW* calculations that take into account more Si-C bi-layers in the substrate are regarded indispensable.

Lastly, the relaxation dynamics and pathway of excited charge carriers in bismuthene could be resolved for the first time. The exceptionally fast decay times observed for a bismuthene film grown on a planar SiC substrate and a bismuthene film grown on a stepped SiC substrate could be explained by the presence of an in-gap DOS that facilitates carrier relaxation. This in-gap DOS around the Γ-point was predominantly attributed to the metallic DB states in bismuthene.

Part III

Appendix

APPENDIX A

Theoretical concepts for describing condensed matter

Within a fundamental quantum mechanical description of a condensed matter system one has to deal with the motion of $\sim 10^{23} - 10^{24}$ electrons per cm^3 and a similar amount of nuclei. In principle, a fundamental set of differential equations govern all the dynamics of this incredibly complex system. They are given in form of a Schrödinger equation for which relativistic corrections are taken into account perturbatively (in orders of the ratio between electron velocity and the speed of light). However, there is a wide disparity between just knowing these fundamental set of equations for the condensed matter system and the ability to start from those laws and reconstruct the empirical observations. Oftentimes unforeseen effects emerge as a consequence of electronic interactions and correlations, i.e., the collection of those effects which are a result of the interaction of the electrons with each other [250].

The following provides a brief overview of the theoretical concepts typically used to approach the many-body problem of condensed matter, which cannot simply be done by using brute force computational power. This overview is given, because many of these techniques are used throughout this thesis to explain the presented experimental findings. These include in particular density functional theory, many-body perturbation theory and the *GW* approach, and the Bethe-Salpeter equation.

A.1 The many-body Hamiltonian

Non-relativistic limit. – A first and immense simplification of the condensed matter problem is to assume that the N electrons move in the static potential of the N_n-nuclei with charge Z_l that sit at fixed positions $\{\mathbf{R}_l\}$ (Born-Oppenheimer approximation). Omitting relativistic corrections for a moment, the Hamiltonian of the system can be given as [53]

$$\mathcal{H}_0 = \sum_{j=1}^{N} \Bigg\{ \frac{(-i\hbar\nabla_{\mathbf{x_j}})^2}{2m_\mathrm{e}} \underbrace{- \sum_{l=1}^{N_\mathrm{n}} Z_l \frac{e^2}{4\pi\epsilon_0 \left|\mathbf{x}_j - \mathbf{R}_l\right|}}_{\equiv V_\mathrm{n}(\mathbf{x}_j)} \Bigg\} + \underbrace{\frac{1}{2} \sum_{\substack{i,j=1 \\ i\neq j}}^{N} \frac{e^2}{4\pi\epsilon_0 \left|\mathbf{x}_i - \mathbf{x}_j\right|}}_{\equiv V_\text{e-e}(\mathbf{x}_i - \mathbf{x}_j)} \ , \tag{A.1}$$

where $\mathbf{x}_i$ is the position of the i-th electron. The stationary solution of the many-body problem obeys the Schrödinger equation

$$\mathcal{H}_0 \Psi^N = E_\Psi^N \Psi^N \ , \tag{A.2}$$

where Ψ^N is the N-electron wave function, and E_Ψ^N is the total energy of the system. In Eq. (A.1) no spin-dependent interactions enter and for many materials with light elements, $\mathcal{H}_0$ includes all the dominant interactions, such as the potential energy of the j-th electron in the Coulomb field of the nuclei $V_\mathrm{n}(\mathbf{x}_j)$ and the inter-electron Coulomb interaction $V_\text{e-e}(\mathbf{x}_i -$

$\mathbf{x}_j$).

The spin-orbit interaction. – A crucial ingredient for the correct description of materials containing heavy elements like bismuthene on SiC(0001), however, is the inclusion of the *spin-orbit coupling* (SOC) as an additional term ($\mathcal{H}_{\mathrm{SOC}}$) to the Hamiltonian. The SOC arises in the relativistic description of electrons and can formally be included into the description of condensed matter by performing a systematic expansion of the Dirac equation [251, 252] in orders of $1/(m_{\mathrm{e}}c^2)$. Oftentimes it is sufficient to only include the lowest order relativistic corrections [53]. The SOC contribution to the Hamiltonian is then given as [53]

$$\mathcal{H}_{\mathrm{SOC}} = -\frac{1}{2(m_{\mathrm{e}}c)^2}\sum_{j=1}^{N}\mathbf{s}_j\cdot\left\{\nabla_{\mathbf{x}}\left[V_{\mathrm{n}}(\mathbf{x})+\underbrace{\sum_{\substack{k=1\\k\neq j}}^{N}\frac{e^2}{4\pi\epsilon_0\left|\mathbf{x}-\mathbf{x}_k\right|}}_{\equiv -e\varphi(\mathbf{x})}\right]_{\mathbf{x}=\mathbf{x}_j}\times(-i\hbar\nabla_{\mathbf{x}_j})\right\}, \tag{A.3}$$

where $\mathbf{s}_i = \frac{\hbar}{2}\vec{\sigma}$ ($\vec{\sigma}$ being the vector of Pauli matrices) is the spin variable of the i-th electron.

A further simplification of Eq. (A.3) is reached within a mean field description of the Coulomb interaction, i.e., $V(\mathbf{x}) \approx V_{\mathrm{n}}(\mathbf{x}) - e\langle\varphi(\mathbf{x})\rangle$, where $\langle\varphi(\mathbf{x})\rangle$ is a mean field of $\varphi(\mathbf{x})$. Additionally one can approximate $V(\mathbf{x})$ by spherically symmetric potentials $\tilde{V}(r)$ centered at the position of the nuclei, motivated by the fact that the gradient term $\nabla_{\mathbf{x}}V_{\mathrm{n}}(\mathbf{x})$ in Eq. (A.3) leads to the SOC being stronger towards the center positions of the nuclei. With these simplifications one arrives at [53]

$$\mathcal{H}_{\mathrm{SOC}} \approx -\frac{1}{2(m_{\mathrm{e}}c)^2}\sum_{j=1}^{N}\sum_{l=1}^{N_{\mathrm{n}}}\frac{1}{r}\frac{d}{dr}\tilde{V}(r)\Big|_{r=|\mathbf{x}_j-\mathbf{R}_l|}\mathbf{s}_j\cdot\mathbf{l}_{jl}\ , \tag{A.4}$$

where $\mathbf{l}_{jl} \equiv (\mathbf{x}_j - \mathbf{R}_l)\times(-i\hbar\nabla_{\mathbf{x}_j})$ is the orbital momentum operator of the j-th electron. Within this approximation one can see that the energy correction due to SOC scales strongly with atomic number. For a wave function that takes the form of an atomic orbital near the nucleus $\langle\mathbf{r}^{-3}\rangle \propto Z_l^3$ [253] holds and Eq. (A.4) leads to an energy correction scaling with $\sim Z_l^4$. Here, emphasize is on the SOC interaction, because it is a crucial ingredient of the many-body Hamiltonian of bismuthene on SiC(0001) and ultimately the motivation behind studying this material, as it drives the large topological band gap.

A.2 Concepts of density functional theory

Solving the inhomogeneous electron gas problem of Eq. (A.1) is a formidable problem, due to the Coulomb mediated electron-electron interaction. The following provides an overview of the basic ideas of density functional theory (DFT) for calculating the ground state properties of a many-body system and roughly follows the description given in Ref. [53]. The interested reader is also devised to more specific literature such as Ref. [254]. In the above given literature it is also described how the spin-degrees of freedom, and in particular relativistic

corrections are included in DFT. For simplicity, the following description is limited to the Kohn-Sham scheme of DFT without the explicit inclusion of the electron spin.

The Hohenberg-Kohn theorems

The Hohenberg-Kohn theorems proved that despite the presence of the many-body interactions, the ground-state expectation value $\langle\cdot\rangle_0$ of any observable $\hat{O}$ is a functional of the local ground state electronic density $n(\mathbf{x})$, i.e., $\langle\Psi_0[n]|\,\hat{O}\,|\Psi_0[n]\rangle = O[n(\mathbf{x})]$, where $|\Psi_0\rangle$ is the ground-state wavefunction. Moreover, it proved that the ground state energy can be determined by varying the density n in order to minimize $E_0 = E_{V_\mathrm{n}}[n] = \langle\Psi_0[n]|\,\mathcal{H}_0\,|\Psi_0[n]\rangle$, where the parametric dependence on the Coulomb potential generated from the nuclei V_n is made explicit. Focusing on the electron density $n(\mathbf{x})$ instead of the many-body wave-function $|\Psi_0\rangle$ is much more convenient, since it is only a function of three coordinates.

An inverse map $\mathcal{D}^{-1} : n \to |\Psi_0\rangle$ exists, which in principle allows to retrieve the N-particle ground state wave function. The Hohenberg-Kohn theorems are the foundation of DFT, which in principle could provide an *exact* solution for the ground-state $|\Psi_0\rangle$ of the interacting many-body problem. To get to this solution one simply has to solve a variational problem for the scalar valued density n self-consistently in order to minimize $E_{V_\mathrm{n}}[n]$ given by

$$E_{V_\mathrm{n}}[n] = \langle\Psi_0[n]|\,\hat{T} + \hat{U}\,|\Psi_0[n]\rangle + \int d^3\mathbf{x} V_\mathrm{n}(\mathbf{x}) n(\mathbf{x}) \;, \tag{A.5}$$

where $\hat{T}$ accounts for the kinetic energy and $\hat{U}$ for the Coulomb mediated electron-electron interaction in Eq. (A.1), which is typically written as a sum of the Hartree and the exchange-correlation potentials.

The Kohn-Sham scheme

In practice DFT is approached by the so called *Kohn-Sham* scheme which motivates to solve the variational problem for a non-interacting auxiliary system with an effective external potential, such that the non-interacting system has the same ground-state density as the real interacting system. In the Kohn-Sham approach the functional equation is therefore replaced by another functional equation

$$E_\mathrm{KS}[n] = T_\mathrm{KS}[n] + \int d^3\mathbf{x} V_\mathrm{ext}(\mathbf{x}) n(\mathbf{x}) + E_\mathrm{H}[n] + E_\mathrm{XC}[n] \;. \tag{A.6}$$

The exchange correlation functional is not explicitly known. Therefore, it is replaced by an approximation in the form of a functional of the density as $E_\mathrm{XC}[n] = \int d^3\,\mathbf{x} n(\mathbf{x})\,\epsilon_\mathrm{XC}(\mathbf{x};[n])$. This has led to many implementations of the Kohn-Sham approach to DFT which use different forms of approximations of the exchange-correlation functional. The most prominent ones are the *local density approximation* (LDA) and the *generalized gradient approximation* (GGA). These can work especially well if the electronic density is homogeneous, e.g., in the case of metals.

The Kohn-Sham energy eigenvalues & the derivative discontinuity

In any given implementation of DFT (within the above Kohn-Sham scheme), the ground state density is found by a variational approach to Eq. (A.6). Then a Schrödinger-like eigenvalue problem

$$\left[-\frac{\hbar^2}{2m_\mathrm{e}}\Delta_\mathbf{x} + V_\mathrm{n}(\mathbf{x}) + V_\mathrm{H}(\mathbf{x}) + \frac{\delta E_\mathrm{XC}[n]}{\delta n(\mathbf{x})}\right]\varphi_\lambda(\mathbf{x}) = \epsilon_\lambda\varphi_\lambda(\mathbf{x}) \ , \tag{A.7}$$

can be solved to obtain the single-particle orbitals $\varphi_\lambda(\mathbf{x})$ (which define the electron density by $n = \sum|\varphi_\lambda(\mathbf{x})|^2$) and the so called Kohn-Sham eigenvalues ϵ_λ. In practice, the Kohn-Sham energy eigenvalues ϵ_λ are Lagrangian multipliers with no physical meaning (except the energy of the highest occupied Kohn-Sham state, which can be shown to correspond to the negative ionization energy of the interacting electron system). On the one hand, it is often times found that the dispersion of the Kohn-Sham energy eigenvalues is in good agreement with measured quasi-particle band structures, e.g., from ARPES. On the other hand, it is also found that the band gap of semiconductors and insulators given by

$$E_\mathrm{gap} = I_N - A_N = (E_{N-1} - E_N) - (E_N - E_{N+1}) \ , \tag{A.8}$$

(N is the electron number, I the ionization energy, and A the electron affinity) is systematically underestimated when identified with the corresponding DFT Kohn-Sham energy gap $E_\mathrm{gap}^\mathrm{KS}$. This discrepancy originates from the so called derivative discontinuity term [54, 185–188]. It arises in the evaluation of the exchange-correlation term in Eq. (A.7) when the particle number N is approached from positive and negative sides. It therefore accounts for the mismatch of the experimental and Kohn-Sham band gap given by

$$E_\mathrm{gap} = E_\mathrm{gap}^\mathrm{KS} + \lim_{\epsilon\to 0^+}\left\{\left.\frac{\delta E_\mathrm{XC}[n]}{\delta n(\mathbf{x})}\right|_{N+\epsilon} - \left.\frac{\delta E_\mathrm{XC}[n]}{\delta n(\mathbf{x})}\right|_{N-\epsilon}\right\} \ , \tag{A.9}$$

which can be on the order of $\sim$ eV. In order to reduce this mismatch, it is common practice to introduce implementations of the exchange-correlations functional based on empirical observation. A noteworthy example is the HSE06 hybrid functional [49, 50], for which the discrepancy between E_gap and $E_\mathrm{gap}^\mathrm{KS}$ is typically reduced.

A.3 Concepts of many-body perturbation theory

An experiment can not probe the exact ground state of a material. All the presented experiments involve the excitation of the electronic system, which consequently drives it out of its ground state. For example, in an ARPES experiment an electron is removed from the N-electron system by the photoelectric effect. The left-over system of $N-1$ electrons adapts to the accompanied change of the electromagnetic environment mediated by the electron-electron Coulomb interaction. The theoretically adequate method of dealing with such excitations is in terms of a field theoretical description. In this way one can formulate

quantum mechanical expectation values in the form of statistical correlation functions, so called Green's functions. The expectation value for the "process" of removing an electron with spin s at time t and space point $\mathbf{x}$ from the ensemble of electrons in the system, and adding an electron with spin s' at time t' and space point $\mathbf{x}'$ to the ensemble of electrons, i.e., a *hole* propagation, is given by the lesser Green's function

$$G^{<}_{ss'}(\mathbf{x}t,\mathbf{x}'t') = -\frac{1}{i\hbar}\left\langle \Psi^{\dagger}_{s'}(\mathbf{x}',t')\Psi_{s}(\mathbf{x},t)\right\rangle \ . \tag{A.10}$$

Here, $\Psi_s(\mathbf{x},t)$ ($\Psi^{\dagger}_s(\mathbf{x},t)$) is the field operator related to the probability to annihilate (create) an electron with spin s at a space point $\mathbf{x}$ at time t. If the system is in thermal equilibrium than $G^{<}_{ss'}(\mathbf{x}t,\mathbf{x}'t') = G^{<}_{ss'}(\mathbf{x}\mathbf{x}',t-t')$ holds. A similar quantity can be defined for an electron propagation, i.e., $G^{>}_{ss'}(\mathbf{x}\mathbf{x}',t-t')$, and both can be unified within a time-ordered single-particle Green's function: $G_{ss'}(\mathbf{x}\mathbf{x}',t-t')$. Importantly, also two-particle Green's functions can be defined in an analogous way and are formally written as $G_{s_1s_2,s'_1s'_2}(\mathbf{x}_1t_1\mathbf{x}_2t_2,\mathbf{x}'_1t'_1\mathbf{x}'_2t'_2) \equiv G_{s_1s_2,s'_1s'_2}(12,1'2')$. They relate to expectation values containing two creation and two annihilation operators.

The power of the Green's function approach lies in the possibility to describe the excitations in a many-particle system of electrons as an effective one-particle problem by defining the *self-energy* $\tilde{\Sigma}$ by

$$\sum_{s_2}\int d2\,\tilde{\Sigma}_{s1s2}(12)\,G_{s_2s'_1}(21') = -i\hbar\sum_{s_2}\int d2\,V_{\text{e-e}}(\mathbf{x}_1-\mathbf{x}_2)\,G_{s_1s_2,s'_1s_2}(12,1'2^{t+i0^+}) \ . \tag{A.11}$$

For details of the derivation the reader is referred to Refs. [53, 255]. The self-energy $\tilde{\Sigma} = \Sigma^{\text{H}} + \Sigma$ incorporates the Hartree part (Σ^{H}) and the exchange-correlation part (Σ) of the electron-electron interaction. It leads to single-particle excitations that are characterized by a finite life-time. These give thus rise to the notion of *quasi-particles* [53, 255].

Importantly, all many-body effects are encoded into the self-energy. The explicit calculation is still very cumbersome, as it demands to solve the corresponding Dyson equation of motion of the Green's function self-consistently [53], i.e.

$$G_{s_1s'_1}(11') = G^{\text{H}}_{s_1s'_1}(11') + \sum_{s_2,s_3}\int d2\int d3\,G^{\text{H}}_{s_1s_2}(12)\Sigma_{s_2s_3}(12)G_{s_3s'_1}(31') \ , \tag{A.12}$$

where G^{H} is the Green's function within the Hartree approximation.

An established approach developed by Hedin [55, 184, 189–191] is to write the electronic self-energy by $\Sigma = i\hbar GW$, where W is the screened Coulomb potential, which can be formally written as

$$W(11') = \int d2 V_{\text{e-e}}(1-2)\epsilon^{-1}(1'2) \ , \tag{A.13}$$

with the inverse dielectric function ϵ^{-1}. The screened Coulomb potential (W) takes into

account the adjusted electron-electron interaction as a result of the shielding of the excess charge by surrounding charge carriers. It can be computed for example in the Random Phase Approximation. Therefore, the *GW* approach is explicitly devised to model charged single-particle excitations, as for example measured by STS or PES and inverse PES experiments, contrary to DFT-type approaches. In practice, the calculation of G and W is done in iterative steps. Many times the so called *one-shot* approach, i.e., terminating the iterative process after the first step to obtain G_0 and W_0, has proved to be very successful in predicting electronic band gaps [191–194]. It is a well-established procedure to start from the Kohn-Sham energy eigenvalues and wave functions (cf. Eq. (A.7)) to accelerate numerical convergence of the *GW* calculations.

Importantly, the Green's function G is connected to the spectral function A by the formal expression $A = -(1/\pi)\,\mathrm{Im}\,G$ (see e.g., Mahan [255]). In turn, the spectral function A provides a foundation for the mathematical description of the measured quantities in a photoemission (e.g., ARPES) or tunneling (e.g., STM/STS) experiment. At this point it is instructive to discuss the simple case of a non-interacting particle system for which the Green's functions and the spectral function reduce to [53, 255]

$$G_{\text{non. int}}(\mathbf{k},\omega) = \frac{1}{\omega - E(\mathbf{k}) - i0^+} \tag{A.14}$$

$$A_{\text{non. int}}(\mathbf{k},\omega) = \delta(\omega - E(\mathbf{k}))\ . \tag{A.15}$$

Here, $E(\mathbf{k})$ are the eigenenergy solutions to the non-interacting N-particle Hamiltonian. The Fourier transform of the non-interacting Green's function with respect to ω is given as $G_{\text{non. int}}(\mathbf{k},t) = e^{iE(\mathbf{k})t}$ and is thus a plane wave that does not decay as a function of time. Therefore, non-interacting particles are characterized by showing a δ-function as resonance energy and do not decay as a function of time.

On the other hand, the quasi-particle self-energy is non-zero ($\Sigma \neq 0$), if interactions between electrons are non-vanishing. In this case, the Green's functions and the spectral function take the form [53, 255]

$$G_{\text{int}}(\mathbf{k},\omega) = \frac{1}{\omega - E(\mathbf{k}) - \Sigma(\omega)} \tag{A.16}$$

$$A_{\text{int}}(\mathbf{k},\omega) = -\frac{1}{\pi}\frac{\mathrm{Im}\,\Sigma(\omega)}{\left[\omega - E(\mathbf{k}) - \mathrm{Re}\,\Sigma(\omega)\right]^2 + \mathrm{Im}\,\Sigma(\omega)^2}\ . \tag{A.17}$$

Consequently, the imaginary part of the self-energy $\mathrm{Im}\Sigma$ acts as a damping term for the amplitude of the Fourier transform of G, i.e., it decays over time and has a quasi-particle lifetime $\propto [\mathrm{Im}\Sigma(\omega)]^{-1}$. Moreover, the resonance energy of the quasi-particle excitation has a Breit-Wigner lineshape with a FWHM of $2\,\mathrm{Im}\Sigma(\omega)$ centered at an energy $E(\mathbf{k}) + \mathrm{Re}\Sigma(\omega)$.

A.4 The Bethe-Salpeter equation

The Green's function and spectral function given by Eqs. (A.16) and (A.17) yield the solution to the problem of creating a charged single-particle excitation in an interacting many-particle electron system. However, in the process of optical absorption (which will also be performed in this thesis) a hole-like quasi-particle and an electron-like quasi-particle are created. This situation thus corresponds to a neutral two-particle excitation in which the electron-like and hole-like quasi-particles interact with each other by Coulomb interactions. It is conceptually important to bear in mind that this Coulomb interaction is dynamically screened by the presence of the electron-like and hole-like quasi-particles themselves. This is the origin for the computational complexity of the problem. A very crude approximation is to consider this excitation as a condensed-matter analogue of a hydrogen atom with adapted effective hole and electron masses and a mean field Coulomb interaction [256,257]. This simplified picture can already lead to qualitatively correct predictions. However, in order to calculate actual two-particle corrections for a correct quantitative computation of the spectral function, a so-called *Bethe-Salpeter equation* (BSE) must be solved on top of Hedin's *GW* approach [201, 202, 204, 236].

In order to derive the optical excitation spectrum including electron-hole interactions, the BSE is solved for the electron-hole amplitude [201, 202, 204]:

$$(E_{c\mathbf{k}} - E_{v\mathbf{k}})A_{vc\mathbf{k}} + \Sigma_{v'c'\mathbf{k}'}\langle vc\mathbf{k}|K_{eh}|v'c'\mathbf{k}'\rangle A_{v'c'\mathbf{k}'} = \Omega A_{vc\mathbf{k}}\,, \tag{A.18}$$

where the electronic excitations are given in the basis of electron-hole pairs with quasi-particle energies $E_{v\mathbf{k}}$ and $E_{c\mathbf{k}}$ in the valence and conduction bands. The $A_{vc\mathbf{k}}$ are the coefficients of the excitons in the electron-hole basis and Ω are the eigen-energies. The kernel K_{eh} accounts for the screened Coulomb interaction between electrons and holes, and the exchange interaction, including also local field effects which are due to the optical excitations of the periodically arranged atomic orbitals, e.g., in bismuthene on SiC(0001) [258].

It is well established to follow a consecutive scheme for these kinds of calculations. Specifically, this means that the following computations are conducted one after another according to [204, 236] $DFT \rightarrow GW \rightarrow BSE$, whereby the subsequent computation relies on the outcome of the preceding one. Such calculations have proven to be in good agreement with experiments of optical absorption and, particularly, in predicting exciton binding energies in semiconductors [236]. In recent years, such analyses have especially been very successfully applied also to topologically trivial 2D materials in which the Coulomb interactions among electrons are only poorly screened due to dimensionality [197, 259–264].

The effect of excitons for the absorption of light

The optical absorption can only be correctly interpreted, if the effects of exciton formation is taken into account. This can be seen by considering the effect on the imaginary part of the dielectric function ($\epsilon = \mathrm{Re}(\epsilon) + i\mathrm{Im}(\epsilon)$).

When the Coulomb coupling between excited quasi-electrons and quasi-holes is *not* taken into account, the imaginary part of the dielectric function takes the form [234, 236]

$$\mathrm{Im}(\epsilon)^{\text{non int.}} \propto \sum_{v,c} |\vec{\epsilon}\langle v| \mathbf{v} |c\rangle|^2 \delta(\omega - E_{\text{gap}}) \,, \tag{A.19}$$

where $|v\rangle$, $|c\rangle$ are the quasi-particle valence and conduction band states, respectively, and E_{gap} is the direct transition single-particle band gap. The polarization vector of the light is given by $\vec{\epsilon}$ and $\mathbf{v} = i/\hbar[H, \mathbf{r}]$ is the single-particle velocity operator.

In stark contrast thereto, the case in which Coulomb coupling between electron and hole is taken into account is now considered. The optical excitation of a quasi-electron and quasi-hole is described by a transition $|N, 0\rangle \to |N, S\rangle$, where N is the number of electrons and the state $|S\rangle$ describes the excited electron-hole pair wave function (a two-particle excitation) which is mediated by a dynamically screened Coulomb interaction. The imaginary part of the dielectric function then takes the form [234]

$$\mathrm{Im}(\epsilon) \propto \sum_{S} |\vec{\epsilon}\langle 0| \mathbf{v} |S\rangle|^2 \delta(\omega - \Omega) \,, \tag{A.20}$$

where the matrix element $\langle 0| \mathbf{v} |S\rangle$ captures the optical transition from the ground state $|0\rangle$ to the excited electron-hole pair $|S\rangle$. An immediate implication for the absorption spectrum is that the threshold for an interband optical excitation in a semiconductor is $\Omega = E_{\text{gap}} - E_{\text{X}}$, where E_{X} is the Coulomb binding energy of the electron-hole pair.

A.5 Topological classification of condensed matter

The preceding section presented concepts for calculating ground state and excited state properties of a condensed matter system. This allows to extract information about the spectral function from an ab-initio approach and microscopic viewpoint. This section is devoted to a more high-level classification of condensed matter systems, more precisely insulators and semiconductor, by means of topology. It enters in the description of condensed matter, when it comes to the description of the Bloch wave function of electrons [265] moving in the periodic crystal lattice. This interconnection of electronic band theory and topology resulted in a complete description of perfectly crystalline matter. It established the field of "topological quantum chemistry" [266]. Apart from this idealized case, recent theoretical efforts are also directed towards methods to describe more realistic models of condensed matter, in particular, systems that incorporate the effects of disorder [267]. The following limits the description to the perfectly crystalline case. For extensive reviews on this topic, the interested reader is referred to Refs. [11, 20, 268–270].

The following briefly outlines the most important concepts of topological classification of condensed matter, starting with an introduction of the mathematical framework centered around the Berry phase in Sec. A.5.1. It is the foundation of the geometrical description. Then in Sec. A.5.2 we give the mathematical expression for calculating the $\mathcal{Z}_2$ invariant that

is suitable to discern the 2D TI phase from other insulating phases.

A.5.1 Berry phase, Berry connection, and Berry curvature

The physical notion of topology is rooted in the observation that the lattice periodic part of the Bloch wave functions $|u_m(\mathbf{k})\rangle$, where m is a band index, and $\mathbf{k}$ is the crystal momentum, can acquire a geometrical phase which is different from integer multiples of 2π when traced over a closed loop in momentum space. This so called Berry phase and related quantities will be introduced in the following.

The Berry phase can be calculated as the line integral over a parametrized path $\mathcal{C}$ along which the wavefunctions evolve adiabatically according to [271]

$$\gamma_m(\mathcal{C}) = \int_{\mathcal{C}} d\mathbf{k} \cdot \mathcal{A}_m \tag{A.21}$$

$$\mathcal{A}_m = i \langle u_m(\mathbf{k}) | \nabla_{\mathbf{k}} | u_m(\mathbf{k}) \rangle \ , \tag{A.22}$$

where $\mathcal{A}_m$ is called the Berry connection. In general, the Berry phase differs for two different paths with the same start and end points. However, it is always the same on a closed path $\mathcal{C}$ independent of its parametrization. This motivates the definition of the following quantities:

$$\gamma_m(\mathcal{C}) \equiv \oint_{\mathcal{C}} d\mathbf{k} \cdot \mathcal{A}_m = \int_{\mathcal{S}} d\mathbf{S} \cdot \mathcal{F}_m \tag{A.23}$$

$$\mathcal{F}_m(\mathbf{k}) = \nabla_{\mathbf{k}} \times \mathcal{A}_m \ , \tag{A.24}$$

where in the second step of Eq. (A.23) Stokes' theorem has been applied with $\mathcal{S}$ defining a surface enclosed by the closed path $\mathcal{C}$. Therefore, $\mathcal{F}_m$ defines the so called Berry curvature given by Eq. (A.24).

These geometrical objects are the starting point for a topological classification. A particularly descriptive example can be provided by a topological classification of 2D curved surfaces in 3D space. The topological invariant called Euler characteristic is calculated by an integral of the Gaussian curvature of the surface and is strictly related to its genus, i.e., simply the number of holes it comprises [272]. All arbitrary smooth deformations of the surface leave its genus unchanged and thus also its topological classification. The analogous topological classification for the Hilbert space of occupied Bloch wave functions can then be defined with the help of the Berry curvature and gives rise to the Chern number [11]

$$C \equiv \sum_{m=1}^{N} \frac{1}{2\pi} \int_{\mathrm{BZ}} d^2\mathbf{k} \cdot \mathcal{F}_m(\mathbf{k}) \ . \tag{A.25}$$

So far, it could be seen that all Berry phase related quantities (cf. Eqs. (A.21)–(A.24)) can be regarded purely geometrical objects of the Bloch wave function $|u_m(\mathbf{k})\rangle$. To gain some intuition about these quantities, the impact of the Berry curvature on the quantum mechanical phase of the Bloch wave function is compared to the observations made for

a Foucault pendulum [273]. The Foucault pendulum can be regarded an experiment of performing parallel transport movements on a curved surface, the Earth. The effect of the finite curvature of the earth is the intriguing observation that the direction of movement of the pendulum is rotating (except at the equator). The mathematical reason is that a vector attached to a curved surface and performing a parallel transport movement on a closed path on that surface will be oriented differently at the end of the movement than at the beginning. The quantum mechanical phase of the electronic Bloch wavefunction shows a similarity, namely a finite Berry curvature will cause the phase to rotate whilst performing a parallel transport movement along a closed path. This rotation is captured by the Berry phase.

Another noteworthy aspect must be noted in anticipation of the topological classification of insulators and semiconductors which are characterized by an energy gap that separates valence and conduction band states. Imagine a parameter that tunes the gap opening and closing of the band structure. One observes that with regard to this parameter space the points of the band structure where the band gap opening takes place can be regarded as the sources for creating Berry curvature. In that regard the Berry curvature $\mathcal{F}_m$ defined in Eq. (A.24) has mathematical similarities to a magnetic field derived from a vector potential $\mathcal{A}_m$.

A.5.2 $\mathcal{Z}_2$ topological invariant

The $\mathcal{Z}_2$ topological index (ν) is used to discern the quantum spin Hall insulator phase from other insulating phases. It is defined as [18, 274]

$$\nu = \frac{1}{2\pi}\left[\oint_{d\tau} \mathcal{A}(\mathbf{k})dl - \int_{\tau} \mathcal{F}(\mathbf{k})d\tau\right] \bmod 2 \tag{A.26}$$

where $\mathcal{A} = \sum_{m=1}^{N} \mathcal{A}_m$ is the sum of the Berry connections over all occupied bands (cf. Eq. (A.22)) and $\mathcal{F} = \nabla_{\mathbf{k}} \times \mathbf{A}$ is the corresponding total Berry curvature (cf. Eq. (A.24)). The integrals are over half of the 2D BZ surface τ and its boundary $d\tau$. The $\mathcal{Z}_2$ index can only take the values 0 or 1 [17, 19].

A much simpler formula than Eq. A.26 for the $\mathcal{Z}_2$ index (ν) exists if the system is inversion symmetric [19]:

$$\delta_i = \prod_{m=1}^{N} \xi_{2m}(\Gamma_i) \quad , \qquad (-1)^{\nu} = \prod_i \delta_i \, . \tag{A.27}$$

The calculation involves the product of parity eigenvalues ξ_{2m} of the $(2m)^{\text{th}}$ occupied wave function forming the bulk energy bands at the time-reversal invariant points Γ_i in the first Brillouin zone. Then, the product runs over the time reversal invariant points Γ_i indexed by i. Notably, the $2N$ bands are spin-degenerate at Γ_i because of time-reversal symmetry (Kramers degeneracy), and $\xi_{2m} = \xi_{2m-1}$ holds.

Additional Information on the growth of bismuthene on miscut SiC substrates

This supplementary section provides information about the improved growth of bismuthene on miscut SiC substrates achieved during the work of this thesis. Growing bismuthene on intentionally miscut SiC(0001) substrates as presented in Sec. 4.1 generates a higher density of long and straight bismuthene film edges that host the topological edge states. The feasibility of epitaxial growth of bismuthene on the miscut substrates has already been proved in Ref. [7]. Increasing the edge density was motivated by the goal of generating enough edge state DOS in order to find evidence for these quasi 1D states also in ARPES. However, the direct evidence of edge states in ARPES could not be accomplished.

Figures B.1**a, b** show large overview constant current STM images of bismuthene grown with an improved recipe. In principle, the bismuthene film was grown according to the procedure described alongside Fig. 4.5**b** in the main text. First, hydrogen was desorbed from the substrate at $T_{\mathrm{des}} = 600\,^{\circ}\mathrm{C}$ for $t_{\mathrm{des}} = 160\,\mathrm{s}$, followed by the bismuth enrichment phase at $T_{\mathrm{enr\,1}} = (513 \pm 3)\,^{\circ}\mathrm{C}$ for $t_{\mathrm{enr\,1}} = 3500\,\mathrm{s}$ and $T_{\mathrm{enr\,2}} = (500 \pm 3)\,^{\circ}\mathrm{C}$ for $t_{\mathrm{enr\,2}} = 2240\,\mathrm{s}$. Note that here the temperature of the substrate during the bismuth enrichment phase has been slighly lowered from $T_{\mathrm{enr\,1}}$ to $T_{\mathrm{enr\,2}}$. The Bi cell temperature was held at $T_{\mathrm{C}} = 490\,^{\circ}\mathrm{C}$. It can be seen in the STM measurements in Figures B.1**a, b** that it is possible to achieve a near to 100% film coverage with this growth recipe.

The detailed view of one terrace in Fig. B.1**c** shows that the bismuthene film is terminated by the SiC substrate step edge. As the SiC substrate steps are oriented parallel to the $[11\bar{2}0]$ direction, the bismuthene edges naturally favor an armchair type termination. However, straight sections of these bismuthene edges are still frequently interrupted by defects such as domain boundaries or other growth inhomogeneities. Atomically precise armchair sections without interruptions are observed on length scales of only $\sim 10\,\mathrm{nm}$.

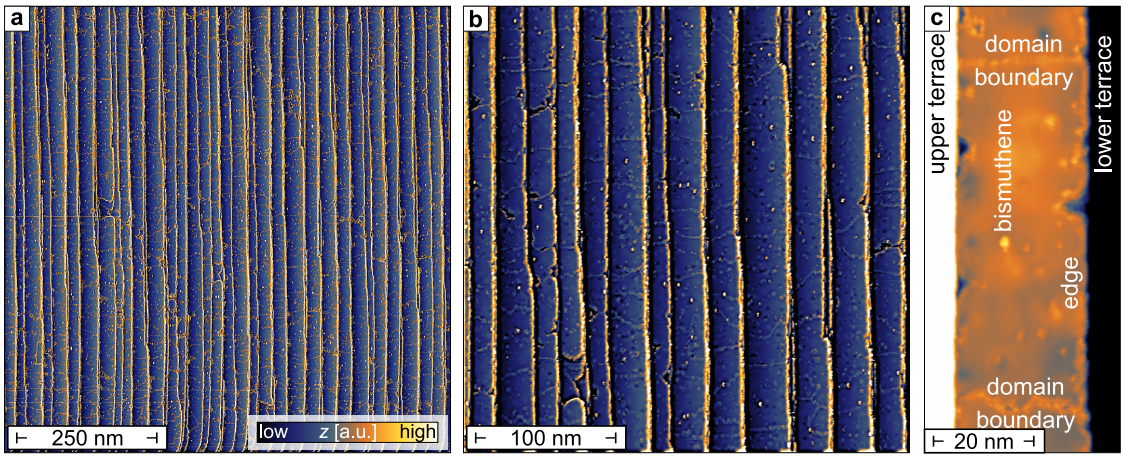

Figure B.1: Growth of bismuthene with high edge state density. **(a), (b),** STM constant current measurements ($I_{\mathrm{set}} = 40\,\mathrm{pA}$, $V_{\mathrm{set}} = 1.8\,\mathrm{V}$, $T = 4.35\,\mathrm{K}$) of bismuthene grown on a 4° miscut SiC substrate. The terrace steps appear as straight lines oriented parallel to the $[11\bar{2}0]$ direction (cf. Fig. 4.2**b**). The meandering line structures within each terrace are domain boundaries of the bismuthene film. For better visualization on a large scale, a spatial high pass filter has been applied to compensate the SiC substrate steps. This leads to a spurious effect of edges appearing qualitatively too high in z-direction. The bismuthene surface coverage is $\approx 100\%$. **(c),** Close-up view from the measurement in **b** showing a bismuthene domain on a single SiC terrace enclosed by edges at SiC substrate steps and domain boundaries within the film.

Additional Information on the growth and spectroscopy of manganese- and cobalt-induced alloys on bismuthene

C.1 STM line profile of the Bi/Mn-alloy

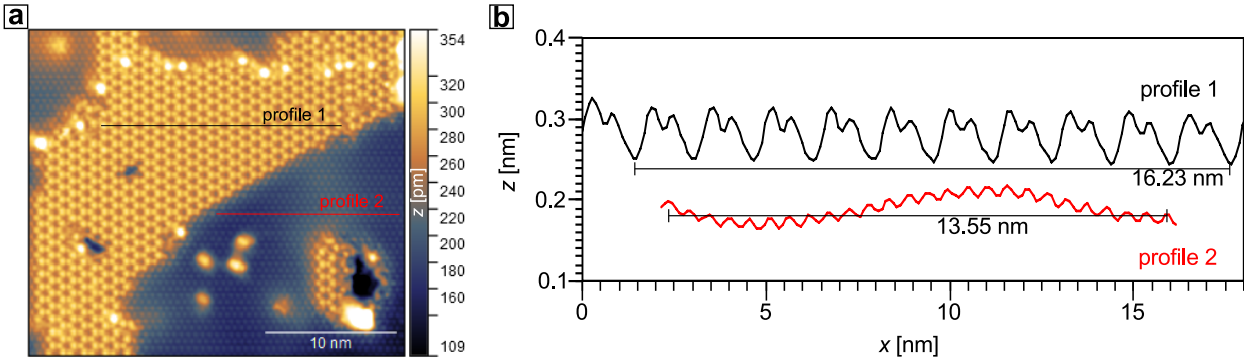

Figure C.1: STM line profile of the Bi/Mn-alloy. **(a),** STM constant current image ($V_{\text{set}} = 2.2\,\text{V}$, $I_{\text{set}} = 40\,\text{pA}$, and $T = 4.35\,\text{K}$) of a mixed phase of bismuthene (blue appearance) and Bi/Mn-alloy (yellow appearance). Line profiles 1 and 2 from both structures are plotted in **b**.

C.2 ARPES from a mixed phase of bismuthene and Bi/Mn-alloy

Figure C.2**a** shows an ARPES band map measured on a sample with a mixed phase of bismuthene and the Bi/Mn-alloy, i.e., at a sub-monolayer coverage of the Bi/Mn-alloy. The corresponding topography of the sample is similar to the one shown in the STM measurement in Fig. 5.1**a**. In the ARPES spectrum and its second derivative image in Fig. C.2**b**, the bismuthene derived bands can be seen in form of the characteristic Rashba split valence bands at the K-point of the $(\sqrt{3} \times \sqrt{3})R30°$) surface BZ, which corresponds to the Γ-point of the (3×3)) surface BZ, see inset of Fig. C.2**a**. In addition the same dispersive features $S1^-$, $S1^+$, $S2^-$, and $S2^+$ as in the ARPES measurements conducted on the Bi/Mn-alloy sample with a full surface coverage are observed, see Fig. 5.2.

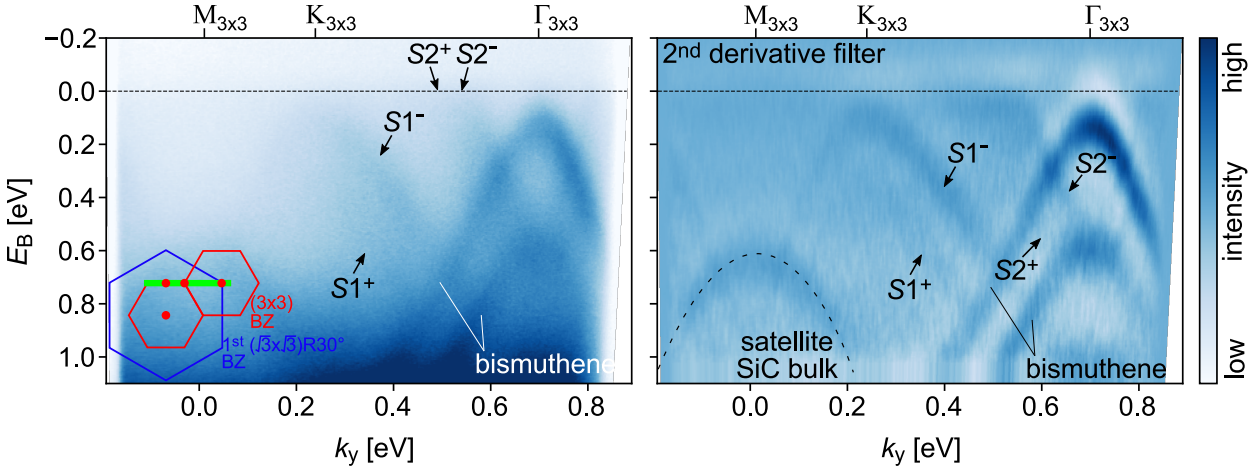

Figure C.2: ARPES from a mixed phase of bismuthene and Bi/Mn-alloy. Direct (**a**) and 2nd derivative with respect to the energy (**b**) ARPES band map along a path between high symmetry points of the Bi/Co-alloy (3×3) surface reconstruction, see schematic drawing. The Bi/Mn-alloy related states $S1^-$, $S1^+$, $S2^-$, and $S2^+$, and the bismuthene related Rashba split valence bands are marked. The dashed line in **b** indicates a satellite replica intensity of the SiC bulk bands due to the non-monochromatized helium discharge lamp that is used. Scan parameters: $h\nu = 21.22\,\text{eV}$ (He I α, not monochromatized), $T = 70\,\text{K}$.

C.3 STM topography of Co-induced defects on bismuthene

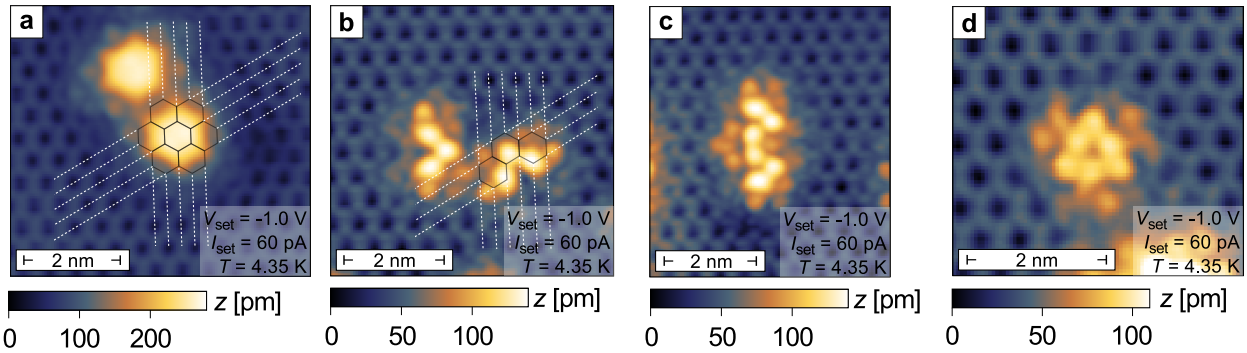

Figure C.3: Co induced atomic defects on bismuthene. STM constant current measurements of a bismuthene sample after an initial Bi/Co-alloy growth with very low amounts of Co-dosing similar to the growth connected to Figs. 5.4**b, c**. **(a) – (d),** Different atomic defects have formed. White and black lines are guides to the eye. Unconnected and connected arrow-shaped trimer structures are observed in **b** and **c**, respectively. As more and more trimer defects connect, a Kagome lattice of the extended Bi/Co-alloy is forming. The situation of two connecting trimer structures is seen in **c**. Therefore, it is proposes that the trimer defects are the basic constituents of the Bi/Co-alloy Kagome lattice.

C.4 CLAHE applied to Bi/Co-alloy constant energy ARPES maps

Contrast enhancement can be a useful image processing technique to adapt images in order to enhance weak features by renormalizing the dynamic range of the image. One strategy frequently applied to scientific microscopy data, but also to spectroscopic data, when a line shape analysis is *not* in the focus, but instead a mere feature detection, is based on nonlinear histogram transformations, e.g., the contrast limited adaptive histogram equalization (CLAHE) routine. As the interest lies on the detection of features in constant energy ARPES maps recorded with a k-space microscope in Figs. 5.5**e** and **f**, a CLAHE routine has been applied with the help of a software implementation in the python programming language provided by Stimper *et al.* [156]. The CLAHE routine was applied after having extracted the Fermi position from the original data. Figure C.4 shows both the original data and the CLAHE enhanced images side by side.

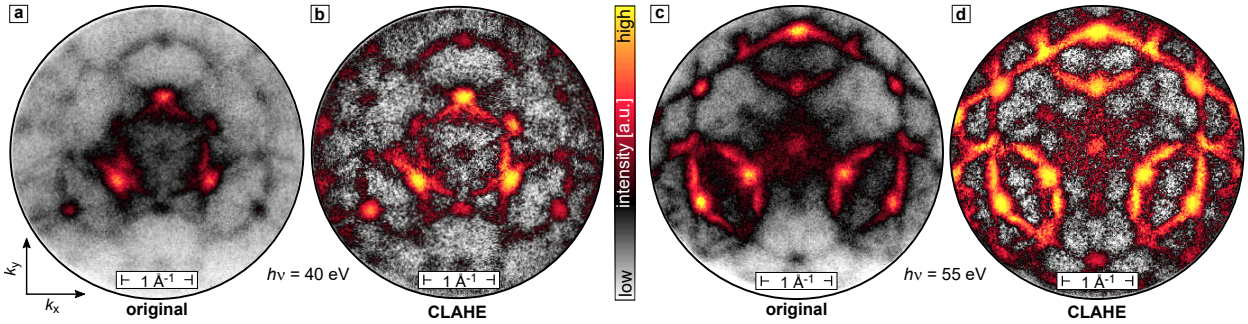

Figure C.4: CLAHE applied to Bi/Co-alloy constant energy ARPES maps. (a), (c), Original constant energy maps recorded with a k-space microscope at the NanoESCA beamline at Trieste synchrotron (extraction voltage of 8 keV; p-polarized light; photon beam incident at 65° from the surface normal) and used for the Figs. 5.5**e** and **f**, respectively. The photon energies are $E_{\mathrm{Ph}} = 40\,\mathrm{eV}$ and $E_{\mathrm{Ph}} = 55\,\mathrm{eV}$ in **a** and **c**, respectively. Each map is an average of the photoemission intensity in the binding energy range $0\,\mathrm{eV} \leq E_{\mathrm{B}} \leq 0.3\,\mathrm{eV}$. **(b), (d),** Same images as in Figs. 5.5**e** and **f**, respectively, with an applied contrast limited adaptive histogram equalization (CLAHE) routine to enhance the contrast [156].

XPS of bismuthene, Bi/Mn-alloy, and Bi/Co-alloy samples

D.1 XPS of pristine bismuthene

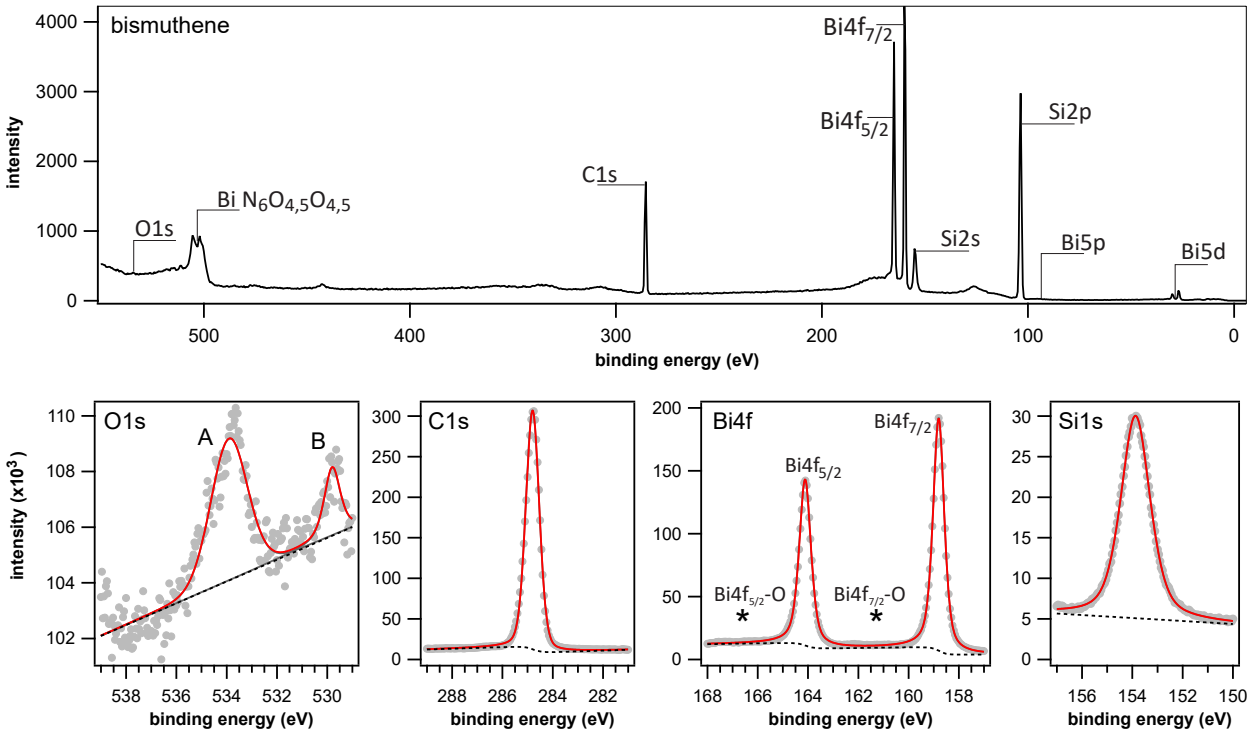

Figure D.1: XPS of pristine bismuthene. The sample was grown in the home laboratory and transferred with the UHV suitcase ($p \sim 5 \times 10^{-10}$ mbar) to the I09 beamline at the Diamond Light Source, where XPS spectra were recorded. Top panel: the XPS survey scan was measured with a photon energy of $h\nu = 600$ eV. Bottom panels: XPS spectra were measured with a photon energy of $h\nu = 700$ eV. All spectra were recorded at RT and at an emission angle of 30° off normal. Best fits to all data (gray dots) are represented by red lines using pseudo-Voigt profiles [275] and a Shirley + linear function as background (dashed line) as implemented in the software package *XPST* (Version: IGOR.7.00.x-1.3-01) for the *WaveMetrics IGOR Pro* program, see Tab. D.1 for fit results. The spin-orbit split Bi4f core levels do not show any relevant contributions due to Bi oxidation which would be observed at energies marked with asterisk; cf. Fig. D.3.

D.2 XPS of bismuthene after storage in N_2 inert gas atmosphere

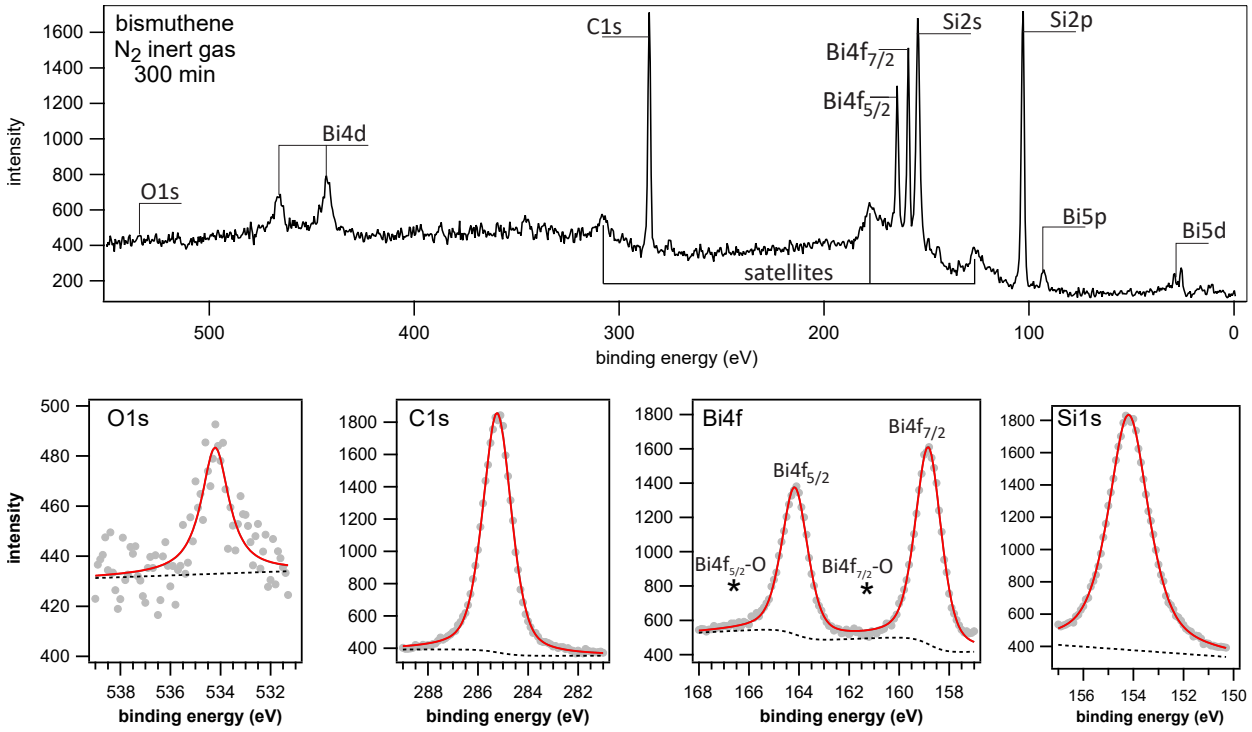

Figure D.2: XPS of bismuthene after storage in N_2 inert gas atmosphere. All XPS spectra were measured at RT and using the Al K_α line and at an emission angle of 0° off normal. Prior to the recording of the XPS spectra, the bismuthene sample was stored in an N_2 inert gas atmosphere (< 0.1 ppm H_2O; < 0.1 ppm O_2) for 300 min and transferred back to the UHV analyis chamber. Best fits to the data (gray dots) are represented by red lines using pseudo-Voigt profiles [275] and a Shirley + linear function as background (dashed line) as implemented in the software package *XPST* (Version: IGOR.7.00.x-1.3-01) for the *WaveMetrics IGOR Pro* program, see Tab. D.1 for fit results. The spin-orbit split Bi4f core levels do not show any relevant contributions due to Bi oxidation which would be observed at energies marked with asterisk; cf. Fig. D.3. *Figure reprinted and adapted from Ref. [124] under a Creative Commons Attribution 4.0 International (CC BY 4.0) License.*

D.3 XPS and STM of bismuthene after exposure to oxygen

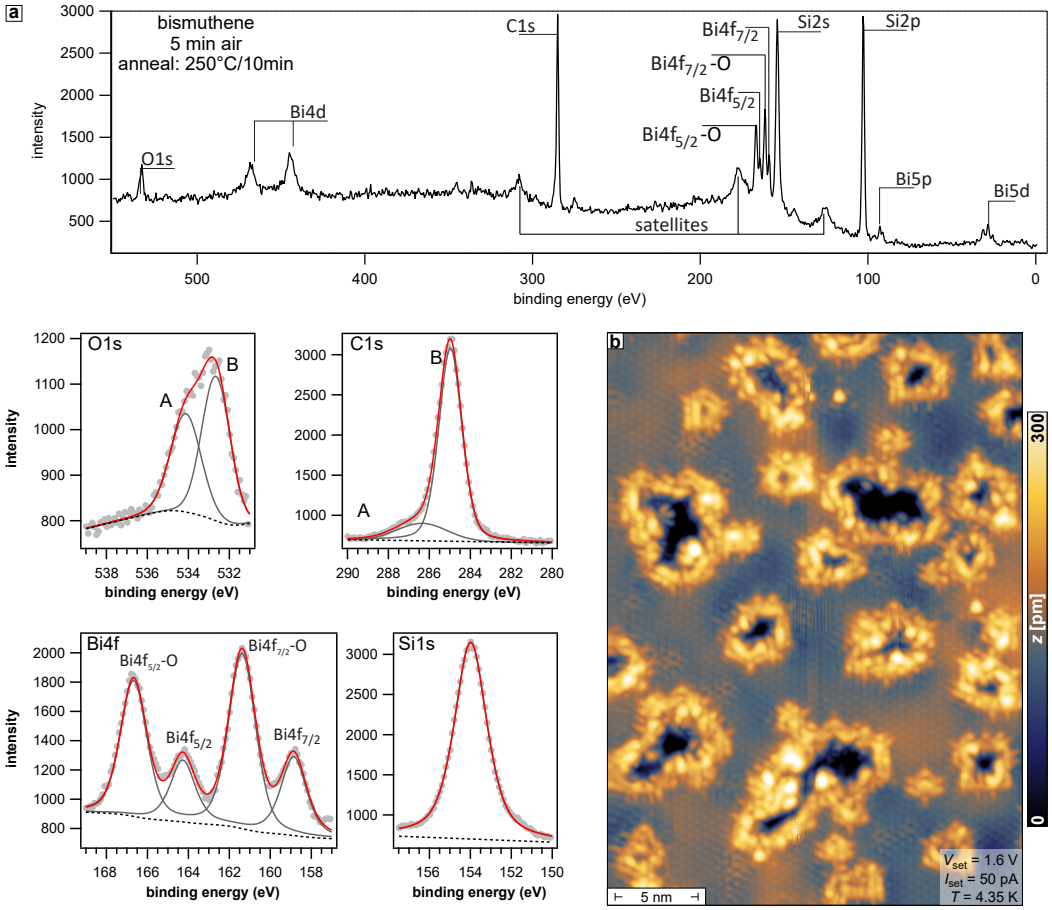

Figure D.3: XPS and STM of bismuthene after exposure to oxygen. **(a),** All XPS spectra were measured at RT and using the Al K_α line and at an emission angle of 0° off normal. Prior to the recording of the XPS spectra, the bismuthene sample was exposed to ambient air for 5 min, reinserted to the UHV analysis chamber, and annealed at 250 °C for 10 min (standard surface cleaning procedure for bismuthene samples). Best fits to the data (gray dots) are represented by red lines using pseudo-Voigt profiles [275] and a Shirley + linear function as background (dashed line) as implemented in the software package *XPST* (Version: IGOR.7.00.x-1.3-01) for the *WaveMetrics IGOR Pro* program, see Tab. D.1 for fit results. The presence of a new oxygen chemical bonding state (B) compared to Fig. D.2 and Fig. D.1 is observed. The presence of a side peak (A) in the C1s core level spectrum can be assigned to a new chemical bonding state of C-atoms of hydrocarbons deposited onto the sample from ambient air, while the main peak (B) corresponds to the chemical bonding state of C-atoms in the SiC substrate. The spin-orbit split Bi4f core levels do show large Bi-Ox peaks indicating that the bismuthene film has degraded by oxidation. **(b),** STM constant current image of a bismuthene film that has been exposed to a small dose of O_2 within a UHV chamber at $p = 2.5 \times 10^{-5}$ mbar for 10 min and subsequent temperature annealing at 400 °C for 10 min. It is known that a temperature annealing at 400 °C is not detrimental to the crystal quality of pristine bismuthene, but the oxidation has caused a high density of defective areas of apparent lower height in the bismuthene film. *Figure (a) reprinted and adapted from Ref. [124] under a Creative Commons Attribution 4.0 International (CC BY 4.0) License.*

D.4 XPS of the Bi/Co-alloy

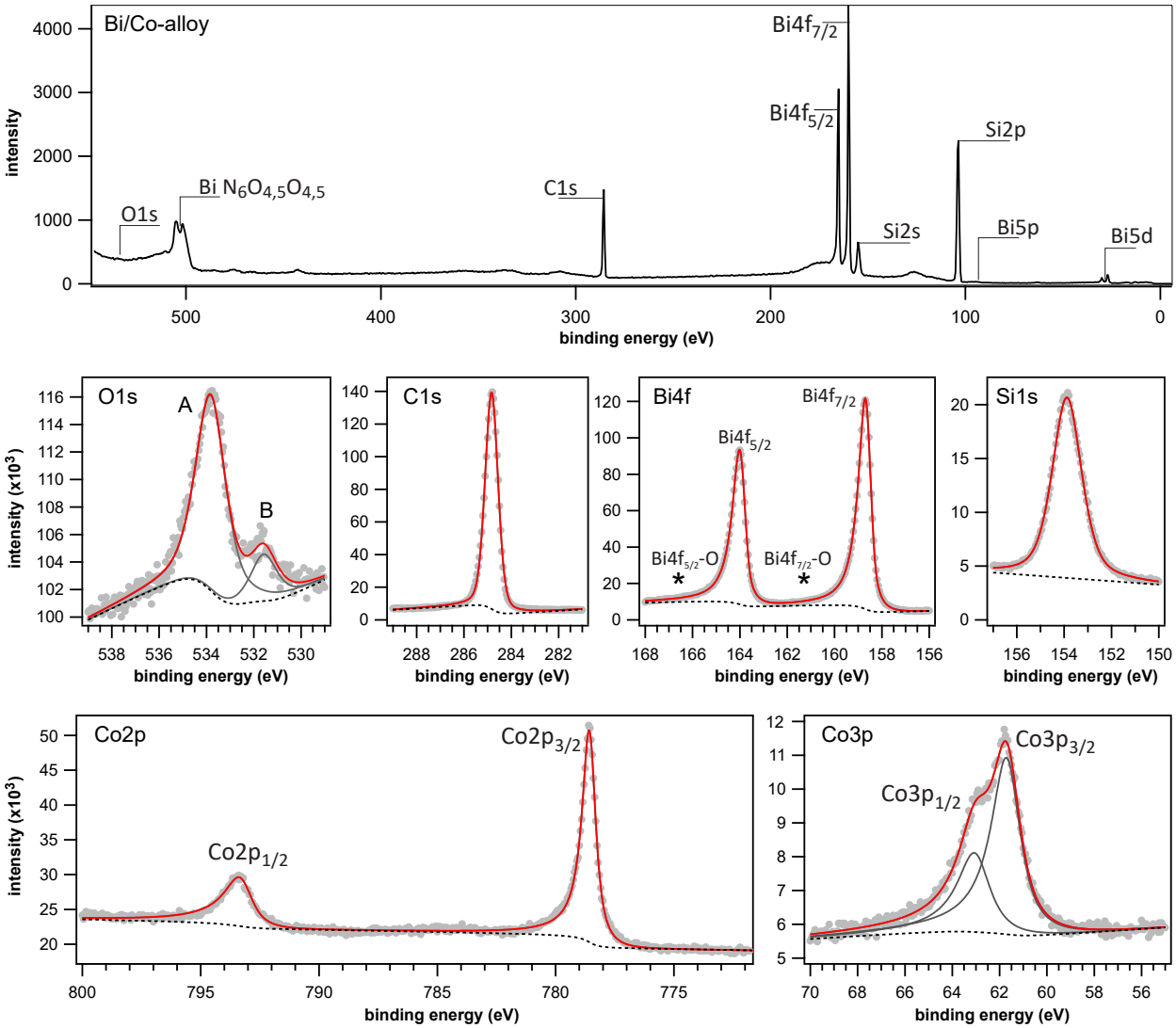

Figure D.4: XPS of the Bi/Co-alloy. The sample was grown in the home laboratory and transferred with the UHV suitcase ($p \sim 5 \times 10^{-10}$ mbar) to the I09 beamline at the Diamond Light Source, where XPS spectra were recorded (cf. Fig. 5.5**a, b** for ARPES spectra of the same sample measured before transfer at the home laboratory). Top panel: the XPS survey scan was measured with a photon energy of $h\nu = 600$ eV. The O1s, C1s, Bi4f, Si1s, and Co3p core levels were measured with a photon energy of $h\nu = 700$ eV. The Co2p core level was measured with a photon energy of $h\nu = 950$ eV. All spectra were recorded at RT and at an emission angle of 30° off normal. Best fits to the data (gray dots) are represented by red lines using pseudo-Voigt profiles [275] and a Shirley + linear function as background (dashed line) as implemented in the software package *XPST* (Version: IGOR.7.00.x-1.3-01) for the *WaveMetrics IGOR Pro* program, see Tab. D.1 for fit results. The spin-orbit split Bi4f core levels do not show any relevant contributions due to Bi oxidation which would be observed at energies marked with asterisk; cf. Fig. D.3.

D.5 XPS of the Bi/Mn-alloy

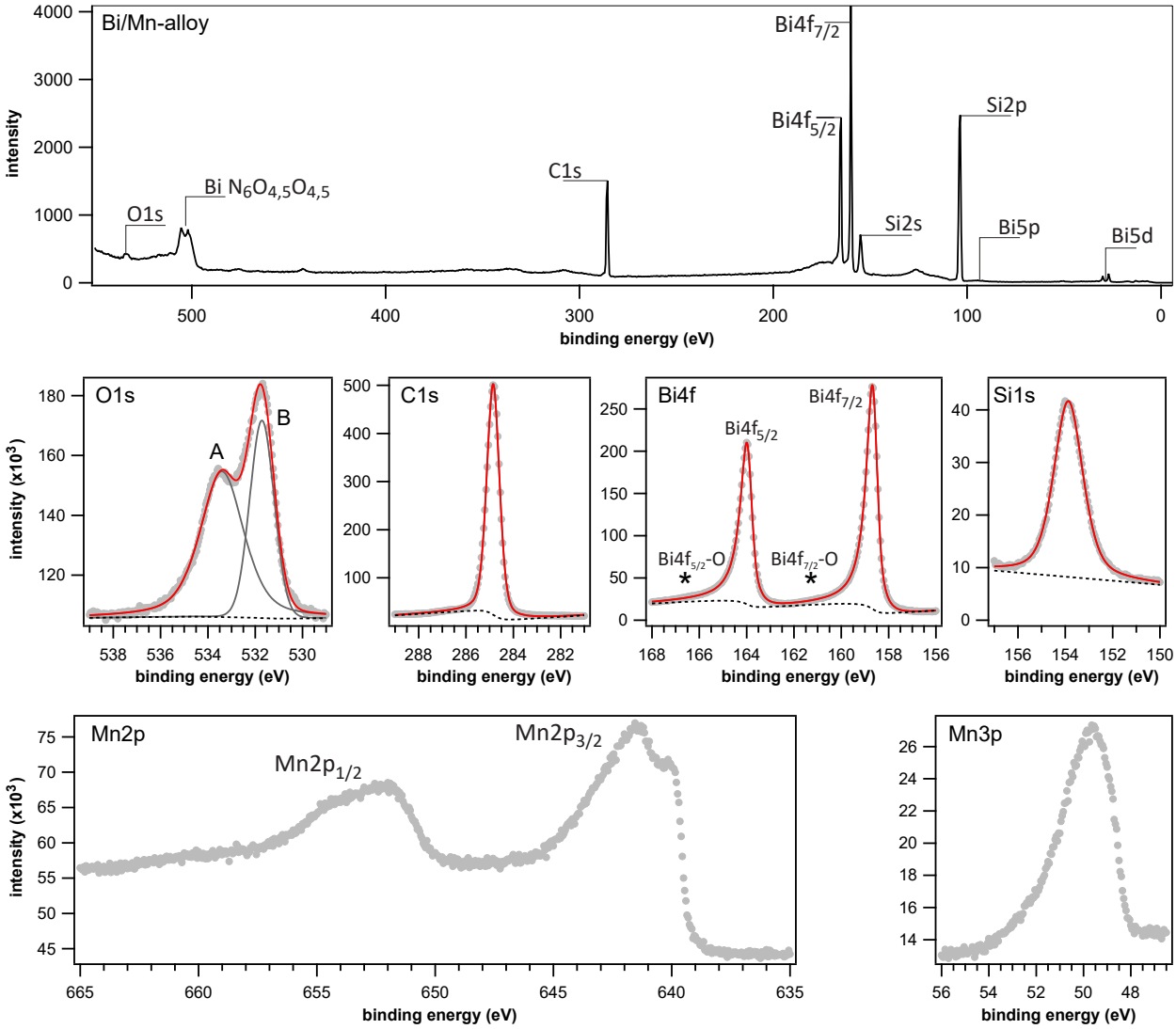

Figure D.5: XPS of the Bi/Mn-alloy. The sample was grown in the home laboratory and transferred with the UHV suitcase ($p \sim 5 \times 10^{-10}$ mbar) to the I09 beamline at the Diamond Light Source, where XPS spectra were recorded. Top panel: the XPS survey scan was measured with a photon energy of $h\nu = 600$ eV. The O1s, C1s, Bi4f, Si1s, and Mn3p core levels were measured with a photon energy of $h\nu = 700$ eV. The Mn2p core level was measured with a photon energy of $h\nu = 800$ eV. All spectra were recorded at RT and at an emission angle of 30° off normal. Best fits to the data (gray dots) are represented by red lines using pseudo-Voigt profiles [275] and a Shirley + linear function as background (dashed line) as implemented in the software package *XPST* (Version: IGOR.7.00.x-1.3-01) for the *WaveMetrics IGOR Pro* program, see Tab. D.1 for fit results. The spin-orbit split Bi4f core levels do not show any relevant contributions due to Bi oxidation which would be observed at energies marked with asterisk; cf. Fig. D.3.

D.6 XPS fit results

sample	Fig.	peak	area [counts eV]	E_B [eV]	FWHM [eV]	GL ratio	asym. [eV^{-1}]	ΔE [eV]
bismuthene	D.1	Si2s	44975	153.87	1.38	0.58	0	-4.93
		$Bi4f_{5/2}$	97680	164.11	0.55	0.63	0*	5.31
		$Bi4f_{7/2}$	130240	158.80	0.53	0.63	0*	–
		O1s:A	9861	533.90	1.73	0.15	0*	375.10
		O1s:B	2466	529.80	0.76	0.61	0*	371.00
		C1s	2589	285.23	1.35	0.55	0*	126.43
bismuthene N_2 inert gas 300 min	D.2	Si2s	3904	154.19	1.92	0.74	0*	-4.64
		$Bi4f_{5/2}$	1368	164.17	1.24	0.55	0*	5.34
		$Bi4f_{7/2}$	1823	158.83	1.23	0.55	0*	–
		O1s	102	534.21	1.33	0.95	0*	375.38
		C1s	2589	285.23	1.35	0.55	0*	126.40
bismuthene 5 min air anneal: 250 °C/10 min	D.3	Si2s	6286	153.98	1.89	0.68	0*	-4.87
		$Bi4f_{5/2}$	794	164.26	1.43	0.62	0*	5.41
		$Bi4f_{7/2}$	1058	158.85	1.49	0.62	0*	–
		$Bi4f_{5/2}$-O	1720	166.67	1.52	0.42	0*	7.82
		$Bi4f_{7/2}$-O	2293	161.37	1.56	0.42	0*	2.52
		O1s:A	428	534.12	1.75	0.18	0*	374.27
		O1s:B	558	532.65	1.62	0.05	0*	373.80
		C1s:A	3831	284.97	1.32	0.36	0*	126.12
		C1s:B	677	286.35	2.88	0.05	0*	127.50
Bi/Co-alloy	D.4	Si2s	32376	153.88	1.47	0.59	0*	-4.86
		$Bi4f_{5/2}$	79343	164.06	0.69	0.75	1.36	5.32
		$Bi4f_{7/2}$	105790	158.74	0.67	0.75	1.36	–
		O1s:A	28638	533.81	1.52	0.62	0*	375.07
		O1s:B	6090	531.57	1.33	0.66	0*	372.83
		C1s	103380	284.83	0.65	0.37	0*	126.09
		$Co2p_{1/2}$	16395	793.52	1.66	0.95	0.84	634.78
		$Co2p_{3/2}$	32790	778.61	0.72	0.95	0.84	619.87
		$Co3p_{1/2}$	6007	63.15	1.72	0.95	0.41	-95.59
		$Co3p_{3/2}$	12014	61.78	1.54	0.95	0.41	-96.96
Bi/Mn-alloy	D.5	Si2s	63308	153.87	1.46	0.56	0*	-4.85
		$Bi4f_{5/2}$	169215	164.03	0.64	0.84	1.55	5.31
		$Bi4f_{7/2}$	225620	158.72	0.61	0.84	1.55	–
		O1s:A	138160	533.40	2.17	0.58	0	374.68
		O1s:B	86838	531.71	1.21	0.05	0*	372.99
		C1s	374130	284.85	0.63	0.42	0*	126.13
		Mn2p	–	–	–	–	–	–
		Mn3p	–	–	–	–	–	–

Table D.1: XPS peak fit results using pseudo-Voigt profiles [275] and a Shirley + linear function as background as implemented in the software package *XPST* (Version: IGOR.7.00.x-1.3-01) for the *WaveMetrics IGOR Pro* program. The parameters marked with (*) are not varied during the fit. $\Delta E \equiv E_B - E_B^{\mathbf{Bi4f_{7/2}}}$.

Additional Information on domain boundaries in bismuthene

E.1 STM of a long domain boundary

It would desirable to have spectroscopic data of much longer defect-free DBs, where the spectra are not dominated by the energetically discretized Fabry-Pérot states. Unfortunately, very long DBs are extremely rare. If they are observed at all, as seen in Fig. E.1 or Fig. 6.9, they typically incorporate additional point defects inside. It was proved in 6.2.4 that the point defect inside the DB already induces backscattering, similar to what is observed at kinks. Finding significantly longer *and* defect free DBs for spectroscopy was found to be very unlikely.

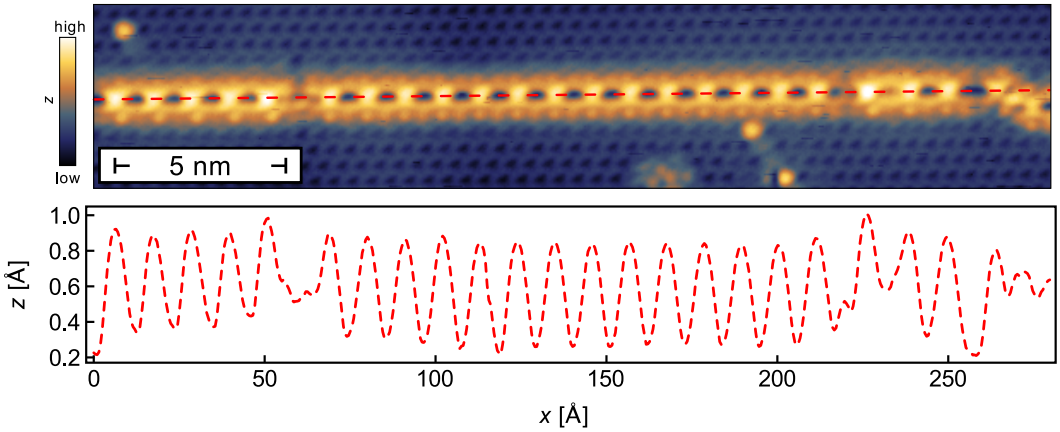

Figure E.1: Upper panel: Constant current STM measurement of a DB with a lengths of $\sim 25\,\mathrm{nm}$. Scan parameters: $V_{\mathrm{set}} = -1.2\,\mathrm{V}$, $I_{\mathrm{set}} = 40\,\mathrm{pA}$. Lower panel: height profile along the red dashed line in the upper panel. *Figure reprinted from Ref. [159] under a Creative Commons Attribution 4.0 International (CC BY 4.0) License.*

E.2 Mirror operation on free zigzag edge

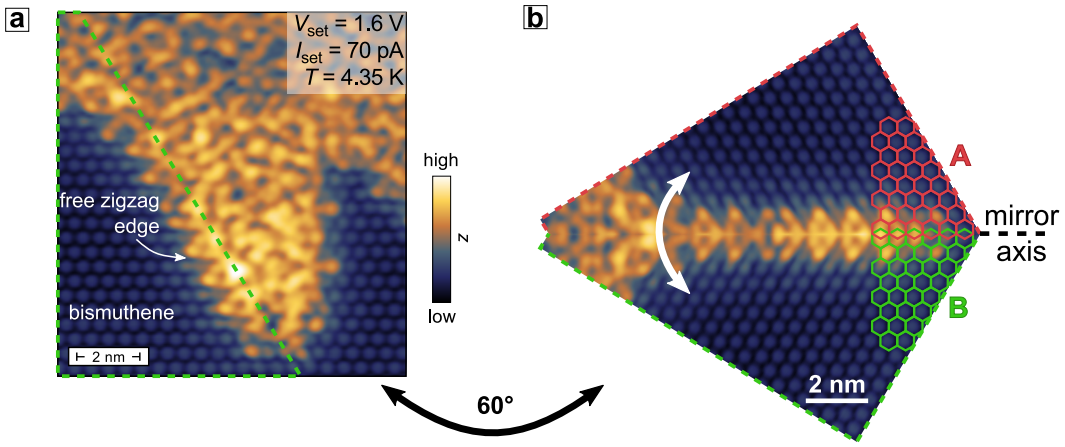

Figure E.2: Mirror operation on free zigzag edge. **(a)**, STM constant current map showing a free zigzag edge of bismuthene. **(b)**, The image is the result of: 1. extracting the region marked with a green-dashed line in **a**; 2. rotating it by 60° ; 3. mirroring at the marked mirror axis such that domain 'A' is mirrored into domain 'B'. This operation results in an image that properly generates an adsorption site shift to mimic the situation at a DB. The registry mismatch between both domains can be seen in the respective hexagonal lattices. *Figure reprinted from Ref. [159] under a Creative Commons Attribution 4.0 International (CC BY 4.0) License.*

E.3 Fabry-Pérot states in different domain boundaries

Figures E.3**a** − **h** show the corresponding dI/dV resonance data for eight more DB segments in order to demonstrate the ubiquitous and fully reproducible character of Fabry-Pérot states observed in bismuthene DBs. The depicted DBs in the constant current STM images in Figs. E.3**a0** − **h0** exhibit different lengths L which are indicated inside the respective image. The L values are estimated from the STM topographies (i.e., from the detected atomic structure) and hence have to be taken with some caution. Importantly, however, this uncertainty connected to L does not enter in the in the presented evaluation of the edge state dispersion relation (presented in Fig. 6.8**a**), as the DB lengths L has not been used as reference points. Instead, the main text laid down how an unbiased method has been employed, by directly inferring the spatial separation of modulation maxima λ as indicated in the dI/dV line profile of level E4 in Fig. 6.7**e**, thus avoiding any a priori assumptions on L.

The differential conductivity maps plotted above each constant current image are taken within the region of the respective DB marked by the red rectangle in Figs. E.3**a0** − **h0**. Each differential conductivity map shows a Fabry-Pérot resonance with its respective energy with respect to E_F indicated on the left side of each panel. The differential conductivity line profiles that result from integrating over the width of the DB in the corresponding differential conductivity map are plotted above each differential conductivity map. The arrows indicate the positions of resonance maxima, which can be obtained by fitting a Gaussian function in the vicinity of each resonance maximum (red dashed lines indicate best fits).

Fig.	V_{set} [V]	I_{set} [nA]	T [K]
a0	-0.50	0.10	4.3
a1 − a2	-1.00	0.10	4.3
b0	-1.00	0.03	4.3
b1 − b3	-0.80	0.10	4.3
c0	-1.00	0.01	4.3
c1 − c2	-1.00	0.30	4.3
d0	-0.60	0.02	4.3
d1 − d3	-0.60	0.20	4.3
e0	-1.00	0.01	4.3
e1 − e4	-1.00	0.30	4.3
f0	-0.50	0.05	4.3
f1 − f4	-0.60	0.50	4.3
g0	-0.50	0.15	4.3
g1 − g4	-0.50	0.15	4.3
h0	-1.00	0.01	4.3
h1 − h4	-0.80	0.30	4.3

Table E.1: Scan parameters for DB segments in Fig. E.3. *Table reprinted from Ref. [159] under a Creative Commons Attribution 4.0 International (CC BY 4.0) License.*

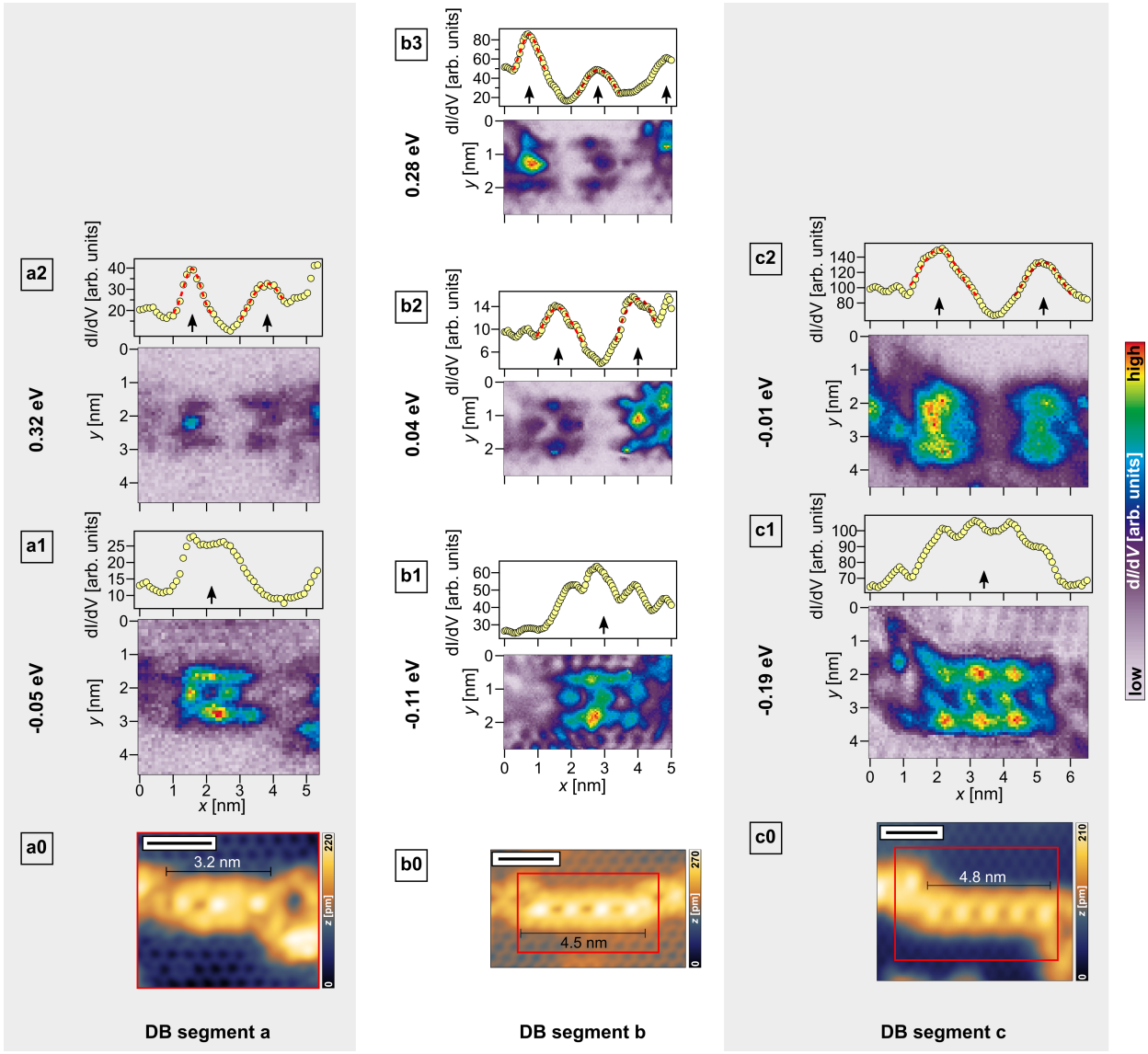

Figure E.3: Fabry-Pérot states in different domain boundaries with varying lengths. – **(a) – (c),** dI/dV resonance data for eight DB segments (see continuation of Fig. E.3 in Figs. E.3d – f, and E.3g – h. **(a0) – (h0),** Constant current STM images of the domain boundaries. The length L of each domain boundary is indicated inside the respective image. The L values are estimated from the STM topographies (i.e., from the detected atomic structure) and are subject to an estimated uncertainty of $\approx \pm 0.5\,\mathrm{nm}$. **(ai) – (hi), i** ≥ 1**,** The differential conductivity maps plotted above each constant current image are taken within the region of the respective domain boundary marked by the red rectangle in Figs. a0 – h0, and correspond to the i^{th} Fabry-Pérot resonance level. The respective energy with respect to E_F is indicated on the left side of each panel. The differential conductivity line profiles resulting from integrating over the width of the domain boundary in the corresponding differential conductivity map are shown above each map. The arrows indicate the positions of resonance maxima, which are obtained by fitting the data in the vicinity of each resonance maximum with a Gaussian function (red dashed lines indicate best fits). Scan parameters are listed in Tab. E.1. *Figure reprinted from Ref. [159] under a Creative Commons Attribution 4.0 International (CC BY 4.0) License.*

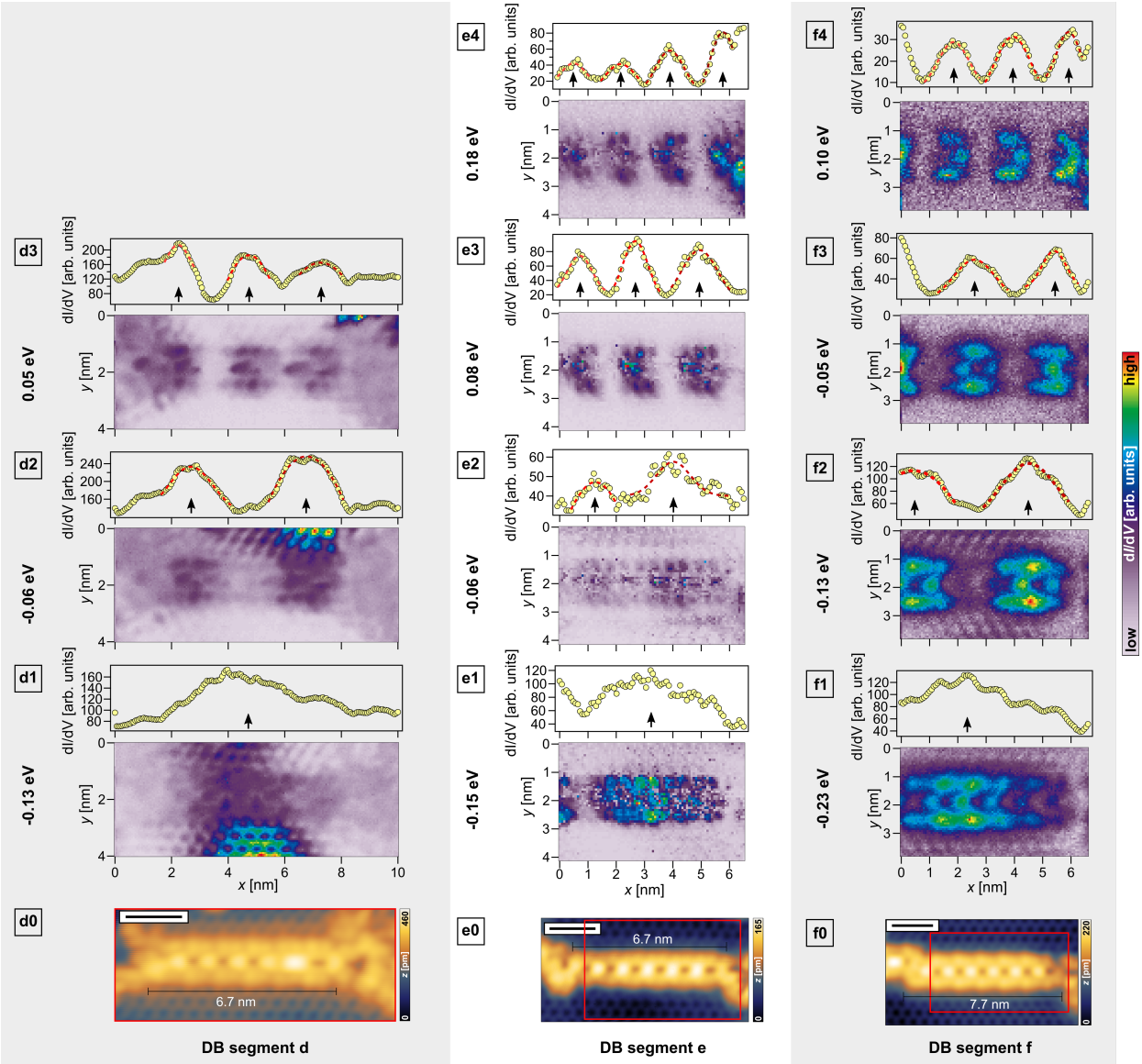

Figure E.3: (d) – (f), Fabry-Pérot states in different domain boundaries with varying lengths; continuation. *Figure reprinted from Ref. [159] under a Creative Commons Attribution 4.0 International (CC BY 4.0) License.*

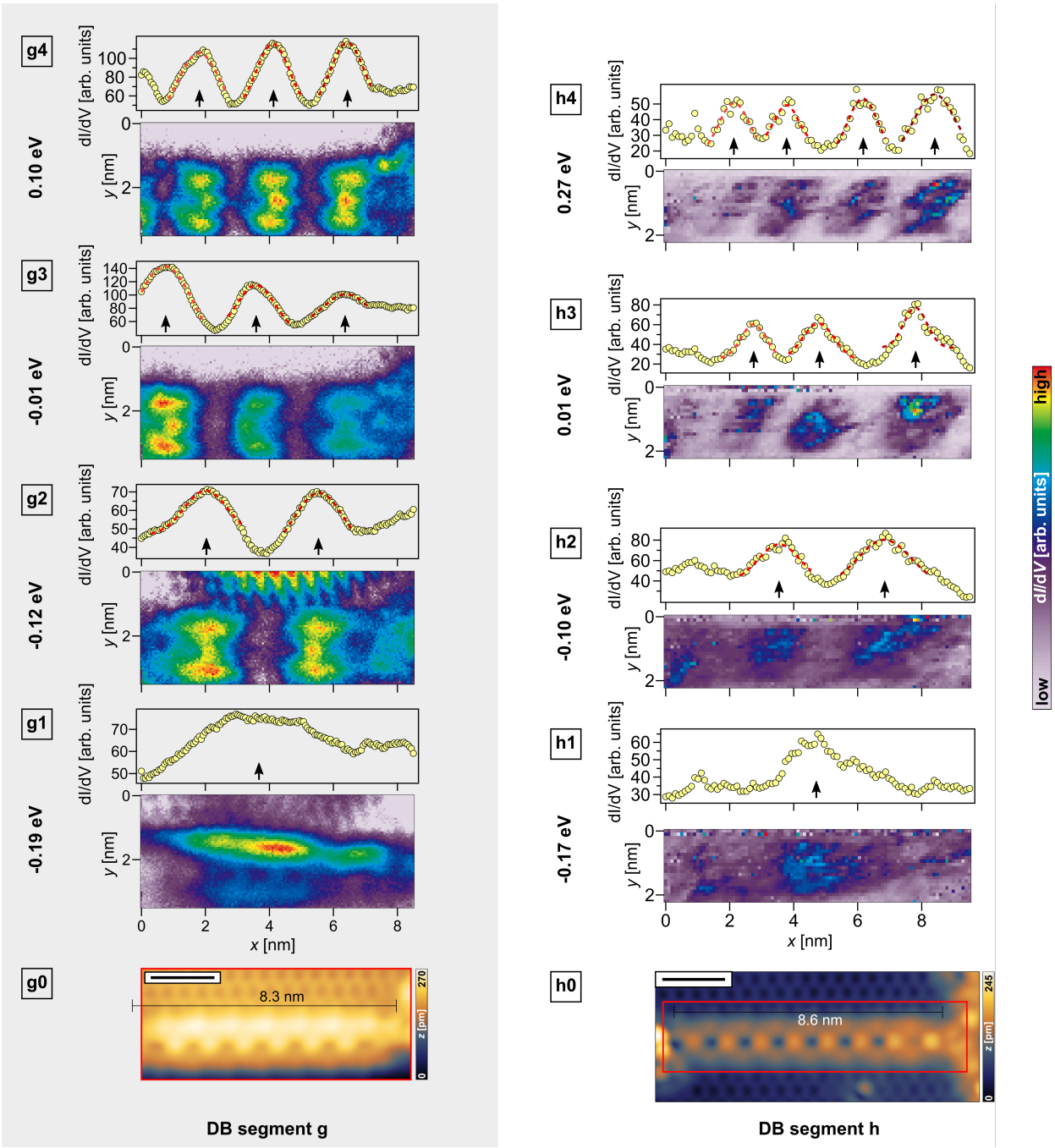

Figure E.3: (g) – (h), Fabry-Pérot states in different domain boundaries with varying lengths; continuation. *Figure reprinted from Ref. [159] under a Creative Commons Attribution 4.0 International (CC BY 4.0) License.*

E.4 Variation of the valence band onset measured at different domain boundaries

Due to a variation of the local chemical potential which is attributed to both the n-doping of the SiC substrate and the local defect/impurity concentration in the bismuthene film, the position of the valence band onset measured at the vicinity of DB is varying accordingly. For the numerical extraction of the valence band onset, first the noise level was fitted using a constant within the single-particle band gap of bismuthene (it determines the mean tunneling intensity within the single particle gap). Then the logarithmically plotted VB edge was fitted with a linear function. The intersection is taken as the valence band onset. The spread of the numerical values across the respective DB is taken as the basis for calculating the standard deviation (s.d.) plotted as error bars in Fig. E.4. Again, the reasons for the variation of the local chemical potential are the nitrogen doping centers in the substrate that display some density variations on length scales of 10 – 100 nm, i.e., on a relevant length scale of the presented investigations. Recently, similar effects were also observed on other SiC-supported monolayers [33]. Moreover, the bismuthene film exhibits local variation of film inhomogeneities, stemming from defects or impurities, which can be seen from Fig. 6.5**a**. It is to be expected that these variations also may cause small local fluctuations of the chemical potential.

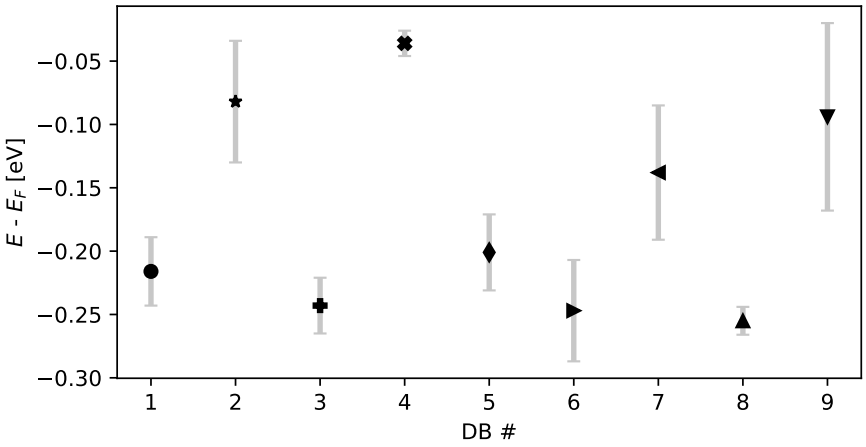

Figure E.4: Valence band onset measured at the vicinity of each DB 1 – 9 (for details on the extrapolation see text). The valence band onsets account for a local variation of the local chemical potential μ, which are found on the bismuthene surface. The error bars indicate the standard deviation (s.d.) from the mean values in an area around each DB. The valence band onsets are used to consistently define an energy onset between all DBs. The data points are assigned marker symbols according to the marker symbols for each DB used in Fig. 6.8a. *Figure reprinted from Ref. [159] under a Creative Commons Attribution 4.0 International (CC BY 4.0) License.*

Additional Information on optical spectroscopy of bismuthene

F.1 Spatial variation of the STS bulk spectrum

Figure F.1**a** shows STS $\mathrm{d}I/\mathrm{d}V$ spectra measured over a wide spatial range spanning multiple unit cells of the pristine bulk bismuthene lattice shown in Fig. F.1**b**. Each $\mathrm{d}I/\mathrm{d}V$ spectrum in Fig. F.1**a** represents an average over spectra measured in a 0.5 nm × 0.5 nm area, as marked by the red grid lines in the constant current STM image in Fig. F.1**b**. Specific attention is devoted to the energy region marked by red dashed lines in Fig. F.1**a** which is located near the conduction band onset. It is apparent that there is a particularly strong variation in this energy region of the spectrum. Whereas it shows a smooth and featureless line shape at some areas as in the spectrum labeled as (3, 4), at other areas the spectra show a more peaky line shape, as for example in the spectrum labeled as (1, 4). The enhanced $\mathrm{d}I/\mathrm{d}V$ connected to the peak in the indicated energy region in the spectrum labeled as (1, 4) is connected to a locally enhanced LDOS and can also be seen in the constant energy $\mathrm{d}I/\mathrm{d}V$ map in Fig. F.1**c**. At the same time the bismuthene monolayer lattice is absolutely homogeneous and fully intact over the entire area that was measured, see Fig. F.1**b**. From this homogeneity one would not expect a locally enhanced LDOS. Thus, the enhanced LDOS which occurs disconnected from the film's topography implies that its origin is not intrinsic to the bismuthene film itself. It is attributed to a localized defect or donor state in the SiC substrate instead. The most obvious candidate is the nitrogen donor level of the n-doped SiC substrate, which has a binding energy of approximately 70 meV with respect to the conduction band minimum of the substrate and/or localized SiC lattice defect states.

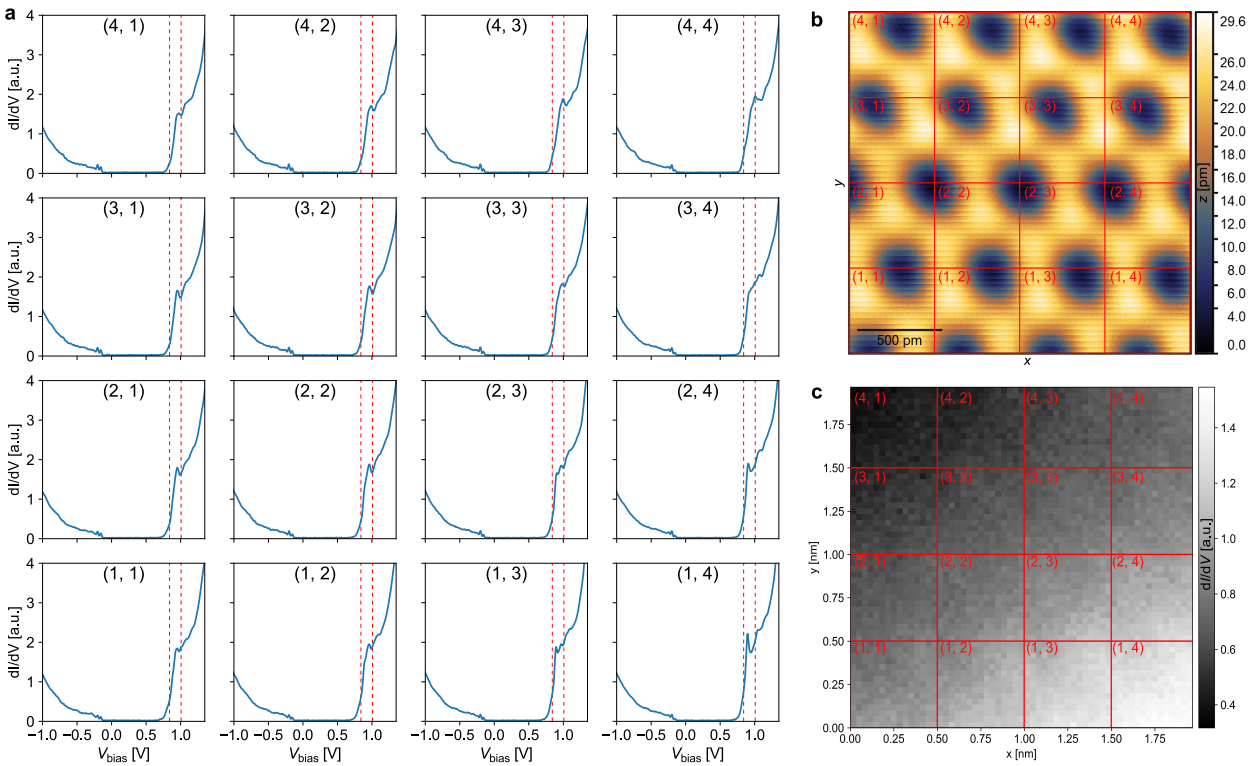

Figure F.1: Local variations of STS spectra. – **(a),** Position dependent $\mathrm{d}I/\mathrm{d}V$ spectra averaged over the respective region of the grid specified in **b**. The total spatial area reflects the 2 nm × 2 nm bismuthene bulk region depicted in **c**. ($T = 4.2\,\mathrm{K}$ and $V_{\mathrm{set}} = -1.4\,\mathrm{V}$, $I_{\mathrm{set}} = 500\,\mathrm{pA}$, $V_{\mathrm{mod}} = 10\,\mathrm{mV}$.) **(b),** Constant-current map of the measured bulk bismuthene area. The bismuthene lattice is intact throughout the whole area and does not show any topographic irregularities such as point defects. ($T = 4.2\,\mathrm{K}$ and $V_{\mathrm{set}} = -0.5\,\mathrm{V}$, $I_{\mathrm{set}} = 50\,\mathrm{pA}$.) **(c),** Constant energy $\mathrm{d}I/\mathrm{d}V$ map averaged over the bias voltage range $V_{\mathrm{bias}} = 0.840...1.008\,\mathrm{eV}$ as indicated by the red dashed lines in the subpanels of **a**. The higher intensity in the section marked by (1, 4) reflects the peak at the onset of the conduction band states in the corresponding $\mathrm{d}I/\mathrm{d}V$ spectrum in **a**. ($T = 4.2\,\mathrm{K}$ and $V_{\mathrm{set}} = -1.4\,\mathrm{V}$, $I_{\mathrm{set}} = 500\,\mathrm{pA}$, $V_{\mathrm{mod}} = 10\,\mathrm{mV}$.) *Figure reprinted and adapted from Ref. [124] under a Creative Commons Attribution 4.0 International (CC BY 4.0) License.*

F.2 Influence of bismuthene oxidation on the photo-reflectance spectrum

Figure F.2 compares a photo-reflectance (PR) spectrum of bismuthene kept under N_2 inert gas atmosphere (as explained in Sec. 7.2.1) with PR spectra after exposure of bismuthene to ambient air. When the bismuthene sample is kept in the inert gas atmosphere (blue spectrum) two prominent peaks (A-/B-peaks) are observed at energies $E_A \approx 1.19\,\text{eV}$ and $E_B \approx 1.6\,\text{eV}$, respectively. Notably, the same quality of the optical PR spectrum can be preserved over weeks (not shown) as long as the inert gas protection is not lifted. Exposing the same sample to ambient air for only 10 min (orange spectrum) results in a drastic drop of the *A*-peak intensity (the *B*-peak was not measured in this experiment). After one week in ambient air (green spectrum), the PR signal is completely lost. This is clear evidence that oxidation of the bismuthene film results in a full destruction of its optical response.

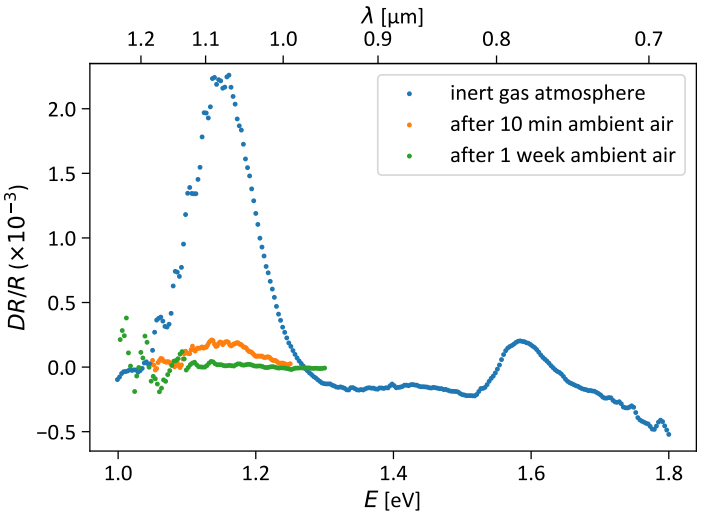

Figure F.2: Influence of oxidation on PR spectrum. – The spectra were recorded on the same sample. After successful preparation under UHV conditions it was transferred to and sealed within a CF-flange metal container filled with a N_2 inert gas atmosphere (< 0.1 ppm H_2O; < 0.1 ppm O_2) and equipped with a window (alkali borosilicate) that is transparent in a suitable optical range for the PR measurements. The blue data points represent the PR spectrum of the bismuthene sample still inside the N_2 inert gas atmosphere (same as for the spectrum in Fig. 2b of the main text). The spectrum shows the A-/B-resonance associated with the excitons in bismuthene centered at $E_A \approx 1.19\,\text{eV}$ and $E_B \approx 1.6\,\text{eV}$ energies, respectively. The orange data points represent the PR spectrum from the same sample after opening the CF-flange metal container to ambient air for 10 min. A drastic decrease of the optical resonance is observed. The green data points correspond to the PR spectrum after exposure of the sample to ambient air for 1 week. The optical response has completely disappeared down to the noise level. *Figure reprinted and adapted from Ref. [124] under a Creative Commons Attribution 4.0 International (CC BY 4.0) License.*

Additional Information on trARPES of bismuthene

G.1 EDC fit of excited states at the K-point

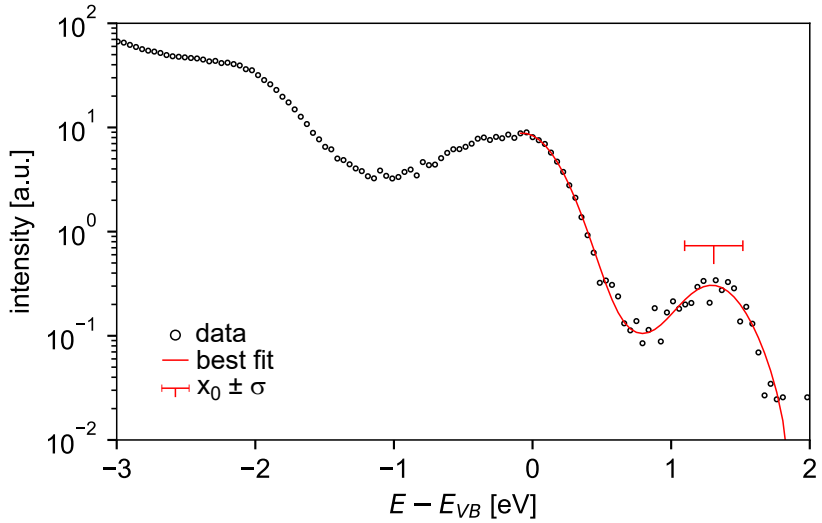

Figure G.1: Data points show orange spectrum from Fig. 8.2**c**. The least-square fit (red curve) to the data uses a Gaussian tail + linear function for the background + a Gaussian peak with center position E_0 and variance σ (red marker) for the CB* states. Best fit: $E_0 \pm \sigma = (1.31 \pm 0.21)\,\mathrm{eV}$.

G.2 Band mapping at $h\nu = 1.55\,\mathrm{eV}$

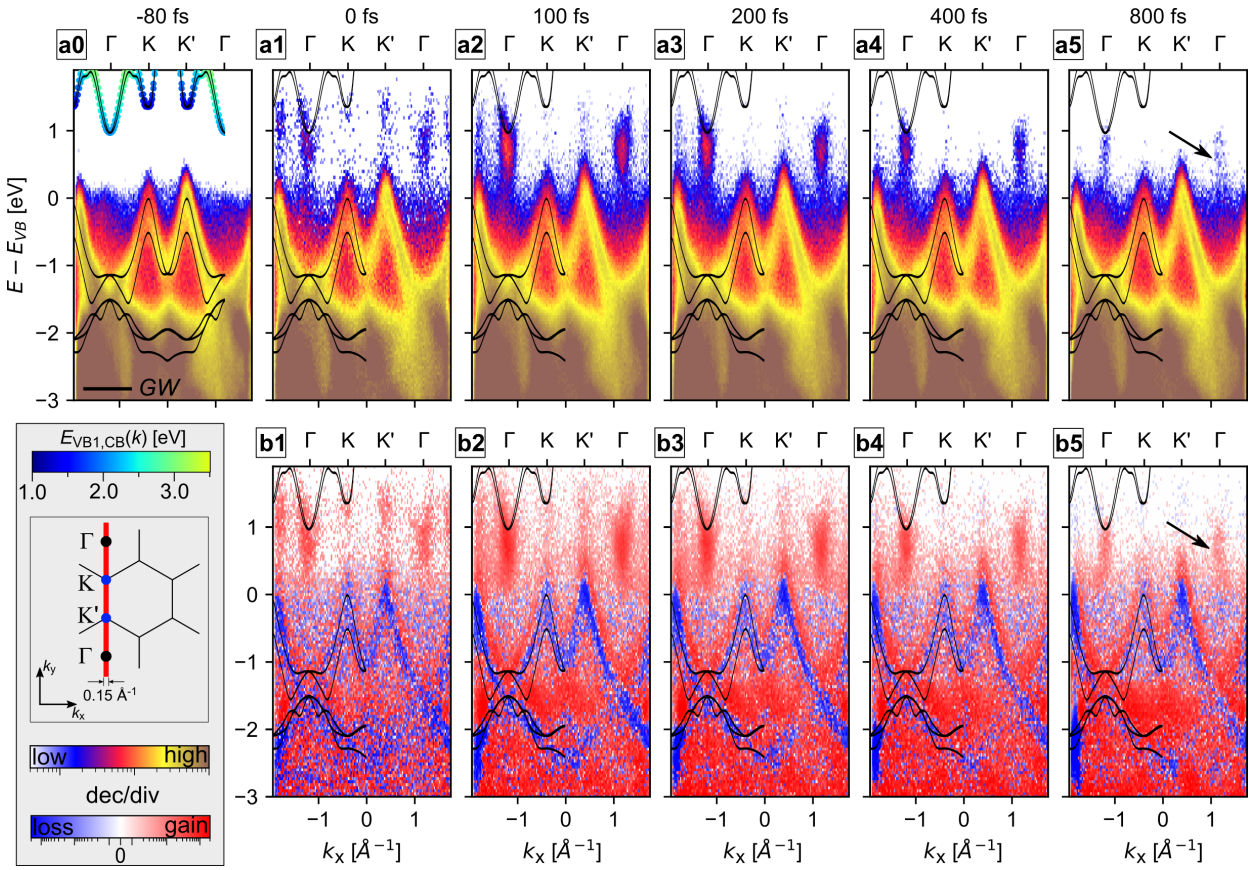

Figure G.2: Transiently occupied in-gap states (complementary to Fig. 8.2b). – **(a0)** – **(a5),** trARPES maps from Fig. 8.2 ($h\nu_{\mathrm{pump}} = 1.55\,\mathrm{eV}$, $h\nu_{\mathrm{probe}} = 21.7\,\mathrm{eV}$, T = RT) on a planar bismuthene sample at the delay times indicated above each image (averaged over a $\pm 50\,\mathrm{fs}$ delay time window). The trARPES maps are cuts along the $\Gamma - K$ direction (red line in the schematic of the bismuthene Brillouin zone underneath **a0**) extracted from the momentum microscope measurements in Fig. 8.2**b**. **(b1)** – **(b5),** Differential photoemission intensity, i.e., the pre-excitation signal from **a0** is subtracted for each delay time step. Black lines in **a0** – **a5** and **b1** – **b5** correspond to the band structure from DFT and *GW* calculations. The *GW* conduction bands in **a** are colored according to $E_{\mathrm{VB1,CB}}(k) = E_{GW,\mathrm{CB}}(k) - E_{GW,\mathrm{VB1}}(k)$, where $E_{GW,\mathrm{VB1}}$ is the topmost *GW* VB to indicate the possibility for photo-excitation with the pump pulse.

G.3 Simulation of photoemission matrix element effects in constant energy ARPES

The trARPES spectra in Fig. 8.2 showed a strong asymmetry of the CB* states at the Γ-valleys, which is due to photoemission matrix elements $M_{f,i} = |\langle\psi_f| \boldsymbol{\Delta} |\psi_i\rangle|^2$ between initial and final states. Figure G.3**a** depicts the excited states in the vicinity of the CB* Γ valleys only. In addition, Figs. G.3**b, c** are the isolated photoemission signal around the Γ valleys of the 2$^{\text{nd}}$ BZs for energies $E - E_{\text{VB}} = 1.35\,\text{eV}$ and $E - E_{\text{VB}} = 0.85\,\text{eV}$, respectively. It can be seen that at $E - E_{\text{VB}} = 0.85\,\text{eV}$, i.e., close to the Γ-valley minima, the photoemission distribution is isotropic around the Γ points in Fig. G.3**c**. At the energy $E - E_{\text{VB}} = 1.35\,\text{eV}$ the photoemission distribution changes from isotropic to anisotropic in Fig. G.3**b**. The direction of anisotropy is indicated by green arrows. The following presents a simple modelling of the measured photoemission matrix elements with the open source software package *chinook* [95] implemented in the Python programming language. It employs the simplifications of using free-electron plane wave final states in the matrix element calculations and is working within a tight-binding framework wherein the initial states can be described by localized atomic-like orbitals.

Concerning the tight-binding approach to the electronic band structure of bismuthene, the black dashed lines in Fig. G.3**e** represent the band structure according to the minimal tight-binding model that includes only Bi p_x, p_y orbitals and nearest neighbor hopping (NN) as first elaborated in Ref. [6]. Furthermore, the red lines in Fig. G.3**e** correspond to an electronic band structure calculation based on a model elaborated in this work that includes next nearest neighbor hopping (NNN) and therefore introduces the additional Slater-Koster parameters $V^2_{pp\sigma}$ and $V^2_{pp\pi}$. In this case, all tight-binding parameters were chosen in order to closely reproduce the *GW* band structure of bismuthene on SiC depicted as green lines in Fig. G.3**e** (see Ch. 7 for details of the computation). The explicit tight-binding parameters that were used for the adapted NNN tight-binding model of bismuthene are listed in Tab. G.1.

The simulated constant energy photoemission map based on the modelling parameters listed in Tab. G.1 and based on the adapted bismuthene tight-binding model with NNN hopping in Fig. G.3**e** is presented in Fig. G.3**d**. It captures the observed anisotropy of the photoemission intensity around the Γ-points in Fig. G.3**b** in a qualitatively correct way.

TB parameters	$V^1_{pp\sigma}$ [eV]	$V^1_{pp\pi}$ [eV]	$V^2_{pp\sigma}$ [eV]	$V^2_{pp\pi}$ [eV]	λ_{SOC} [eV]	λ_{R} [eV]
	1.890	-0.660	-0.200	0.064	0.814	0.043

chinook parameters	pol.	inc. angle	$h\nu$ [eV]	$E - E_{\text{VB}}$ [eV]	k-broadening [Å^{-1}]
	p-pol.	65° from surf. normal	21.7	1.35	0.2

Table G.1: The NN ($V^1_{pp\sigma}$, $V^1_{pp\pi}$) and NNN ($V^2_{pp\sigma}$, $V^2_{pp\pi}$) tight-binding Slater-Koster parameters, SOC parameter (λ_{SOC}), and Rashba parameter (λ_{R}) adapted from the model given in Ref. [6] to adequately reproduce the bismuthene *GW* band structure in Fig. G.3e are given. The model parameters for ARPES simulation with the *chinook* [95] package in Fig. G.3d are also listed.

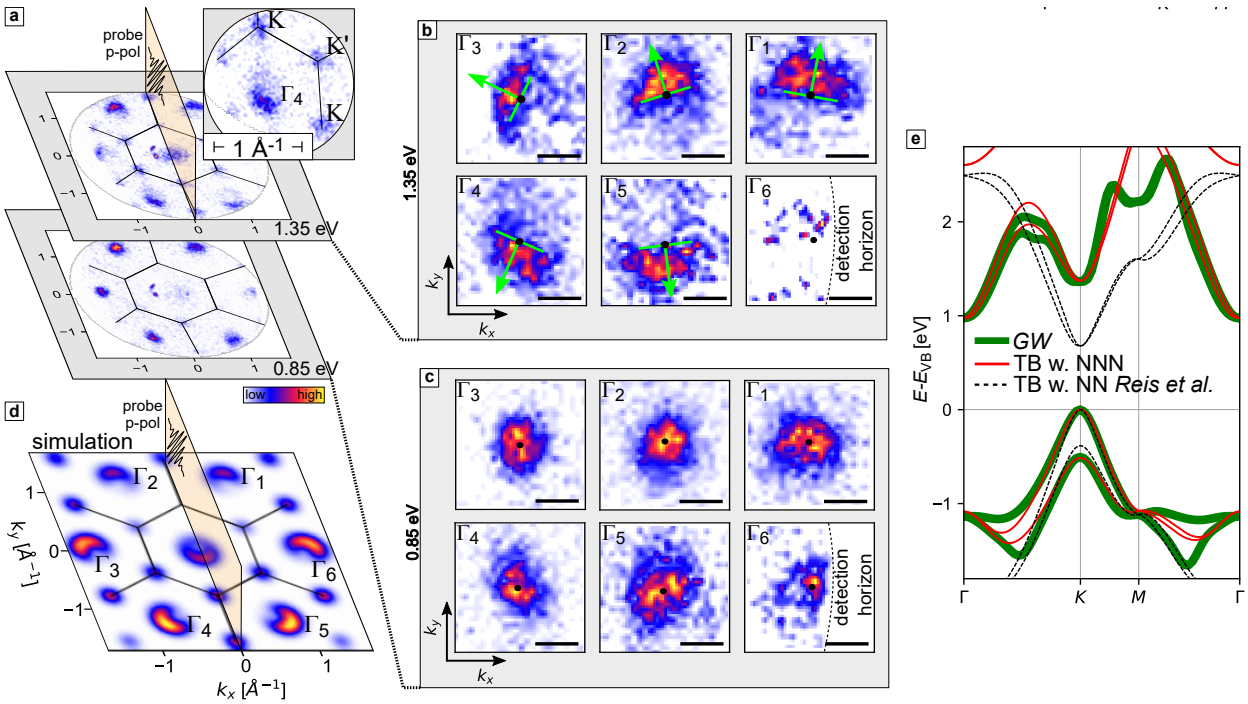

Figure G.3: ARPES simulation using the *chinook* program. **(a),** Constant energy 2D momentum space maps from Fig. 8.2**b** (p-polarized probe pulse incident 65° from surface normal, $h\nu_{\text{probe}} = 21.7\,\text{eV}$, $h\nu_{\text{pump}} = 1.55\,\text{eV}$, $T = \text{RT}$) of the excited states across the 1st and 2nd BZs (indicated by black lines) of a planar bismuthene sample at delay time $\Delta t = (0 \pm 50)\,\text{fs}$ and energies $E - E_{\text{VB}} = (0.85 \pm 0.10)\,\text{eV}$ and $E - E_{\text{VB}} = (1.35 \pm 0.30)\,\text{eV}$. **(b),** Detailed view into the excited states at the Γ-points Γ_1–Γ_6 of the 2nd BZs in **a** at $E - E_{\text{VB}} = (1.35 \pm 0.30)\,\text{eV}$. The green arrows indicate the orientation of increased photoemission intensity around the Γ-points which are marked by black dots. **(c),** Detailed view into the excited states at the Γ-points Γ_1–Γ_6 of the 2nd BZs in **a** at $E - E_{\text{VB}} = (0.85 \pm 0.10)\,\text{eV}$. The photoemission intensity around the Γ-points, which are marked by black dots, is fully symmetric. **(d),** Simulation of a constant energy ARPES map with the simulation program *chinook* [95]. Details are given in the text. **(e),** *GW* band structure (green lines), original tight-binding band structure (black dashed lines) from Reis *et al.* in Ref. [6] taking into account Bi p_x, p_y orbitals and nearest neighbor (NN) hopping, and adapted tight-binding band structure (red lines) taking into account Bi p_x, p_y orbitals and next nearest neighbor (NNN) hopping. The tight-binding parameters of the adapted model are given in Tab. G.1, and this model is used in the ARPES simulation in **d**.

G.4 EDC fits at $h\nu = 3.10\,\mathrm{eV}$

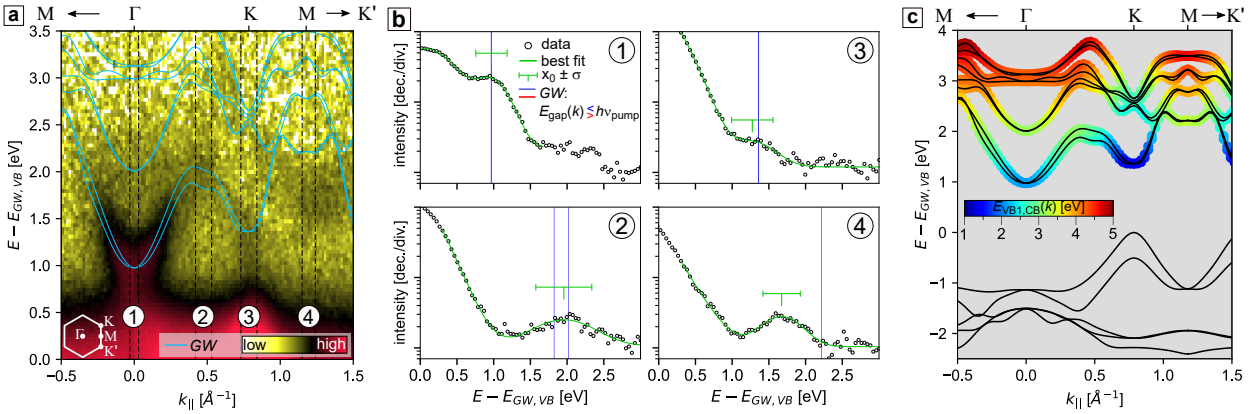

Figure G.4: Excited state mapping with $h\nu_{\mathrm{pump}} = 3.10\,\mathrm{eV}$ (complementary to Fig. 8.3). – **(a),** Excited state trARPES map from Fig. 8.3 ($h\nu_{\mathrm{pump}} = 3.10\,\mathrm{eV}$, $h\nu_{\mathrm{probe}} = 21.7\,\mathrm{eV}$, T = RT, $\Delta t = (0 \pm 50)\,\mathrm{fs}$, $F = 0.03\,\mathrm{mJ\,cm^{-2}}$). Blue lines: *GW* quasi-particle CBs. The experimental energy scale was shifted such that the minimum of the CB* states at the Γ-valley matches the minimum of the *GW* quasi-particle band at the Γ-valley. The energy onset of the *GW* quasi-particle VB at the *K*-point ($E_{GW,\mathrm{VB}}$) is used as zero reference energy. **(b),** Data points show EDCs ① – ④ averaged over the respective $k_{\parallel}$-range indicated with dashed black lines in **a**. For the least-square fits to the data (green lines) a Gaussian tail + linear function for the background + a Gaussian peak with center position E_0 and variance σ (green markers) for the CB* states is used. Best fit results and comparison to *GW* are summarized in Tab. G.2. Blue (red) lines: *GW* quasi-particle excitations for which $E_{\mathrm{VB1,CB}}(k) < h\nu_{\mathrm{pump}}$ ($E_{\mathrm{VB1,CB}}(k) > h\nu_{\mathrm{pump}}$) (cf. **c**). **(c),** The black lines are the *GW* band structure. The *GW* conduction bands are colored according to $E_{\mathrm{VB1,CB}}(k) = E_{GW,\mathrm{CB}}(k) - E_{GW,\mathrm{VB1}}(k)$, where $E_{GW,\mathrm{VB1}}$ is the topmost *GW* VB, to indicate the possibility for photo-excitation with the pump-pulse.

EDC in Fig. 8.3	①	②	③	④
GW	0.97 eV	1.83 eV[a]; 2.03 eV[b]	1.36 eV	2.22 eV
fit: $E_0 \pm \sigma$	(0.97[c] ± 0.21) eV	(1.96 ± 0.38) eV	(1.27 ± 0.28) eV	(1.67 ± 0.25) eV

Table G.2: Best fit results of Gaussian peaks with center positions E_0 and variance σ of the CB* states from EDCs in Fig. G.4 and comparison to values from *GW*. [a] lower energy band; [b] higher energy band; [c] E_0 set as constraint (no fit value). The energy scale is set relative to the onset of the *GW* VB ($E_{GW,\mathrm{VB}}$).

Figure G.4 complements the evaluation accompanying Fig. 8.3 in the main text by showing detailed EDCs ① – ④ and the corresponding best fits. The *k*-averaging windows ① – ④ (marked by dashed lines in Fig. G.4**a**) are chosen around $k_{\parallel}$-values where in the false color plot a clear band dispersion is observed. The quantitative fit analysis of the EDCs at these momenta is presented in Fig. G.4**b**. The least-square fit (green lines) uses a Gaussian tail + linear function for the background + a Gaussian peak characterized by a center position E_0 and Gaussian peak variance σ (green markers) for the dispersive features in the CB* states. The numerical fit results are summarized in Tab. G.2 and compared to the energy position of

the *GW* bands at the respective point in k-space (blue and red lines in Fig. G.4**b**). Note that the energy E_0 matches the corresponding value from the *GW* band at Γ exactly because the experimental energy scale has been shifted accordingly (cf. EDC ①). Further, the energy position of the CB* for the EDCs ② and ③ match very well the *GW* value. Importantly, however, these energy positions are only meaningful relative to the minimum of the CB* Γ-valley and the onset of the *GW* quasi-particle CB states at Γ, because of the adapted experimental energy scale as described above. Interestingly, the observed peak position of the dispersive CB* feature around the M-point (cf. EDC ④ in Fig. G.4**b**) lies 0.55 eV below the energy position of the *GW* CB. Note that according to the *GW* calculations no direct optical VB → CB excitations are even expected here, i.e., $E_{\mathrm{VB1,CB}}(k) > h\nu_{\mathrm{pump}}$ holds in the vicinity of the M-point, see Fig. G.4**c**. Possible explanations for this strong discrepancy are discussed in connection to Fig. 8.3 in the main text.

G.5 Thickness dependence of the DFT band structure of bismuthene

Section 8.1.2 showed that the excited state conduction band spectrum measured by trARPES exhibits a spectral feature ($S1$) that deviates strongly from the GW quasi-particle band structure. One explanation that has been discussed in the main part was that considering only four Si-C bi-layers as substrate in the GW simulation could have led to this discrepancy of experiment and GW simulation close to the M-point CB valley. Figure G.5 presents the influence of the number of included Si-C bi-layers based on DFT band structure calculations. These calculations were performed by A. Consiglio with the Quantum Espresso simulation package [195]. Here, norm-conserving pseudo-potentials were used to quantify the electron-ion interactions and the Perdew-Burke-Ernzerhof (PBE) functional [48] was used for the exchange-correlation potential. Spin-orbit coupling was included self-consistently. The structure that was simulated contained either four Si-C bi-layers for the substrate (see Fig. G.5**a**) or eight Si-C bi-layers for the substrate (see Fig. G.5**b**). In both cases the bismuthene monolayer is placed on top.

The contribution to the band from the Bi (purple), Si (grey), and C (black) orbital character is indicated separately in Fig. G.5. From this projection it can be seen that the lowest CB states around the M-point relate almost exclusively to substrate atoms. The comparison of Fig. G.5**a** and Fig. G.5**b** shows that these states occupy lower energies, the more Si-C bilayers are included in the calculation. It is assumed that both aspects do qualitatively also hold true for GW quasi-particle calculations.

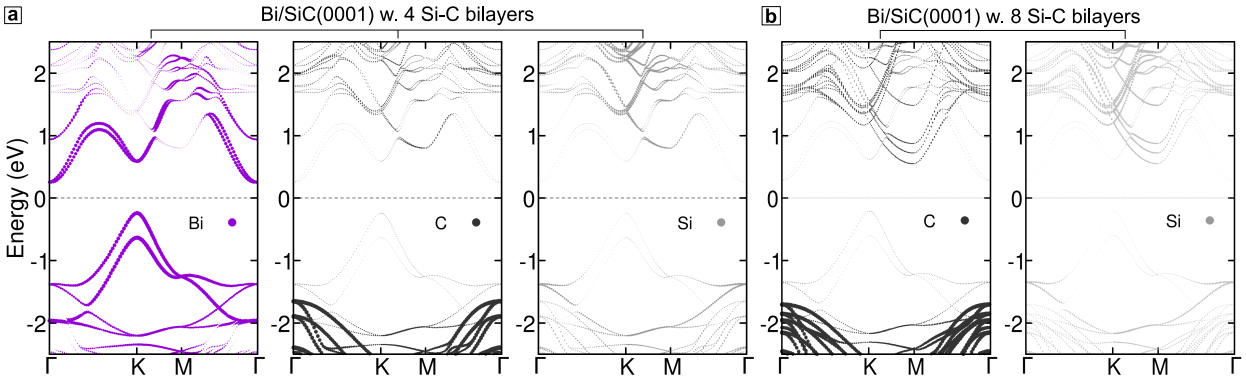

Figure G.5: Thickness dependence of DFT band structure. – Ab-initio electronic structure modeling by DFT of monolayer bismuthene on SiC(0001) with inclusion of SOC. The band strucure is plotted along a path connecting high-symmetry points of bismuthene's Brillouin zone. **(a),** The simulated structure contained four Si-C bi-layers for the substrate and the bismuthene monolayer placed on top. **(b),** The simulated structure contained eight Si-C bi-layers for the substrate and the bismuthene monolayer placed on top. The low-energy conduction band states around the M-point relate mostly to the SiC substrate. These states show a tendency of occupying lower energies the more Si-C bilayers are included. *Figures **a** and **b** were provided by courtesy of Armando Consiglio.*

G.6 Numerical fit of excited state valence and conduction band dispersions

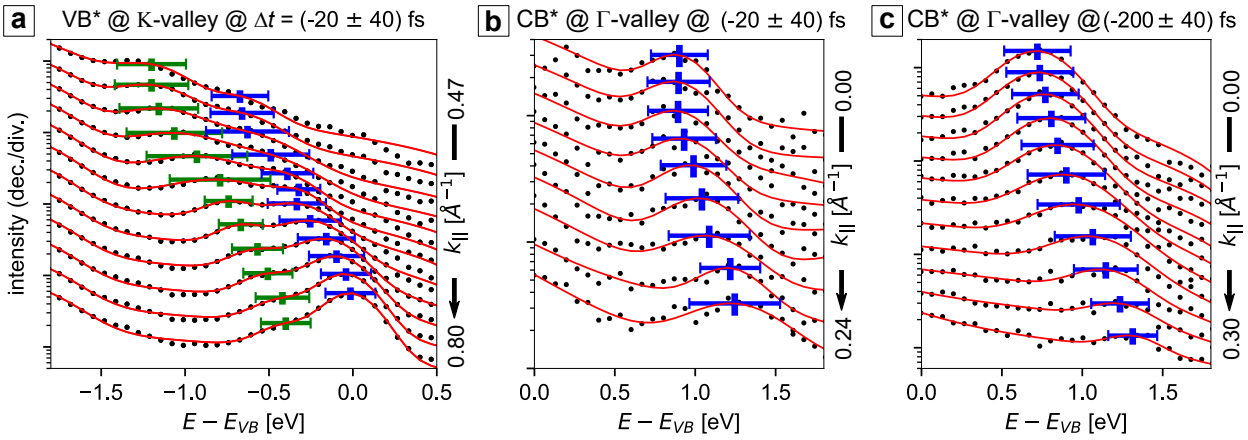

Figure G.6: EDC fits for the determination of the band gap re-normalization. (a), EDCs around the K-valley extracted from Figs. 8.4**a** used for fitting of the VB* peak positions (black dots in Figs. 8.4**a**). For the least-square fits (red lines) a Gaussian tail + linear function for the background + two Gaussian peaks for the VB* states were used. The best fit Gaussian peak position for the lower Rashba split VB* state is given by a green marker where the error bar relates to the variance σ of the Gaussian peak. The best fit Gaussian peak position for the upper Rashba split VB* state is given by a blue marker where the error bar relates to the variance σ of the Gaussian peak. **(b), (c),** EDCs around the Γ-valley extracted from Figs. 8.4**a, b**, respectively, and used for fitting of the CB* peak positions at two different delay times (green dots in Figs. 8.4**a, b**). For the least-square fits (red lines) in **b, c** a Gaussian tail + linear function for the background + a Gaussian peak for the CB* states were used. The best fit Gaussian peak position for the CB* state is given by a blue marker where the error bar relates to the variance σ of the Gaussian peak. A k-bin window of 0.06 Å^{-1} and a E-bin window of 67 meV were used for all EDCs.

Bibliography

[1] C. L. Kane and E. J. Mele, Phys. Rev. Lett. **95**, 226801 (2005).

[2] B. A. Bernevig and S.-C. Zhang, Phys. Rev. Lett. **96**, 106802 (2006).

[3] B. A. Bernevig, T. L. Hughes and S.-C. Zhang, Science **314**, 1757 (2006).

[4] M. König, S. Wiedmann, C. Brüne, A. Roth, H. Buhmann, L. W. Molenkamp, X.-L. Qi and S.-C. Zhang, Science **318**, 766 (2007).

[5] S. Wu, V. Fatemi, Q. D. Gibson, K. Watanabe, T. Taniguchi, R. J. Cava and P. Jarillo-Herrero, Science **359**, 76 (2018).

[6] F. Reis, G. Li, L. Dudy, M. Bauernfeind, S. Glass, W. Hanke, R. Thomale, J. Schäfer and R. Claessen, Science **357**, 287 (2017).

[7] F. Reis, *Realization and Spectroscopy of the Quantum Spin Hall Insulator Bismuthene on Silicon Carbide*, Ph.D. thesis, Julius-Maximilians-Universität Würzburg (2021).

[8] R. Stühler, F. Reis, T. Müller, T. Helbig, T. Schwemmer, R. Thomale, J. Schäfer and R. Claessen, Nature Physics **16**, 47 (2020).

[9] G. Li, W. Hanke, E. M. Hankiewicz, F. Reis, J. Schäfer, R. Claessen, C. Wu and R. Thomale, Phys. Rev. B **98**, 165146 (2018).

[10] D. J. Thouless, M. Kohmoto, M. P. Nightingale and M. den Nijs, Phys. Rev. Lett. **49**, 405 (1982).

[11] M. Z. Hasan and C. L. Kane, Rev. Mod. Phys. **82**, 3045 (2010).

[12] J. E. Avron, R. Seiler and B. Simon, Phys. Rev. Lett. **51**, 51 (1983).

[13] M. Kohmoto, Annals of Physics **160**, 343 (1985).

[14] K. v. Klitzing, G. Dorda and M. Pepper, Phys. Rev. Lett. **45**, 494 (1980).

[15] M. J. Gilbert, Communications Physics **4**, 70 (2021).

[16] F. D. M. Haldane, Phys. Rev. Lett. **61**, 2015 (1988).

[17] C. L. Kane and E. J. Mele, Phys. Rev. Lett. **95**, 146802 (2005).

[18] L. Fu and C. L. Kane, Phys. Rev. B **74**, 195312 (2006).

[19] L. Fu and C. L. Kane, Phys. Rev. B **76**, 045302 (2007).

[20] Y. Ando, J. Phys. Soc. Jpn. **82**, 102001 (2013).

[21] S. Datta, *Electronic Transport in Mesoscopic Systems*, Cambridge Studies in Semiconductor Physics and Microelectronic Engineering, Cambridge University Press (1995).

[22] A. Roth, C. Brüne, H. Buhmann, L. W. Molenkamp, J. Maciejko, X.-L. Qi and S.-C. Zhang, Science **325**, 294 (2009).

[23] C. Brüne, A. Roth, H. Buhmann, E. M. Hankiewicz, L. W. Molenkamp, J. Maciejko, X.-L. Qi and S.-C. Zhang, Nature Physics **8**, 485 (2012).

[24] K. Bendias, S. Shamim, O. Herrmann, A. Budewitz, P. Shekhar, P. Leubner, J. Kleinlein, E. Bocquillon, H. Buhmann and L. W. Molenkamp, Nano Letters **18**, 4831 (2018).

[25] E. Sajadi, T. Palomaki, Z. Fei, W. Zhao, P. Bement, C. Olsen, S. Luescher, X. Xu, J. A. Folk and D. H. Cobden, Science **362**, 922 (2018).

[26] V. Fatemi, S. Wu, Y. Cao, L. Bretheau, Q. D. Gibson, K. Watanabe, T. Taniguchi, R. J. Cava and P. Jarillo-Herrero, Science **362**, 926 (2018).

[27] B. Sun, W. Zhao, T. Palomaki, Z. Fei, E. Runburg, P. Malinowski, X. Huang, J. Cenker, Y.-T. Cui, J.-H. Chu, X. Xu, S. S. Ataei, D. Varsano, M. Palummo, E. Molinari, M. Rontani and D. H. Cobden, Nature Physics **18**, 94 (2022).

[28] S. Tang, C. Zhang, D. Wong, Z. Pedramrazi, H.-Z. Tsai, C. Jia, B. Moritz, M. Claassen, H. Ryu, S. Kahn, J. Jiang, H. Yan, M. Hashimoto, D. Lu, R. G. Moore, C.-C. Hwang, C. Hwang, Z. Hussain, Y. Chen, M. M. Ugeda, Z. Liu, X. Xie, T. P. Devereaux, M. F. Crommie, S.-K. Mo and Z.-X. Shen, Nature Physics **13**, 683 (2017).

[29] P. Sternativo and F. Dolcini, Phys. Rev. B **89**, 035415 (2014).

[30] K. F. Mak, D. Xiao and J. Shan, Nature Photonics **12**, 451 (2018).

[31] A. Molle, J. Goldberger, M. Houssa, Y. Xu, S.-C. Zhang and D. Akinwande, Nature Materials **16**, 163 (2017).

[32] T. Seyller, Applied Physics A **85**, 371 (2006).

[33] M. Bauernfeind, J. Erhardt, P. Eck, P. K. Thakur, J. Gabel, T.-L. Lee, J. Schäfer, S. Moser, D. Di Sante, R. Claessen and G. Sangiovanni, Nature Communications **12**, 5396 (2021).

[34] K. Järrendahl, R. F. Davis and Y. Soo Park, *Chapter 1 Materials Properties and Characterization of SiC*, in *Semiconductors and Semimetals*, Band 52, pages 1–20, Elsevier (1998).

[35] M. Stockmeier, R. Müller, S. A. Sakwe, P. J. Wellmann and A. Magerl, Journal of Applied Physics **105**, 033511 (2021).

[36] T.-L. Lee, *Private communication with Dr. Tien-Lin Lee, Principal Beamline Scientist on I09 at Diamond Light Source, Harwell Science and Innovation Campus, Didcot OX11 0DE, UK.*

[37] Z.-Q. Huang, C.-H. Hsu, F.-C. Chuang, Y.-T. Liu, H. Lin, W.-S. Su, V. Ozolins and A. Bansil, New Journal of Physics **16**, 105018 (2014).

[38] G.-F. Zhang, Y. Li and C. Wu, Phys. Rev. B **90**, 075114 (2014).

[39] C.-C. Liu, S. Guan, Z. Song, S. A. Yang, J. Yang and Y. Yao, Phys. Rev. B **90**, 085431 (2014).

[40] M. Zhou, W. Ming, Z. Liu, Z. Wang, Y. Yao and F. Liu, Scientific Reports **4**, 7102 (2014).

[41] M. Zhou, W. Ming, Z. Liu, Z. Wang, P. Li and F. Liu, Proceedings of the National Academy of Sciences **111**, 14378 (2014).

[42] C.-H. Hsu, Z.-Q. Huang, F.-C. Chuang, C.-C. Kuo, Y.-T. Liu, H. Lin and A. Bansil, New Journal of Physics **17**, 025005 (2015).

[43] S. Sun, J.-Y. You, S. Duan, J. Gou, Y. Z. Luo, W. Lin, X. Lian, T. Jin, J. Liu, Y. Huang, Y. Wang, A. T. S. Wee, Y. P. Feng, L. Shen, J. L. Zhang, J. Chen and W. Chen, ACS Nano (2021).

[44] Y. Xu, B. Yan, H.-J. Zhang, J. Wang, G. Xu, P. Tang, W. Duan and S.-C. Zhang, Phys. Rev. Lett. **111**, 136804 (2013).

[45] C. Niu, G. Bihlmayer, H. Zhang, D. Wortmann, S. Blügel and Y. Mokrousov, Phys. Rev. B **91**, 041303 (2015).

[46] G. Kresse and J. Furthmüller, Phys. Rev. B **54**, 11169 (1996).

[47] G. Kresse and D. Joubert, Phys. Rev. B **59**, 1758 (1999).

[48] J. P. Perdew, K. Burke and M. Ernzerhof, Phys. Rev. Lett. **77**, 3865 (1996).

[49] J. Heyd, G. E. Scuseria and M. Ernzerhof, The Journal of Chemical Physics **118**, 8207 (2003).

[50] A. V. Krukau, O. A. Vydrov, A. F. Izmaylov and G. E. Scuseria, J. Chem. Phys. **125**, 224106 (2006).

[51] P. Hohenberg and W. Kohn, Phys. Rev. **136**, B864 (1964).

[52] W. Kohn and L. J. Sham, Phys. Rev. **140**, A1133 (1965).

[53] F. Bechstedt, *Many-Body Approach to Electronic Excitations*, Springer, Berlin, Heidelberg (2015).

[54] L. J. Sham and M. Schlüter, Phys. Rev. Lett. **51**, 1888 (1983).

[55] L. Hedin, Phys. Rev. **139**, A796 (1965).

[56] J. C. Slater and G. F. Koster, Phys. Rev. **94**, 1498 (1954).

[57] C. Wu, B. A. Bernevig and S.-C. Zhang, Phys. Rev. Lett. **96**, 106401 (2006).

[58] C. Xu and J. E. Moore, Phys. Rev. B **73**, 045322 (2006).

[59] J. Voit, Phys. Rev. B **47**, 6740 (1993).

[60] F. D. M. Haldane, Journal of Physics C: Solid State Physics **14**, 2585 (1981).

[61] Y. Jompol, C. J. B. Ford, J. P. Griffiths, I. Farrer, G. A. C. Jones, D. Anderson, D. A. Ritchie, T. W. Silk and A. J. Schofield, Science **325**, 597 (2009).

[62] M. Bockrath, D. H. Cobden, J. Lu, A. G. Rinzler, R. E. Smalley, L. Balents and P. L. McEuen, Nature **397**, 598 (1999).

[63] A. N. Aleshin, H. J. Lee, Y. W. Park and K. Akagi, Phys. Rev. Lett. **93**, 196601 (2004).

[64] C. Blumenstein, J. Schafer, S. Mietke, S. Meyer, A. Dollinger, M. Lochner, X. Y. Cui, L. Patthey, R. Matzdorf and R. Claessen, Nature Physics **7**, 776 (2011).

[65] W. Jolie, C. Murray, P. S. Weiß, J. Hall, F. Portner, N. Atodiresei, A. V. Krasheninnikov, C. Busse, H.-P. Komsa, A. Rosch and T. Michely, Phys. Rev. X **9**, 011055 (2019).

[66] A. M. Chang, L. N. Pfeiffer and K. W. West, Phys. Rev. Lett. **77**, 2538 (1996).

[67] M. Hohenadler, Z. Y. Meng, T. C. Lang, S. Wessel, A. Muramatsu and F. F. Assaad, Phys. Rev. B **85**, 115132 (2012).

[68] T. Li, P. Wang, H. Fu, L. Du, K. A. Schreiber, X. Mu, X. Liu, G. Sullivan, G. A. Csáthy, X. Lin and R.-R. Du, Phys. Rev. Lett. **115**, 136804 (2015).

[69] M. A. Van Hove, W. H. Weinberg and C.-M. Chan, *Low-Energy Electron Diffraction - Experiment, Theory and Surface Structure Determination*, Springer Science & Business Media, Berlin Heidelberg (2012).

[70] M. P. Seah and W. A. Dench, Surface and Interface Analysis **1**, 2 (1979).

[71] G. Binnig, H. Rohrer, C. Gerber and E. Weibel, Appl. Phys. Lett. **40**, 178 (1982).

[72] G. Binnig, H. Rohrer, C. Gerber and E. Weibel, Phys. Rev. Lett. **50**, 120 (1983).

[73] R. Wiesendanger, *Scanning Probe Microscopy and Spectroscopy - Methods and Applications*, new.. Aufl., Cambridge University Press, Cambridge (1994).

[74] C. J. Chen, *Introduction to Scanning Tunneling Microscopy*, 2nd edition. Aufl., OUP Oxford (2008).

[75] O. Fischer, M. Kugler, I. Maggio-Aprile, C. Berthod and C. Renner, Rev. Mod. Phys. **79**, 353 (2007).

[76] J. Bardeen, Phys. Rev. Lett. **6**, 57 (1961).

[77] M. H. Cohen, L. M. Falicov and J. C. Phillips, Phys. Rev. Lett. **8**, 316 (1962).

[78] J. Tersoff and D. R. Hamann, Phys. Rev. Lett. **50**, 1998 (1983).

[79] J. Tersoff and D. R. Hamann, Phys. Rev. B **31**, 805 (1985).

[80] M. Ternes, *Scanning tunneling spectroscopy at the single atom scale*, Ph.D. thesis, Laboratoire de physique des surfaces, Séction de physique, École polytechnique fédérale de Lausanne (2006).

[81] J. Klein, A. Léger, M. Belin, D. Défourneau and M. J. L. Sangster, Phys. Rev. B **7**, 2336 (1973).

[82] J.-F. Ge, M. Ovadia and J. E. Hoffman, Review of Scientific Instruments **90**, 101401 (2019).

[83] J. A. Sobota, Y. He and Z.-X. Shen, Rev. Mod. Phys. **93**, 025006 (2021).

[84] S. Hüfner, *Photoelectron Spectroscopy*, Springer, Berlin, Heidelberg (1995).

[85] A. Damascelli, Z. Hussain and Z.-X. Shen, Rev. Mod. Phys. **75**, 473 (2003).

[86] H. Hertz, Annalen der Physik **267**, 983 (1887).

[87] W. Hallwachs, Annalen der Physik **270**, 731 (1888).

[88] A. Einstein, Annalen der Physik **322**, 132 (1905).

[89] F. Himpsel, Advances in Physics **32**, 1 (1983).

[90] E. W. Plummer and W. Eberhardt, *Angle-Resolved Photoemission as a Tool for the Study of Surfaces*, pages 533–656, John Wiley & Sons, Ltd (1982).

[91] C. N. Berglund and W. E. Spicer, Phys. Rev. **136**, A1030 (1964).

[92] G. D. Mahan, Phys. Rev. B **2**, 4334 (1970).

[93] J. Minár, J. Braun, S. Mankovsky and H. Ebert, Journal of Electron Spectroscopy and Related Phenomena **184**, 91 (2011).

[94] S. Moser, Journal of Electron Spectroscopy and Related Phenomena **214**, 29 (2017).

[95] R. P. Day, B. Zwartsenberg, I. S. Elfimov and A. Damascelli, npj Quantum Materials **4**, 54 (2019).

[96] M. Schüler, T. Pincelli, S. Dong, T. P. Devereaux, M. Wolf, L. Rettig, R. Ernstorfer and S. Beaulieu, Phys. Rev. X **12**, 011019 (2022).

[97] J. D. Koralek, J. F. Douglas, N. C. Plumb, Z. Sun, A. V. Fedorov, M. M. Murnane, H. C. Kapteyn, S. T. Cundiff, Y. Aiura, K. Oka, H. Eisaki and D. S. Dessau, Phys. Rev. Lett. **96**, 017005 (2006).

[98] S. Tougaard and B. Jørgensen, Surface and Interface Analysis **7**, 17 (1985).

[99] D. A. Shirley, Phys. Rev. B **5**, 4709 (1972).

[100] M. Puppin, *Time- and angle-resolved photoemission spectroscopy on bidimensional semiconductors with a 500 kHz extreme ultraviolet light source*, Ph.D. thesis, Freie Universität Berlin (2017).

[101] M. Puppin, Y. Deng, C. W. Nicholson, J. Feldl, N. B. M. Schröter, H. Vita, P. S. Kirchmann, C. Monney, L. Rettig, M. Wolf and R. Ernstorfer, Review of Scientific Instruments **90**, 023104 (2019).

[102] A. McPherson, G. Gibson, H. Jara, U. Johann, T. S. Luk, I. A. McIntyre, K. Boyer and C. K. Rhodes, J. Opt. Soc. Am. B **4**, 595 (1987).

[103] M. Kotsugi, W. Kuch, F. Offi, L. I. Chelaru and J. Kirschner, Review of Scientific Instruments **74**, 2754 (2003).

[104] J. Maklar, S. Dong, S. Beaulieu, T. Pincelli, M. Dendzik, Y. W. Windsor, R. P. Xian, M. Wolf, R. Ernstorfer and L. Rettig, Review of Scientific Instruments **91**, 123112 (2020).

[105] R. Haight, J. A. Silberman and M. I. Lilie, Review of Scientific Instruments **59**, 1941 (1988).

[106] L. Perfetti, P. A. Loukakos, M. Lisowski, U. Bovensiepen, H. Berger, S. Biermann, P. S. Cornaglia, A. Georges and M. Wolf, Phys. Rev. Lett. **97**, 067402 (2006).

[107] J. K. Freericks, H. R. Krishnamurthy and T. Pruschke, Phys. Rev. Lett. **102**, 136401 (2009).

[108] T. Xu, T. Morimoto, A. Lanzara and J. E. Moore, Phys. Rev. B **99**, 035117 (2019).

[109] U. Fano, Phys. Rev. **124**, 1866 (1961).

[110] G. Drera, G. Salvinelli, F. Bondino, E. Magnano, M. Huijben, A. Brinkman and L. Sangaletti, Phys. Rev. B **90**, 035124 (2014).

[111] B. V. Shanabrook, O. J. Glembocki and W. T. Beard, Phys. Rev. B **35**, 2540 (1987).

[112] B. O. Seraphin and N. Bottka, Phys. Rev. **145**, 628 (1966).

[113] R. Enderlein, D. Jiang and Y. Tang, Phys. Stat. Sol.(b) **145**, 167 (1988).

[114] F. H. Pollak and O. J. Glembocki, *Modulation Spectroscopy Of Semiconductor Microstructures: An Overview*, in O. J. Glembocki, F. H. Pollak and F. A. Ponce, editors, *Spectroscopic Characterization Techniques for Semiconductor Technology III*, Band 0946, pages 2 – 35, International Society for Optics and Photonics, SPIE (1988).

[115] O. Glembocki and B. Shanabrook, Superlattices and Microstructures **3**, 235 (1987).

[116] K. V. Emtsev, A. Bostwick, K. Horn, J. Jobst, G. L. Kellogg, L. Ley, J. L. McChesney, T. Ohta, S. A. Reshanov, J. Rohrl, E. Rotenberg, A. K. Schmid, D. Waldmann, H. B. Weber and T. Seyller, Nature Materials **8**, 203 (2009).

[117] S. Glass, F. Reis, M. Bauernfeind, J. Aulbach, M. R. Scholz, F. Adler, L. Dudy, G. Li, R. Claessen and J. Schäfer, J. Phys. Chem. C **120**, 10361 (2016).

[118] M. J. X. Bauernfeind, *Bismuten auf SiC(0001): Optimierung der Substratgüte und Charakterisierung des Materialsystems*, Master's thesis, Julius-Maximilians Universität Würzburg (2016).

[119] T. Seyller, Journal of Physics: Condensed Matter **16**, S1755 (2004).

[120] U. Starke, physica status solidi (b) **202**, 475 (1997).

[121] J. A. Venables, G. D. T. Spiller and M. Hanbucken, Reports on Progress in Physics **47**, 399 (1984).

[122] Y. W. Mo, J. Kleiner, M. B. Webb and M. G. Lagally, Phys. Rev. Lett. **66**, 1998 (1991).

[123] A. Pimpinelli, J. Villain and D. E. Wolf, Phys. Rev. Lett. **69**, 985 (1992).

[124] M. Syperek, R. Stühler, A. Consiglio, P. Holewa, P. Wyborski, Ł. Dusanowski, F. Reis, S. Höfling, R. Thomale, W. Hanke, R. Claessen, D. Di Sante and C. Schneider, Nature Communications **13**, 6313 (2022).

[125] L. Wang, I. Meric, Y. Huang P., Q. Gao, Y. Gao, H. Tran, T. Taniguchi, K. Watanabe, M. Campos L., A. Muller D., J. Guo, P. Kim, J. Hone, L. Shepard K. and R. Dean C., Science **342**, 614 (2013).

[126] K. Komatsu, Y. Morita, E. Watanabe, D. Tsuya, K. Watanabe, T. Taniguchi and S. Moriyama, Science Advances **4**, eaaq0194 (2018).

[127] Z. Wu, B. T. Zhou, X. Cai, P. Cheung, G.-B. Liu, M. Huang, J. Lin, T. Han, L. An, Y. Wang, S. Xu, G. Long, C. Cheng, K. T. Law, F. Zhang and N. Wang, Nature Communications **10**, 611 (2019).

[128] F. Dominguez, B. Scharf, G. Li, J. Schäfer, R. Claessen, W. Hanke, R. Thomale and E. M. Hankiewicz, Phys. Rev. B **98**, 161407 (2018).

[129] R. Yu, W. Zhang, H.-J. Zhang, S.-C. Zhang, X. Dai and Z. Fang, Science **329**, 61 (2010).

[130] C.-X. Liu, S.-C. Zhang and X.-L. Qi, Annu. Rev. Condens. Matter Phys. **7**, 301 (2016).

[131] M. M. Otrokov, I. I. Klimovskikh, H. Bentmann, D. Estyunin, A. Zeugner, Z. S. Aliev, S. Gaß, A. U. B. Wolter, A. V. Koroleva, A. M. Shikin, M. Blanco-Rey, M. Hoffmann, I. P. Rusinov, A. Y. Vyazovskaya, S. V. Eremeev, Y. M. Koroteev, V. M. Kuznetsov, F. Freyse, J. Sánchez-Barriga, I. R. Amiraslanov, M. B. Babanly, N. T. Mamedov, N. A. Abdullayev, V. N. Zverev, A. Alfonsov, V. Kataev, B. Büchner, E. F. Schwier, S. Kumar, A. Kimura, L. Petaccia, G. Di Santo, R. C. Vidal, S. Schatz, K. Kißner, M. Ünzelmann, C. H. Min, S. Moser, T. R. F. Peixoto, F. Reinert, A. Ernst, P. M. Echenique, A. Isaeva and E. V. Chulkov, Nature **576**, 416 (2019).

[132] R. C. Vidal, A. Zeugner, J. I. Facio, R. Ray, M. H. Haghighi, A. U. B. Wolter, L. T. Corredor Bohorquez, F. Caglieris, S. Moser, T. Figgemeier, T. R. F. Peixoto, H. B. Vasili, M. Valvidares, S. Jung, C. Cacho, A. Alfonsov, K. Mehlawat, V. Kataev, C. Hess, M. Richter, B. Büchner, J. van den Brink, M. Ruck, F. Reinert, H. Bentmann and A. Isaeva, Phys. Rev. X **9**, 041065 (2019).

[133] Y. Deng, Y. Yu, M. Z. Shi, Z. Guo, Z. Xu, J. Wang, X. H. Chen and Y. Zhang, Science **367**, 895 (2020).

[134] C.-Z. Chang, J. Zhang, X. Feng, J. Shen, Z. Zhang, M. Guo, K. Li, Y. Ou, P. Wei, L.-L. Wang, Z.-Q. Ji, Y. Feng, S. Ji, X. Chen, J. Jia, X. Dai, Z. Fang, S.-C. Zhang, K. He, Y. Wang, L. Lu, X.-C. Ma and Q.-K. Xue, Science **340**, 167 (2013).

[135] C.-Z. Chang, W. Zhao, D. Y. Kim, H. Zhang, B. A. Assaf, D. Heiman, S.-C. Zhang, C. Liu, M. H. W. Chan and J. S. Moodera, Nature Materials **14**, 473 (2015).

[136] G. Li, *Private communication with Dr. Gang Li, School of Physical Science and Technology, Shanghai Tech University, Shanghai 200031, China.*

[137] S. Wozny, K. Vyborny, W. Belzig and S. I. Erlingsson, Phys. Rev. B **98**, 165423 (2018).

[138] B. Jäck, Y. Xie, B. Andrei Bernevig and A. Yazdani, Proceedings of the National Academy of Sciences **117**, 16214 (2020).

[139] S. Barja, S. Wickenburg, Z.-F. Liu, Y. Zhang, H. Ryu, M. Ugeda, Z. Hussain, Z.-X. Shen, S.-K. Mo, E. Wong, M. Salmeron, F. Wang, M. F. Crommie, D. F. Ogletree, J. Neaton and A. Weber-Bargioni, Nature Physics **12**, 751 (2016).

[140] S. Hüfner, G. Wertheim and J. Wernick, Solid State Communications **17**, 417 (1975).

[141] S. Doniach and M. Sunjic, Journal of Physics C: Solid State Physics **3**, 285 (1970).

[142] Y. A. Bychkov and E. I. Rashba, Soviet Journal of Experimental and Theoretical Physics Letters **39**, 78 (1984).

[143] Y. A. Bychkov and E. I. Rashba, Journal of Physics C: Solid State Physics **17**, 6039 (1984).

[144] C. R. Ast, J. Henk, A. Ernst, L. Moreschini, M. C. Falub, D. Pacilé, P. Bruno, K. Kern and M. Grioni, Phys. Rev. Lett. **98**, 186807 (2007).

[145] I. Gierz, T. Suzuki, E. Frantzeskakis, S. Pons, S. Ostanin, A. Ernst, J. Henk, M. Grioni, K. Kern and C. R. Ast, Phys. Rev. Lett. **103**, 046803 (2009).

[146] K. Sakamoto, H. Kakuta, K. Sugawara, K. Miyamoto, A. Kimura, T. Kuzumaki, N. Ueno, E. Annese, J. Fujii, A. Kodama, T. Shishidou, H. Namatame, M. Taniguchi, T. Sato, T. Takahashi and T. Oguchi, Phys. Rev. Lett. **103**, 156801 (2009).

[147] K. Sakamoto, T. Oda, A. Kimura, K. Miyamoto, M. Tsujikawa, A. Imai, N. Ueno, H. Namatame, M. Taniguchi, P. E. J. Eriksson and R. I. G. Uhrberg, Phys. Rev. Lett. **102**, 096805 (2009).

[148] D. Marchenko, A. Varykhalov, M. R. Scholz, G. Bihlmayer, E. I. Rashba, A. Rybkin, A. M. Shikin and O. Rader, Nature Communications **3**, 1232 (2012).

[149] J. H. Dil, Journal of Physics: Condensed Matter **21**, 403001 (2009).

[150] Y. M. Koroteev, G. Bihlmayer, J. E. Gayone, E. V. Chulkov, S. Blügel, P. M. Echenique and P. Hofmann, Phys. Rev. Lett. **93**, 046403 (2004).

[151] C. Brun, K. H. Müller, I.-P. Hong, F. Patthey, C. Flindt and W.-D. Schneider, Phys. Rev. Lett. **108**, 126802 (2012).

[152] E. Frantzeskakis, S. Pons and M. Grioni, Phys. Rev. B **82**, 085440 (2010).

[153] M. H. Berntsen, O. Götberg and O. Tjernberg, Phys. Rev. B **97**, 125148 (2018).

[154] L. Chi, J. Nogami and C. V. Singh, Phys. Rev. B **103**, 075405 (2021).

[155] D. V. Gruznev, L. V. Bondarenko, A. V. Matetskiy, A. A. Yakovlev, A. Y. Tupchaya, S. V. Eremeev, E. V. Chulkov, J.-P. Chou, C.-M. Wei, M.-Y. Lai, Y.-L. Wang, A. V. Zotov and A. A. Saranin, Scientific Reports **4**, 4742 (2014).

[156] V. Stimper, S. Bauer, R. Ernstorfer, B. Schölkopf and R. P. Xian, IEEE Access **7**, 165437 (2019).

[157] A. M. Tokmachev, D. V. Averyanov, O. E. Parfenov, A. N. Taldenkov, I. A. Karateev, I. S. Sokolov, O. A. Kondratev and V. G. Storchak, Nature Communications **9**, 1672 (2018).

[158] D. V. Averyanov, I. S. Sokolov, M. S. Platunov, F. Wilhelm, A. Rogalev, P. Gargiani, M. Valvidares, N. Jaouen, O. E. Parfenov, A. N. Taldenkov, I. A. Karateev, A. M. Tokmachev and V. G. Storchak, Nano Research **13**, 3396 (2020).

[159] R. Stühler, A. Kowalewski, F. Reis, D. Jungblut, F. Dominguez, B. Scharf, G. Li, J. Schäfer, E. M. Hankiewicz and R. Claessen, Nature Communications **13**, 3480 (2022).

[160] J. Lahiri, Y. Lin, P. Bozkurt, I. I. Oleynik and M. Batzill, Nature Nanotechnology **5**, 326 (2010).

[161] L. Wang, Y. Wu, Y. Yu, A. Chen, H. Li, W. Ren, S. Lu, S. Ding, H. Yang, Q.-K. Xue, F.-S. Li and G. Wang, ACS Nano **14**, 8299 (2020).

[162] E. N. Lima, T. M. Schmidt and R. W. Nunes, Nano Lett. **16**, 4025 (2016).

[163] B. Zhou, H.-Z. Lu, R.-L. Chu, S. Q. Shen and Q. Niu, Phys. Rev. Lett. **101**, 246807 (2008).

[164] V. Krueckl and K. Richter, Phys. Rev. Lett. **107**, 086803 (2011).

[165] F. Romeo, R. Citro, D. Ferraro and M. Sassetti, Phys. Rev. B **86**, 165418 (2012).

[166] R. P. Maciel, A. L. Araújo, C. H. Lewenkopf and G. J. Ferreira, Phys. Rev. B **103**, 205124 (2021).

[167] H. Ishida and A. Liebsch, Phys. Rev. Research **2**, 023242 (2020).

[168] Y. Takagaki, Journal of Physics: Condensed Matter **24**, 435301 (2012).

[169] Y. Takagaki, Journal of Applied Physics **118**, 054304 (2015).

[170] J. Strunz, J. Wiedenmann, C. Fleckenstein, L. Lunczer, W. Beugeling, V. L. Müller, P. Shekhar, N. T. Ziani, S. Shamim, J. Kleinlein, H. Buhmann, B. Trauzettel and L. W. Molenkamp, Nature Physics **16**, 83 (2020).

[171] J. Jung, A. Odobesko, R. Boshuis, A. Szczerbakow, T. Story and M. Bode, Phys. Rev. Lett. **126**, 236402 (2021).

[172] P. Koskinen, S. Malola and H. Häkkinen, Phys. Rev. Lett. **101**, 115502 (2008).

[173] P. Koskinen, S. Malola and H. Häkkinen, Phys. Rev. B **80**, 073401 (2008).

[174] c. O. Girit, J. C. Meyer, R. Erni, M. D. Rossell, C. Kisielowski, L. Yang, C.-H. Park, M. F. Crommie, M. L. Cohen, S. G. Louie and A. Zettl, Science **323**, 1705 (2009).

[175] W. Liang, M. Bockrath, D. Bozovic, J. H. Hafner, M. Tinkham and H. Park, Nature **411**, 665 (2001).

[176] J. Seo, P. Roushan, H. Beidenkopf, Y. S. Hor, R. J. Cava and A. Yazdani, Nature **466**, 343 (2010).

[177] J. Maklar, R. Stühler, M. Dendzik, T. Pincelli, S. Dong, S. Beaulieu, A. Neef, G. Li, M. Wolf, R. Ernstorfer, R. Claessen and L. Rettig, *Time- and momentum-resolved signatures of edge states in a 2D topological insulator* (2021).

[178] Z. Pedramrazi, C. Herbig, A. Pulkin, S. Tang, M. Phillips, D. Wong, H. Ryu, M. Pizzochero, Y. Chen, F. Wang, E. J. Mele, Z.-X. Shen, S.-K. Mo, O. V. Yazyev and M. F. Crommie, Nano Letters **19**, 5634 (2019).

[179] S. Howard, L. Jiao, Z. Wang, N. Morali, R. Batabya, P. Kumar-Nag, N. Avraham, H. Beidenkopf, P. Vir, E. Liu, C. Shekhar, C. Felser, T. Hughes and V. Madhavan, Nature Communications **12**, 4269 (2021).

[180] J. Liu, T. H. Hsieh, P. Wei, W. Duan, J. Moodera and L. Fu, Nature Materials **13**, 178 (2013).

[181] P. Michetti and B. Trauzettel, Appl. Phys. Lett. **102**, 063503 (2013).

[182] X. Qian, J. Liu, L. Fu and J. Li, Science **346**, 1344 (2014).

[183] G. Strinati, H. J. Mattausch and W. Hanke, Phys. Rev. Lett. **45**, 290 (1980).

[184] G. Strinati, H. J. Mattausch and W. Hanke, Phys. Rev. B **25**, 2867 (1982).

[185] J. P. Perdew and M. Levy, Phys. Rev. Lett. **51**, 1884 (1983).

[186] M. K. Y. Chan and G. Ceder, Phys. Rev. Lett. **105**, 196403 (2010).

[187] M. Jain, J. R. Chelikowsky and S. G. Louie, Phys. Rev. Lett. **107**, 216806 (2011).

[188] J.-D. Chai and P.-T. Chen, Phys. Rev. Lett. **110**, 033002 (2013).

[189] M. S. Hybertsen and S. G. Louie, Phys. Rev. B **34**, 5390 (1986).

[190] G. Strinati, La Rivista del Nuovo Cimento (1978-1999) **11**, 1 (1988).

[191] G. Onida, L. Reining and A. Rubio, Rev. Mod. Phys. **74**, 601 (2002).

[192] M. Shishkin and G. Kresse, Phys. Rev. B **75**, 235102 (2007).

[193] H. Jiang and P. Blaha, Phys. Rev. B **93**, 115203 (2016).

[194] M. Grumet, P. Liu, M. Kaltak, J. c. v. Klimeš and G. Kresse, Phys. Rev. B **98**, 155143 (2018).

[195] P. Giannozzi, S. Baroni, N. Bonini, M. Calandra, R. Car, C. Cavazzoni, D. Ceresoli, G. L. Chiarotti, M. Cococcioni, I. Dabo, A. D. Corso, S. de Gironcoli, S. Fabris, G. Fratesi, R. Gebauer, U. Gerstmann, C. Gougoussis, A. Kokalj, M. Lazzeri, L. Martin-Samos, N. Marzari, F. Mauri, R. Mazzarello, S. Paolini, A. Pasquarello, L. Paulatto, C. Sbraccia, S. Scandolo, G. Sclauzero, A. P. Seitsonen, A. Smogunov, P. Umari and R. M. Wentzcovitch, J. Phys. Condens. Matter **21**, 395502 (2009).

[196] A. Marini, Phys. Rev. Lett. **101**, 106405 (2008).

[197] D. Y. Qiu, F. H. da Jornada and S. G. Louie, Phys. Rev. Lett. **111**, 216805 (2013).

[198] K. F. Mak, C. Lee, J. Hone, J. Shan and T. F. Heinz, Phys. Rev. Lett. **105**, 136805 (2010).

[199] D. Sangalli, A. Ferretti, H. Miranda, C. Attaccalite, I. Marri, E. Cannuccia, P. Melo, M. Marsili, F. Paleari, A. Marrazzo, G. Prandini, P. Bonfà, M. O. Atambo, F. Affinito, M. Palummo, A. Molina-Sánchez, C. Hogan, M. Grüning, D. Varsano and A. Marini, J. Condens. Matter Phys. **31**, 325902 (2019).

[200] A. Marini, C. Hogan, M. Grüning and D. Varsano, Comput. Phys. Commun. **180**, 1392 (2009).

[201] W. Hanke and L. J. Sham, Phys. Rev. B **12**, 4501 (1975).

[202] W. Hanke and L. J. Sham, Phys. Rev. Lett. **43**, 387 (1979).

[203] W. Hanke and L. J. Sham, Phys. Rev. B **21**, 4656 (1980).

[204] M. Rohlfing and S. G. Louie, Phys. Rev. Lett. **81**, 2312 (1998).

[205] X. Zhang, W.-Y. Shan and D. Xiao, Phys. Rev. Lett. **120**, 077401 (2018).

[206] T. Cao, M. Wu and S. G. Louie, Phys. Rev. Lett. **120**, 087402 (2018).

[207] G. Xu, T. Zhou, B. Scharf and I. Žutić, Phys. Rev. Lett. **125**, 157402 (2020).

[208] B. Scharf et al., (to be published).

[209] B. Seradjeh, J. E. Moore and M. Franz, Phys. Rev. Lett. **103**, 066402 (2009).

[210] D. I. Pikulin and T. Hyart, Phys. Rev. Lett. **112**, 176403 (2014).

[211] L. Du, X. Li, W. Lou, G. Sullivan, K. Chang, J. Kono and R.-R. Du, Nature Communications **8**, 1971 (2017).

[212] K. Chen and R. Shindou, Phys. Rev. B **96**, 161101 (2017).

[213] A. Blason and M. Fabrizio, Phys. Rev. B **102**, 035146 (2020).

[214] A. Blason and M. Fabrizio, Phys. Rev. B **102**, 035146 (2020).

[215] D. Varsano, M. Palummo, E. Molinari and M. Rontani, Nature Nanotechnology **15**, 367 (2020).

[216] F. Wu, T. Lovorn and A. H. MacDonald, Phys. Rev. Lett. **118**, 147401 (2017).

[217] A. Janot, B. Rosenow and G. Refael, Phys. Rev. B **93**, 161111 (2016).

[218] J. Maklar, R. Stühler, M. Dendzik, T. Pincelli, S. Dong, S. Beaulieu, A. Neef, G. Li, M. Wolf, R. Ernstorfer, R. Claessen and L. Rettig, Nano Lett. **22**, 5420 (2022).

[219] J. C. Johannsen, S. Ulstrup, F. Cilento, A. Crepaldi, M. Zacchigna, C. Cacho, I. C. E. Turcu, E. Springate, F. Fromm, C. Raidel, T. Seyller, F. Parmigiani, M. Grioni and P. Hofmann, Phys. Rev. Lett. **111**, 027403 (2013).

[220] S. Ulstrup, A. G. Čabo, D. Biswas, J. M. Riley, M. Dendzik, C. E. Sanders, M. Bianchi, C. Cacho, D. Matselyukh, R. T. Chapman, E. Springate, P. D. C. King, J. A. Miwa and P. Hofmann, Phys. Rev. B **95**, 041405 (2017).

[221] M. Julien, L. Man Michael K., S. Chakradhar, C. Marshall, P. Vivek, W. E. Laine, A.-M. Abdullah, S. Chan Nicholas, K. Arka, M. B. M. Krishna, L. Xiaoqin, F. Heinz Tony, C. Ting and M. Dani Keshav, Science **370**, 1199 (2020).

[222] L. Man Michael K., M. Julien, S. Chakradhar, X. Kaichen, C. Marshall, P. Vivek, K. Arka, W. E. Laine, A.-M. Abdullah, S. Chan Nicholas, R. Bacon David, Z. Xing, M. Abdelrasoul Mohamed M., L. Xiaoqin, F. Heinz Tony, da Jornada Felipe H., C. Ting and M. Dani Keshav, Science Advances **7**, eabg0192 (2021).

[223] A. Sven, R. Antonio, C.-C. Mariana, K. Razvan, A. Benito, S. Benjamin, A. Martin, F. Stiven, F. Filippo, C. Camilla and G. Isabella, Science Advances **6**, eaay0761 (2021).

[224] F. Liu, Q. Li and X.-Y. Zhu, Phys. Rev. B **101**, 201405 (2020).

[225] R. Wallauer, R. Perea-Causin, L. Münster, S. Zajusch, S. Brem, J. Güdde, K. Tanimura, K.-Q. Lin, R. Huber, E. Malic and U. Höfer, Nano Lett. **21**, 5867 (2021).

[226] S. Ulstrup, A. G. Čabo, J. A. Miwa, J. M. Riley, S. S. Grønborg, J. C. Johannsen, C. Cacho, O. Alexander, R. T. Chapman, E. Springate, M. Bianchi, M. Dendzik, J. V. Lauritsen, P. D. C. King and P. Hofmann, ACS Nano **10**, 6315 (2016).

[227] F. Liu, M. E. Ziffer, K. R. Hansen, J. Wang and X. Zhu, Phys. Rev. Lett. **122**, 246803 (2019).

[228] W. Lee, Y. Lin, L.-S. Lu, W.-C. Chueh, M. Liu, X. Li, W.-H. Chang, R. A. Kaindl and C.-K. Shih, Nano Lett. **21**, 7363 (2021).

[229] A. G. Čabo, J. A. Miwa, S. S. Grønborg, J. M. Riley, J. C. Johannsen, C. Cacho, O. Alexander, R. T. Chapman, E. Springate, M. Grioni, J. V. Lauritsen, P. D. C. King, P. Hofmann and S. Ulstrup, Nano Lett. **15**, 5883 (2015).

[230] O. Karni, E. Barré, V. Pareek, J. D. Georgaras, M. K. L. Man, C. Sahoo, D. R. Bacon, X. Zhu, H. B. Ribeiro, A. L. O'Beirne, J. Hu, A. Al-Mahboob, M. M. M. Abdelrasoul, N. S. Chan, A. Karmakar, A. J. Winchester, B. Kim, K. Watanabe, T. Taniguchi, K. Barmak, J. Madéo, F. H. da Jornada, T. F. Heinz and K. M. Dani, Nature **603**, 247 (2022).

[231] M. Puppin, C. W. Nicholson, C. Monney, Y. Deng, R. P. Xian, J. Feldl, S. Dong, A. Dominguez, H. Hübener, A. Rubio, M. Wolf, L. Rettig and R. Ernstorfer, Phys. Rev. B **105**, 075417 (2022).

[232] E. J. Baerends, O. V. Gritsenko and R. van Meer, Phys. Chem. Chem. Phys. **15**, 16408 (2013).

[233] F. Himpsel, Surface Science Reports **12**, 3 (1990).

[234] M. Rohlfing and S. G. Louie, Phys. Rev. B **62**, 4927 (2000).

[235] E. Perfetto, Y. Pavlyukh and G. Stefanucci, Phys. Rev. Lett. **128**, 016801 (2022).

[236] M. Rohlfing and J. Pollmann, Phys. Rev. Lett. **84**, 135 (2000).

[237] H. Wang Y., H. Steinberg, P. Jarillo-Herrero and N. Gedik, Science **342**, 453 (2013).

[238] E. J. Sie, T. Rohwer, C. Lee and N. Gedik, Nature Communications **10**, 3535 (2019).

[239] S. Dong, M. Puppin, T. Pincelli, S. Beaulieu, D. Christiansen, H. Hübener, C. W. Nicholson, R. P. Xian, M. Dendzik, Y. Deng, Y. W. Windsor, M. Selig, E. Malic, A. Rubio, A. Knorr, M. Wolf, L. Rettig and R. Ernstorfer, Natural Sciences **1**, e10010 (2021).

[240] E. Perfetto, D. Sangalli, A. Marini and G. Stefanucci, Phys. Rev. B **94**, 245303 (2016).

[241] A. Steinhoff, M. Florian, M. Rösner, G. Schönhoff, T. O. Wehling and F. Jahnke, Nature Communications **8**, 1166 (2017).

[242] A. Rustagi and A. F. Kemper, Phys. Rev. B **97**, 235310 (2018).

[243] E. Perfetto, D. Sangalli, A. Marini and G. Stefanucci, Phys. Rev. Materials **3**, 124601 (2019).

[244] D. Christiansen, M. Selig, E. Malic, R. Ernstorfer and A. Knorr, Phys. Rev. B **100**, 205401 (2019).

[245] E. Perfetto, S. Bianchi and G. Stefanucci, Phys. Rev. B **101**, 041201 (2020).

[246] G. Stefanucci and E. Perfetto, Phys. Rev. B **103**, 245103 (2021).

[247] S.-L. Yang, J. A. Sobota, D. Leuenberger, Y. He, M. Hashimoto, D. H. Lu, H. Eisaki, P. S. Kirchmann and Z.-X. Shen, Phys. Rev. Lett. **114**, 247001 (2015).

[248] R. Bertoni, C. W. Nicholson, L. Waldecker, H. Hübener, C. Monney, U. De Giovannini, M. Puppin, M. Hoesch, E. Springate, R. T. Chapman, C. Cacho, M. Wolf, A. Rubio and R. Ernstorfer, Phys. Rev. Lett. **117**, 277201 (2016).

[249] P. Hein, A. Stange, K. Hanff, L. X. Yang, G. Rohde, K. Rossnagel and M. Bauer, Phys. Rev. B **94**, 205406 (2016).

[250] B. Keimer and J. E. Moore, Nature Physics **13**, 1045 (2017).

[251] P. A. M. Dirac, Proceedings of the Royal Society of London. Series A, Containing Papers of a Mathematical and Physical Character **117**, 610 (1928).

[252] L. L. Foldy and S. A. Wouthuysen, Phys. Rev. **78**, 29 (1950).

[253] L. D. Landau and E. M. Lifshitz, *Relativistic quantum theory*, Pergamon Press (1971).

[254] R. M. Martin, *Electronic Structure - Basic Theory and Practical Methods*, Cambridge University Press, Cambridge (2004).

[255] G. D. Mahan, *Many-Particle Physics*, Springer, Boston, MA (2000).

[256] G. H. Wannier, Phys. Rev. **52**, 191 (1937).

[257] R. J. Elliott, Phys. Rev. **108**, 1384 (1957).

[258] W. Hanke, Festkörperprobleme **19**, 43 (1979).

[259] H. Shi, H. Pan, Y.-W. Zhang and B. I. Yakobson, Phys. Rev. B **87**, 155304 (2013).

[260] D. Y. Qiu, F. H. da Jornada and S. G. Louie, Phys. Rev. B **93**, 235435 (2016).

[261] M. M. Ugeda, A. J. Bradley, S.-F. Shi, F. H. da Jornada, Y. Zhang, D. Y. Qiu, W. Ruan, S.-K. Mo, Z. Hussain, Z.-X. Shen, F. Wang, S. G. Louie and M. F. Crommie, Nature Materials **13**, 1091 (2014).

[262] A. Ramasubramaniam, Phys. Rev. B **86**, 115409 (2012).

[263] F. Hüser, T. Olsen and K. S. Thygesen, Phys. Rev. B **88**, 245309 (2013).

[264] H.-P. Komsa and A. V. Krasheninnikov, Phys. Rev. B **86**, 241201 (2012).

[265] F. Bloch, Zeitschrift für Physik **52**, 555 (1929).

[266] B. Bradlyn, L. Elcoro, J. Cano, M. G. Vergniory, Z. Wang, C. Felser, M. I. Aroyo and B. A. Bernevig, Nature **547**, 298 (2017).

[267] E. Prodan and H. Schulz-Baldes, *Bulk and Boundary Invariants for Complex Topological Insulators - From K-Theory to Physics*, Springer, Cham (2016).

[268] X.-L. Qi and S.-C. Zhang, Rev. Mod. Phys. **83**, 1057 (2011).

[269] A. B. Bernevig and T. L. Hughes, *Topological Insulators and Topological Superconductors*, Princeton University Press, Princeton and Oxford (2013).

[270] C.-K. Chiu, J. C. Y. Teo, A. P. Schnyder and S. Ryu, Rev. Mod. Phys. **88**, 035005 (2016).

[271] M. V. Berry, Proceedings of the Royal Society of London. A. Mathematical and Physical Sciences **392**, 45 (1984).

[272] M. Nakahara, *Geometry, Topology and Physics*, second edition. Aufl., CRC Press, Boca Raton, Fla (2003).

[273] J. E. Avron, D. Osadchy and R. Seiler, Physics Today **56**, 38 (2003).

[274] A. Bansil, H. Lin and T. Das, Rev. Mod. Phys. **88**, 021004 (2016).

[275] M. Schmid, H.-P. Steinrück and J. M. Gottfried, Surface and Interface Analysis **46**, 505 (2014).

List of publications

Published research articles:

- M. Syperek†, R. Stühler†, A. Consiglio†, P. Holewa, P. Wyborski, Ł. Dusanowski, F. Reis, S. Höfling, R. Thomale, W. Hanke, R. Claessen, D. Di Sante, and C. Schneider, "Observation of room temperature excitons in an atomically thin topological insulator", *Nat Commun* **13**, 6313 (2022). DOI: 10.1038/s41467-022-33822-8
  †These authors contributed equally.

- J. Maklar, R. Stühler, M. Dendzik, T. Pincelli, S. Dong, S. Beaulieu, A. Neef, G. Li, M. Wolf, R. Ernstorfer, R. Claessen, and L. Rettig, "Ultrafast Momentum-Resolved Hot Electron Dynamics in the Two-Dimensional Topological Insulator Bismuthene", *Nano Lett.* **22**, 5420 – 5426 (2022). DOI: 10.1021/acs.nanolett.2c01462

- R. Stühler, A. Kowalewski, F. Reis, D. Jungblut, F. Dominguez, B. Scharf, G. Li, J. Schäfer, E. M. Hankiewicz, and R. Claessen, "Effective lifting of the topological protection of quantum spin Hall edge states by edge coupling", *Nat Commun* **15**, 3480 (2022). DOI: 10.1038/s41467-022-30996-z

- R. Stühler, F. Reis, T. Müller, T. Helbig, T. Schwemmer, R. Thomale, J. Schäfer, and R. Claessen, "Tomonaga–Luttinger liquid in the edge channels of a quantum spin Hall insulator", *Nature Physics* **16**, 47–51 (2020). DOI: 10.1038/s41567-019-0697-z

- S. Bieker, R. Stühler, T. Kiessling, W. Ossau, and L. W. Molenkamp, "Dimensional crossover of free exciton diffusion in etched GaAs wire structures", *Appl. Phys. Lett.* **107**, 122106 (2015). DOI: 10.1063/1.4931369

Danksagung

Viele Menschen haben mich während der Zeit, in der diese Arbeit entstanden ist, begleitet, mich unterstützt, und mir letzlich das erfolgreiche Abschließen meiner Promotion ermöglicht. Meinen besonderen Dank richte ich dabei an:

- Prof. Dr. Ralph Claessen, für die Aufnahme an diesem tollen Lehrstuhl, die Möglichkeit durch die Bereitstellung der nötigen Rahmenbedingungen meine Promotion durchführen zu können und schließlich für die Betreuung dieser Arbeit. Ihr konstruktives Feedback half mir stets wissenschaftlich über den eigenen Tellerrand hinaus zu sehen und mündete so erst in der erfolgreichen Anfertigung wissenschaftlicher Publikationen. Ich möchte mich besonders für die geförderte Teilnahme an Tagungung, Workshops, Sommerschulen, und ganz besonders der Nobelpreisträger Tagung in Lindau, bedanken.

- Prof. Dr. Jörg Schäfer, für die wissenschaftlichen Diskussionen, für Rat und Tat, und für die stets motivierenden Worte. Die kreativen experimentellen Vorschläge lieferten dabei oft Denkanstöße in neue Richtungen.

- Alle Kollegen aus der Experimentellen Physik IV, besonders an diejenigen mit denen ich in den Jahren meiner Promotion Zeit verbringen durfte. Dabei will ich zu aller erst Felix Reis danken, der mich als Betreuer meiner Masterarbeit mit der Thematik meiner späteren Promotion vertraut machte. Das Arbeiten mit Dir hat mir großen Spaß bereitet. Zudem will ich besonders André Kowalewski, Jonas Erhardt, Tim Wagner, Maximilian Bauernfeind, Berengar Leikert, Philipp Keßler, Matthias Schmitt, Victor Rogalev, Florian Adler, Louis Veyrat, Philipp Schütz, Philipp Scheiderer, Judith Gabel, und Lenard Dudy danken, die mir alle bestimmt unzählige Male mit einer helfenden Hand tatkräftig zur Seite standen.

- Armando Consiglio, Dr. Domenico Di Sante und Prof. Dr. Werner Hanke für interessante Diskussionen über die theoretischen Aspekte meiner Arbeit und natürlich für die gute Zusammenarbeit. Eure unterstützende Arbeit hat mich besonders zu einem tieferen theoretischen Verständnis rund um mein Thema geführt.

- Julian Maklar, Dr. Laurenz Rettig, Dr. Maciej Dendzik, Prof. Dr. Martin Wolf und Prof. Dr. Ralph Ernstorfer für die mehrmalige gastfreundliche Einladung nach Berlin und die ermöglichten Messungen an eurem tollen trARPES setup. Die Zusammenarbeit war immer sehr angenehm und überaus produktiv.

- Dr. Marcin Syperek, Dr. Łukasz Dusanowski und Prof. Dr. Christian Schneider für die tolle Zusammenarbeit und das lange Durchhaltevermögen das nach langen Anlaufschwierigkeiten schließlich die ersten erfolgreichen optischen Messungen an Wismuten erst ermöglicht hat.

- Dimitri Jungblut, Dr. Fernando Dominguez, Dr. Benjamin Scharf und Prof. Dr. Ewelina Hankiewicz für die wichtige theoretische Unterstützung bei dem Thema Domänengrenzen und die daraus gewonnenen Erkentnisse.

- Monika Seifer für Deine herzliche Art, die Hilfe bei allem was an Problemen während der Arbeit so aufgetreten kann und dafür immer ein offenes Ohr für mich und alle EP4'ler zu haben.

- Janina, die mich in all der Zeit begleitet hat und mir in guten und schlechten Zeiten immer zur Seite stand. Vielen Dank für deine Geduld und deine Liebe!

- Meine Eltern und meine Schwester, die mich immer bedingungslos unterstützt haben. Ich weiß ich werde auch in Zukunft immer auf eure Unterstützung zählen können!